Low-Energy Ion Beamline-Scattering Apparatus with Application to Charge Exchange Collisions at Surfaces

Thesis By

Michael J. Gordon

In Partial Fulfillment of the Requirements

for the Degree of

Doctor of Philosophy

CALIFORNIA INSTITUTE OF TECHNOLOGY

Pasadena, California

2004

(Defended 1 October 2003)

To my parents

Acknowledgements

Writing this section has been very difficult because it is simply not possible to reduce the past many years of friendship, assistance, and experiences to just a few pages. However, I shall try. I would first like to thank my advisor, Dr. Kostas Giapis, for sticking with me all these long years in constructing ″the machine″ by devoting so much of his research efforts and interest to just one project. His support and encouragement over the years along with our common desire to look at things in a very careful and fundamental way have made the scattering system a reality. The freedom to build up the lab and the entire scattering machine has been an invaluable experience, which I know I would never have obtained in any other place or lab. For this, I am extremely grateful and also well prepared to set up my own lab in the coming years. On the lighter side, we have had some memorable times together rebuilding countless vacuum pumps (the first few were fun), cleaning up water floods, car talk, and wine at the Ath.

I would also like to thank my thesis committee: Dr. Mark Davis, Dr. Noel Corngold, and Dr. Mitchio Okumura. In addition, I must thank the Intel Foundation and Applied Materials for personal funding during my thesis work.

Building the ion beamline and scattering system has been an enormous undertaking and I would have never been able to accomplish it without the unending help, guidance, and hard work of Mr. Mike Roy in the Chemistry machine shop. Mike and I joined Caltech around the same time and our friendship has developed over the years. Mike has taught me how to machine using the lathe, mill, and CNC system as well as TIG weld. Both of us have personally lived the ups and downs of building the ion beamline as almost every piece of the system has been machined by our hands. I have not met anyone in my life that is more genuine, tirelessly helpful, and willing to go the extra mile than Mike Roy. In many respects, my second lab has been the Chemistry machine shop because of the countless hours I have spent bent over the mill and lathe. I want to also thank Mr. Ray Garcia in the machine shop for all his help over the years. The gentlemen in the shop were gracious enough to let me be their apprentice (although Mike says I’m definitely a journeyman now) throughout the years, and they were always

willing to listen, encourage, and laugh ─ all of which lessened the effect of difficult times. They allowed me unlimited access to the machines in the main shop and put up with all my complicated and off-the-wall machining needs ─ which has made the difference in getting the entire scattering system up and running. I enjoyed having these friends in the shop immensely and I will be very sad to say goodbye.

When I first joined the Giapis group, Dr. Cheryl Anderson introduced me to the lab, vacuum stuff, cryo-pumps, and the CO_2 laser ″beast.″ I think we both have lived more than 2 million pulses (at 1 Hz) beating away at a small puff of SF_6, as well as rebuild after rebuild on the piezo-valve. I have fond memories of her snowflakes in the ziplock baggie, the lab squid, happy clam, and the endless ″mousie″ references. In addition, I must thank Mohan Sankaran, whose help and camaraderie over the years has been very valuable.

Several years ago, I had the pleasure of working with Dr. Toshiki Nakano, who visited our group over one summer to help set up an LIF system. His expertise and ″midas″ touch with our stubborn (and very old) nitrogen pumped dye laser enabled an important LIF experiment on the initial beam source we were considering for scattering studies. As a result of the LIF, we switched gears and focused on constructing the ion beamline system as a more idealized beam source. I have not met any other professor so willing to work tirelessly, day after day, to get something going. He and I made quite a team and I hope I have the pleasure of working with someone like Toshiki in the future.

During my time at Caltech, I met the best friend I have ever had ─ Dr. Patrick Piccione. Patrick was such a great fellow in many ways and someone who really understood and appreciated so many aspects of life in the way that I do. He was open-minded, willing to chat, goof off, and talk till the wee hours of the morning about philosophy, off the wall (recreational?) math, religion, plants, rocks, sea-life, and other more esoteric stuff. His company and kind words during hard times were invaluable. We have had some wonderful times at Christmas tree cove diving in the kelp forests (freezing our butts off), Joshua Tree with the coyotes (″….do what you can″), taking out the telescope, and climbing in the mountains.

Finally, I want to thank the most important people in my life: my parents. They have lived the roller-coaster ride of building the machine, long hours of being sick of

machining parts, and struggling along as one problem got solved – only to open up others. Their many visits, cute cards, and constant encouragement have kept me going till the end, all these long years. Their love and unending desire for my happiness and satisfaction in whatever I set out to do have made *all the difference in the world*. I would like to say them that their LBS has finally ″done all the steps.″

Additionally, I would like to thank Phileas, Phyllis, St. Peter, Stingy, Perlmutter, and last but not least, my good buddy Alex, who continually popped up in so many conversations at just the right moment to lighten up the mood.

Michael J. Gordon
Pasadena, California
October, 2003

Abstract

Ion-surface interactions are important in a variety of fields such as plasma physics, surface analysis, and semiconductor manufacturing. However, the low-energy regime (50 eV - 1 keV) has been generally avoided by the research community because of the experimental challenges associated with providing sufficient ion beam current at low impact energy to conduct surface scattering studies. This energy regime is a useful range to study because threshold physical and chemical processes occur at low energies. We have set out to probe this neglected energy range by developing an ion scattering system to investigate a wide variety of ion-surface interaction phenomena below 1 keV. This thesis describes the design and construction of our system and its application to charge exchange collisions at surfaces.

Our design philosophy has been to take an inductively coupled plasma (ICP) source and couple it to a high-voltage ion beam transport line with magnetic mass-filtering to provide a clean ion beam surface probe with high current (>100 $\mu A/cm^2$) and tunable energy (~50 eV - 1 keV). Space charge repulsion between the ions, which usually precludes high current at low energy, is circumvented using the accel-decel scheme for transport. In this arrangement, ions are created at the desired collision energy in the plasma source, extracted and accelerated to high transport energy (to fight space charge forces), and then decelerated back down to their original creation potential right before impacting the grounded target. In this way, the beam current is high, the collision energy is easily tunable (just by floating the whole plasma source above ground), and the target is always kept grounded. The ICP-based beamline is a generic and robust system because any ion created in the plasma can be individually singled out and delivered to the target as a clean surface probe composed of only one species and one charge state.

The particle flux leaving the target surface is analyzed with a hybrid scattered product detector which allows simultaneous mass and energy filtering. The detector combines an electron-impact ionizer, hemispherical electrostatic sector, and quadrupole mass filter in series with single ion detection capabilities so that small signals of both ions and neutrals can be analyzed. Energy dispersion, followed by mass dispersion, is an

effective combination because overlapping signals can be separated easily (i.e., multiple charge states or a mix of ion species leaving the target).

The performance of the entire scattering system has been evaluated in an investigation of Ne^{+} scattering off lighter target materials (Mg, Al, Si , and Ti), where the scattered particle flux can contain inelastic Ne^{+} and Ne^{++} exit channels as a result of charge exchange between the projectile and target nuclei. Specifically, we have seen a sudden ″turn-on″ in Ne^{++} generation as the collision energy is raised above a threshold value. This turn-on seems indicative of inelastic loss channels that open up as the distance-of-closest-approach gets smaller during the hard collision. Values for the inelastic loss in the center-of-mass frame for Ne^{+} and Ne^{++} have been evaluated with our system for collision energies up to 1.3 keV and compared with literature data at higher energies. The inelasticity values we see in the threshold region are too small to be readily explained by the mechanisms proposed for higher collision energies in the literature for both Ne^{+} and Ne^{++}. Finally, a simple orbital overlap model is presented which suggests that Ne^{++} generation is coincident with a required atomic orbital overlap between the projectile and target atom L-electron shells, which signify that the Ne 2p orbital is promoted through the 4fσ molecular orbital at some threshold internuclear distance.

Contents

List of Figures

List of Tables

Nomenclature

Acronyms and Abbreviations

AES	Auger Electron Spectroscopy
AO	Atomic Orbital
AN	Auger Neutralization
AWG	American Wire Gauge
BCA	Binary Collision Approximation
CAE	Constant Acceptance Energy
CM	Center-of-Mass Reference Frame
DAC	Digital to Analog Converter
DR	Direct Recoil
DS	Double Scattering
EFF	Extended Fringe Field
FWHM	Full Width at Half Maximum
ICP	Inductively Coupled Plasma
IEDF	Ion Energy Distribution Function
ISS	Ion Scattering Spectroscopy
K	Kinematic factor from the BCA theory for a single collision
LSS	Lindhard-Scharff-Schiott
MCS	Multi-Channel Scalar
ML	Monolayer
MO	Molecular Orbital
MS	Multiple Scattering
PID	Proportional – Integral – Differential process control scheme
PMT	Photomultiplier Tube
RBS	Rutherford Backscattering Spectrometry
RC	Resonant Capture
RF	Radio Frequency
SIMS	Secondary Ion Mass Spectrometry

SRS	Stanford Research Systems
SS	Single Scattering
TFM	Molierè approximation to the Thomas-Fermi interatomic potential
TOF	Time of Flight
XPS	X-ray Photoelectron Spectroscopy
UHV	Ultra High Vacuum
VLSI	Very Large Scale Integrated

English Symbols

a	screening length
A	parameter from LSS theory in Oen and Robinson loss formula
b	impact parameter
B	magnetic field strength
c_i	fitting parameter for Oen and Robinson loss formula
C	reduction factor for empirical screening length
d	decay length for the electron exchange probability
e	elementary charge = $1.602 \bullet 10^{-19}$ C
E	electrostatic force between sector field electrodes
E	particle kinetic energy
E^*	particle kinetic energy after continuous loss Q_1 occurs
E_{exit}	exit energy of projectile (scattered projectile energy)
E_{pass}	pass energy (kinetic energy of particles passing through energy analyzer at mean radius)
E_3	particle kinetic energy after hard collision but before continuous loss Q_3 occurs
f	focal length for a magnetic sector field
g_{air}	air gap width between pole shoes of an electromagnet
H_z	Herzog constant for electrostatic sector analyzer

$I(E_i)$	scattered ion intensity (cross section corrected) for projectile energy E_i
l	second quantum number for an electron state (angular momentum)
l'	source point distance from magnetic sector pole shoe (or) second quantum number for excited electron state
l''	image point distance from magnetic sector pole shoe (or) second quantum number for excited electron state
L	angular momentum in the CM frame
m	mass of the particle
M	mass of the particle
n	primary quantum number for an electron state
N	number of incident particles impinging on the target per unit area
P	overall survival probability for the ion
P_{in}	probability that the ion survives along the incoming path
P_{out}	probability that the ion survives along the outgoing path
q	particle charge
Q_{bin}	binary inelasticity occurring in the hard collision
Q_1	continuous electron straggling loss along incoming particle trajectory
Q_3	continuous electron straggling loss along outgoing particle trajectory
r	distance between nuclei for the Coulomb potential (or) radius of curvature for particle trajectory
R	retarding voltage for electrostatic sector field energy analyzer
$R_{\min}$	distance of closest approach or apsis
U	particle kinetic energy (for electrostatic sector field)
v	particle velocity
v_{in}	particle velocity perpendicular to surface on incoming path
v_n	characteristic ″neutralization″ velocity
v_{out}	particle velocity perpendicular to surface on outgoing path
$V(r)$	interatomic potential

Y^+	fraction of projectile ions surviving neutralization upon scattering
z	ion charge state (+1, +2,…) (or) distance between the ion and surface (electron exchange equations)
Z	nuclear charge (atomic number)

Greek Symbols

α	divergence angle of ion beam at the source point of the magnetic sector
χ	CM scattering angle
ε_0	permittivity of free space
ϕ	incident beam angle from the substrate surface
ϕ_L	lab frame recoil angle of the target atom
$\Phi(X)$	empirical screening function for screened Coulomb potential
Φ_e	electrostatic sector field angle
Φ_{eff}	effective field angle for electrostatic field
Φ_s	magnetic sector field angle
γ	target-to-projectile atomic mass ratio
$\Gamma_{in,\,out}$	electron exchange transition rate on the incoming or outgoing paths
Γ_0	maximum bulk transition rate at zero distance
$\Gamma(z)$	electron exchange transition rate vs. distance from the surface
θ_L	lab frame scattering angle of projectile
η	fringe field parameter for electrostatic sector field
μ	mass of the CM particle
μ_{Fe}	permeability of iron core material of an electromagnet
μ_0	permeability of free space
σ_{diff}	differential scattering cross section
$\sigma_{diff,i}$	differential scattering cross section for impact energy E_i

$\sigma_{diff,\max}$	maximum cross section for the data set (lowest impact energy)

Subscripts

p	related to projectile atom or ion
t	related to target atom
0	related to projectile before the collision
1	related to projectile after the collision (except for θ)
2	related to target atom after the collision (except for θ)
L	related to lab reference frame
CM	related to center-of-mass reference frame

Miscellaneous Symbols

$dN_{d\Omega}$	number of incident particles (ions and neutrals) scattered into solid angle $d\Omega$
$dN^{+}_{d\Omega}$	intensity of scattered ions measured in the lab frame
$dN^{+}_{d\Omega,i}$	scattered ion signal measured at the detector for impact energy E_i
$d\Omega$	solid angle for sampling the scattered flux
ΔE_{bin}	binary inelasticity partitioned to projectile (measured in lab frame)
$\Delta E_{exit}\left(\Delta E_0\right)$	partial error connected with uncertainty in incident energy, E_0
$\Delta E_{exit}\left(\Delta \theta_L\right)$	partial error connected with uncertainty in scattering angle, θ_L
ΔE_0	raw measurement error in incident energy, E_0
$\Delta \theta_L$	raw measurement error in scattering angle, θ_L
ΔV	absolute potential difference between inner and outer sectors of electrostatic sector energy filter
Δx	lateral displacement of an ion trajectory at magnetic sector image point

1. Introduction and Background

1.1 Survey of Ion-Surface Interactions

A broad range of physical and chemical phenomena can occur when energetic ions interact with a solid surface. The nature of the collision processes involved depends directly on the impact energy. The ability to ″tune″ the interactions through the energy is the basis for many manufacturing processes in the semiconductor field (such as plasma etching and ion-assisted film growth) as well as analytical tools for studying surface composition and structure (ion scattering spectroscopy, ISS; Rutherford backscattering, RBS; and secondary ion mass spectroscopy, SIMS).

From an analytical point of view, ion-surface interactions function as a direct diagnostic probe of surface composition and structure. Depending on the projectile species and impact energy, the energy and angular distribution of the scattered particle flux from a surface can provide information on the identity of surface atoms and their locations as well as compositional information with respect to depth for different thin film layers. Low impact energies (1-5 keV) provide a preferential sensitivity to the top-most atomic layers (10's of Å) while high energies (MeV) can probe much deeper into the target lattice (1 MeV protons can reach 10-20 μm in Si). Ion scattering is a direct technique for interrogating the surface region because the final state (charge, energy, and scattering angle) of the scattered projectile is determined by the individual atomic collisions and electron exchange processes which occur.

Although ion-surface interactions have a significant technological importance, a rigorous understanding of the fundamental physics and chemistry involved is often lacking. Specifically, interactions that occur in the hyperthermal energy range (1-500 eV) are poorly understood because of both experimental challenges and theoretical complexities. One has to only look to the literature to see that most of the scientific research emphasis has been placed on thermal energy collisions (< 1eV) or higher impact energies (>2 keV). In addition, it has been said that describing the dynamics of charge transfer processes that occur during ion scattering from surfaces is still a major unsolved problem in the field of surface physics (Rabalais, 1993, 2003). We would like point out

that some of the most interesting and industrially relevant collision phenomena occur in the hyperthermal regime. A brief introduction to ion-surface collisions and the importance of the hyperthermal energies is given below to set the stage for our experimental work.

A schematic representation of various interaction phenomena which can occur as ions impinge upon a solid surface is given in Fig. 1.1 for selected energy ranges. The spectrum of collision energies spans nearly eight orders of magnitude and is customarily divided into five regions: (1) thermal, < 1eV; (2) hyperthermal, 1-500 eV; (3) low energy, 0.5-10 keV; (4) medium energy, 10-500 keV; and (5) high energy for > 500 keV. Increasing the collision energy provides a direct means of probing a wide range of interaction distances where forces between the particles evolve from weak, long-range effects at tens of Å to strong, purely Coulombic repulsion between the nuclear cores at the higher collision energies.

Specific interaction phenomena are dominant in each range because the chemical and physical processes that occur between the projectile and target atoms are directly governed by how close the collision partners approach each other during impact. This interaction distance depends directly on the collision energy and the potential forces acting between the atoms. For instance, charge exchange processes begin to occur for collisions in the ~1 keV range. The projectile and target nuclei become close enough (< 0.5 Å) to one another for significant overlap of the inner electron shells of the two atoms. During the overlap, a short-lived (10^{-15}-10^{-16} s) quasi molecule is formed where electronic excitations and electron promotions can happen. As the collision partners recede, electrons can be trapped in higher lying electronic states that decay much slower than the collision time. As a result, scattered projectiles and target atoms in highly excited electronic states are often generated in the keV collision range.

Some of the processes which can occur in ion-solid collisions include:

(1) *Ion scattering* – Ions can be scattered from the surface through elastic-like collisions that cause displacements of the target atoms. The energy transferred in the collision can often be treated using classical mechanics. Target atoms recoil in the collision and may be deflected into or outward from the surface as neutrals or ions.

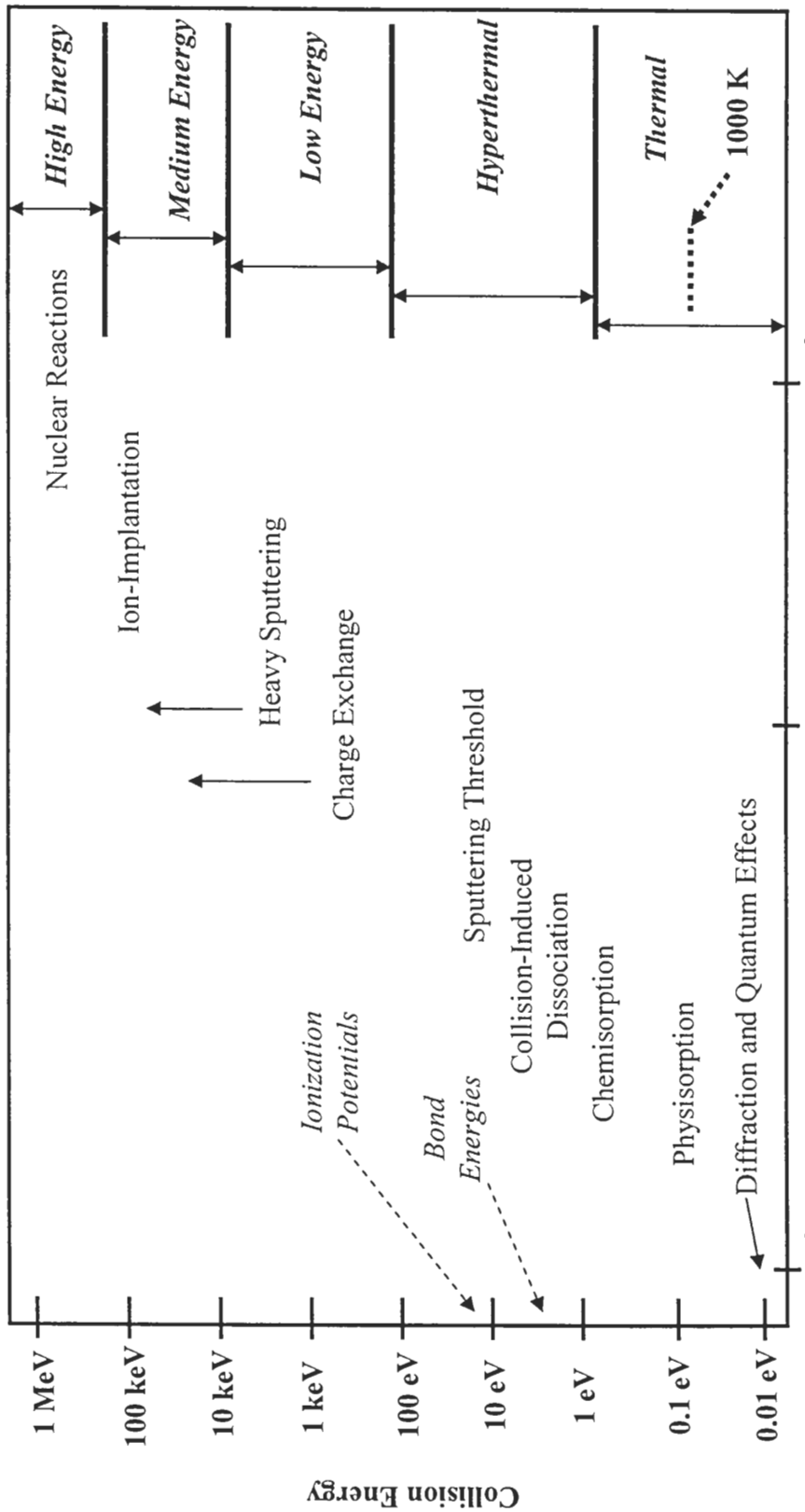

Figure 1.1: Survey of ion-surface interactions with their respective energy ranges and interaction distances. The spectrum of impact energies is customarily divided into the five regions shown at the right.

(2) *Electronic interactions* – Electron transfer processes between the projectile ions and target atoms can occur which results in projectile neutralization or electronic excitation of either or both of the collision partners. Charge exchange processes begin to happen when the inner electron shells of the projectile and target atoms overlap at short interaction distances, typically less than 0.5 Å.

(3) *Sputtering* – Removal of target atoms from the surface occurs from the sheer momentum of the projectile ion causing bond cleavage in the target lattice. Typical sputtering thresholds for most materials are in the 20-40 eV impact energy range with the sputtering yield dependent on the specific projectile ion.

(4) *Secondary electron and photon generation* – Ion impact results in secondary electron release from the valence band of the target atom. Excited states formed in the collision can also decay through Auger electron release or radiative transitions.

(5) *Adsorption and reaction* – Impinging ions can directly adsorb on the target surface or cause desorption of atoms or molecules from the surface through momentum transfer. Chemical reaction can occur between projectile ions and surface atoms.

(6) *Lattice damage* – Displacement of target atoms and a ″stirring″ of the target lattice near the surface occurs during bombardment. Projectiles ions can even be implanted directly into the target lattice as interstitials if the impact energy is high enough. Bombardment of crystalline materials causes amorphization of the surface layers.

The fact that the aforementioned phenomena occur in different collision energy ranges has served as the basis for many analytical tools for surface study as well as industrial processes in semiconductor manufacturing. For example, energy analysis of scattered He^+ particles at keV energies in ion scattering spectrometry (ISS) and Rutherford backscattering (RBS) at MeV collision energies provides a means of probing surface structure and thin film composition. On the practical side, the entire field of integrated circuit manufacture hinges on plasma etching technologies for high-fidelity pattern transfer in silicon based devices. Plasma etching processes require a high ion flux directed at the wafer surface using impact energies below 500 eV for activating surface chemical reactions and stimulating etch product removal from the substrate surface (Coburn and Winters, 1979; Lieberman and Lichtenburg, 1994). Tailoring the ion-surface collision phenomena through the impact energy is an integral part in ″tuning″ the etching process. High etch rates and good anisotropy (features with straight sidewalls and flat trench bottoms) require a delicate balance between chemical reactions at the

surface and momentum assisted product removal without causing damage to wafer structures from excessive sputtering. From these perspectives, the study of ion-surface collisions is useful from both a scientific and a practical point of view.

1.2 The ″Neglected″ Energy Regime: 1-500 eV

Although there is a tremendous body of work on particle-surface interactions at thermal energies as well as higher energies in the keV range, the hyperthermal regime (1-500 eV) has largely been neglected because of the experimental challenges associated with producing ion beams of high enough intensity *at low energy*. This difficulty arises simply because space charge repulsion between the ions causes problems with focusing, beam transport, and mass-filtering (Rabalais, 2003). Hyperthermal energies are a useful range to study because some of the most interesting and industrially useful phenomena occur when the collision energy is of comparable order to the energies required for chemical reactions, bond breaking, and sputtering atoms from the surface. Processes such as collision-induced dissociation and desorption, ion-assisted ″stirring″ of the surface atomic layers, and charge exchange can occur at hyperthermal collision energies. Other processes like physical sputtering and lattice penetration also accompany ion scattering in this range. In fact, the whole field of plasma-based processing of semiconductors including surface cleaning, ion-assisted film deposition, and dry etching, all rely on interactions that occur at hyperthermal energy. For these reasons, ion scattering at collision energies between 1-500 eV using both inert and reactive (*especially*) projectiles is of great importance.

It is the main goal of this dissertation work to show that the difficulties at lower impact energy can be sufficiently *circumvented*, so that hyperthermal scattering experiments can be carried out using well-characterized ion beam surface probes with *tunable* energy and high current. This work will also show how ion scattering with *mass* and *energy* detection of scattering products leaving the target surface can give a more clear view of the complex processes occurring at surfaces.

1.3 Charge Exchange Collisions at Surfaces

The collision of ions with surfaces can exhibit multi-faceted charge exchange behavior based on the identity of the collision partners and the range of internuclear distances that are reached in the close encounter of the two nuclei. Many collision systems are quite complex and not often amenable to one single experimental technique. For instance, the $(NaNe)^+$ collision is a many-channel system for which a ″zoological garden″ of different charge exchange mechanisms becomes active at different inter-nuclear separation distances (minimum separation distance is called the collision apsis).

The study of these different mechanisms requires several experimental techniques all working together to make a consistent interpretation possible. The identity and exit energies of the species (ions and neutrals) after the collision depend strongly on which electronic excitation processes are dominant. Varying the collision energy provides a direct means of sampling different apsis distances between the nuclei, effectively giving the experimenter a means of probing specific charge exchange mechanisms. For instance, one-electron excitations of either collision partner can result in excited neutral states (Na^* or Ne^*), ionization ($Ne^0 \rightarrow Ne^+$), or ion excitations ($Na^+ \rightarrow Na^{+*}$). Two-electron transfer processes can also occur, giving a rich mix of doubly excited neutrals ($Ne^0 \rightarrow Ne^{**}$ or $Na^+ \rightarrow Na^{**}$) and ions (Ne^{+**}) as well direct ionization events ($Ne^0 \rightarrow Ne^{++}$). As a general rule, one-electron processes dominate at large apsis (lower energy or smaller scattering angle), while two-electron transitions occur for smaller apsides (higher energy or larger scattering angle) (Ostgaard *et al*., 1979).

The nature of which process occurs depends on the interatomic potential between the two particles and the relative energy levels of the two atoms. As the collision partners approach one another, hybrid molecular orbitals (MO) develop as a short-lived quasi-molecule is formed at small internuclear distance (<1 Å). It is during this MO formation that excitation can occur through electron promotion to higher MO states as well as electron exchange between the two atoms.

Threshold processes are inherently interesting because they give us a look at the important physical parameters which affect the outcome of the particle-particle interactions. Collisions involving charge exchange are possible below 1 keV in systems

where significant overlap of inner electron shells can occur ─ violent collisions (large scattering angle) of lighter projectiles with target atoms of nearby atomic number. In these cases, significant orbital overlap of the projectile and target atoms enables charge exchange to take place.

It will be shown later in this work that charge exchange processes are important and also very rich for ion-solid collisions (Ne^{+}→Mg, Al, Si) at lower energy (<1 keV). Our experimental system provides a means of tuning the projectile incident energy and carefully measuring the exit energy of scattered projectiles. Interesting phenomena such as inelastic losses of Ne^{+} and the ″opening-up″ of an Ne^{++} generation channel in the 500 eV collision range will be demonstrated in Chapter 7. The utility of mass and energy dispersion in our detection system will prove extremely helpful in clearly separating the Ne^{+} and Ne^{++} exit channels in the scattered particle flux.

1.4 Plasma Etching and the Need for Clean Ion Beam Studies

We have mentioned that ion-surface collisions in the hyperthermal energy range dominate the plasma etching field. As such, fundamental scattering studies aimed at understanding the surface mechanisms and reactions occurring during etching are highly needed. Historically, the plasma etching field has been very mission oriented with emphasis on *how* to produce the most idealized feature profiles at the highest packing density rather than understanding the underlying mechanisms involved on the surface. To be fair, etching is an extremely complex system to study because it combines charged particle physics of plasmas with gas-phase chemical reactions along with all the physical and chemical processes occurring on the wafer surface. It is no real surprise that plasma etching is often treated as a ″black box″ where sensitivity studies on gas mix, plasma power, operating pressure, gas flow geometry, etch time, *etc*., are conducted to establish the optimal operating conditions to give the best profiles. This approach is obviously market driven, but breaks down when a deeper understanding of surface phenomena is needed to solve difficult problems. It is painfully clear that the technology of making devices has greatly surpassed our understanding of the surface phenomena involved in making it all possible. This suggests that fundamental scattering studies in the

hyperthermal energy range with reactive systems are imperative to determine the basic physical and chemical mechanisms that occur during etching processes.

A considerable amount of effort has been spent in trying to study the basic scattering phenomena and surface chemistry that occur in plasma etching. These studies rely on establishing trends in etch rates using different projectile species or impact energies (Coburn *et al*., 1977; Coburn and Winters, 1979; Winters *et al*., 1983). As well, *ex situ* surface analysis of etched surfaces with X-ray photoelectron spectroscopy (XPS) or Auger electron spectroscopy (AES) has given hints about the dynamic layers on the wafer surface which mediate the etching process (Bello *et al*., 1994; Coburn *et al*., 1977; Fuoco and Hanley, 2002). Unfortunately, the experimental difficulties of beam work in the hyperthermal energy range are great and, as such, most scattering data and etch yields for reactive projectiles have been measured at energies >1 keV. One has to wonder the relevance of such measurements to real etching situations where ion impact energies above 500 eV can not be tolerated because of damage to the wafer surface from sputtering. In addition, history has shown that studies without mass-filtered ion beam surface probes can give incorrect pictures of collision phenomena and the processes occurring on the surface.

Many ″fundamental studies″ of surface scattering and sputtering phenomena have been conducted using mixed beams, where more than one ion species or charge state is present in the beam probe. These experiments are difficult to interpret and frequently give ambiguous results, further clouding the picture of surface scattering processes. Such an observation is not totally unexpected because ion scattering at low energy is extremely surface-sensitive. In fact, ion impact energies in the low keV range are used to specifically study the first few atomic layers of a surface because projectile ions can not penetrate to deeper layers at such low energy (Rabalais, 2003). Therefore, minor components in an unfiltered beam will have a dramatic effect on the overall scattering and sputtering process if they could alter the target surface through adsorption or chemical reaction. In addition, beam impurities can give false scattered product signatures which can overlap or mask the real processes occurring on the surface. Consider the following two examples.

Gas-gas scattering experiments with Ar^+ projectiles on a variety of static gas targets has indicated the presence of Ar^{++} that is formed through charge exchange during the hard collision (Fayeton, 1976ab). Clear inelastic losses are seen in the collision which can be attributed to discrete electron promotions and excitation in the collision partners. Having seen this charge exchange process in the gas phase, interest then turned to Ar^+ collisions with solid targets (Mg, Al, and Si) to examine if the Ar^{++} generation mechanism could also occur for an ion-solid system. Several studies have claimed that Ar^{++} is also seen off solid targets through a hypothesized inner electron shell charge exchange process involving autoionizing Ar^{**} states (Blum *et al*., 1994; Nixon *et al*., 1994). It has since been shown by numerous authors (using mass-filtered Ar^+ beams) that the Ar^{++} exit channel is most probably false and results from a small amount of Ar^{++} contamination in the probing beam that survives neutralization upon impact with the surface (Guillemot *et al*., 1996a).

Along the same vein, beam studies of Si etching using CF_3^+ beams were conducted many years ago to measure the etch rate with respect to ion impact energy (Coburn *et al*., 1977). The CF_3^+ ion beam was formed by electron impact ionization of CF_4 and was not mass filtered. Although the probing beam was thought to contain a very small amount of CF_2^+ (~7%), it was not deemed to be important in determining the overall Si etching rate and surface physics. This etch rate data has remained steadfast in the plasma etching community for the last 20 years and has served as the basis for theoretical models, simulation studies, and interpretation of experimental scattering work. Several years after the Coburn work, etch rate measurements were conducted with pure CF_3^+ and CF_2^+ ion beams using a mass-filtered ion implantation system adapted for lower collision energies (Miyake *et al*., 1982; Tachi *et al*., 1981). The results of these clean-beam experiments showed that CF_2^+ is remarkably sticky and even *deposits* on the Si surface at 100's of eV impact energy to form a Teflon-like polymer layer. In light of the new data, the Coburn etch rate measurements with CF_3^+ beams having small levels of CF_2^+ impurities are totally suspect. Unfortunately, there has not been widespread acknowledgement of the Tachi work in the plasma etching community (Coburn is considered by many to be the pioneer in the plasma etching field). Tachi's work demonstrates that low etch rates for unfiltered CF_3^+ beams can now be explained by the

competition between sputtering from CF_3^+ and very efficient deposition by a minor CF_2^+ impurity in the beam which totally changes the character of the surface. It is still not known why CF_2^+ forms the polymer-like layer at 100's of eV and CF_3^+ does not.

The previous two examples demonstrate clearly why we think fundamental scattering studies must be carried out with clean, pure ion beam probes with only one ion species and one charge state. We believe this is an *absolute* necessity and must be clearly demonstrated by any serious study of surface scattering, especially for reactive systems. The preliminary work mentioned in Chapter 8 on CF_3^+ scattering off Si will give a flavor for the importance of a clean beam probe along with the necessity of mass and energy dispersion of products leaving the target surface for a reactive scattering system.

1.5 Our Approach to Ion Scattering at Hyperthermal Energies

Our approach to hyperthermal-energy ion scattering experiments has been a mission-oriented one where many of the shortcomings of previous work have been eliminated so that unambiguous, fundamental studies can be targeted. In addition, our goal has been to extend ion scattering at hyperthermal energies to reactive systems relevant to plasma etching which have largely been ignored. In fact, it seems odd that more emphasis has not been placed on combining clean beams (*monoenergetic* with a *single* ion species) with broad-based detection (*mass* and *energy*) of the particle flux leaving the target surface (*ions* and *neutrals*). Undoubtedly, this is a tall task.

However, detailed studies using clean, rare-gas ion beams and multi-product detection schemes have been carried out on surfaces at keV impact energies. Their value as a routine diagnostic probe of surface structure (impurities, reconstruction, etc.) and as tools for studing charge exchange and other collision phenomena is invaluable. Outside this realm, experiments at hyperthermal energies with rare-gas ions or reactive projectiles (even less so) are very hard to find in the literature. Part of the problem lies with providing mass-filtered ion beam probes with reasonable currents (many microamps/cm^2) at impact energies below 500 eV. High flux at hyperthermal energy is very demanding in its own right, but the mass-filtering requirement for reactive beams makes the problem worse. Reactive ion species are most often generated by cracking a less reactive

molecular precursor (i.e., CF_x^+ from CF_4 or SF_x^+ from SF_6), which usually leads to impurity species which contaminate the beam. Undesirable daughter ions from reactive ion precursors must be removed from the beam so as to not complicate the scattering behavior and change the nature of the surface under study.

Many surface scattering experiments in the past involving mixed beams, higher collision energy, and limited product detection capabilities foreshadow some of the unique interaction phenomena that can occur at hyperthermal impact energies. However, a robust, mass-filtered, tunable-energy ion beam probe coupled with mass and energy analysis of the scattered product flux leaving the target surface is needed for more concrete, fundamental studies. We have tried to fill this niche.

Our philosophy has been to take a high-density ion source (an ICP plasma discharge), like those used for actual plasma etching, and couple it with a high-voltage ion accelerator (3 m length) using magnetic mass-filtering to generate clean ion beam surface probes. The ion beamline is joined with a very sensitive scattered product detection system where ultra high vacuum (UHV) scattering studies can be conducted with mass and energy analysis of the ion and neutral particle flux leaving the surface. The integral step in joining these two systems is the *accel-decel* approach where ions are created in the plasma at the final impact energy (10-500 eV), accelerated for transport and mass-filtering, and then decelerated back down right before hitting the target. In this way, high beam current at hyperthermal impact energies is possible because space charge repulsion between the ions is *circumvented*. The high transport energy at ~15-20 keV significantly decreases the influence of space charge spreading between the ions, making transport and mass-filtering of high beam currents possible. Also, the target is kept in a totally field-free, *grounded* environment so that the charged particle flux leaving the target surface can be energy analyzed directly and accurately.

The main goal of this dissertation work was to show how such a system can be built and demonstrate its performance through several case studies. Ultimately, such a system, which combines a clean ion beam probe with mass and energy analysis of surface scattered species, may open the doorway to a wealth of new understanding in the hyperthermal energy range.

1.6 Dissertation Outline

This work begins in Chapter 2 with a review of classical two-body scattering theory to provide a context for the case studies on binary collisions of rare-gas ions presented in the results section. Chapter 3 discusses the basics of plasma science, charged particle optics, and ion beam generation along with ideas from the high-energy physics field which were used in the design of the ion beamline accelerator.

The experimental section (Chapter 4) contains a historical perspective of constructing and testing the ion beam scattering system. The system design from the plasma source all the way to the sample and scattered product detector is discussed in progression along the ion beam's flight path. Since the entire scattering system was built from the ground-up, great detail will be given to each piece, outlining the important design features which allowed the overall system to function as a whole. Chapter 5 contains the performance details of the ion beamline with respect to mass resolution, ion beam energy-tunability, and beam current that can be obtained in the hyperthermal impact energy range. This chapter also highlights the operation of the scattered product detector for energy and mass analysis of the scattered particle flux leaving the target surface. Chapter 6 contains the results of one case study on the applicability of the binary collision approximation in the hyperthermal collision energy range using Ne^+ and Ar^+ projectiles off a variety of heavier target surfaces.

The results section ends in Chapter 7 with a second case study of Ne^+ scattering off light targets (Mg, Al, Si, and Ti). Inelastic losses in the scattered ion energy spectrum can be seen for Ne^+ off Mg, Al, and Si targets which indicate that strong electronic excitation occurs in the hard collision. The threshold energy behavior for Ne^+ inelasticity is shown to correlate with an Ne^{++} generation mechanism that once a threshold collision distance between the projectile and target atoms is reached. This sudden ″turn-on″ represents the opening-up of electronic excitation channels which are accessible once the collision partners become close enough in the close encounter. The threshold distance for Ne^{++} formation is shown to correlate well with a required overlap of the Ne 2p with the 2s or 2p orbitals of the target atom. Chapter 8 contains a mix of future studies for Ne^+ and Ar^+ projectiles on lighter target materials to examine the charge transfer processes

that can occur below 1 keV collision energy. Preliminary scattering studies of mass-filtered CF_3^+ beams on Si are included to demonstrate the entire ion beamline and scattered product detection system as applied to a real etching system. Rather than a single conclusion section at the end, individual summary sections are given throughout the text to highlight important concepts and experimental results in a more topic-oriented fashion.

2. Classical Picture of Atomic Collisions

This chapter begins with a simple description of two-body elastic collisions and the view if ion-surface collisions as given by the binary collision approximation (BCA). The transformation from laboratory to center-of-mass (CM) reference frames from classical scattering theory is discussed next. The classical ″scattering integral″ in the CM frame will then be introduced in an effort to calculate the distance of closest approach (apsis) for various projectile-target combinations to illustrate important points in experimental scattering data. Inelastic loss terms due to electron straggling on the incoming and outgoing portions of the ion trajectory as well as a binary loss term due to electronic excitation in the hard collision are finally added to the BCA framework.

2.1 Single Collision Model

The collision phenomena which occur when ions impact a surface in the 100 eV-10 keV range can be satisfactorily described as a sequence of elastic two-body scattering events (BCA theory) (Rabalais, 2003). Such a model is reasonable because ion velocities are high (10^5 $^m/_s$) compared to the thermal motion of target atoms (10^2 $^m/_s$) and collision times (10^{-15}-10^{-16} s) are small compared to phonon vibrational periods (10^{-13} s) (Rabalais *op. cit*.). Collective interactions involving multiple target atoms can be neglected because the collision occurs much faster than energy can be transferred through the lattice. In addition, the distance of closest approach (apsis) reached between the two nuclei (projectile-target) during the close encounter (<1 Å) is usually much smaller than the bond distance between target atoms (2-5 Å).

A classical picture for atomic collisions is justified because quantum-mechanical effects are usually ″washed-out″ by laboratory observations that are averaged over thermal distributions of molecular velocities. Also, diffraction effects are not relevant because the De Broglie wavelength of the incident particle (~10^{-2} Å) becomes negligible

at higher energies compared to the lattice parameter of the target (2-5 Å) (Rabalais *op. cit.*).

A single, elastic scattering (SS) event between two particles in the laboratory reference frame can be described by the energy transfer during the collision for a specific scattering angle. Consider a hard-sphere collision (see Fig. 2.1) between a projectile atom with kinetic energy E_0 and a target atom on a surface, initially at rest. If no energy loss occurs in the close encounter (it is elastic), the final energies and deflection angles of the projectile atom (E_1, θ_L) and the recoiled target atom (E_2, ϕ_L) after the collision can be obtained from conservation of energy and momentum:

$$\tfrac{1}{2} M_p \mathrm{v}_0^2 = \tfrac{1}{2} M_p \mathrm{v}_1^2 + \tfrac{1}{2} M_t \mathrm{v}_2^2 \tag{2.1}$$

$$M_p \mathrm{v}_0 = M_p \mathrm{v}_1 \cos\theta_L + M_t \mathrm{v}_2 \cos\phi_L \tag{2.2}$$

$$M_p \mathrm{v}_1 \sin\theta_L - M_t \mathrm{v}_2 \sin\phi_L = 0 \tag{2.3}$$

where,

$M_p, M_t =$ projectile and target masses
$\mathrm{v}_0, \mathrm{v}_1 =$ projectile velocity before and after the collision
$\mathrm{v}_2 =$ target recoil velocity after the collision
$\theta_L, \phi_L =$ lab frame scattering angle for projectile and target atoms

It is common to eliminate the recoil angle and velocity components from these equations and define a new quantity known as the kinematic factor (K), which is commonly used in ion scattering spectrometry (ISS) and Rutherford backscattering (RBS). The kinematic factor represents the fractional energy loss suffered by the projectile during the collision for any scattering angle observed in the lab frame (Rabalais *op. cit.*):

$$K(\theta_L) = \frac{E_1}{E_0} = \frac{\left(\cos\theta_L \pm \sqrt{\gamma^2 - \sin^2\theta_L}\right)^2}{(1+\gamma)^2} \tag{2.4}$$

$$\gamma \equiv \frac{M_t}{M_p} \tag{2.5}$$

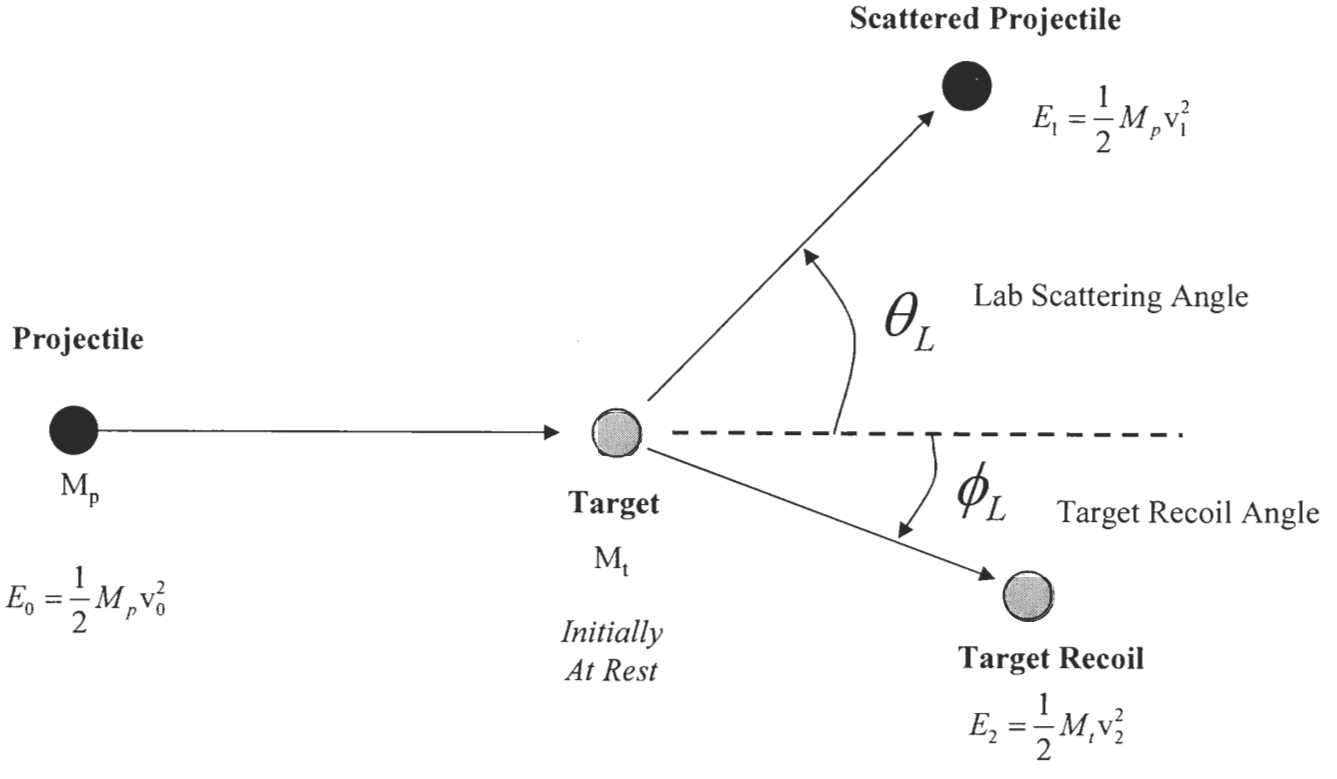

Figure 2.1: Elastic binary collision in the lab reference frame showing the final energies and scattering angles of the collision partners.

where,

$K(\theta_L) =$ kinematic energy transfer factor which depends on scattering angle
$\gamma =$ target-to-projectile mass ratio

For ″normal″ collisions where the projectile is lighter than the target ($\gamma > 1$), only the plus sign applies and a unique scattered projectile energy is observed for each lab angle. If the projectile becomes heavier than the target within the $(\sin\theta_L < \gamma < 1)$ range, both signs apply and there exist two final energies for each scattering angle. In this case, only a limited regime of scattering angles is accessible for heavier projectiles.

When the laboratory scattering angle (θ_L) becomes 90°, the kinematic factor becomes particularly simple:

$$K(90^\circ) = \frac{(\gamma - 1)}{(\gamma + 1)} = \frac{M_t - M_p}{M_t + M_p} \tag{2.6}$$

Multiple collision phenomena can also be handled with this same kinematical description by applying Eqn. 2.4 for consecutive collisions of the projectile with target atoms in succession. Scattering occurs step-wise through angles θ_1, θ_2, θ_3, *etc.* to yield the overall scattering angle ($\theta_L = \theta_1 + \theta_2 + \ldots$). For instance, double-scattering (DS) peaks sometimes appear in ISS spectra and occur at energies higher than the single-scattering (SS) elastic peak (Czanderna and Hercules, 1991; Rabalais *op. cit.*):

$$E_{DS} = K(\theta_2) * K(\theta_1) * E_0 \quad > \quad E_{SS} = K(\theta_L) * E_0 \tag{2.7}$$

Higher-order collisions are rarely seen in ISS because the incident ions cannot survive several consecutive collisions with target atoms without being resonant or Auger-neutralized (Rabalsis *op. cit.*). Multiple bouncing and rolling along the surface do occur, but these processes usually result in efficient neutralization of the projectile. As a result, higher-order scattering is not typically seen in an ISS experiment when looking at only the charged particle flux leaving the target surface.

One may ask what happens when $(\gamma < \sin\theta_L)$ and the kinematic factor becomes ill-defined. Under these conditions, scattering events have been observed in the laboratory, but the interactions giving rise to these events are no longer easily explainable within the BCA framework. Theories involving a large surface effective mass (10-100 atoms) or a projectile which repeatedly skips across the surface (i.e., Ar^+ on Si at 90°) suffering many glancing angle (θ_i very small) collisions are often invoked to explain such phenomena (Yang *et al*., 1996). The physical reality of these explanations is debatable because most ions that undergo several collisions with surface atoms are efficiently neutralized. Such effects are beyond the scope of our work.

The simple relations presented above show that the energy spectrum of ions scattered from a target directly reflects the elemental composition of the surface because Eqn. 2.4 depends only on the mass ratio and the scattering angle. Direct application of this fact serves as the basis for many of today's surface and thin film characterization techniques such as ISS (5-10 keV) and Rutherford backscattering (RBS) at MeV energies. In the low energy regime (<1 keV), ion scattering has the added benefit of high surface sensitivity because projectile atoms can not penetrate the target to any appreciable degree (<1-5 atom layers).

2.2 Interaction Potentials

The binary collisions which occur in ion scattering can be described by an interaction between the two particles through conservative, central forces. When an ion of nuclear charge Z_1e approaches a target atom with charge Z_2e along some radius vector $\vec{\mathbf{R}}$, the ion will be deflected (scattered) by the Coulomb repulsive force present between the two nuclei. For all energies below the MeV range, the force is not purely Coulombic because the electrons surrounding the two nuclei screen out the nuclear charges causing the potential to fall off faster than $1/r$. It is customary to modify the standard Coulomb potential with a screening function to account for the influence of the electron clouds (Rabalais *op. cit.*):

$$V(r) = \frac{Z_1 Z_2 e^2}{4\pi\varepsilon_0 r}\Phi\left(\frac{r}{a}\right) \tag{2.8}$$

where,

$V(r) =$ potential acting between the two nuclei
$Z_1 e, Z_2 e =$ nuclear charges of the ion and target atom
$r =$ internuclear distance during the collision
$\Phi(r/a) =$ empirical screening function with screening length (a)
$\varepsilon_0 =$ permitivitty of free space

Many screening functions have been proposed, but the Molière approximation to the Thomas-Fermi model (TFM) is commonly used in low energy ion scattering because it gives reasonable results[1] (Czanderna *op. cit.*; Rabalais *op. cit.*):

$$\Phi\left(\frac{r}{a}\right) \equiv \Phi(X) = 0.35e^{-0.3X} + 0.55e^{-1.2X} + 0.1e^{-6.0X} \tag{2.9}$$

The TFM potential model uses either the Firsov (Firsov, 1957) or Lindhard (Lindhard *et al.*, 1968) screening length parameters based on the nuclear charges:

$$a_{Firsov} = \frac{0.4685}{\left(\sqrt{Z_1} + \sqrt{Z_2}\right)^{2/3}} \quad [\text{Å}] \tag{2.10}$$

$$a_{Lindhard} = \frac{0.4685}{\sqrt{(Z_1)^{2/3} + (Z_2)^{2/3}}} \quad [\text{Å}] \tag{2.11}$$

[1] At collision energies in the thermal range up to perhaps 10 eV, an attractive part is sometimes added to the screened Coulomb potential to give better agreement between experiments and theory. In addition, scattering at the low end of the hyperthermal energy range with alkali ion projectiles often requires an attractive part. See McEachern *et al*. 1989 or DiRubio *et al*. 1996 for examples.

A further reduction in the screening length by a factor, C, which depends on the nuclear charges of both the projectile and target nuclei is commonly done to give better fits to experimental data (O'Conner and Beirsack, 1986):

$$C = 0.54 + 0.045 * \left(\sqrt{Z_1} + \sqrt{Z_2} \right) \tag{2.12}$$

2.3 Laboratory to Center-of-Mass Frame Transformation

The particle trajectories in the classical model of two-body scattering can be calculated once a suitable potential (Molière in our case) has been chosen. The standard approach is to reduce the two-body problem to the motion of a fictitious particle deflected by a spherically symmetric, central force. This can be accomplished by switching from the laboratory scattering frame to the center-of-mass (CM) frame (see Fig. 2.2) and recognizing the following (Mahan, 1986):

(1) The center of mass of the two-body system moves at a constant velocity relative to the laboratory frame.

(2) Angular momentum must be conserved.

(3) Conservation of energy and momentum result in a differential equation for the particle orbit which can be solved to give the trajectory.

The transformation from the lab reference frame to the CM reference frame is given by (Möller, 2001):

$$\mu = \frac{M_p M_t}{M_p + M_t} \tag{2.13}$$

$$E_{CM} = \frac{M_p}{M_p + M_t} E_0 \tag{2.14}$$

$$\chi = \theta_L + \arcsin\left[\frac{M_p}{M_t} \sin\theta_L \right] \tag{2.15}$$

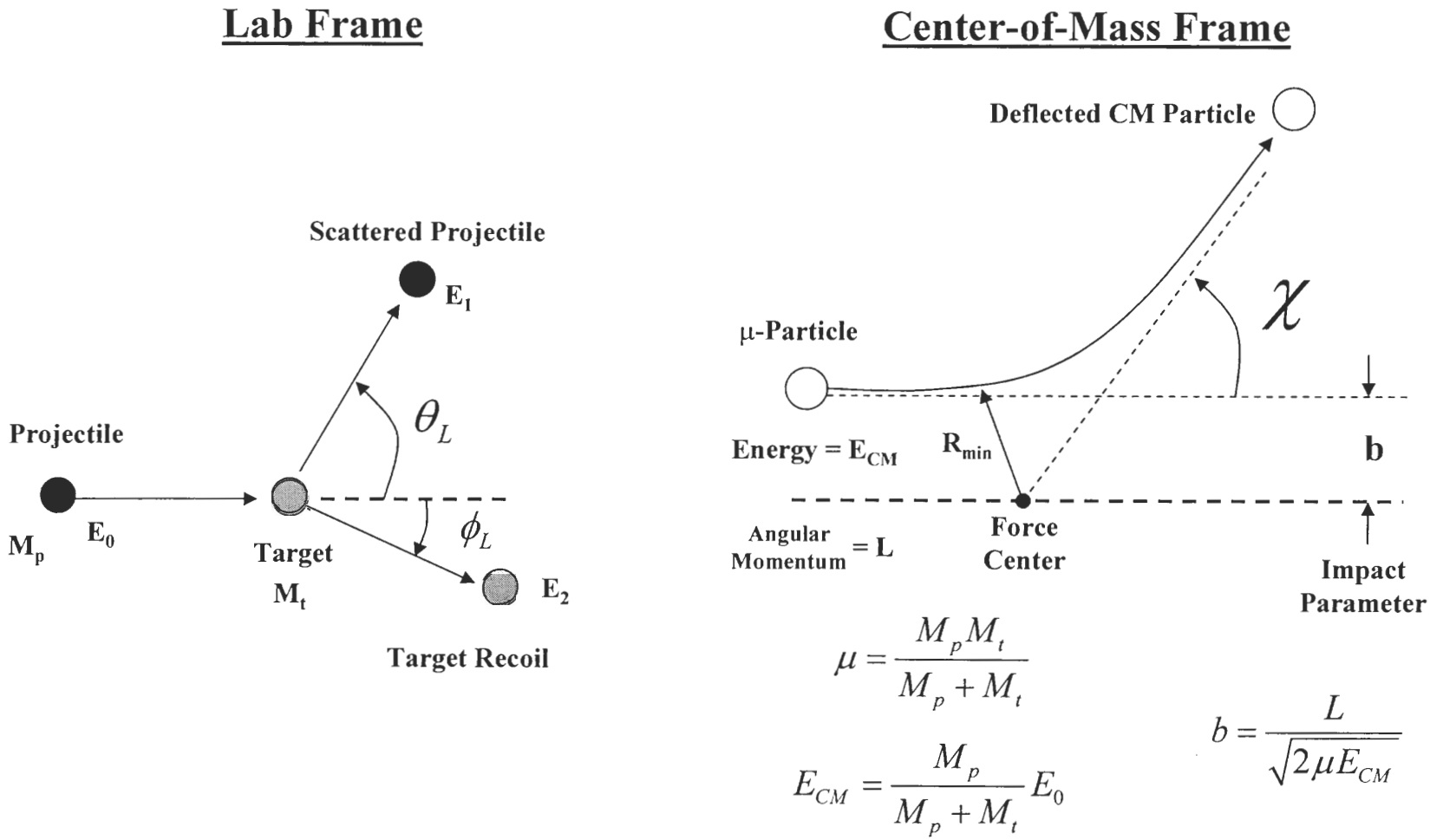

Figure 2.2: Lab reference frame to center-of-mass reference frame transformation. The two-particle system in the lab frame is reduced to the motion of a fictitious μ-particle deflected by a central force.

where,

$\mu =$ CM particle mass
$E_{CM} =$ collision energy in the CM frame
$M_p, M_t =$ projectile and target atoms masses
$\chi, \theta_L =$ CM particle deflection angle and lab frame scattering angle

Since the derivation of the ″scattering integral″ can be found in most textbooks on classical scattering theory (Rabalais, 2003), only the highlights of this treatment will be given here.

Suppose a particle of mass μ is moving in a central field $V(r)$ with total energy E_{CM} and total angular momentum L. The equation of motion for this particle in polar coordinates (r, φ) with the origin at the force center can be shown to be equivalent to (Mahan *op. cit.*):

$$E_{CM} = \frac{\mu}{2}\left(\frac{\partial r}{\partial t}\right)^2 + \frac{L^2}{2\mu r^2} + V(r) \tag{2.16}$$

We can further define an impact parameter (b) for the collision:

$$b = \frac{L}{\sqrt{2\mu E_{CM}}} \tag{2.17}$$

It can be shown that a minimum distance between the particle and the force origin occurs at some point in the trajectory. This distance $(R_{\min})$ is known as the closest approach or apsis distance for the collision. Ultimately, the particle orbit can be obtained by integration to yield the ″classical scattering integral″ which relates the CM scattering angle (χ), impact parameter (b), and apsis $(R_{\min})$ to the scattering potential $V(r)$.

$$\chi = \pi - 2b\int_{R_{\min}}^{\infty} \frac{\partial r}{r^2\sqrt{1 - \frac{b^2}{r^2} - \frac{V(r)}{E_{CM}}}} \tag{2.18}$$

It can further be shown that the apsis occurs when

$$b = R_{\min}\sqrt{1-\frac{V(R_{\min})}{E_{CM}}} \tag{2.19}$$

Unfortunately, it is no easy task to calculate $R_{\min}$ when the CM angle and potential are known because the scattering integral (Eqn. 2.18) is transcendental and can not be integrated analytically for the screened Coulomb potential. To complicate matters, numerical integration becomes difficult because Eqn. 2.18 has a singularity at $R_{\min}$. Several authors have addressed this fact in literature because a quick and efficient method is required to routinely find $R_{\min}$ to evaluate laboratory scattering data.

For the purpose of our work, the scattering integral was transformed after the method of Mendenhall and Weller (1990), so numerical integration could be performed quickly using Mathematica. The distance of closest approach for specific projectile-target combinations was evaluated by iteratively picking $R_{\min}$ values and calculating the CM scattering angle via numerical integration of Eqn. 2.18 until a laboratory angle of $\theta_L = 90^\circ$ (thru Eqn. 1.15) was obtained at each impact energy.

2.4 Inelasticity

Although the BCA model provides a powerful framework to view ion surface collisions, it does not allow for any inelastic energy losses along the projectile ion trajectory. Discrete inelastic losses can occur during the hard collision as the result of electron promotions, inner shell ionization, and charge exchange phenomena (Rabalais, 2003). As well, the projectile experiences a continuous friction-like slowing or electron ″straggling″ in the near surface region due to interaction with the electrons of the solid surface.

In a discussion of inelastic loss mechanisms, it is traditional to divide the ion scattering process into three steps: (1) the incoming trajectory, (2) the hard collision with the surface atom, and (3) the outgoing trajectory. See Fig. 2.3.

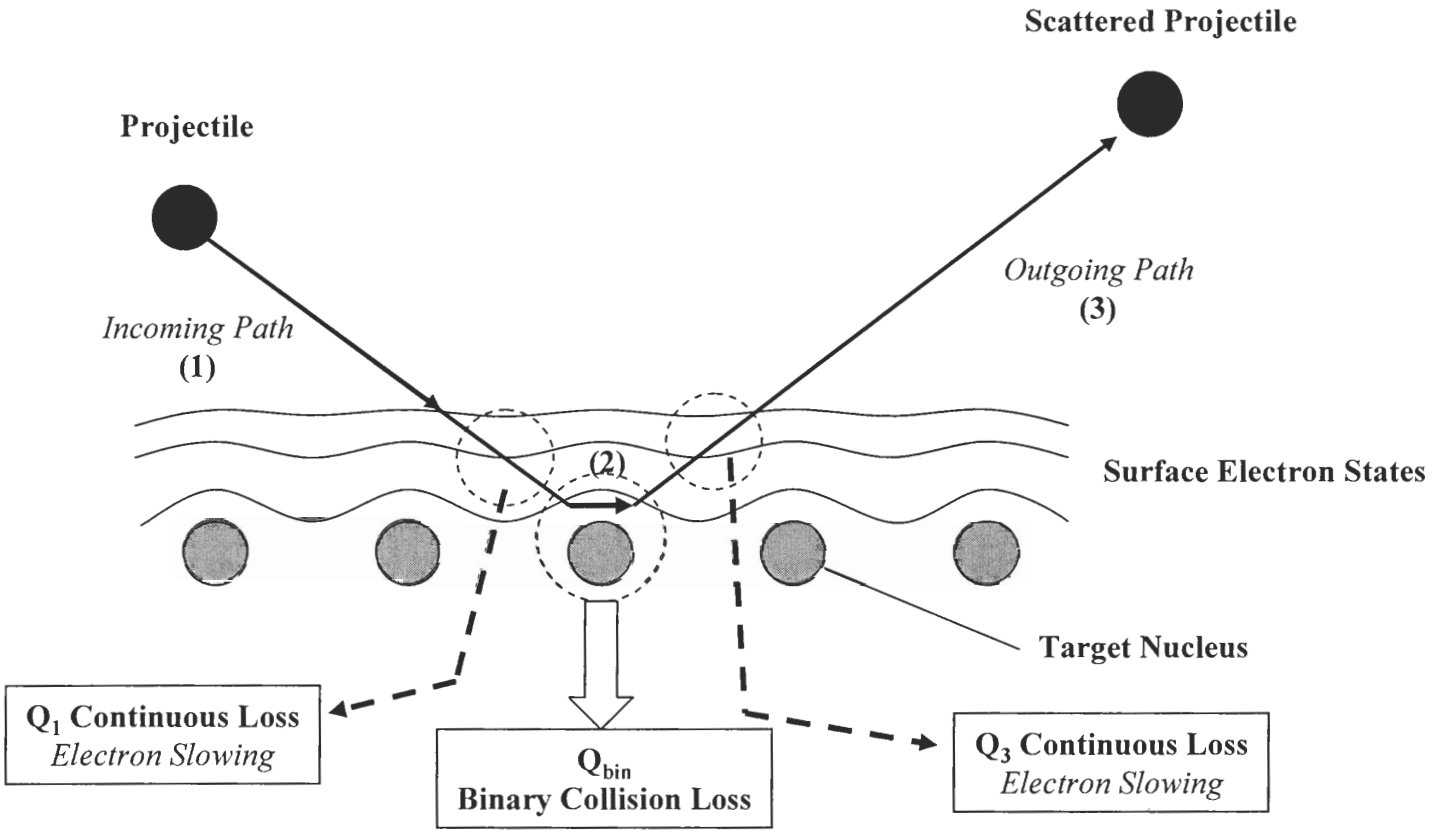

Figure 2.3: Depiction of where inelasticities can occur in the particle trajectory: (1) along the incoming path, (2) during the binary collision, and (3) along the outgoing path. Note: the dotted circles are only intended to distinguish that the continuous loss due to electron slowing is different in character from electronic excitation (charge exchange or electron promotion) that can occur in the hard collision.

On the incoming and outgoing paths, one-electron processes at distances of 5-7 Å such as resonant ionization [RI] and capture [RC] can occur with high probabilities if they are energetically allowed. Also, transitions involving two-electron processes such as Auger neutralization [AN] and de-excitation [AD] occur at closer distances in the 1-3 Å range (Rabalais *op. cit.*). These ionization and neutralization processes are competitive and their relative importance is determined by the overlap of vacant energy levels in the ion with the valence band of the target atom.

Loss mechanisms at relatively large distances are usually treated as an ″electronic friction″ where the particle interacts with the surfaces as a whole. A rough estimate for this energy loss associated with electron straggling can be obtained by assuming the projectile to be moving through an electron gas of constant density. Oen and Robinson, 1976 have introduced a further refinement of this idea, based on the electron density distribution of the hydrogen atom which gives better quantitative agreement with experimental loss data (reference Fig. 2.3):

$$Q_{1,3} = c_i \left(\frac{0.045 A \sqrt{E}}{\pi a^2} \right) \exp\left[\frac{-0.3 R_{\min}}{a} \right] \quad \text{[eV]} \tag{2.20}$$

where,

$Q_{1,3}$ = energy loss along the incoming (1) or outgoing (3) paths
c_i = fitting parameter
A = parameter from the LSS theory (Lindhard and Sharff, 1961)
E = particle energy
a = Firsov or Lindhard screening length
$R_{\min}$ = apsis distance

Although these models are essentially atomic in nature, they can be applied to ion scattering from surfaces so long as the incident and scattering angles are not too small. This is possible because most of the energy loss occurs very close to the target atom (Xu *et al*., 1998).

The most interesting part of the scattering process occurs during the violent collision (step 2) because a short-lived (10^{-13}-10^{-15} s) quasi molecule is formed between the projectile and target atoms. The internuclear distance in this quasi molecule is often

very small (0.2-1 Å), resulting in considerable overlap of the inner electron shells of the two colliding atoms. In fact, the collision energy and laboratory observation angle gives the experimenter a direct way to probe different nuclear distances and hence, excitation mechanisms in the quasi molecule.

As one might expect, charge exchange phenomena and electron promotions into hybrid molecular orbitals (MO) can occur in the quasi molecule. These events depend strongly on the minimum distance reached during the collision (apsis). ″Virtual″ MO's are formed as a result of the atomic orbital (AO) crossings of the collision partners (Fano-Lichten theory ─ Fano and Lichten, 1965). When the partners recede, excited electrons are often trapped in higher AO states (often autoionizing) which can last much longer (10^{-7}-10^{-9} s) than the collision time. These electron promotions occur at the expense of the incident ion kinetic energy and become directly observable as discrete energy losses that occur during the hard collision. As a result, the scattered projectile ion has a kinetic energy that is less than the BCA predicted value. In fact, discrete energy losses in the projectile exit energy that suddenly ″turn-on″ as the impact energy is increased provide direct evidence for these electron promotions and charge exchange processes. As an example, scattering of Ne^{+} off Si surface at 2 keV shows a significant shift (~45 eV in CM frame) from the BCA predicted value that has been attributed to the formation of Ne^{**} in the hard collision, which later autoionizes to Ne^{+} far away from the surface (Xu *op. cit.*).

Due to the discrete nature of electronic excitations which can occur during the close encounter, a fixed inelastic energy loss associated with the binary collision (Q_{bin}) is usually defined (Rabalais *op. cit.*). Looking at all three trajectory steps in Fig. 2.3, we can see that the energy loss process occurs as follows:

(1) The projectile ion enters the near surface region on the incoming path and experiences a slight slowing due to interactions with the surface electron states from the target valence band. This slowing causes an inelastic loss Q_1, so that the hard collision occurs with the target atom for a projectile having slightly lower energy $E^* = E_0 - Q_1$.

Along this incoming path, the projectile ion may be neutralized through resonant electron transfers with the surface or two-electron Auger processes in the 1-3 Å range.

(2) The hard collision between the projectile ion (or neutral particle if neutralization occurs) and the target atom occurs with an impact energy E^*. During the overlap of projectile and target atoms electron states, electronic excitation of either or both collision partners can occur, which results in a discrete energy loss Q_{bin} in the CM frame. It is important to remember that the binary inelasticity (Q_{bin}) is *partitioned between both collision partners in the lab frame*. In simple terms, the electronic excitation energy loss occurs at the expense of the final energies of *both* of the collision partners. The projectile is ″scattered″ by the target atom with the energy transfer predicted by the BCA kinematic factor at the same time as the Q_{bin} inelasticity occurs. Because the Q_{bin} loss technically occurs in the CM frame, the exit energy of the scattered projectile suffers only part of the Q_{bin} loss based on the transformation between the lab and CM frames. The energy loss suffered by the projectile that is seen in the lab frame (due to the Q_{bin} loss in the CM frame) is referred to as ΔE_{bin}.

(3) Finally, on the outgoing trajectory, the projectile may experience a second slowing due to electron straggling as it leaves the surface region. The straggling loss along the exit is different than the incoming path because the particle kinetic energy is lower and the projectile may be in a different charge state after the hard collision than when it entered.

Since we can only measure that portion of the binary inelastic loss that is suffered by the scattered projectile in the lab frame, ΔE_{bin}, a relation can be derived from conservation laws to ″back-out″ the binary collision inelasticity (Q_{bin}) (Rabalais *op. cit.*). This relation depends on the transformation from lab frame to CM frame, so it must depend on both the scattering angle and the target-to-projectile mass ratio:

$$\frac{\Delta E_{bin}}{E^*} = \left(\frac{\gamma}{\gamma+1}\right)\frac{Q_{bin}}{E^*} + \left(\frac{2\cos\theta_L\sqrt{\gamma^2-\sin^2\theta_L}}{(1+\gamma)^2}\right)* \left\{1-\left[1-\left(\frac{\gamma(\gamma+1)}{\gamma^2-\sin^2\theta_L}\right)\frac{Q_{bin}}{E^*}\right]^{1/2}\right\} \quad (2.21)$$

where,

ΔE_{bin} = energy loss suffered by projectile in hard collision in lab frame
Q_{bin} = binary collision inelasticity
E^* = projectile energy after straggling loss occurs along incoming path (1)

Armed with models for electron slowing and electronic excitation during the hard collision, we are now ready to look carefully at the energy loss processes which may cause deviations from the classical BCA theory. The exit energy of the scattered projectile ion including inelastic losses along the incoming and outgoing paths with allowance for a fixed inelasticity during the hard collision can now be evaluated:

$$E_{exit} = K(\theta_L)*(E_0 - Q_1) - \Delta E_{bin} - Q_3 \quad (2.22)$$

where,

E_{exit} = scattered projectile energy measured in the lab frame (with losses)
$K(\theta_L)$ = BCA kinematic factor given by Eqn. 2.4
E_0 = projectile incident energy in lab frame
$Q_{1,3}$ = straggling loss along incoming (1) or outgoing (3) paths given by Eqn. 2.20
ΔE_{bin} = projectile energy loss in hard collision given by Eqn. 2.21

For the present study, all scattering experiments were carried out at a lab scattering angle of 90°, where the scattered projectile energy form Eqn. 2.22 becomes quite simple:

$$E_{exit} = \frac{\gamma-1}{\gamma+1}*(E_0 - Q_1) - \frac{1}{\gamma+1}Q_{bin} - Q_3 \quad (2.23)$$

Equation 2.23 will be used extensively in the data analysis for the two case studies on BCA validity at hyperthermal energies in Chapter 6 and for determining the binary inelasticities for the Ne^{+} and Ne^{++} exit channels seen in the Ne^{+}→Mg, Al, and Si systems presented in Chapter 7.

3. Plasmas Physics and Ion Beam Production

The information in this chapter starts with a look at the basic physical characteristics of plasmas and how they operate. Important underlying concepts such as plasma potential, space charge, and sheath theory are introduced. Issues associated with extracting ions from a plasma source and the generation of high-intensity ion beams are also discussed. Much of the material presented here was integral to the design of the plasma source, extractor, and ion beamline system. Many of these fundamental concepts will be revisited later (Chapter 4) in the details of the beamline design and construction.

3.1 Plasmas

A plasma is a quasi-neutral collection of positive ions, electrons, and neutral particles where interactions between the particles are quite different than those between molecules in an ordinary low-pressure gas. In the plasma, energy and momentum are exchanged between charged species through long-range Coulombic forces rather than discrete, hard-sphere like collisions that occur randomly (Considine, 1976). For this reason, the plasma is often said to exhibit a ″collective″ behavior because particles interact with each other and their surroundings through a large number of distant encounters controlled by electrostatic forces. In addition, any space charge imbalance that may result from a macroscopic segregation of positive and negative charge carriers ultimately leads to electrostatic restoring or ″screening″ forces. These screening forces tend to balance the electron (n_e) and positive ion (n_i) densities over a macroscopic scale, making the bulk of any plasma volume *quasi neutral*.

The physical nature of a plasma is quantified at the particle level using the number density and kinetic energy distributions of ions, electrons, and neutrals. Quite often though, only the average kinetic energy is required for a qualitative understanding of particle-particle and particle-wall interactions. Therefore, an average kinetic energy is usually defined for each plasma species and expressed as a particle ″temperature″ in electron-volts [eV]. The physical characteristics of a plasma are commonly described by the following parameters:

n_o = plasma density = $n_e = n_i$ (quasi neutrality) [particles/cm^3]

n_n = neutral particle density [particles/cm^3]

ξ = ionization fraction = $\frac{n_i}{n_i + n_n} = \frac{n_o}{n_o + n_n}$

T_e, T_i, T_n = electron, ion, and neutral temperatures [eV]

The dynamic range of the plasma state is simply amazing. See Fig. 3.1. Charged particle densities can span nearly twenty orders of magnitude (10^1-10^{20}/cm^3) and electron temperatures can vary from 0.01 eV to 100 keV (Andersen, 1989). The typical plasma sources used for semiconductor etching have particle densities in the 10^{10}-10^{13}/cm^3 range with electron temperatures from 0.1-10 eV. Operating pressures for etching reactors are frequently in the 1-50 mTorr range. A comparison of etching plasmas with several other types of plasmas is shown in Table 3.1. Silicon at room temperature is given for reference.

Table 3.1: Typical plasmas and their corresponding regimes of particle density and electron temperature. Data from Andersen, 1989.

Plasma	n_0 [particles/cm^3]	T_e [eV]
Solar Wind	10^1-10^2	0.01-1
Earth's Ionosphere	10^5-10^7	0.01-0.1
DC Glow Discharges	10^7-10^9	1-10
Low Pressure Processing Plasmas	Cap: 10^9-10^{10}	1-10
Capacitive or Inductive RF	Ind: 10^{10}-10^{12}	0.1-10
Fusion Plasma	~10^{15}	100 eV-100 keV
Silicon at 300K	Atom density = 5•10^{22}	kT = 0.026 eV

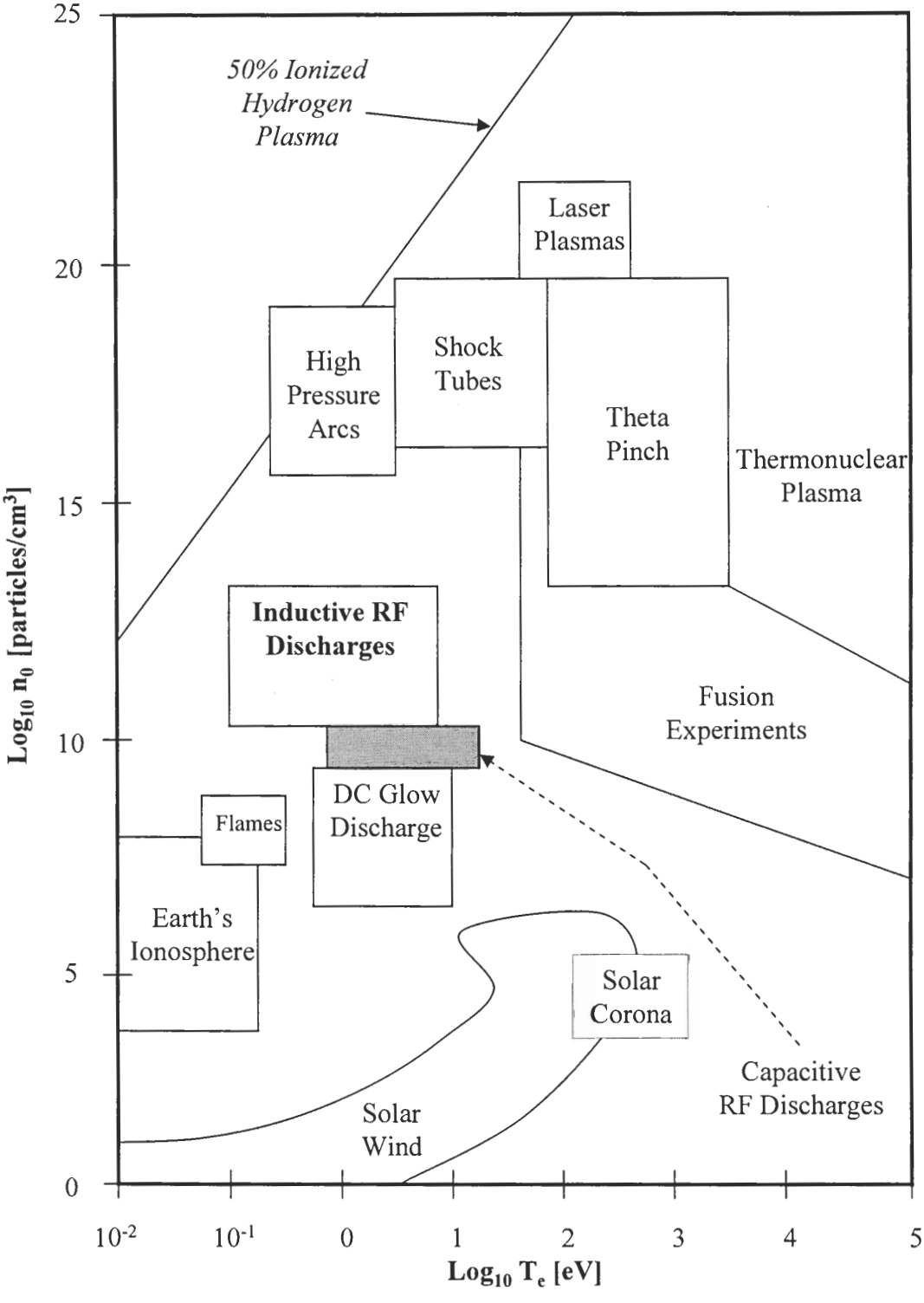

Figure 3.1: Diversity of the plasma state showing the range of particle densities and electron temperatures that can be encountered. Adapted from Andersen 1989.

3.2 Semiconductor Processing and Plasma Etching

Plasmas are ubiquitous in the semiconductor processing industry. More than one-third of all processing steps used today in integrated circuit (IC) manufacture rely on plasma-based processes for pattern transfer, thin-film deposition, or surface modification (Lieberman and Lichtenburg, 1994). Plasmas are commonly employed to sputter deposit metal films, grow SiO_2 and Si_3N_4 films on Si via plasma-enhanced chemical vapor deposition (PECVD), incorporate dopants, and selectively etch thin films of Si, SiO_2, and photoresist on all kinds of substrates.

In thin film etching, the unique environment of the plasma discharge can provide highly reactive ion species which can be *directed* toward a substrate for high-fidelity pattern transfer on semiconductors, metals, and dielectrics. Reactive ion etching (RIE) using a photolithographic mask affords high aspect ratio (depth to width) features and anisotropic profiles with incredible selectivity which are simply not possible by any other means. In fact, very large scale integrated (VLSI) circuit devices of today which require sub-micron pattern transfer and tight critical dimension (CD) control would not be possible without plasma-based etching technologies.

All etching plasmas are electrically driven, low pressure (0.1 mTorr-1 Torr) gas discharges that act like chemical factories to break down feedstock gases to form reactive species that interact physically and/or chemically with a substrate (Lieberman *op cit*.). The plasma behaves as a chemical mixture of reactive ions and neutrals as well as a rich source of ions (mA/cm^2 of ion current) which can be pulled toward the substrate at well defined energies to drive momentum-assisted surface processes.

Plasma sources for dry etching are typically driven with RF (13.56 MHz) or microwave (2.45 GHz) power in either a capacitive or inductive configuration along with a separate RF bias on the substrate to bring the ion impact energy within the hyperthermal range. A schematic representation of both the capacitive and inductive coupling schemes used for plasma etching reactors is given in Fig. 3.2. Historically, capacitively coupled RF plasma sources with low ionization rates ($\xi \approx 0.001$-0.01) were used, but over the last 10 years, inductively coupled sources have taken over exclusively.

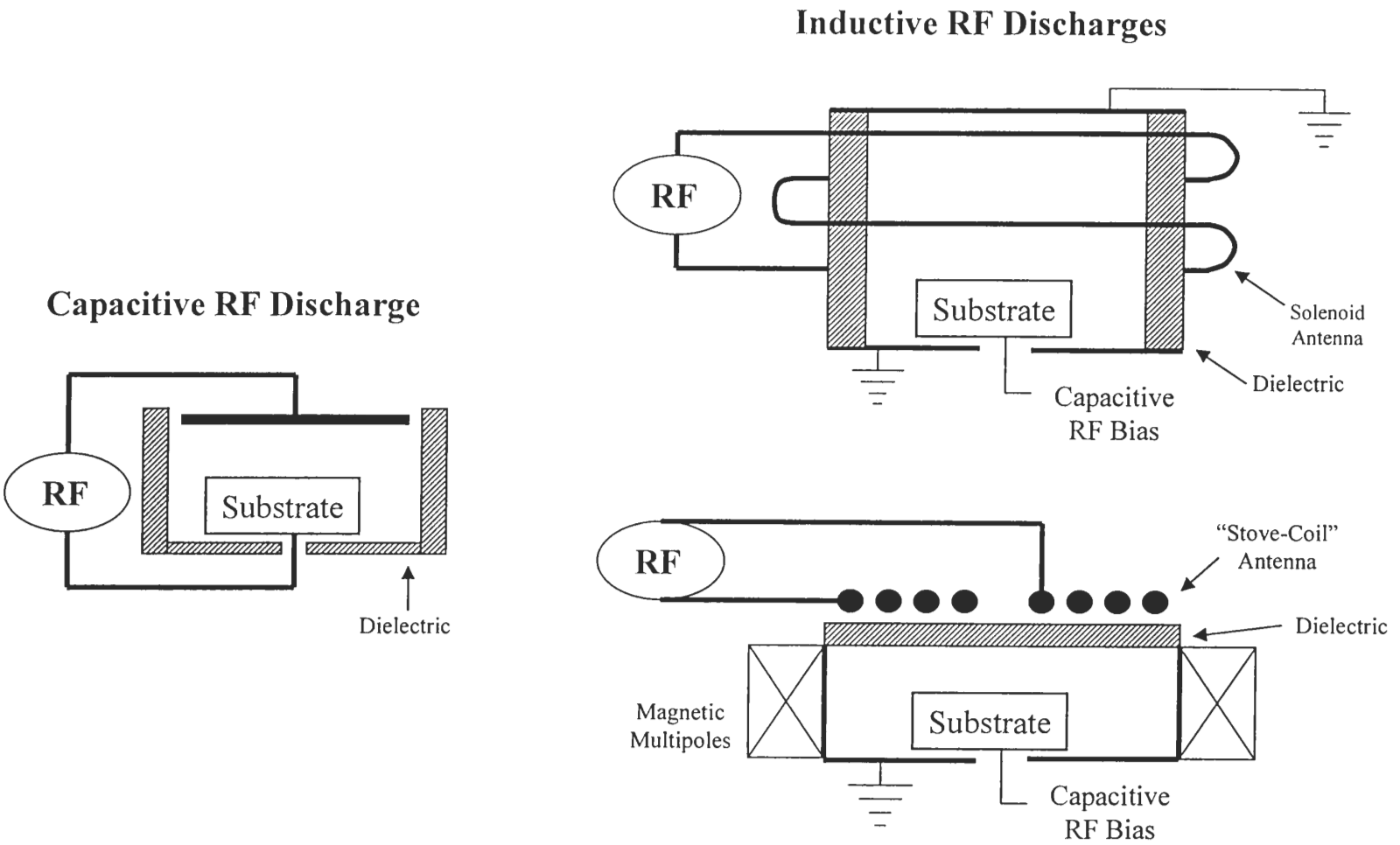

Figure 3.2: Capacitive and inductive RF plasma sources for semiconductor etching. Adapted from Leiberman and Lichtenberg, 1994.

Inductive coupling provides high ion density (10^{11}-10^{13} /cm^3) with low plasma potential (<20 eV) and narrow ion energy distributions (2-5 eV), all at low processing pressure (0.1-5 mTorr) (Lieberman *op. cit.*). In a sense, the inductive coupling scheme ″separates″ the plasma operation from the etching operation. Plasma density can be independently varied (while keeping plasma potential low) by adjusting the input excitation power without affecting the ion bombardment energy (set by the wafer bias). This is simply not possible with a capacitive discharge.

The versatility of the ICP discharge, which has made it the workhorse of dry plasma etching technologies, provides a good starting point towards a robust ion source that can be adapted to ion beam scattering studies in the hyperthermal energy regime. It combines tunable-energy (by adjusting the plasma potential externally) with narrow energy spread, high ion currents (1-10 mA/cm^2), and low operating pressure that are well-suited for generating high current ion beams at low energy.

3.3 Inductive RF Discharges

Gas breakdown in an inductive discharge is accomplished by an initial coupling of free electron motion with the large potential field variation of the antenna. These free electrons are given a ″kick″ in energy with each RF field oscillation until they reach the ionization potential of the working gas. Electron impact ionization of the gas occurs, which provides the discharge with more and more electrons (as well as ions). Eventually, an ionization cascade develops where electron and ion creation processes fuel further gas breakdown through collisions.

Ultimately, the magnetic field variation from the RF drive antenna sustains the plasma discharge through continual ″heating″ of the electrons formed from ionization of neutral gas atoms (Lieberman *op. cit.*). Inductive operation is a far more efficient mode of power coupling than purely capacitive excitation. As such, ICP discharges often have plasma densities that are 100-1000 times greater than capacitively coupled RF plasmas at the same gas pressure. However, inductive operation requires enough electron density so that the plasma electrons can behave *collectively* like a large fixed inductance to the RF antenna. The magnetic field from the antenna excites the plasma electron inductance like

the secondary coil of a transformer. Power is transferred because the antenna ″rings″ with the electron inductance and causes current to flow through the plasma itself (which acts like a load resistance). See Section 4.4 for more details.

3.4 Basics of Plasma Theory

3.4.1 Debye Length

One physical parameter which is critical in understanding how a plasma interacts with its surroundings is the electron Debye length (λ_d) (Lieberman and Lichtenberg, 1994):

$$\lambda_d = \sqrt{\frac{\varepsilon_o T_e}{e n_e}} \tag{3.1}$$

where,

T_e = electron temperature
n_e = plasma electron density
ε_0 = permittivity of free space
e = elementary charge

This characteristic length scale represents the effective shielding or screening distance of a plasma to external EM fields. Over distances that are several times the Debye length, the electron and ion space charge densities can redistribute themselves to cancel out external fields to screen the bulk plasma volume. As a reference, the Debye length in a high-density argon ICP discharge at 1 mTorr ($T_e \approx 1$ eV, $n_e \approx 10^{11}/cm^3$) is equivalent to 23 μm. Electric field disturbances from reactor walls, bias electrodes, or a substrate are ″washed-out″ through local rearrangement of the charge carrier densities very near the perturbing surface to maintain quasi neutrality in the bulk. This layer where the electron and ion densities are no longer equal is known as the *sheath*.

3.4.2 DC Sheath Theory

All surfaces that are exposed to a plasma develop a positively charged sheath region where a local imbalance in electron and ion space charge density occurs (Lieberman and Lichtenberg, 1994). The unequal positive and negative carrier density causes a potential gradient to develop between the bulk plasma volume and the surface. To see why a sheath forms, one has to consider what happens when a volume of plasma is brought in contact with a wall surface.

Over a very short timescale, fast moving electrons leave the bulk plasma volume at a greater rate than the more massive ions causing wall surfaces to instantaneously charge negative with respect to the plasma. The irreversible electron loss to the wall results in an increased ion space charge ($n_i > n_e$) in the sheath region to offset this loss in an effort to maintain neutrality in the bulk. As a result, the bulk plasma volume always charges positive relative to the wall potential (Φ_{wall}). Once this positive potential develops, electrons are attracted back to the bulk as they drift into the sheath. Ions, on the other hand, are repelled by the positive potential toward the wall through the sheath with kinetic energy (V_p), known as the plasma ″self-potential.″ A qualitative picture of the space charge variation near a plasma-wall interface is shown in Fig. 3.3 for a time-invariant sheath in a typical DC glow discharge plasma. Strictly speaking, there also exists a transition layer, or ″pre-sheath″ region between the bulk of the plasma and sheath. This intermediate layer is formed because continuity in the ion flux must be maintained between the neutral plasma bulk and the non-neutral sheath.

The thickness of the sheath boundary layer for a DC discharge is given by the Child sheath law (Lieberman *op. cit.*):

$$s = \frac{\sqrt{2}}{3}\lambda_d \left(\frac{2V_p}{T_e}\right)^{3/4} \tag{3.2}$$

where,

$s =$ sheath thickness for DC discharge
$\lambda_d =$ electron Debye length given by Eqn. 3.1
$V_p =$ plasma potential
$T_e =$ plasma electron temperature

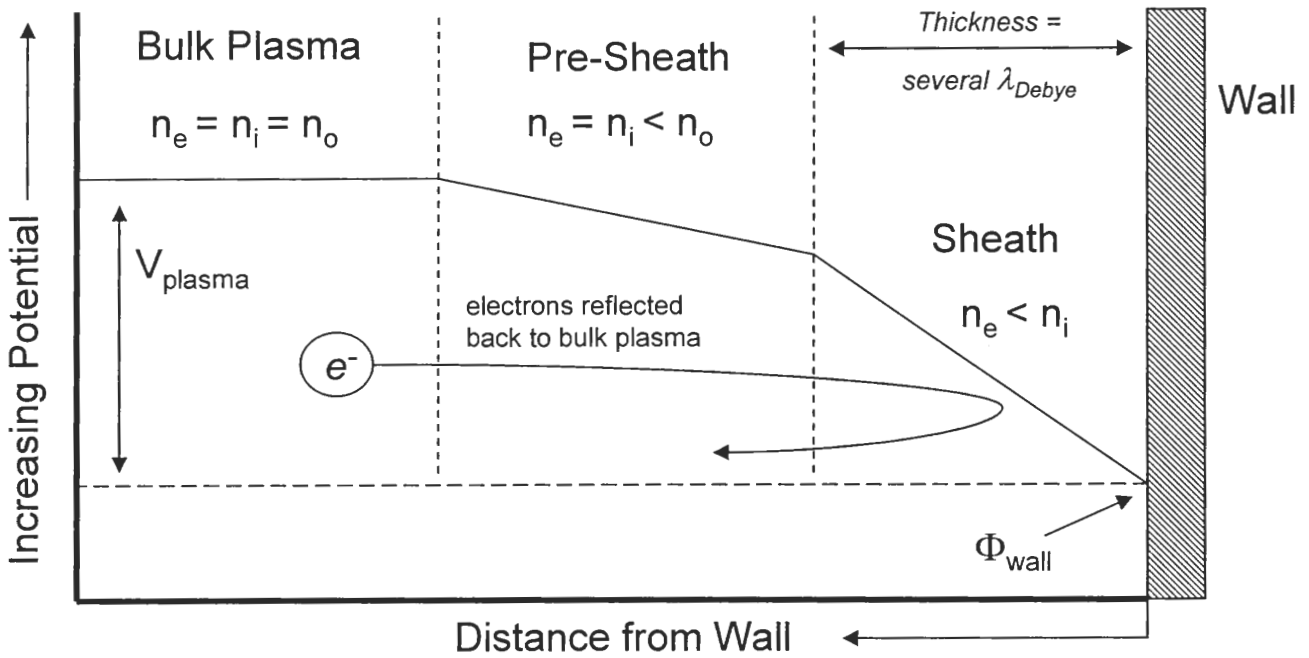

Figure 3.3: Sheath transition for a DC plasma showing the potential gradient which develops between the bulk plasma and any wall surface. Adapted from Leiberman and Lichtenberg 1994.

For most weakly ionized plasmas, the sheath thickness can be many times the electron Debye length (λ_d) for large plasma potentials. In fact, as plasma conditions (n_o, ξ, etc.) or wall potentials (Φ_{wall}) change, the plasma potential V_p and sheath thickness change correspondingly to maintain neutrality in the bulk by equalizing the positive and negative currents across the sheath edge. In this way, the electrostatic forces within the plasma act to ″screen″ out the influence of the surroundings to preserve quasi neutrality, irrespective of charge carrier losses.

3.4.3 RF Sheaths

The utility of DC sheath theory may seem of little use when a time-dependent EM field is used to excite the plasma discharge or bias a wall surface (other electrodes or the wafer itself) that is directly exposed to the plasma. In these cases, one would suppose that a *dynamic* sheath should form where the electron and ion densities are constantly changing in response to the oscillatory nature of the imposed RF potentials. It is important to remember that the plasma electrons can respond almost instantaneously to changing external potentials while the more massive ions (at least 10^3-10^4 times heavier) can not. As a result, the plasma potential and electron current to the walls oscillate in phase with the applied RF field. However, a DC ″self-bias″ develops between the bulk plasma and the wall just like we saw earlier in DC sheath theory. This occurs because the ions are simply too massive to respond to the RF field variation on a time scale that appreciably changes the ion space charge density.

Figure 3.4 gives a qualitative representation of the RF variation in the plasma potential and the DC self-bias voltage. It can be seen that the plasma potential is composed of a pure RF variation (from the electrons) with a positive DC offset from the wall potential due to the ions (Williams, 1997). It should be noted that this picture is valid for high frequency RF (≈ 5 MHz and up) excitation or bias voltages only, where the ions can simply not respond fast enough to the time-dependent field. Analogous to a DC glow discharge, ions that drift into the sheath are accelerated toward a wall surface with their kinetic energy equal to the DC self-bias voltage.

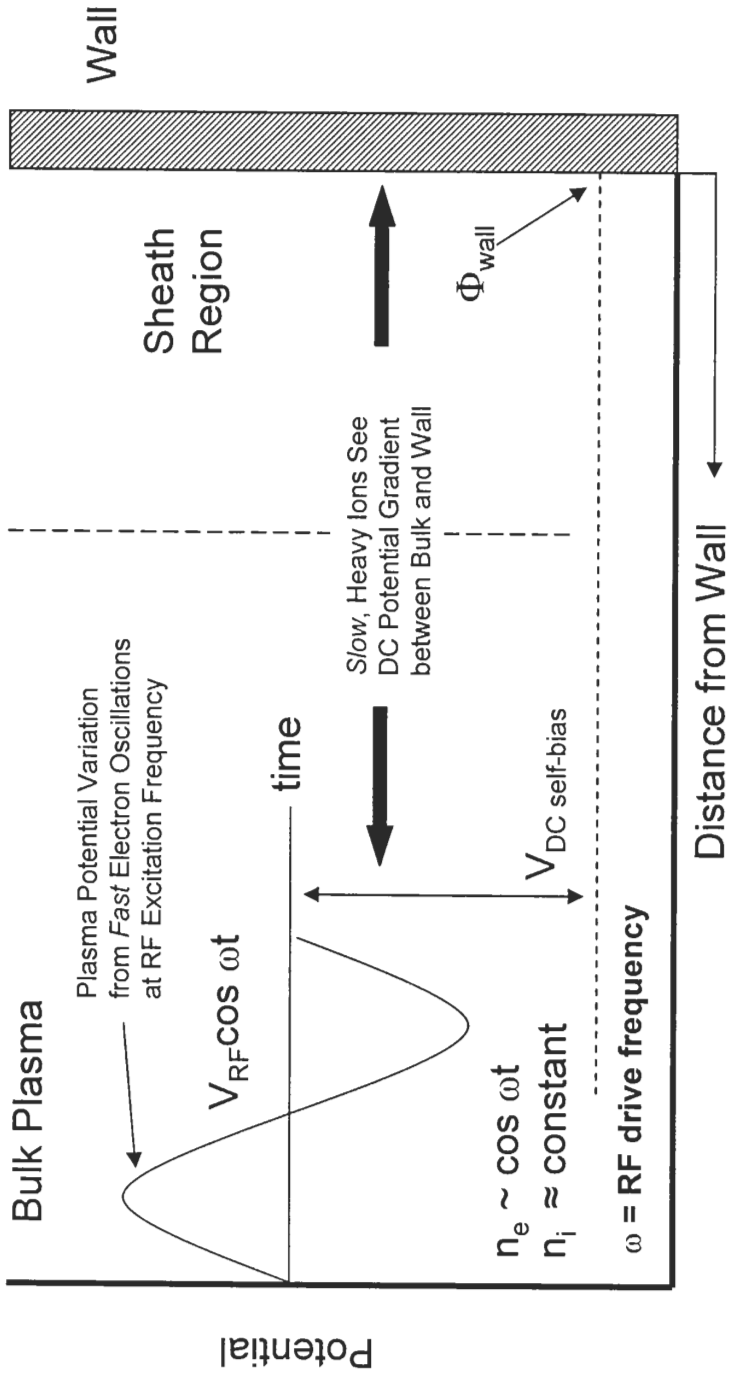

Figure 3.4: Dynamic RF sheath and plasma self-bias which develops. Adapted from Williams 1997.

Inductive plasma discharges usually have much higher density than typical DC plasmas and as a result, the charge flux balance across sheath is different for the inductive case. The voltage drop across the sheath becomes much smaller for an inductive plasma discharge and so does the sheath thickness. The Child law sheath prediction is no longer valid in these instances. However, the sheath thickness for most inductive discharges is only a few times the electron Debye length (Lieberman *op. cit.*).

3.5 Extracting Ions from a Plasma

If an aperture is cut into a wall surface or electrode which confines a plasma volume, the plasma will effuse out into vacuum because of the inherent velocity of its charge carriers. The expansion causes the plasma to ″bulge″ out from the main discharge forming a jet where ambipolar electric fields are set up to maintain quasi neutrality. It is possible to artificially set up an electric field within this region using an ″extraction″ electrode biased negative with respect to the bulk plasma which will *force* a space charge sheath to form in free space (Septier, 1983). This is possible because the space charge created by the extractor lens repelling the electron flux from the jet *just* counter-balances the space charge of the ions at some point within the free space of the aperture region. The aperture region, *because it has a sheath*, behaves just like a solid physical wall to the bulk plasma discharge.

The ″virtual″ sheath around the aperture behaves as an ion-emitting surface or meniscus where high fluxes of ions can be harvested. This phenomenon is schematically represented in Fig. 3.5. The ion-emitting or plasma free-surface is concave outward when the extraction field is weak (3.5a), causing the ion beam to diverge immediately. By analogy, an overly strong extraction field causes the plasma meniscus to become concave inward (3.5c) and push back into the aperture region toward the bulk plasma volume. In this situation, ions are automatically focused to a crossover point much too soon. When the extraction field strength is just right (3.5b), an almost parallel, low-divergence positive ion column can be formed along the center axis of the extractor electrodes. It is obvious from this figure that the exact field geometry and strength in the extraction region is critical for proper formation of low-divergence beams.

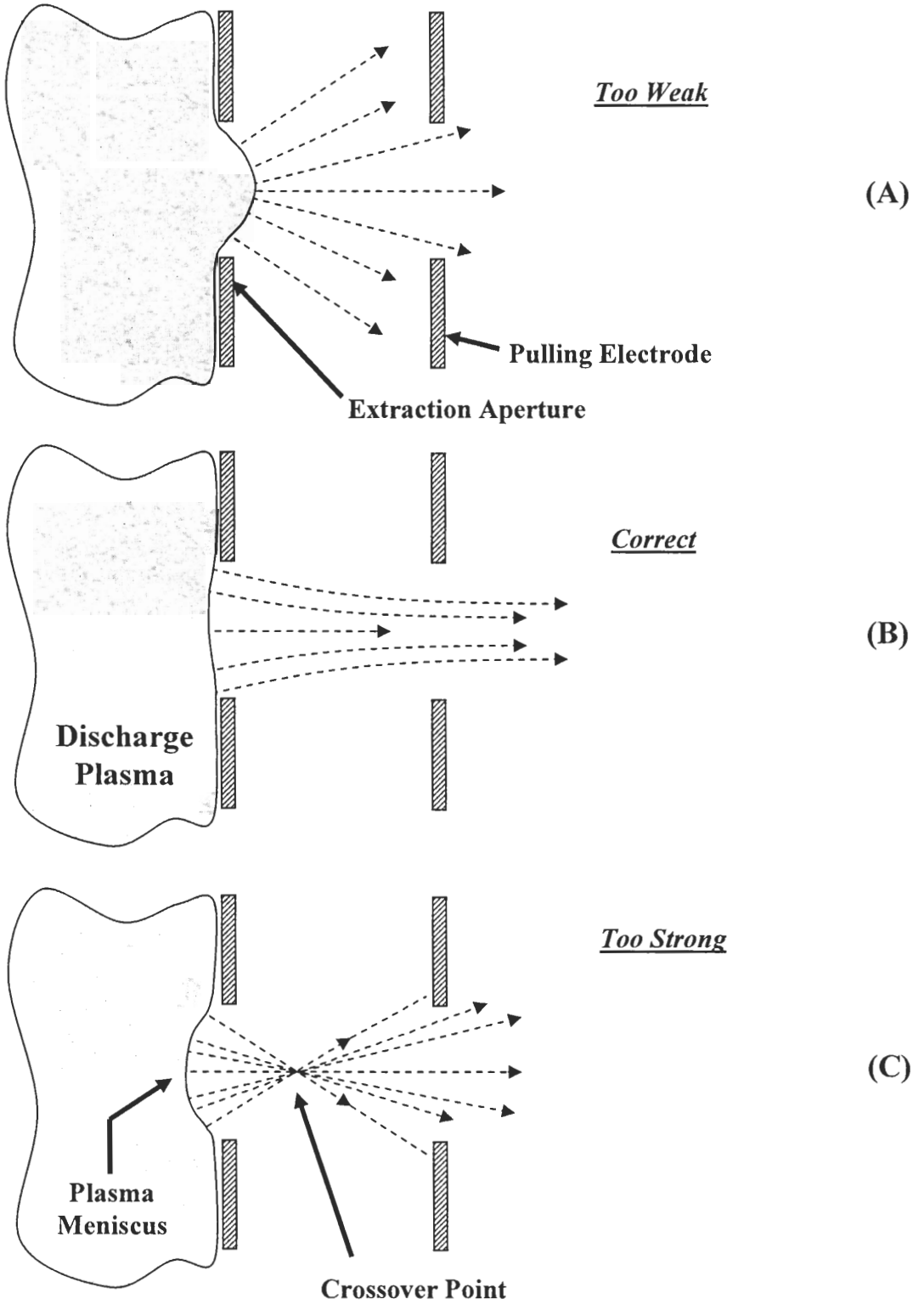

Figure 3.5: Ion-emitting surface of the discharge plasma at the extraction aperture showing ion beam formation with different puller electrode field strengths. (A) too weak, (B) correct, and (C) too strong. Adapted from Septier 1967.

In addition, the extractor field is intimately tied to the plasma operating characteristics because anything that changes the space charge in the plasma bulk (power input, working gas, pressure, *etc*.) also changes the extraction, which in turn, directly affects beam current, divergence, and focusing.

One must remember that the electric field strength at the plasma free surface as well as any nearby focusing fields in the extraction lens system must be fully screened from the bulk plasma volume by the ″virtual″ sheath. In such a case, the sheath thickness increases accordingly to offset the applied high voltage potential. Extraction voltages can only be increased so far however. At some point, the sheath cannot screen out the electric field disturbance; the sheath collapsides and the bulk plasma begins to bulge out the extraction aperture. The vacuum gap between the aperture and the extractor fills with plasma and high voltage breakdown occurs. As a result, a high voltage arc strikes intermittently between the plasma and the extraction system disrupting the ion beam and often the entire electrical system of the beamline. Clearly, such a condition can not be tolerated for stable operation of the plasma source and ion beam. Note however, that maximum beam current usually occurs under heavy extraction conditions (strong fields) near the limit the sheath can sustain.

A plasma is by no means an infinite source of ions. There exists a physical limit to the maximum ion current that can be extracted from any area of plasma discharge envelope. This saturation value for the current density is given by (Wolf, 1995):

$$J_s = 1.57 \bullet 10^{-10} n_i \sqrt{\frac{T_e}{M_i}} \tag{3.3}$$

where,

$J_s =$ saturation current density in [mA/cm^2]
$n_i =$ plasma ion density in [ions/cm^3]
$T_e =$ electron temperature in [eV]
$M_i =$ ion mass in [AMU]

As a frame of reference, a low-pressure (~1 mTorr), inductively coupled RF discharge in argon has $n_i \approx 10^{11}$ ions/cm^3 and $T_e \approx$ 1eV. If this plasma was used as an ion source, no

more than approximately 2.5 mA/cm^2 of ion current could be obtained from any extraction area.

Unfortunately, the size, position, and shape of the emitting surface depend on plasma discharge parameters (T_e and n_e through λ_d) as well as extraction electrode shapes and voltages. It is this ion-emitting surface which ultimately sets the maximum useful beam current, geometry, and divergence (emittance). The challenge is to develop a geometry where ions are extracted from a plasma near the limit the sheath can sustain to form a high current ion beam while maintaining low divergence, aberration, and bombardment damage to focusing electrodes. In addition, this extraction system must be adaptable and robust. Ions should be collected, focused, and transported downstream of the plasma efficiently for a wide variety of space charge conditions that exist when operating the plasma with different source gases, power input, and pressure.

3.6 Space Charge and the Langmuir–Child Limit

The extraction of ions from a plasma to form a high current ″ion beam″ using an electrostatic lens system to focus the ions as they leave the sheath may seem straightforward at first glance. However, one very important aspect must not be overlooked: Coulombic repulsion between the ions. Unfortunately, the very force that allows the quasi-neutral plasma to exist makes focusing and transporting high ion currents very difficult because of mutual repulsion between the particles. In fact, there is a well defined space-charge-limited current density which can be sustained within a potential gap. This density is given by the Langmuir─Child law (Lieberman and Lichtenberg, 1994) for a planar diode which relates the maximum current density that can be supported between two electrodes with potential difference (V), and spacing (d):

$$J_0 = \frac{4}{9}\varepsilon_0 \left(\frac{2e}{M_i}\right)^{1/2} \frac{V^{3/2}}{d^2} \tag{3.4}$$

where,

$J_0 =$ maximum current density
$V =$ potential difference between two planar electrodes
$d =$ electrode spacing
$M_i =$ ion mass

The experimental implications of this limit can be easily seen in the *V* scaling: high current ion beams must be extracted and transported at the highest possible voltage to minimize space charge repulsion between the charge carriers. However, practical considerations in the laboratory often dictate an upper bound on beam focusing and transport voltages:

- Electrical isolation of vacuum components and power supplies can become unwieldy with potentials above 30 kV.
- Vacuum gaps between focusing electrodes must become greater to withstand high voltage breakdown, making the optical column physically larger and beam transport distances longer.
- Magnetic-steering or mass-filtering requires larger and larger fields (> 1 Tesla) as beam energies rise above 20 kV for all but the lightest ions. Large area fields in the 1 Tesla range made with electromagnets require significant power and cooling, not to mention their large size.
- High voltage arcing can become catastrophic and destroy electronic components because of stored energy in any stray capacitance.
- Safety becomes paramount.

3.7 High-Intensity Ion Beams

Many sources have been used to generate ion beams to study gas-surface interactions. Some methods include direct electron impact ionization from hot filaments or field emitters, high voltage arcs, DC/RF plasmas, and hybrid sources. An excellent review of nearly all types of ion sources can be found in Wolf, 1995. Most sources fall into one of two categories: low pressure (< 10^{-5} Torr) where beam currents are usually very small (<1 nA/cm^2) or intermediate pressure (0.1-100 mTorr) where beam currents can reach 1 mA/cm^2, at the expense of several stages of differential pumping. The latter is considered a necessity if gas-surface interactions are to be studied at bombardment rates in the monolayer per second range. For example, a beam fluence (ions/cm^2 s) of approximately one monolayer per second ($2 \cdot 10^{15}$/cm^2 s) on crystalline silicon translates

to a beam current density of 320 $\mu A/cm^2$. It should not be overlooked that reactive beams are almost always formed by cracking or exciting a less reactive or even inert molecular precursor. Clean, conclusive scattering experiments with this type of system require mass-filtering of the incident beam, thereby reducing the useful beam current even further.

Many of the processes that occur when ions or neutral molecules interact with surfaces are both fluence and total dose dependent. Processes such as adsorption and desorption, diffusion, chemical reaction, and even simple physical sputtering can have a strong dependence on arrival rate through surface coverage. Therefore, any ion beam experiments used to investigate surface interactions which occur during industrial processing conditions (*i.e.*, dry etching of Si) must keep in mind that realistic fluences should be the ″design goal″ if relevant conclusions are to be drawn.

Unfortunately, all ion sources have one disadvantage: conversion of neutrals to ions is rather low. Electron impact sources are dismal performers and can only achieve ~1 ion in 10^4-10^5 neutrals at the best. On the other hand, high density plasma sources such as the ICP can provide a conversion efficiency of perhaps ~1 ion in 10^2-10^3 neutrals. The high conversion comes at the cost of increased power input and higher operating pressure range (1-50 mTorr). Significant power input is not a problem, so long as construction materials can withstand the large amount of wasted energy (heat) that is dissipated directly in the ion source itself.

Higher operating pressures, however, mandate several stages of differential pumping between the ion source and scattering region because the target sample must be held under ultra high vacuum (UHV) conditions (10^{-10}-10^{-8} Torr). UHV is necessary to prevent background gas adsorption on the target surface. Contaminant species on the target surface at sub-monolayer coverages can significantly change the surface scattering behavior.

Operating the ion source in the mTorr range also requires huge pumping speeds in the ion extraction region. Particle collisions in the region where the ions are extracted from the source can be detrimental to overall beam quality and limit the maximum obtainable beam current. Some of the undesirable effects include:

- Energetic positive ions can be neutralized upon impact with background gas atoms severely decreasing the beam current.
- Repeated inelastic collisions with background gas atoms will broaden the ion energy distribution.
- Secondary ions formed when primary ions strike residual gas atoms can be accelerated by the focusing electrodes and ″contaminate″ the beam.
- Sputtered material from focusing electrodes can be entrained in the beam.

Fortunately, all these effects can be minimized with good focus electrode design, huge pumping speeds in the extraction region, and operating the plasma source in a region where the ion yield is high while trying to minimize the gas load to the rest of the beamline system. Unfortunately, the majority of the gas load comes from the neutrals that are not ionized in the source. This is undesirable, yet, totally unavoidable. Therefore, the beam transport line must be differentially pumped at several points along the ion beam path to make the leak-rate of neutrals into the scattering chamber negligible. In this way, several differential pumping steps ensures that the target is always kept at UHV conditions.

3.8 Neutralization of Intense Ion Beams

The formation of slow secondary electrons through collision with residual gas or electrode surfaces can sometimes be advantageous. Electrons created from ion impact are usually quite low in energy and they can in effect ″neutralize″ the positive space charge column of the ion beam (Lawson, 1988). These electrons are attracted by the potential well created from the positive space charge of the beam and carried along with the ions in regions of low electric field. In a sense, a ″plasma-like″ beam column forms which can lessen the effect of charge repulsion between the ions. It is even possible to achieve partial neutralization along the entire mass-filtering portion of a beamline because the steering field is always normal to the beam propagation direction, allowing electrons to oscillate laterally through the ion column (Lawson *op. cit.*).

This phenomenon of partial beam neutralization will be mentioned again in Chapter 4 on the discussion of the ion beam decelerator (Section 4.10). It is believed that having a potential well to trap secondary electrons in the region where the ion beam begins to decelerate from the high transport velocity helps to prevent the beam from spreading as it slows. Also, our beamline utilizes magnetic steering to remove any fast neutrals from the beam right before the deceleration step (see Section 4.9.2). We have taken the magnet approach, rather than use an electrostatic field, so as to preserve any natural space charge neutralization that exists in the beam. Electrostatic fields in the bending region of the ion transport line would undoubtedly ruin any inherent neutralization.

3.9 Summary

Many important concepts pertaining to plasma physics, plasma source operation, and ion beam generation have been introduced in this chapter. A fundamental understanding of the plasma potential, sheath, and the influence of space charge forces will be shown to be critical in the design of the ICP ion source and beam extraction electrostatic lens system. We have mentioned that the ICP plasma is an industrially proven, high-density ion source which can be used for both inert and reactive chemistries. Since the ICP has many appealing features such as low plasma potential, narrow ion energy distribution, and high ion current capabilities, we believe it is a good starting point for developing a high current ion beam surface probe. Also, we have foreshadowed some of the beamline design issues which will allow high ion currents to be transported to the target surface for UHV scattering studies.

4. Design of the Low-Energy Ion Beamline Scattering System

4.1 The Overall System

A schematic representation of the four main parts of the low-energy ion scattering system built for this dissertation work is shown in Fig. 4.1. It is composed of the ICP plasma ion source and extractor (I), high-voltage beamline with mass-filter, focusing components and decelerator (II), scattering chamber (III), and scattered product detector (IV). The design, construction details, and performance of each part will be addressed in sequence with relevant analytical formulae and background provided when necessary. There will be emphasis on the key aspects of each piece which makes their overall joining and adaptation to low energy beam studies possible. Detailed engineering plans drawn to scale are provided for most components with explanations in the text given for how and why the specific design was reached. This approach was deemed more appropriate than lengthy textual descriptions.

4.2 Why Must the Target Be Grounded?

Early attempts at hyperthermal ion scattering from surfaces were conducted in surface analysis (XPS, Auger) systems using ion sputter guns (1-5 keV) by back-biasing the target to lower the effective impact energy. This method was necessary because most ion guns (e-impact and especially cold cathodes) run poorly below 1 keV (low beam current into large spots) due to space charge problems with extraction and focusing. Some other experiments even use a mild pulling field (~100 volts) near the target to encourage low energy ions to enter the energy analyzer (just like in secondary ion mass spectrometry, SIMS). Unfortunately, vacuum chambers are almost always grounded. Any stray electric fields between the target, energy analyzer, and the grounded vacuum chamber can affect ion collection and transmittance in an unpredictable way (see Wittmaack, 1996). Estimates of how these fields affect the lab scattering angle and energy analyzer acceptance must be made to ″calibrate out″ their influence. Furthermore, the presence of fields near the target can be detrimental in the hyperthermal regime.

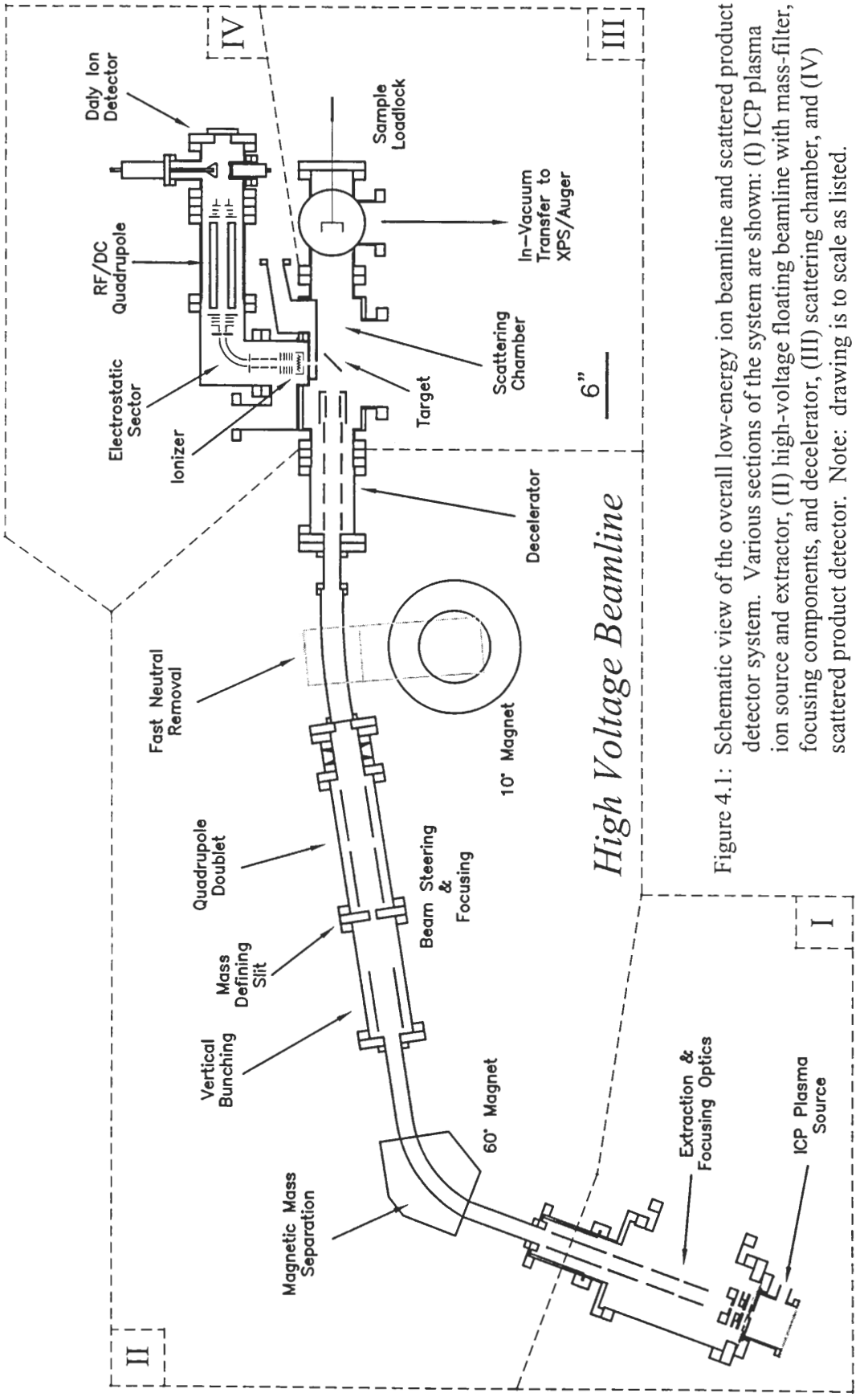

Figure 4.1: Schematic view of the overall low-energy ion beamline and scattered product detector system. Various sections of the system are shown: (I) ICP plasma ion source and extractor, (II) high-voltage floating beamline with mass-filter, focusing components, and decelerator, (III) scattering chamber, and (IV) scattered product detector. Note: drawing is to scale as listed.

The incoming ion beam can impact the target at different angles and different locations depending on the beam energy; the lower the impact energy, the worse the problem. The solution to all this, and the one taken in this work, is to ground the target and everything in its vicinity. The incoming trajectory of the ion beam is not affected by a target bias and charged species leaving the interaction surface see a *field-free* region all the way to the detector. In this way, the solid angle sampled by the detector for all exit energies is fixed by mechanical means only.

4.3 The Accel-Decel Scheme

Our approach to the high current at low energy problem is not a new one (Gordon *et al*., 1991ab; Ishikawa *et al*., 1986; Qin *et al*., 1991). The basic premise is to *create* ions at a low potential, accelerate them to high voltage (many keV) where we can manipulate them more easily, and then decelerate them back down to low energy right before striking the grounded target. Transport at high voltage is the only way to fight the force of space charge between the ions and maintain high beam current (except for fully neutralized beams). The entire *accel-decel* process is possible because electric fields along the ion's flight path are *irrelevant* in determining the collision energy. Ions may speed up or slow down, but the final collision energy is set *only* by the absolute potential difference between where they are *created* and where they *impact*.

In light of the latter statement, what makes high-current, low-energy beam work more demanding experimentally than other energies? First, the only way to mass-filter a high-energy beam of heavy projectiles is a large magnetic field. RF fields like those used in quadrupole mass spectrometers are useless because the ion velocity is simply too high. The ions would stay in the quad for only a small fraction of an RF period, so filtering would not even occur (good resolution takes >50 periods). Second, the beam can never be allowed to decelerate unnecessarily, or it will diverge. This means that all beam quality adjustments (size, shape, divergence) should occur at high voltage and the beam must *never* be allowed to see grounded surfaces (like vacuum chamber walls). Third, the beam will definitely diverge when it decelerates near the grounded target. Therefore, we must try to *pre*-correct the ion trajectories at high voltage before slowing to *offset* the

space charge spreading that occurs when the ions decelerate. Finally, high transport energy for the beam should be maintained as long as possible with most of the deceleration step occurring very near the target (see Section 4.10).

Since we have chosen to ground the target, impact energy can only be adjusted by varying the potential where the ions are created – the plasma source. Therefore, adjusting the beam energy means *floating* the plasma volume above ground by the desired impact energy (less the plasma potential). The plasma can be biased by placing a large metal electrode connected to an adjustable DC voltage within the plasma volume. As mentioned in chapter two, the plasma will always charge positive, by the plasma potential V_p, with respect to this disturbance. If we make this surface a conductor with a potential above earth, we can artificially raise the ion creation potential with respect to the target and hence, change the impact energy. All we need to do is create ions in the plasma at the desired impact energy, extract and mass-filter at high voltage, then deliver them to the target in a collimated, low divergence beam with high current. A schematic representation of how this accel-decel process occurs in our system is shown in Fig. 4.2.

4.4 ICP Plasma Reactor

The plasma reactor (see Fig. 4.3) is constructed from a pyrex half-nipple adapter (~ 4″ OD x 4″ long) having an o-ring face sealing groove from Larson Scientific Glassware with a gas inlet and pumping port added. The reactor is sealed on one end by an aluminum plate which houses a pyrex protection disk and 3″ OD x 0.060″ molybdenum (to avoid excessive sputtering) bias plate directly exposed to the plasma. On the opposing end, an O-ring on the reactor OD seals against an 8″ Conflat flange that houses another pyrex disk containing the extraction aperture (304 stainless steel). This aperture (see next section) is composed of two pieces which key together through a 3/4″ hole in the pyrex plate (electrically isolating the aperture) with a snap ring on the high vacuum side. The high vacuum side of this flange also serves as the mounting surface for the puller, buncher, and front beamline acceleration electrodes using alumina standoffs.

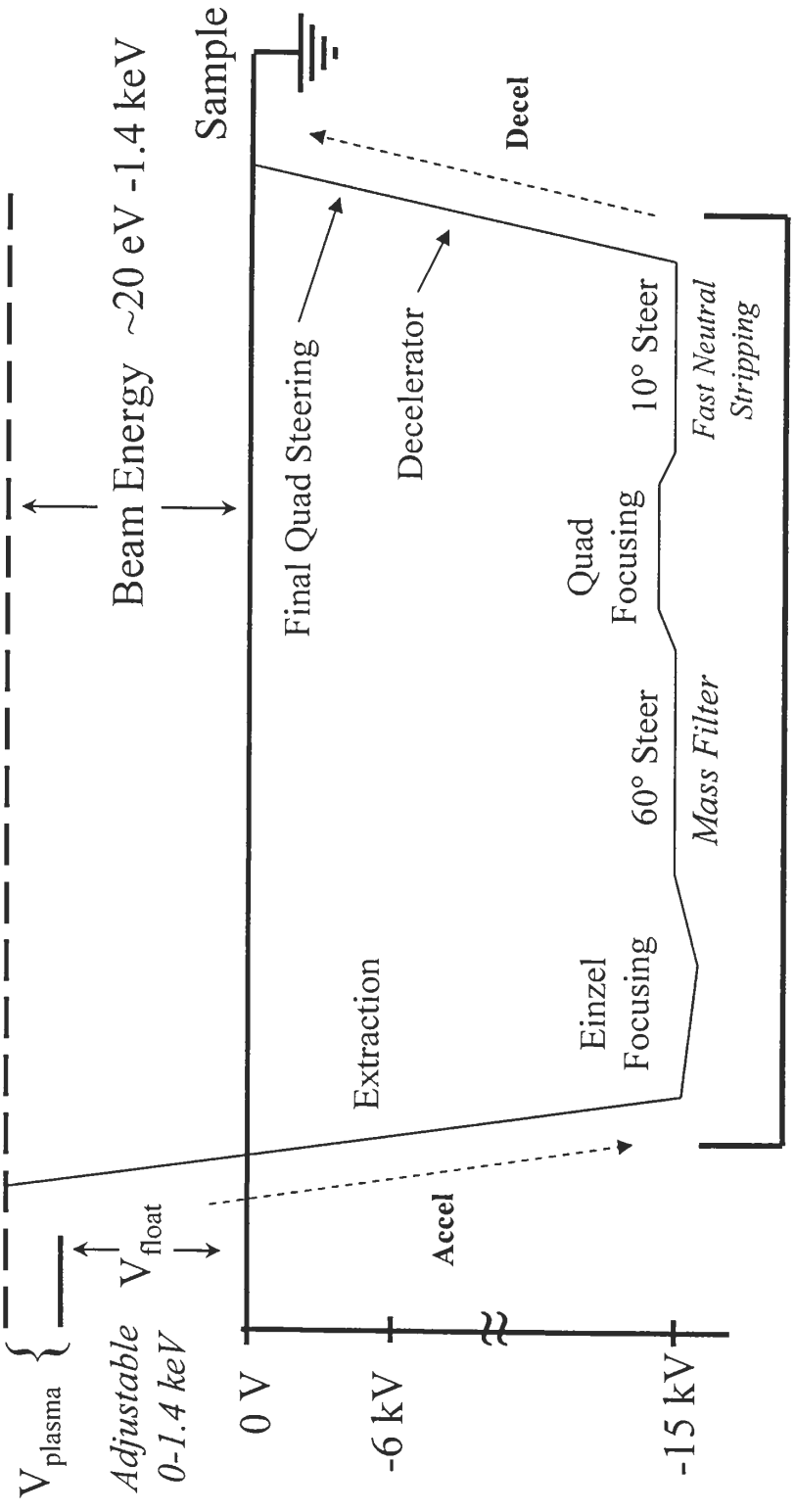

Figure 4.2: Schematic representation of the *accel-decel* scheme used in our ion beamline system. The beamline potentials where mass-filtering and focusing occur are listed.

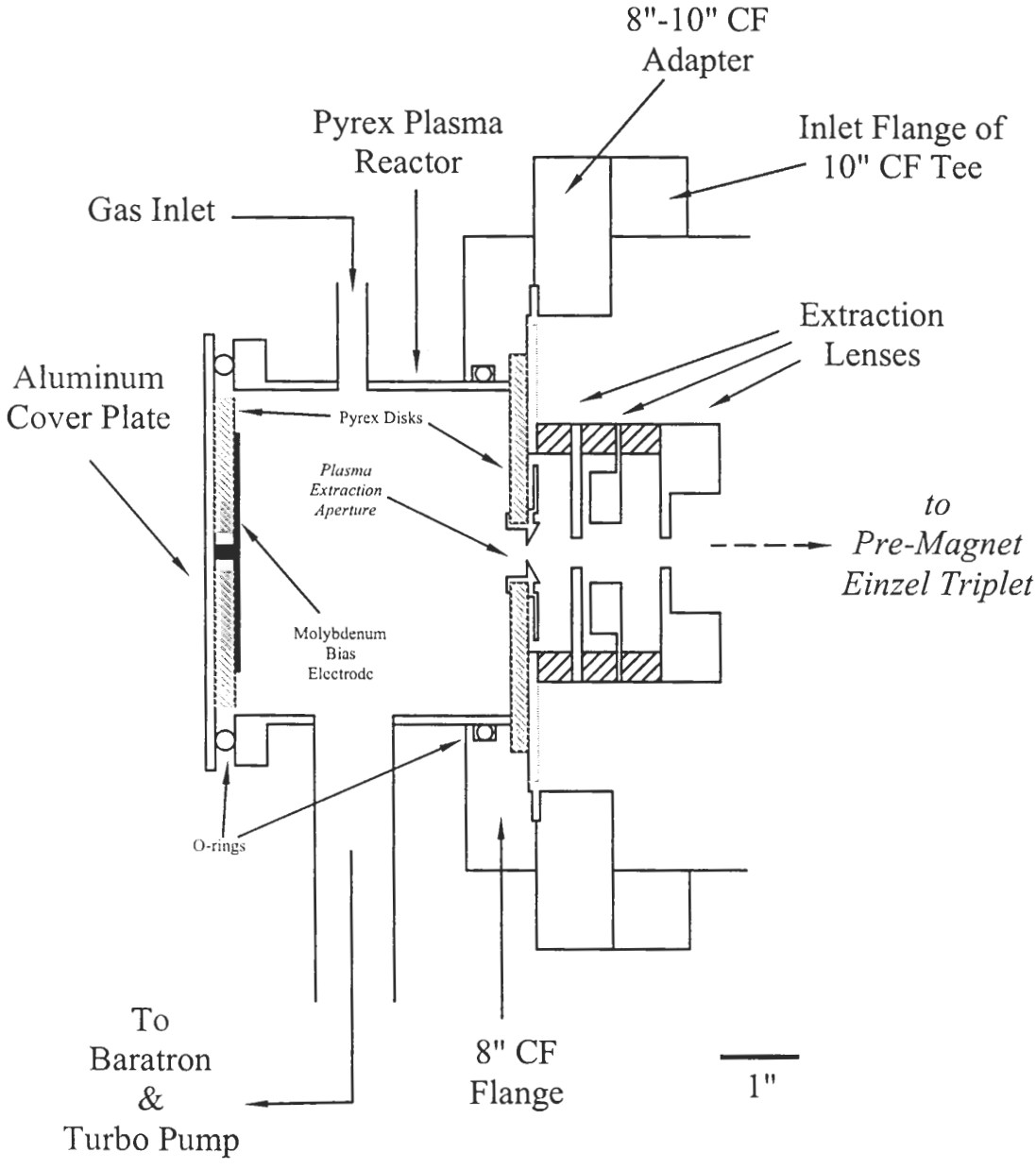

Figure 4.3: ICP plasma reactor and extractor electrodes for ion beam generation. Plasma bias plate and ion extraction aperture are shown.

Gases are introduced through separate mass flow controllers to a mixing station before entering the reactor through Teflon tubing (to maintain electrical isolation). As well, the pumping arm of the reactor is excessively long to keep the plasma volume electrically isolated from the grounded turbo-pump and pressure readout. The whole reactor setup is pumped by a Balzers 210 L/s drag turbo and mechanical backing pump (both were Fomblin oil prepped for oxygen and corrosive gas service). A heated 50 mTorr Baratron functions for pressure readout and the operating pressure (0.2-10 mTorr) is set by adjusting the gas inlet flowrate.

The plasma is excited by a two-turn, solenoid-type RF antenna (1/8″ copper tube cooled with a glycol bath) wound around the glass reactor with a grounded Faraday shield sandwiched in-between. The shield was made of copper sheet after Johnson, (1993) with several 1 mm wide slits lengthwise to aid in striking the discharge in capacitive mode initially. Several layers of Kapton sheeting prevent electric breakdown between the antenna and Faraday shield. Capacitive coupling between the antenna and plasma is minimized because the induced eddy-currents in the shield cancel out the E-field of the antenna. It is imperative that capacitive coupling be minimized to keep the plasma potential low (< 20 eV) and ion energy distribution narrow (Leiberman and Lichtenburg, 1994). The entire reactor is forced air cooled with two high volume fans because of the high RF levels used to power the discharge.

The electrical circuit used to excite and bias the plasma is shown in Fig. 4.4. The RF antenna is driven through a Π-network match box from an ENI 1250W RF power supply operating at 13.56 MHz. Bird power meters are used to monitor the forward and reflected power from the antenna. The plasma bias is supplied by a Spellman +3 kV, DC switching power supply (25 kHz) which had to be protected from the high frequency electron oscillation in the plasma potential (5 V peak-to-peak @ 13.56 MHz). A 4-stage low-pass LC filter was necessary to reduce the 13.56 MHz noise to < 0.1V peak-to-peak on the bias line to allow the feedback regulator in the DC supply to function properly.

In the inductive excitation scheme, plasma electrons behave like an inductor (L_e) in series with a ″plasma resistance″ (R_p). A ″transformer-like″ equivalent circuit for the antenna and plasma is shown in Fig. 4.5.

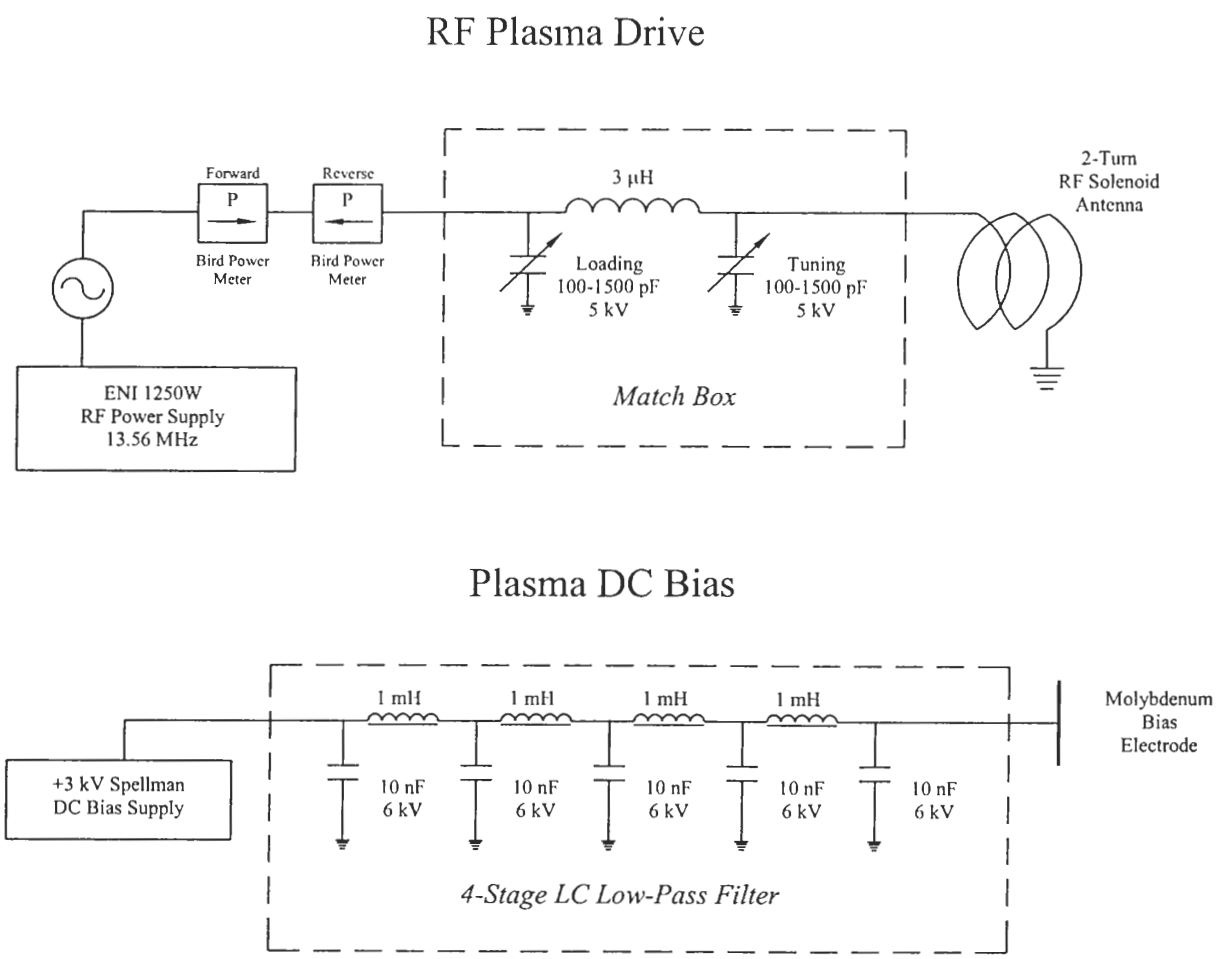

Figure 4.4: RF drive circuit for the ICP plasma and DC bias circuit for floating the entire plasma volume above ground.

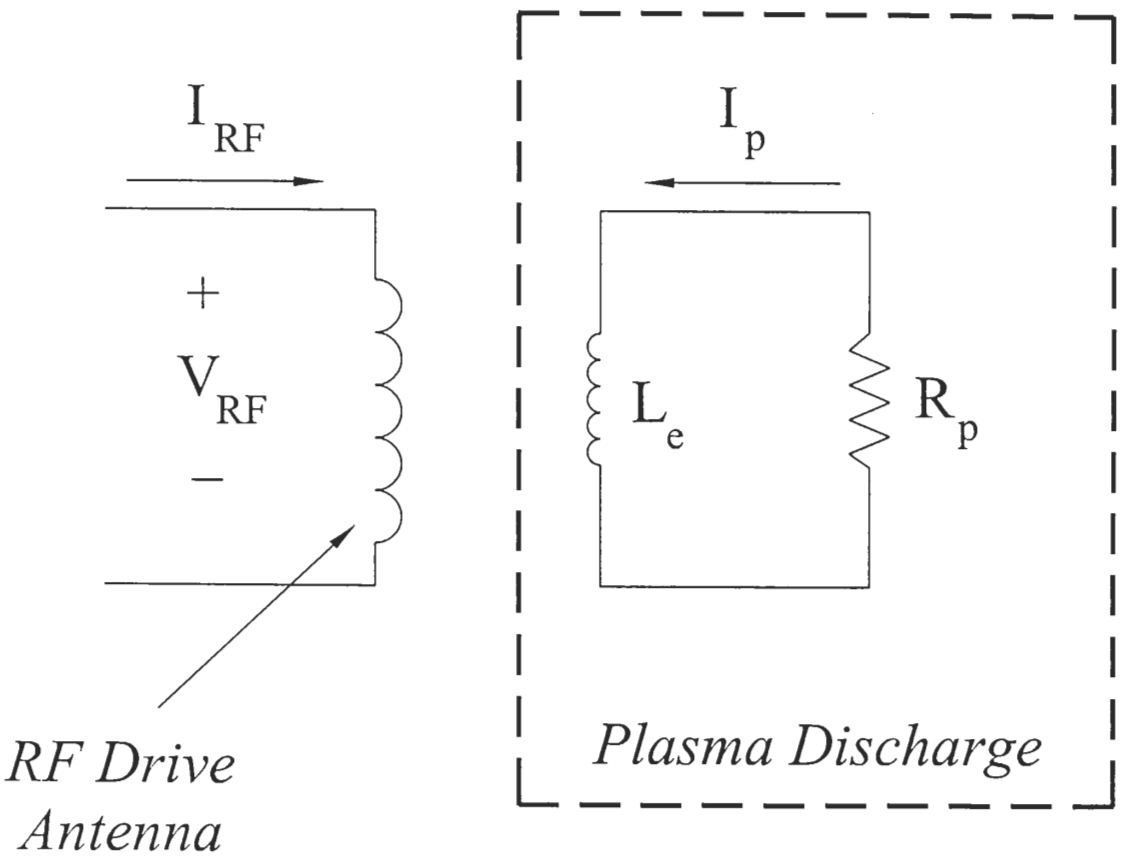

Figure 4.5: Equivalent circuit for an ICP plasma discharge.

The oscillating B-field from the antenna, when properly matched, can induce a standing wave in the plasma ″tank″ circuit, thereby transferring power. Maximum coupling efficiency occurs when the plasma inductance is large (high electron density) and impedance matched to the antenna circuit. As one might expect, this coupling through magnetic induction depends directly on the ″tank″ circuit of the plasma. If the effective inductance $\left(L_e\right)$ due to the plasma electrons is small (low plasma density), then inductive coupling does not occur, and power can not be transferred through the antenna B-field. This behavior manifests itself in the lab as a weak, capacitively coupled plasma formed initially that will suddenly jump to inductive mode once a threshold electron density is reached. The initial discharge couples to the E-field of antenna and as power input increases, more and more electrons are produced through ionization. A point is reached when the plasma electron inductance becomes large enough and the tank circuit of the plasma begins to ″ring″ with B-field of the antenna like the secondary winding of a transformer. When this occurs, the electron density (ion density too) jumps up abruptly by several orders of magnitude. The transition from capacitive to inductive mode depends strongly on the operating pressure, working gas, and power input (Leiberman and Lichtenberg, 1994). At low pressures or when working with highly electronegative gases, inductive coupling will just not occur without a strong magnetic field around the plasma to keep the electron density high.

For our reactor, operating pressures were routinely 1-5 mTorr with input powers of 300-700W (depending on the working gas) needed for reasonable inductive coupling. One important point that should not be overlooked is the extremely high resonance Q-factor. Proper impedance matching of the antenna to the plasma to within ± 2 pF on the match box was *critical* to maintain inductive operation. Gases that were hard to break down and drive ″inductive″ were routinely mixed with argon to provide enough electrons for good coupling. Therefore, the need for magnetic confinement was avoided. Mixing gases was not deemed a concern because the ion beam was mass filtered downstream.

4.5 Extraction Electrode System

Geometric details of the beam aperture and three-stage lens system designed for ion extraction from the plasma source are shown in Fig. 4.6. The extraction aperture on the plasma chamber is a 0.2″ ID sharp-edge hole with 120° full angle backside bevel that feathers all the way out to the lens perimeter. The bevel allows the electrostatic field from the floating aperture to fall away smoothly to the pulling electrode. Smooth field variation in the vicinity of the virtual sheath is necessary to form an ion beam column with uniform cross section. In close proximity are three cylindrically symmetric electrostatic lenses in series (puller, buncher, and front beamline acceleration electrodes) made from 6061 aluminum with tantalum cover plates to prevent excessive sputtering. The three-lens setup attaches via alumina standoffs to the high-vacuum side of the 8″ Conflat that seals to the plasma reactor. The back side of the front beamline accelerating electrode joins to another cylindrical lens by a removable, stainless mesh sleeve that allows the whole extractor setup to be removed in one piece and separately cleaned (metal films get sputter deposited on the ceramic standoffs). This entire setup, via the 8″ CF flange, is attached to a 10″ Conflat Tee pumped by a 1000 L/s Seiko maglev turbo with matching dry scroll backing pump. The large turbo is used as the main differential pumping step to significantly decrease the background gas load to the rest of the ion beamline. Typical pressures in this chamber are $5 \bullet 10^{-6}$ torr on a nude ion gauge with the plasma source running at 5 mTorr.

Many plasma extraction lens schemes can be found in the literature, but most are based on an accel-decel triode (high-low-then high again) scheme whose exact geometry is specific to each individual ion source (Holmes and Thompson, 1980; Septier 1967, 1983). Since high-density ICP plasma sources have only come onto the scene within the last 10 years, they have not been used as beamline ion sources (most beamlines are very old). As a result, there are no quick-and-easy design rules to be found in literature. So, the triode scheme was used as a starting point for our system with SIMION simulations of actual ion trajectories to help refine the geometry. One very important design goal was to keep the lens system as ″open″ as possible to maximize the pumping speed in the extraction region to keep collisions to a minimum.

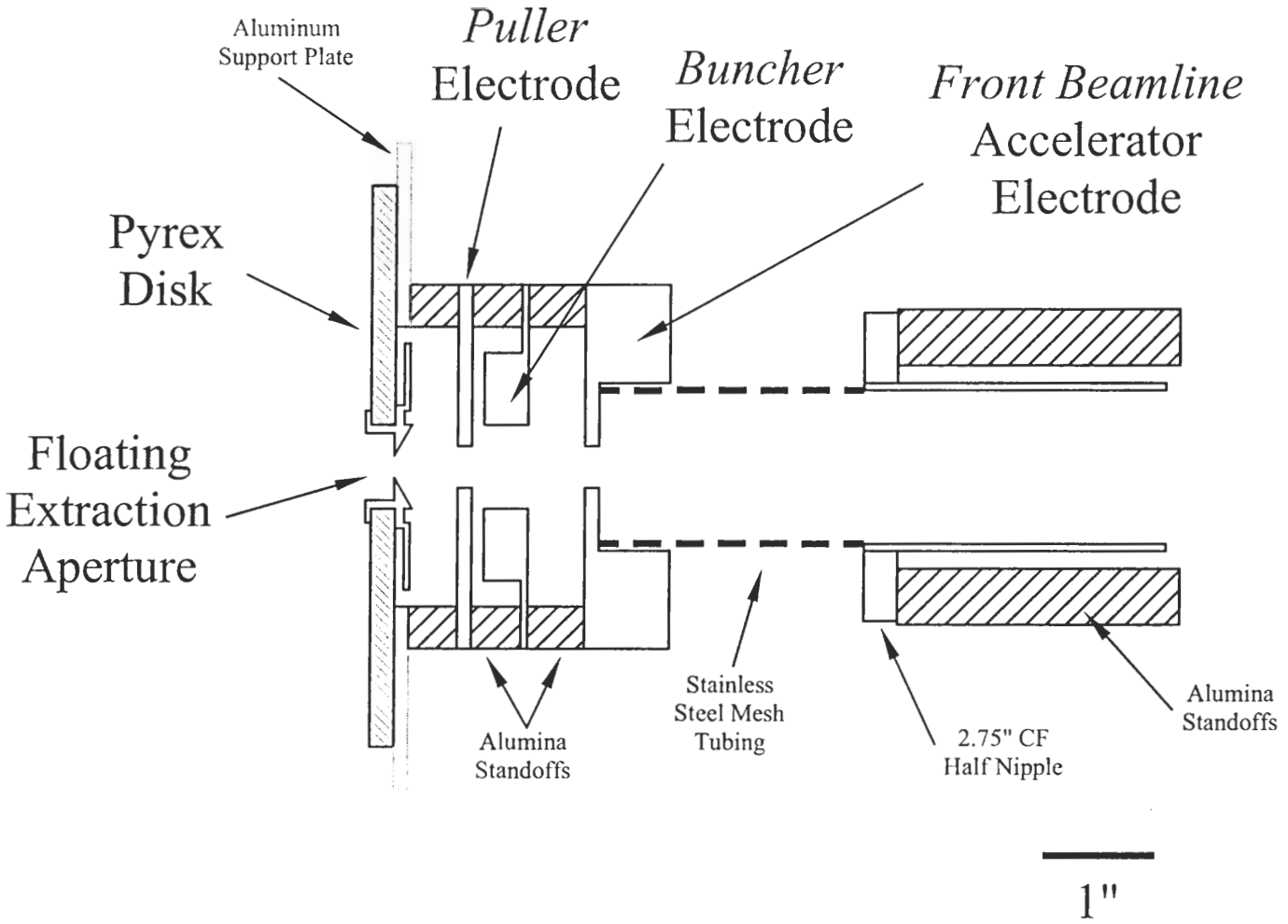

Figure 4.6: Extraction electrode scheme for ion beam generation from the ICP plasma source.

Unfortunately, realistic space charge conditions are hard to simulate accurately (the SIMION author himself specifically point out to be very careful with the code when trying to model space charge (Dahl, 2000). Therefore, a few operational tests of SIMION-designed lens systems were conducted to evaluate their performance, specifically looking for maximum obtainable beam current and decent spot size (using a phosphor screen from Kimbal Physics). In some cases, the lens elements removed from these tests were horribly sputtered or covered with electron burns – a good indicator of how to change the geometry. An ion trajectory simulation is shown in Fig. 4.7 for two different Ar^+ ion beam at 100 μA and 200 μA with 50 eV beam energy leaving the plasma extraction aperture. The problems associated with space charge repulsion can easily be seen between these two cases. The virtual sheath in the aperture region where the ions originate was modeled as an infinitely thin, fixed voltage surface. Simulation details can be found in Appendix 1.

The puller electrode bias is provided by a hefty neon light step-up transformer (driven by variac) through a high-voltage full-wave diode bridge (15 kV @ 0.5A, typically used in microwave ovens) and RC filter clean-up stage. This scheme was chosen because it could tolerate frequent high-voltage arcs from the plasma extraction aperture without any ill effects (we blew up 2 other regulated DC supplies). Whenever the plasma operating characteristics were changed, new ″optimal″ extraction conditions had to be found by varying the field strengths in the extractor. This process invariably lead to high-voltage arcing in some cases. Finally, a -6kV adjustable DC supply (Ultravolt, model 6A12N) is used on the buncher while the front beamline acceleration electrode is connected to a -25 kV adjustable DC power supply (Deltona, model 250651).

4.6 Pre-Magnet Focusing

After the ion beam is extracted from the plasma and accelerated to -15 to -20 kV by the front beamline electrode, it must be ″prepared″ for mass filtering. This entails having the ability to minimize the beam waist at an arbitrary point between the last extraction electrode and the magnet pole shoe (this will become clear in the next section). The easiest way to accomplish this is an Einzel triplet (Dahl, *op. cit.*).

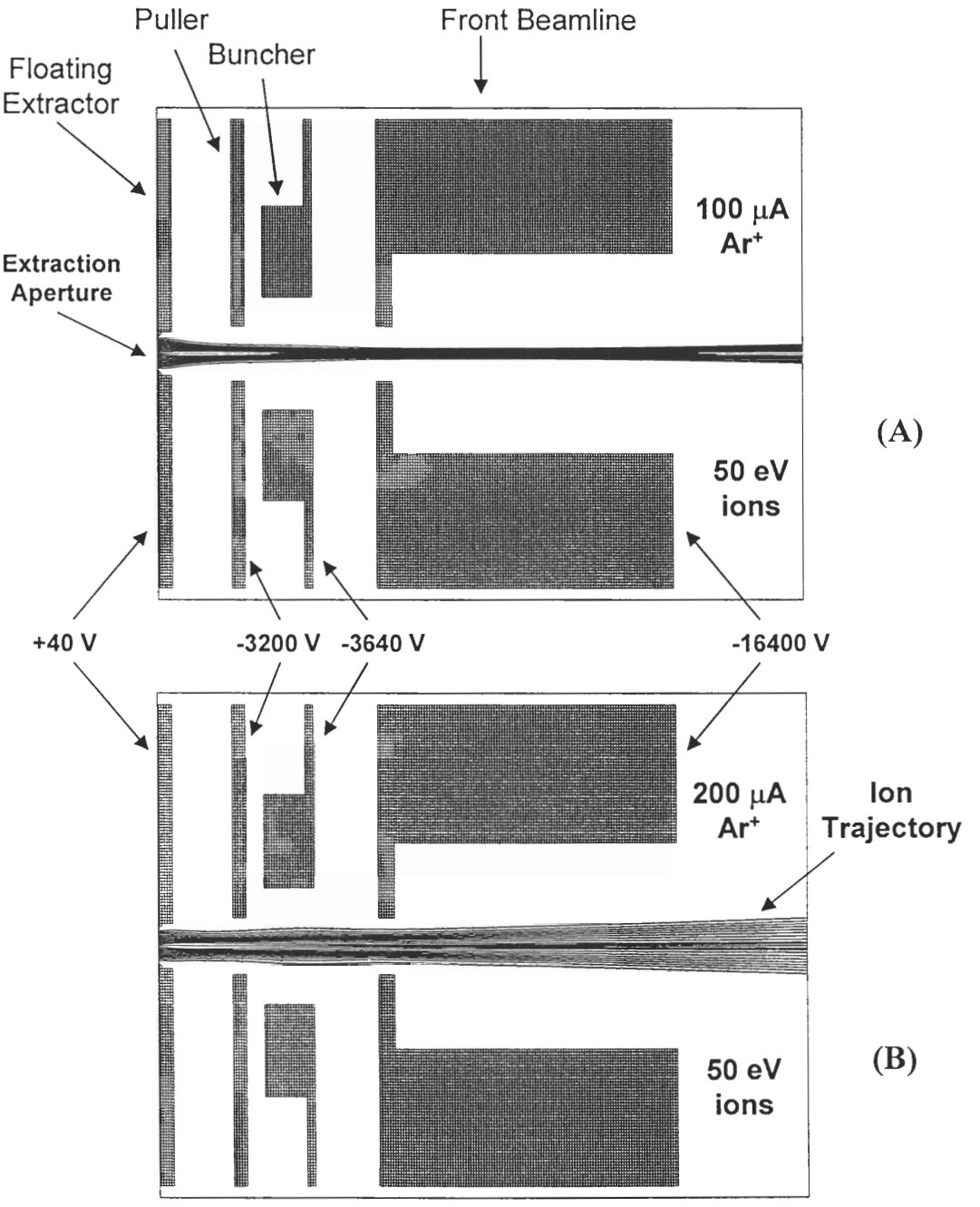

Figure 4.7: SIMION simulations of the plasma extractor for a 50 eVAr^+ beam showing space charge divergence at elevated beam currents. (A) 100 μA extracted ion beam current and (B) 200 μA.

Three cylindrical tube lenses (independently variable) in series allow for ion focusing to an arbitrary point downstream of the lens elements along their longitudinal centerline. In this way, the ion beam can be focused to an arbitrary cross-over point (the source point mentioned in the next section) before entering the magnetic sector field.

The triplet Einzel lens designed for pre-magnet focusing is given in Fig. 4.8, with a photograph of the assembled system presented in Fig. 4.9. The lens system is asymmetric (two short and one long lens) and made from standard 2.75″ CF half nipple vacuum flange adapters (304SS). The tube portion of the adapter serves as the electrostatic lens (1.35″ ID) while the 2.75″ flange face is the lens mount via threaded alumina ceramic standoffs. The flange knife-edges are turned off to make the lens faces smooth. Modifying off-the-shelf vacuum flanges made this lens scheme simple to construct, align, and adapt for other uses. The whole triplet lens setup was attached to a multi-port 10″ CF adapter that seals the 10″ CF Tee of the first differential pumping stage. SIMION simulations were used to establish the exact geometry. The design goal was to provide a minimum waist in the beam shortly after the #3 lens exit for proper introduction of the beam to the magnetic sector field. Each lens has its own -25 kV adjustable DC bias supply (Deltona, model 250651).

4.7 Mass Separation

The motion of a charged particle in a uniform magnetic field orthogonal to its velocity vector is circular because the centripetal force is balanced by the Lorentz force. The radius of curvature for the trajectory in terms of the particle's kinetic energy can be found by simply equating these two forces:

$$r = \frac{\sqrt{2mE}}{qB} \tag{4.1}$$

where,

$r =$ radius of curvature of the particle trajectory
$m,\ q =$ mass and charge of the particle
$E =$ particle kinetic energy
$B =$ magnetic field strength

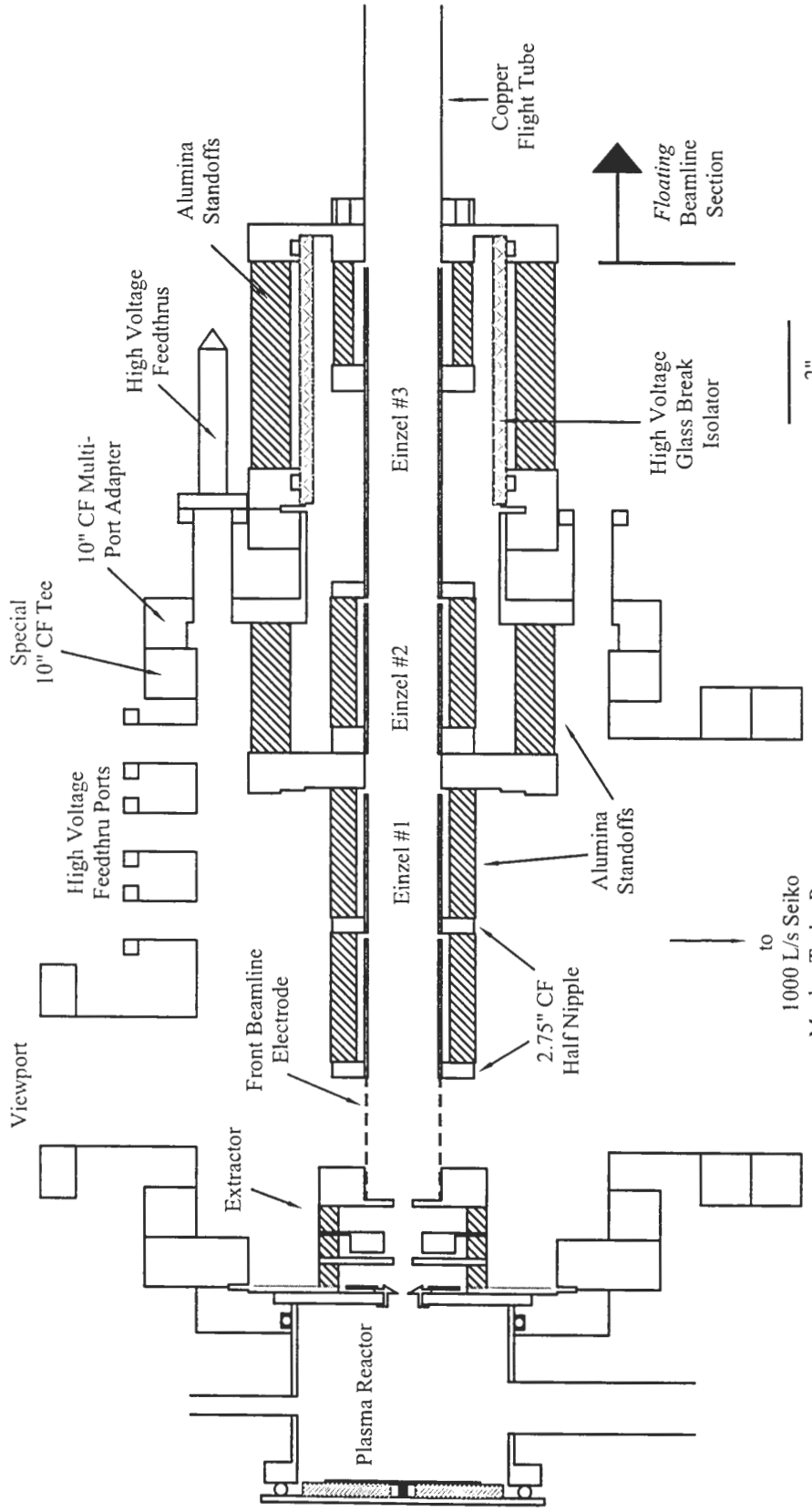

Figure 4.8: Schematic showing plasma reactor, extraction electrodes, and pre-magnet Einzel lens focusing system.

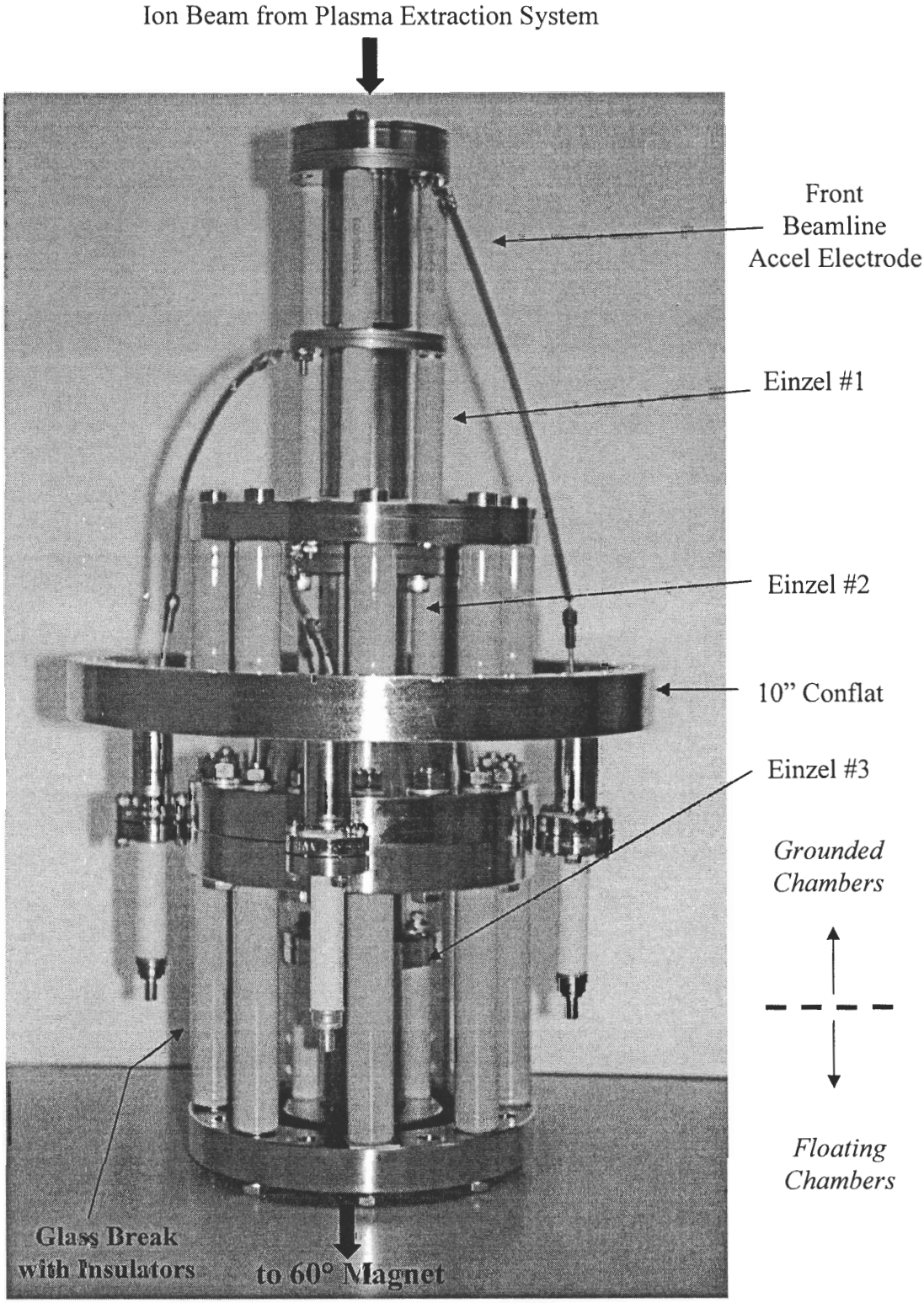

Figure 4.9: Photograph of the pre-magnet Einzel lens system with individual components specified. The insulating glass break between the grounded and floating beamline sections is also shown.

All magnetic mass filtering devices and beam steering components that use sector fields are governed by this basic relation.

Consider a beam of ions having uniform mass and energy passing through an ideal, homogeneous sector field of angle Φ_s as shown in Fig. 4.10a. The ions are assumed to emanate from a source point S, located a distance l' from the pole boundary with a small angle of divergence α. When the beam enters and leaves the field normal to the pole boundaries, it can be shown that the source point, center of curvature, and image point all lie on a straight line. Ions originating at the source point enter the magnetic field after traversing a distance l', are bent through a mean angle Φ_s, and come to first order focus at an image point located at distance l'' after leaving the field. This theorem is known as ″Barber's rule″ (Ingram and Hayden, 1954; Septier, 1967) and can be expressed mathematically by the following relations:

$$\left(l' - r\cot\Phi_s\right)\left(l'' - r\cot\Phi_s\right) = f^2 \tag{4.2}$$

$$f = \frac{r}{\sin\Phi_s} \tag{4.3}$$

where,

l', l'' = source point and image point distances, respectively
Φ_s = magnetic sector field angle
f = overall system focal length
r = radius of curvature of the particle trajectory

The radius of curvature for the trajectory is equal to the pole diameter for circular pole pieces. Ions of different mass but the same kinetic energy originating from the source point will enter the field normal to the pole boundary, but will not exit normal to the field edge. As a result, the masses are dispersed along an imaginary locus of focal points with different image point distances $\left(l''\right)$ as shown in Fig. 4.10b. The sector field becomes a mass filter when an ″exit slit″ is placed somewhere along the locus of foci to select only one mass.

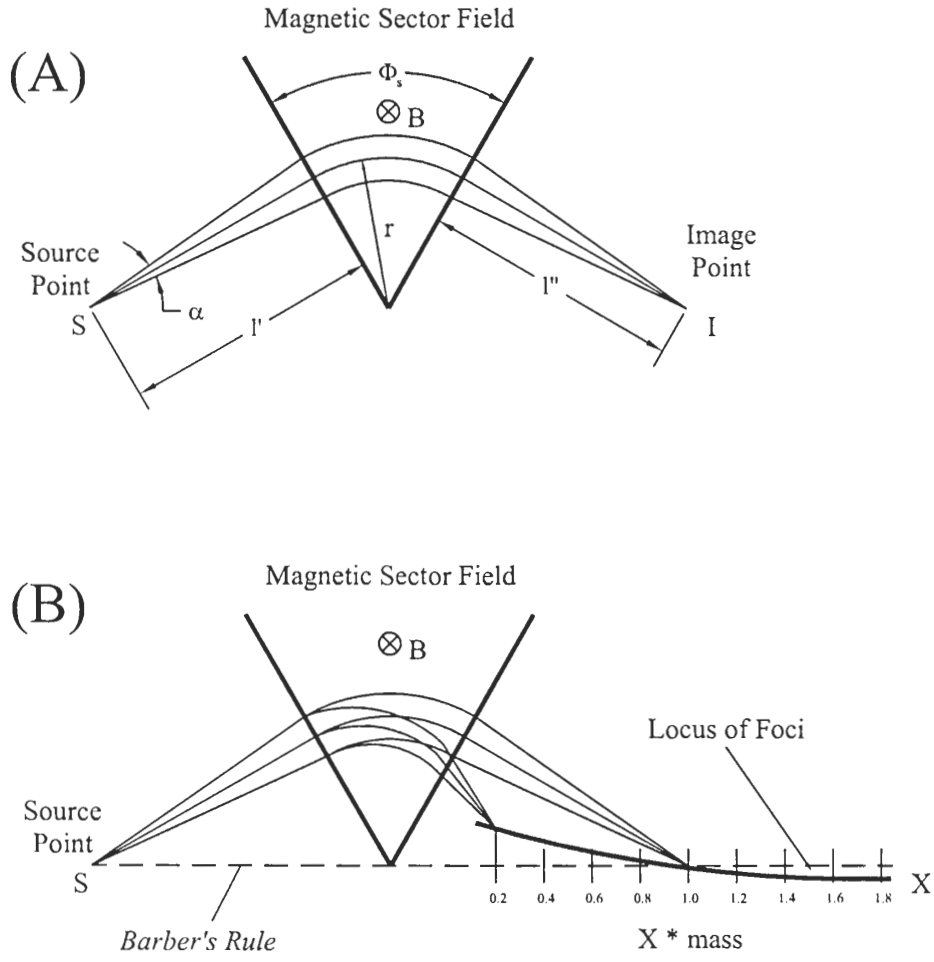

Figure 4.10: Focusing characteristics of an ideal magnetic sector field with important distances shown. The locus of foci for different particle masses at fixed magnetic field strength is given. Barber's rule is also indicated. Adapted from Ingrham and Hayden, (1954).

The application of Barber's rule is based on ideal sectors where the magnetic field terminates abruptly at the physical pole boundary. This situation never occurs in practice because fringe fields extend out beyond the physical pole shoe boundary. The extent of the field depends on the ratio of gap width between the pole shoes to the pole dimension itself. As a result, the actual deflection and pole shoe size that the ion beam ″feels″ is larger than the physical one. A method based on EFF (extended-fringe field) calculations has been developed to deal with these issues in sector design (Coggeshall, 1947; Enge, 1963). This method was *absolutely* necessary for our magnet design because the gap width used for our sector was not negligible compared to the pole shoe dimensions (discussed later).

The mass dispersion at the exit slit can be represented by the lateral separation Δx in the dispersion plane, between ions of mass m and $m+\Delta m$ after drifting the distance l'' from the pole boundary (Briggs and Seah, 1992).

$$\Delta x = -\frac{1}{2}\frac{\Delta m}{m}\left[r\left(1-\cos\Phi_s + l''\sin\Phi_s\right)\right] \tag{4.4}$$

where,

$\Delta x =$ lateral displacement of mass $\left(m+\Delta m\right)$ from mass $\left(m\right)$ at distance l''

An iron core electromagnet with a ″not too large″ air gap interrupting the magnetic circuit is shown in Fig. 4.11. The high permeability $\left(\mu_{Fe}\right)$ of the iron core choke is used to carry the magnetic field generated in an electrical solenoid with N total turns carrying a DC current I to the air gap. The field relation for the magnetic circuit can be written as (Anderson, 1989):

$$I \bullet N\left[amp-turns\right] = \frac{Bg_{air}}{\mu_0} + \frac{BL_{Fe}}{\mu_0}\left(\frac{\mu_0}{\mu_{Fe}}\right) \tag{4.5}$$

Iron Core Electromagnet

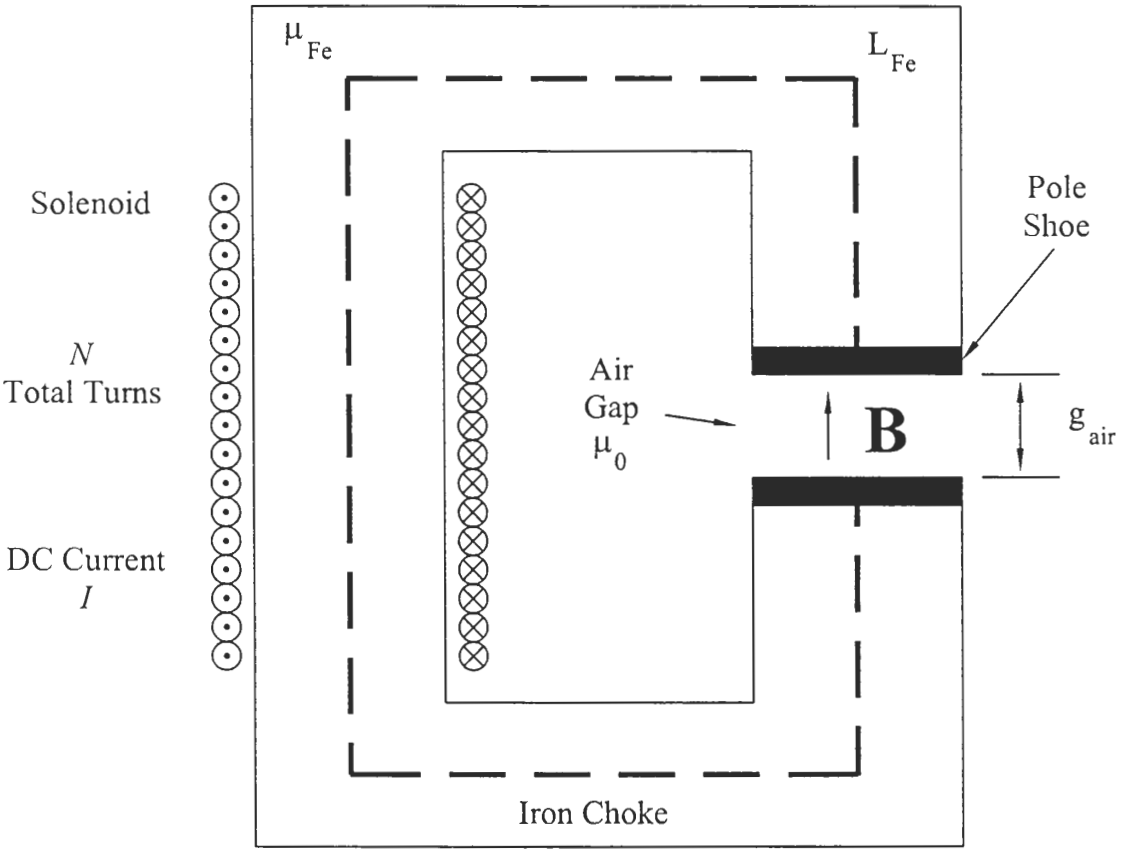

Figure 4.11: Magnetic circuit for an iron core electromagnet having "not-to-large" air gap interrupting the field. The path length for the circuit through the iron choke is shown by the dashed line.

where,

$B =$ magnetic field strength at mid-pole gap
$g_{air} =$ air gap width
$L_{Fe} =$ total magnetic circuit length within the iron core, as shown
$\mu_0 =$ permeability of free space $= 4\pi \bullet 10^{-7}\ {}^{T}\!/_{m \cdot A}$
$\mu_{Fe} =$ permeability of the iron core

Since the permeability of the iron core choke is much greater than free space $\left(\mu_{Fe} \gg \mu_0\right)$, the second term on the right-hand side of Eqn. 4.5 vanishes. This shows that the field strength is governed by the dominate resistance of the circuit—the air gap.

The design of a magnetic mass filter is a tradeoff between many conflicting things as to the mass dispersion requirement, range of ion energies, sector angle, and desired focal length. Further, the maximum field obtainable and fringe field falloff depend on the air gap size, exciter coil characteristics (operating voltage/current, wire size/number of turns, cooling requirements), and pole shoe geometry.

A schematic of the 60° sector magnet we built for the beamline mass filter is given in Fig. 4.12. The design goal was a ~10-12″ radius of curvature for ^{132}Xe at 20 keV maximum transport energy, which gives a field requirement of ~0.7-0.9 Tesla. The air gap between the pole shoes was chosen to be 2.25″ to allow clearance for the 1.5″ OD ion flight tube. The 2.25″ gap width along with an 8″ OD pole shoe size was used for the EFF calculations of the fringing field. By consulting nomographs in Enge, *op. cit.*, for the ″long-tail″ fringe falloff, the virtual pole boundaries were found to be approximately 1.5″ beyond the physical pole shoe boundary on either side. This calculation was necessary because the radius of curvature for the 60° bend with 8″ poles (no fringing) increases to nearly 11″ when the fringe field is included for the large air gap. The beam flight tube was bent appropriately for the 11″ expected radius.

Our air gap width of 2.25″, through Eqn. 4.5, results in ~ 38,000 amp-turns required for the 0.83 Tesla field (11″ radius) with no core saturation losses. A total of 45,000 amp-turns was used as a safety margin to account for possible core losses (which did occur). The large amp-turn requirement mandated that the windings be water cooled because upwards of 2 kW of power was required for the highest field strengths.

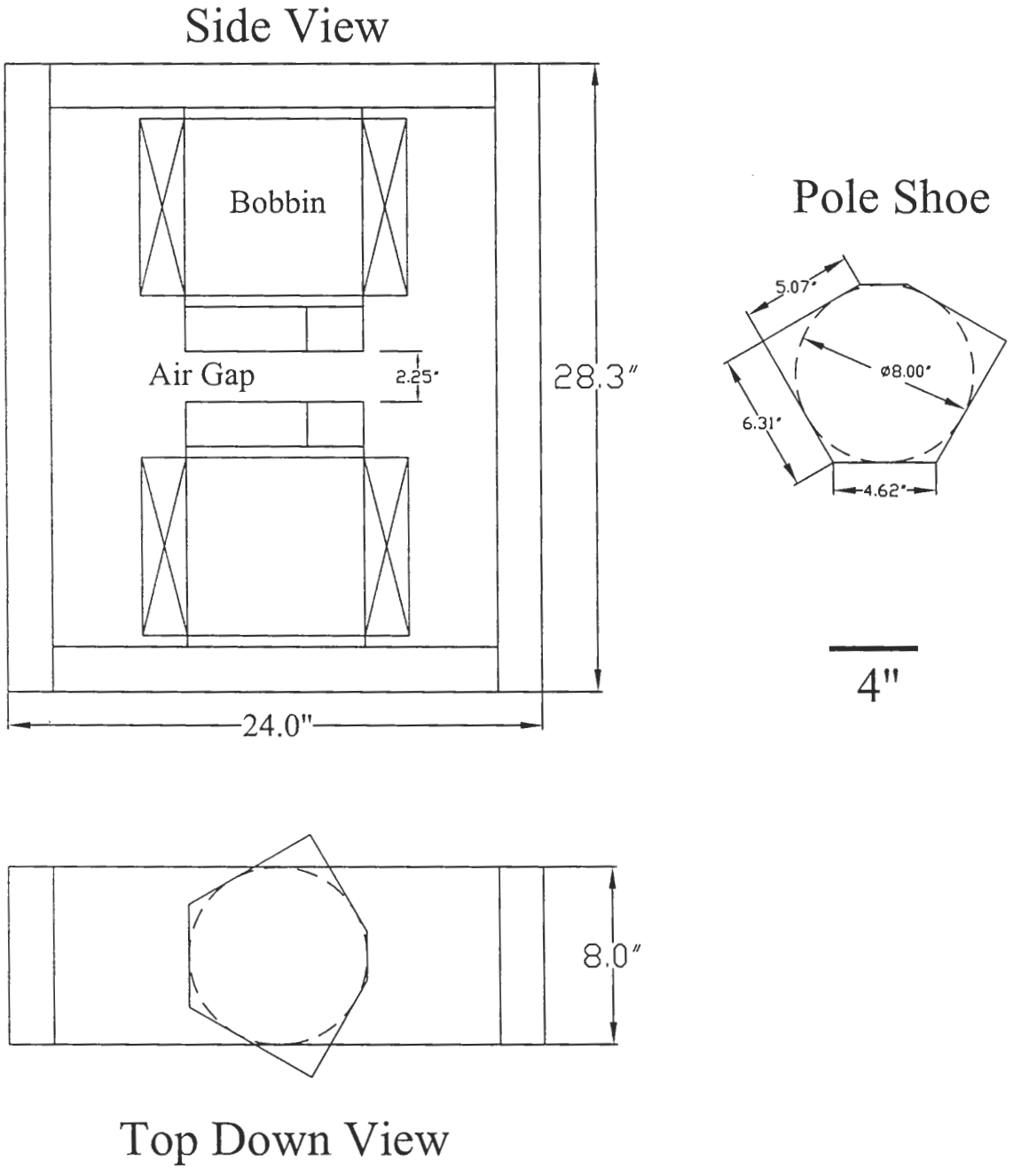

Figure 4.12: Schematic of the 60° sector magnet built for the ion beamline mass filter.

The H-frame magnet choke was constructed from 2″ x 8″ C1018 low carbon steel rectangular bar stock to keep the permeability high. Each pole bobbin was 8″ OD x 9″ long round stock (C1018) and wound by hand in the Caltech chemistry machine shop using #14 AWG heavy build HTAI solid copper magnet wire (3 x 80 lb spools). Each bobbin was tightly wound with 4 sequential sections, each composed of 8 copper wire passes followed by one pass of ¼″ copper tubing for cooling. A total of 24 wire passes and 4 cooling passes were used for each bobbin with the windings of the individual sections wired in series. Each bobbin has approximately 3000 turns for a total resistance of 18-20 ohms. The bobbins are joined in parallel and powered by a Lambda ENI 0-300V @ 0-16A SCR phase-fired DC supply with remote programming in constant current mode. The pole shoes, as shown in Fig. 4.12, were asymmetric hexagons cut from 2″ thick C1018 plate, designed in a similar fashion to early isotope separators (Neir, 1940, 1947).

Performance of the magnet is shown in Fig. 4.13 using a gauss meter at mid pole gap in the centerline of the pole shoes. Saturation of the choke above 0.4 Tesla can be seen. It was found in later operation of the ion beamline that a field stability of better than ±10 gauss on top of 0.3-0.8 Tesla was required to keep the beam spot from drifting on the target sample. This variation represents field stability better than ±0.15% which could simply not be maintained without implementing a hall-probe feedback control circuit on the magnet.

The magnet control system was built from scratch using a 2-axis hall sensor from GMW Magnetics mounted at mid-pole gap to measure the field strength continuously. The sensor was excited with a 1 mA constant current source and its output was digitized at 12 bits by an SRS 245 NIM-bin A/D-D/A computer interface module. A PID control algorithm was written in LABVIEW to sample the hall probe output and re-trim the magnet power supply output current (through the SRS module) at 10 Hz. This scheme allowed excellent field stability.

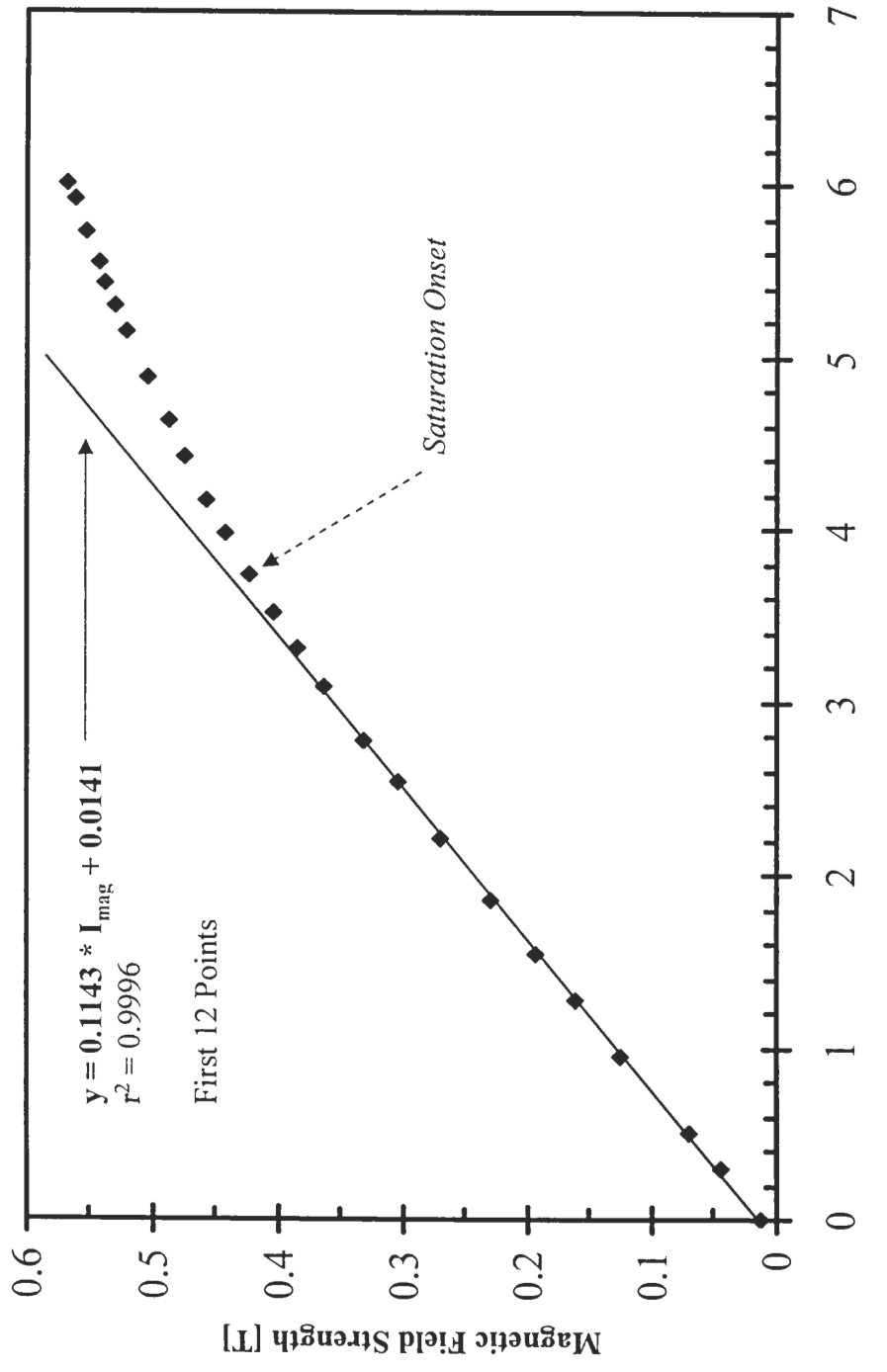

Figure 4.13: Magnetic field strength at mid-pole gap for the 60° sector magnet (beamline mass filter).

On a final note, the sector magnet designed for this study has parallel pole shoes and therefore does *not* produce a stigmatic image of the source point. This fact manifests itself as an ion beam which enters the magnet with circular cross section, but leaves the field elongated in the nondispersive (Y) direction as an ellipse with less on axis brightness (Septier, 1967). Stigmatic focusing with a sector field requires a slightly in-homogeneous field in the radial direction to offset the radii of curvature differences for different ion flight trajectories. The usual fix for this problem is to tilt the pole shoe surface slightly, making the air gap get larger with increasing radius of curvature. We decided that shaping the pole shoes to get stigmatic imaging was not worth the effort for our beamline design. However, the *loss of beam current* because of spread in the Y-direction was considered very important. An alternate way to solve this problem is to use a weak vertical ″bunching″ field in the Y-direction at the magnet exit to slightly re-focus and regain lost beam current. The change in the overall beam trajectory due to this operation was not deemed too ″risky″ because the ion beam is focused on the target sample some 62″ downstream. Also, small misalignments of the sector magnetic field vector to the ion beam propagation direction can be ″trimmed″ out by adjusting these two vertical bunching plates independently.

4.8 The Floating Region

As we said in Section 4.3, the ion beam cannot be allowed to see any grounded surfaces along its flight path unnecessarily, *lest it diverge*. Any decelerating fields, especially if they are asymmetric, will cause the beam to change shape or bloom (diverge) and require re-focusing to keep the current up. Continual re-focusing is cumbersome and undoubtedly leads to a reduction in beam current because there are always charged carrier losses in each focusing step. The solution is to not let the beam ″see″ *any* surfaces that are not at or near the beam energy (unless they are used to purposefully focus the beam). What we desire is a symmetric (usually cylindrical), pumpable, high-voltage ″shield″ around the beam throughout the entire transport line including the magnetic sector. This situation is difficult to realize because it essentially means putting a high-voltage pumpable envelope inside a grounded external vacuum

chamber that can stand off the ~20 kV beamline potential. Such an approach does work at the expense of large vacuum chambers, sputtering of beamline components, and electrical isolation issues throughout the beamline. Also, what does one do in the magnetic sector section where a large air gap (to fit the chamber) means a much larger field requirement?

The answer is to float the entire vacuum system, chambers included, at the beam energy. We took this philosophy because it avoids all the problems associated with high-voltage isolation inside vacuum where space is tight and pumping conductance must be maximized. All the isolation problems have now been brought outside vacuum and we can avoid making a chamber-within-a-chamber. Safety becomes more important now because the vacuum chambers are at -20 kV, but these issues can be dealt with easily.

The high-voltage *floating* section of our beamline system spans all the way from lens #3 of the pre-magnet Einzel triplet up to and including the decelerator where it joins to the grounded scattering chamber. Refer back to Fig. 4.1. There are two custom made glass electrical breaks at both ends of the floating beamline section made from 6″ CF flanges and 4″ OD x ¼″ wall pyrex tubing sealed with Viton O-rings. Each glass break is approximately 8″ long with aluminum flange supports at both ends held in place firmly by four 2″ OD polyethylene insulators. The vacuum chambers themselves are supported at many points along the line using a scaffold system of 3″ PVC threaded pipe and pipe fittings fixed down to a 2'x 8' laser breadboard table from Newport. There is always a minimum of 12″ of creep distance along any PVC surface between the beamline and ground to stand off the floating potential. The two vacuum pumps (CT7 cryopump and Alcatel 200 L/s turbo) on this portion of the beamline are grounded and joined to the floating chambers by similar glass electrical breaks for isolation.

The 60° arc chamber which passes between the magnet pole shoes was fabricated from a 1.5″ OD x 0.035″ wall hard copper pipe bent with an 11″ radius using an electrical conduit bender and oxy-acetylene torch. On each end, 2.75″ CF flanges were silver soldered to mate with the rest of the vacuum system. The small clearance (3/8″ on each side) between the floating chamber wall (up to -20 kV) and the grounded pole shoes of the magnet was a site for potential breakdown, so two layers of 1/8″ thick pressed mica sheeting were used on each shoe to prevent high-voltage striking.

The lengths of the tangents on the arc chamber were determined through Barber's rule to image the source point (beam waist minimum from the pre-magnet Einzel triplet) on a mass-defining slit 20″ downstream from the exit side of the pole shoe. An intermediate chamber at the magnet exit serves as the second differential pumping stage for the ion beam. It contains two vertical bunching plates (mentioned earlier) to squeeze the beam in the Y-direction (non dispersive direction) and adjustable exit slit assembly. The exit slit (0.75″ high) could be adjusted from 0-0.5″ wide using a micrometer stage from outside vacuum to set the mass resolution. A photograph of the adjustable exit-slit system is given in Fig. 4.14. For reference, the mass dispersion relation, Eqn. 4.4, at the exit slit for our sector magnet becomes Eqn. 4.6, indicating that very high resolution (>1000) can easily be obtained at modest slit width:

$$\Delta x[in] \approx -98\frac{\Delta m}{m} \tag{4.6}$$

Since only the ″tune″ mass passes through the exit slit, this intermediate chamber was gas loaded (~$1 \cdot 10^{-6}$ torr) by the undesirable portion of the ion beam. A CT7 cryopump (~1500 L/s air speed) with manual gate valve on a 24″ glass electrical break was used to meet this pumping requirement.

The floating beamline section (60° arc chamber, 2nd pump stage with exit slit, series quads, and decelerator) is biased with one main beamline floating supply (-25 kV adjustable, Deltona, model 250651) that sets the beam transport energy for the entire line. Two separate, +1kV DC power supplies (Ultravolt, model 1A12P), *floating on the beamline bias*, drive the vertical bunching electrodes. Their control circuits and AC line were also floating. A 20 kV line isolation transformer is used to provide the floating power.

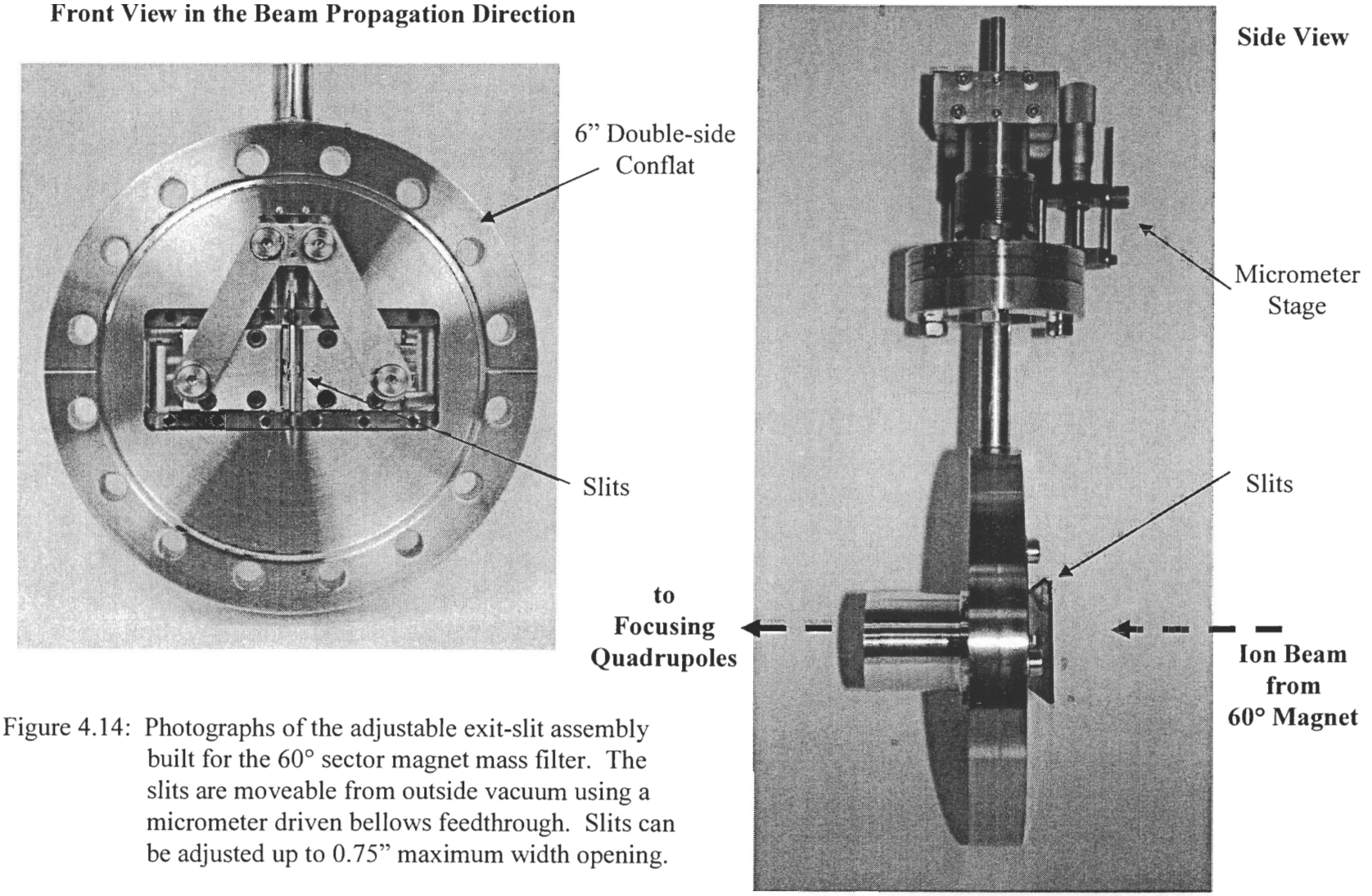

Figure 4.14: Photographs of the adjustable exit-slit assembly built for the 60° sector magnet mass filter. The slits are moveable from outside vacuum using a micrometer driven bellows feedthrough. Slits can be adjusted up to 0.75" maximum width opening.

4.8.1 Quadrupole Focusing

In Section 4.7, it was shown that the ion beam passing through the sector field exit slit (the magnet image point) should exhibit a crossover point in the dispersive direction (X) and an elliptical cross section in the non-dispersive direction (Y). The sector field has essentially removed the inherent cylindrical symmetry of the plasma extracted ion beam because of its ″handed-ness.″ The crossover and slight vertical divergence was fixed so the deceleration step could be carried out on an as-symmetric-as-possible, parallel beam having circular cross section and small waist. This was accomplished using electrostatic quadrupole fields in the beam drift space between the exit slit and decelerator. A quadrupole field scheme was chosen because its two plane symmetry seemed better suited to fix the unequal divergences of the beam in the X and Y directions separately. Also, a quadrupole field provides much stronger focusing action than an axially symmetric lens of comparable length and field strength making the beamline shorter (Lawson, 1988).

A single quadrupole lens focuses in one plane and defocuses in the other. However, two lenses arranged in a focusing-defocusing pair have an overall *net* focusing effect (Lawson *op. cit.*). Along this idea, a quadrupole doublet with eight independently adjustable lens elements was constructed for focus correction of the ion beam after the magnet exit slit. This system is shown in Fig. 4.15. It consists of eight rectangular aluminum plates held in place using a Delrin support structure that slips inside and keys to the ID of a custom 6-way cross (6″ CF flanges) attached after the magnet exit slit chamber. This chamber is also floating with the beamline and pumped by a 200 L/s Alcatel turbo-pump through another glass electrical break. The lenses were biased for Y-focus correction in the first of the quads and then X-correction in the second. The idea being that the first quad is used to *over*-correct the Y-divergence to account for the defocusing action in the Y-direction of the second quad. The two Y-plates in the first quad and the two X-plates of the second were independently adjustable with the remaining plates connected directly to the beamline floating potential.

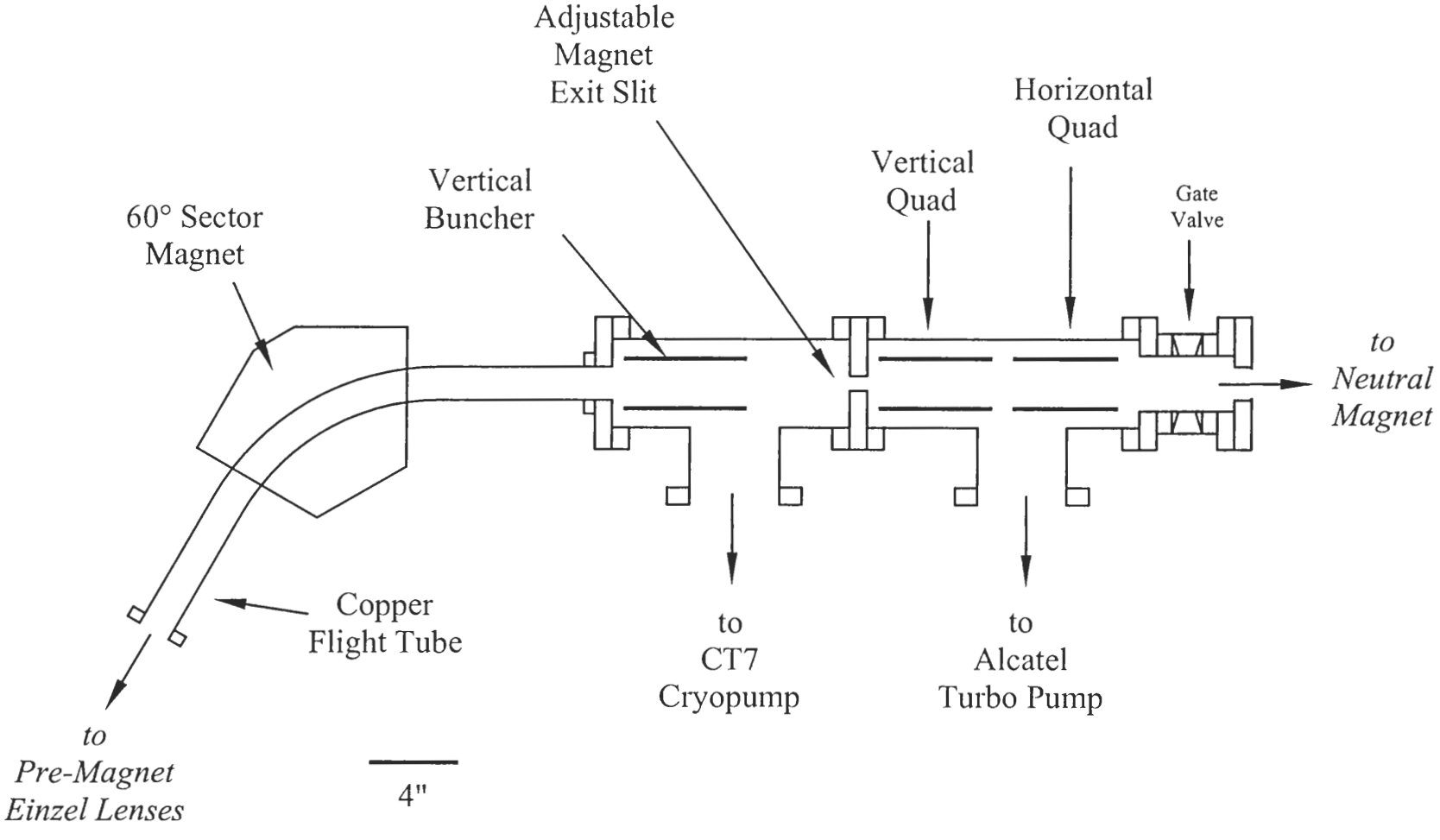

Figure 4.15: Schematic of the floating beamline section showing the 60° sector magnet, mass exit slit, and quadrupole doublet for beam focusing.

Four separate floating (on the beamline) +4 kV DC supplies (Ultravolt, model 4A12P) serve as the individual quad plate biases. Line power for these supplies is provided by the same 20 kV isolation transformer mentioned earlier.

Finally, there was a 6″ CF gate valve at the quad chamber exit to isolate the front beamline from the scattering chamber when the plasma chamber must be taken apart and cleaned. This allows UHV to always be maintained in the scattering chamber and scattered product detector. Typical pressures in this chamber were 1-5•10^{-7} torr, irrespective of plasma operating pressure. The huge cryopump on the previous stage as well as the Alcatel turbo provided significant reduction in the pressure load to the downstream portions of the beamline.

4.8.2 10° Ion Deflector Magnet

Collisions of energetic ions with background gas atoms can generate fast neutrals through charge exchange processes. In fact, fast neutral beams are produced using this method by shooting fast ions through a charge exchange cell containing a background gas in the mTorr range (Souda *et al*., 1995). This process of fast neutral generation, although much less significant in our system, could possibly influence scattering results. Unfortunately, fast neutrals are very difficult to measure quantitatively, because they must be ionized and detected as charged species. The efficiency for ionization scales inversely with velocity because faster particles spend less time in the active ionization region, therefore, neutrals in the keV range are extremely hard to detect (Scoles, 1988). We have therefore taken the approach to rid the beam of fast neutrals on purpose, even if they may not exist to a significant degree in our system. This is simply done by deflecting the ion beam 10° with a small magnetic sector field right before the decelerator entrance so that any fast neutrals in the upstream beam are not within line-of-sight of the target. The short flight distance through the decelerator to the sample is unimportant because this region is held at 1-5•10^{-8} torr.

A schematic diagram of the 10° magnet is given in Fig. 4.16. Since the field requirement was much less (600 gauss max for ~ 50″ radius), magnet cooling was not important. A C-frame choke of C1018 low carbon steel (2″ x 5″ rectangle) and 5″ OD bobbin support was used. The air gap was 2.5″ with 5″ square pole shoes which gave an EFF calculated virtual pole surface ~1.2″ past the physical pole boundary. The exciter coil was an 80 lb spool of #20 AWG magnet wire (~25,000 ft, estimated @ 12,000 turns) that was specially re-wound by REA Magnet Wire Company on an industry standard 12″ x 7″ reel to have both ends of the continuous wire length accessible. The center of the plastic reel was cut out using a CNC mill and simply slipped over the steel choke. Power for the coil was provided by a 0-600V, 0-1.6A current regulated DC supply from Lambda-ENI. Since the beam deflection was only 10° and the deflection occurred much closer to the target, a hall-probe feedback system was not necessary to keep the beam from wandering on the sample surface. Performance of the magnet is shown in Fig. 4.17 for field measurements at mid-pole gap.

The 10° beamline chamber (see Fig. 4.18) in this region was made from a stiff hydroformed vacuum bellows (1.5″ OD x 12″ long) from Varian. It was held in place by bolting the 2.75″ CF flange ends to an aluminum frame structure machined to have a 10° misalignment at 50″ radius of curvature. As arcing was a problem, mica sheets were used between the floating chamber and grounded pole shoes of the magnet.

10° Ion Deflector Magnet

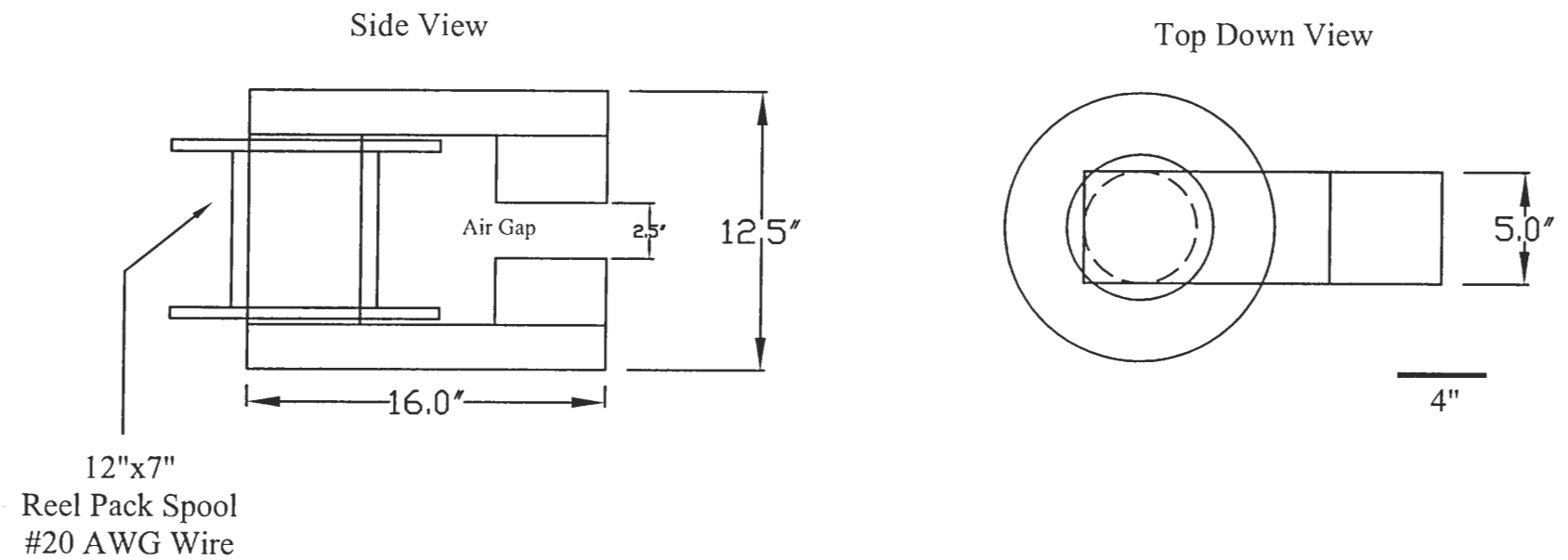

Figure 4.16: Schematic of the 10° deflection magnet constructed to steer the ion beam just before the deceleration step.

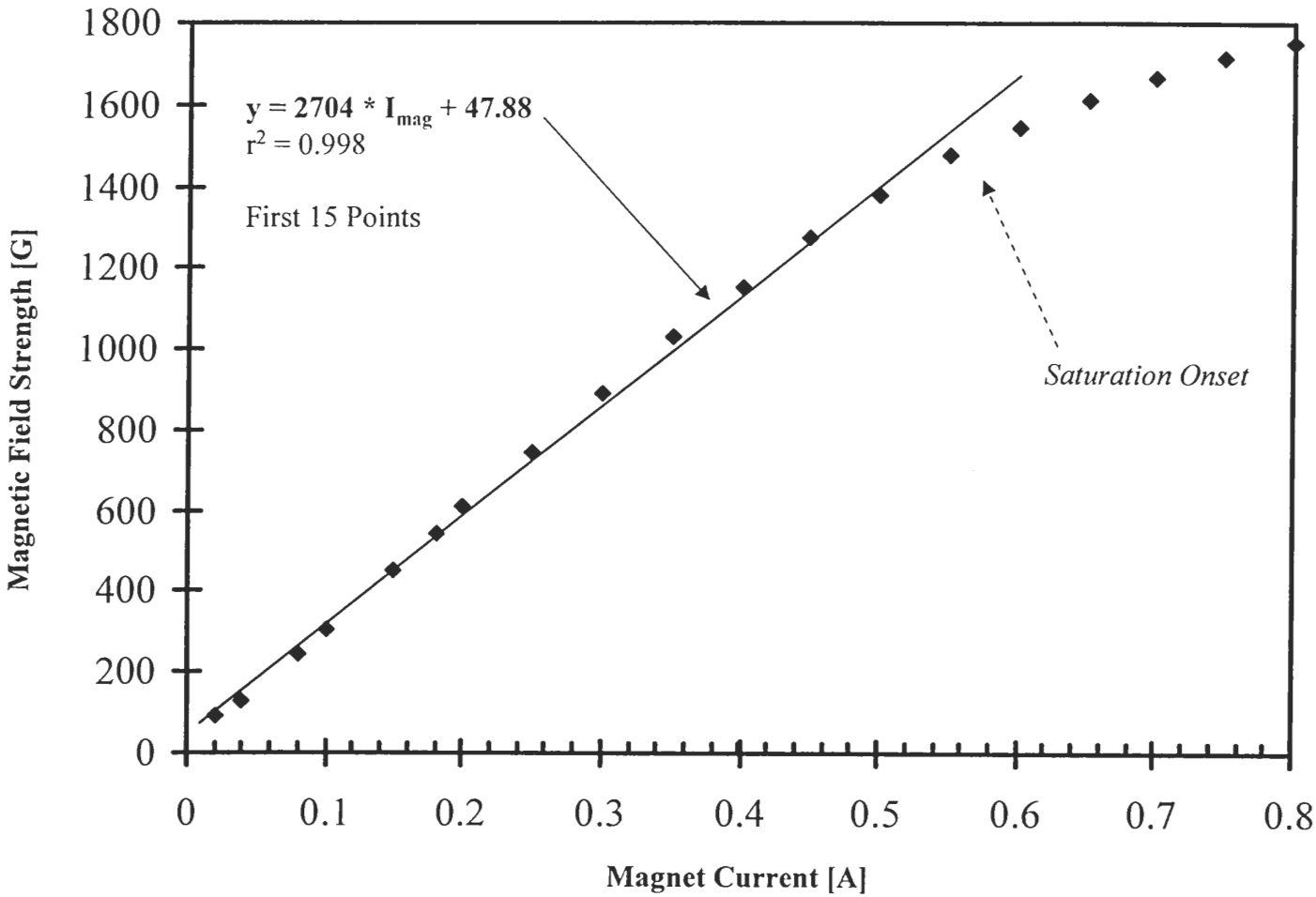

Figure 4.17: Magnetic field strength at mid-pole gap for 10° deflector magnet.

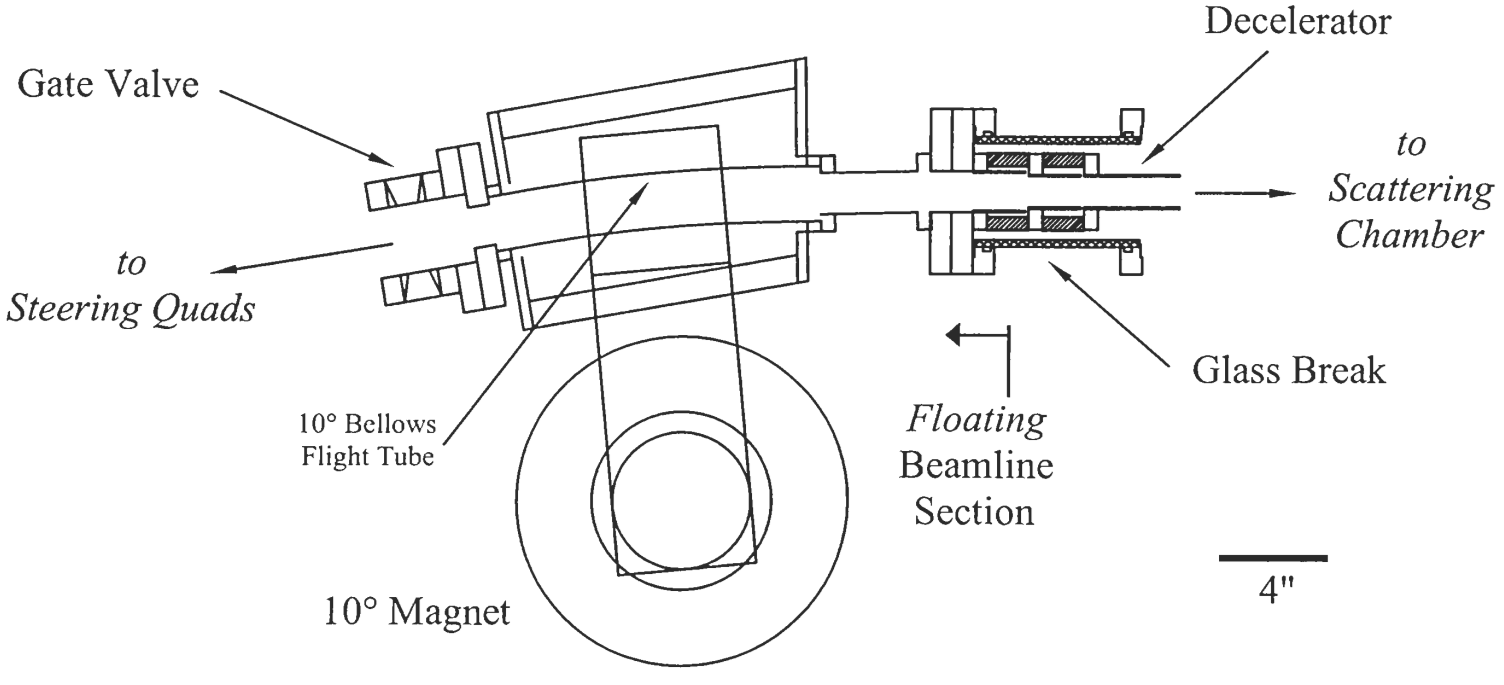

Figure 4.18: Schematic of the floating beamline section where the ion beam is deflected by 10° using a weak magnetic sector field (< 1600 Gauss). The 10°deflection of the ion beam assures that any fast neutral species are not within line-of-sight of the target sample. The glass break between the floating beamline and the grounded scattering chamber is also shown.

4.9 Decelerator

Deceleration lens schemes for high-energy ion beams have traditionally been approached from two very different points of view. Experiments using ion implanters (>50 keV transport energy and milliamp beam currents) have demonstrated that ultra-short, extremely strong slowing fields (50 kV in 10-20 mm) using 2 or 3 thin electrostatic lenses provide the best spots (Amano *et al*., 1975; Freeman *et al*., 1976; Thomas *et al*., 1982). On the other hand, microamp beam currents at lower transport energies are more successfully dealt with using longer, more complex schemes (3-6 tube-like electrodes) (Lau *et al*., 1991; Tsukakoshi *et al*., 1991; Shimizu *et al*., 1985; Yamada *et al*., 1985). Our decel system is rather simple with an asymmetric Einzel triplet (short-long-short) followed by a large ID, short quadrupole with a grounded end cap to shield the target from any high-voltage fields. This design is shown in Fig. 4.19 with a photograph of the assembled lens system given in Fig. 4.20. The #2 and #3 lenses of the triplet are run more negative than the #1 lens to pinch the beam after a first stage of slowing occurs between the main beamline and #1 decel lens. It is thought that the potential drop of a few kV in this region (between decel #1 and #2 in our case) aids in neutralizing the beam space charge for the rest of the deceleration because slow electrons are trapped in the beam channel (Tsukakoshi *op. cit*.). All the cylindrical tube lenses in the decelerator are made in an analogous fashion to the pre-magnet Einzel setup from 2.75″ CF half nipple vacuum adapters with custom lengths. SIMION simulations were used for the basic Einzel design.

The end of the #3 decel lens and the entire quad extend into the grounded scattering chamber. The quadrupole exit setup for final beam steer is short and stubby so the field asymmetries near its plate electrodes are so far away from the bunched beam that they are irrelevant. Operation of the quad is very weak with only 200-400V of asymmetric steer capability on a centerline floating potential of -6 to -10 kV. A floating circular shield encloses the quad to screen the beam from the grounded walls of the scattering chamber. The quad shield, quad centerline float, and the four steering plates are all independently adjustable. A fully grounded end cap over the quad exit shields the target from any high-voltage fields.

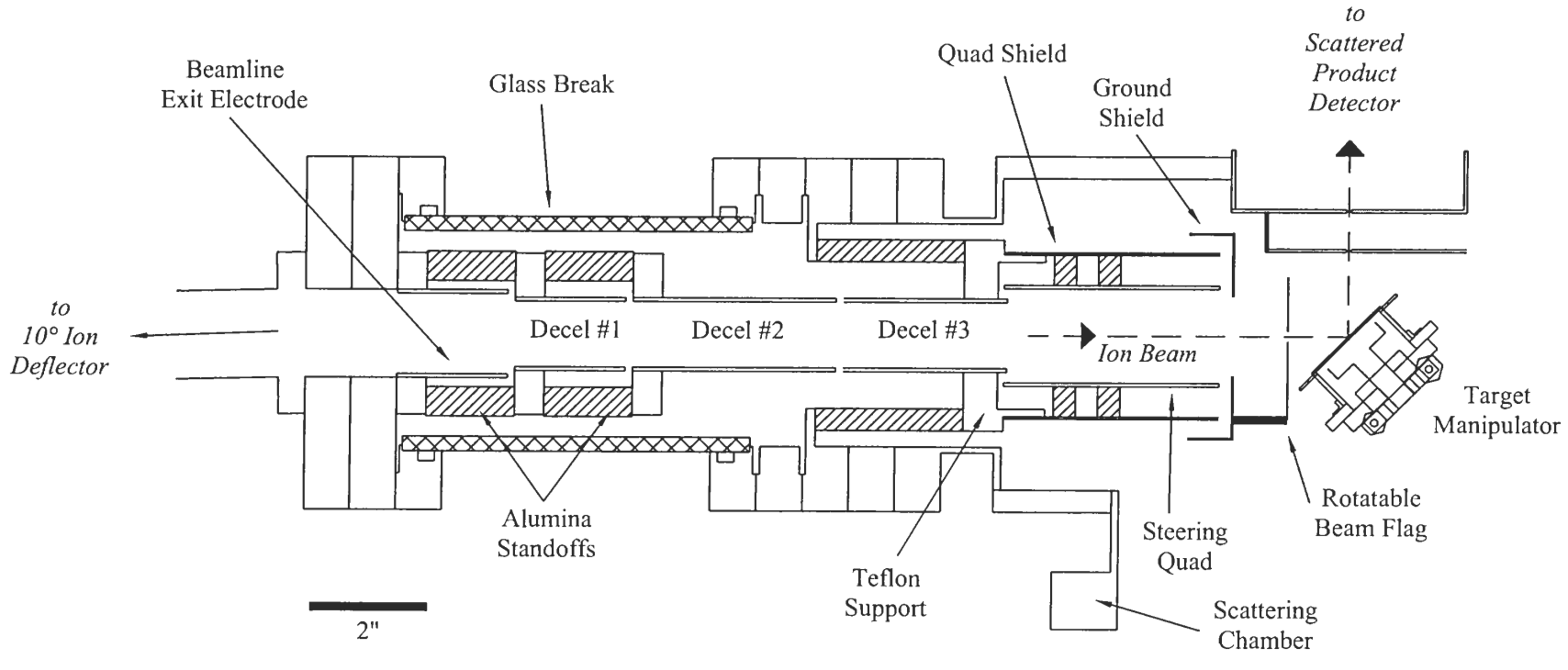

Figure 4.19: Schematic of the decelerator electrode system and final beam steering quadrupole with ground shield. The goniometer head on the manipulator with the target sample is also seen.

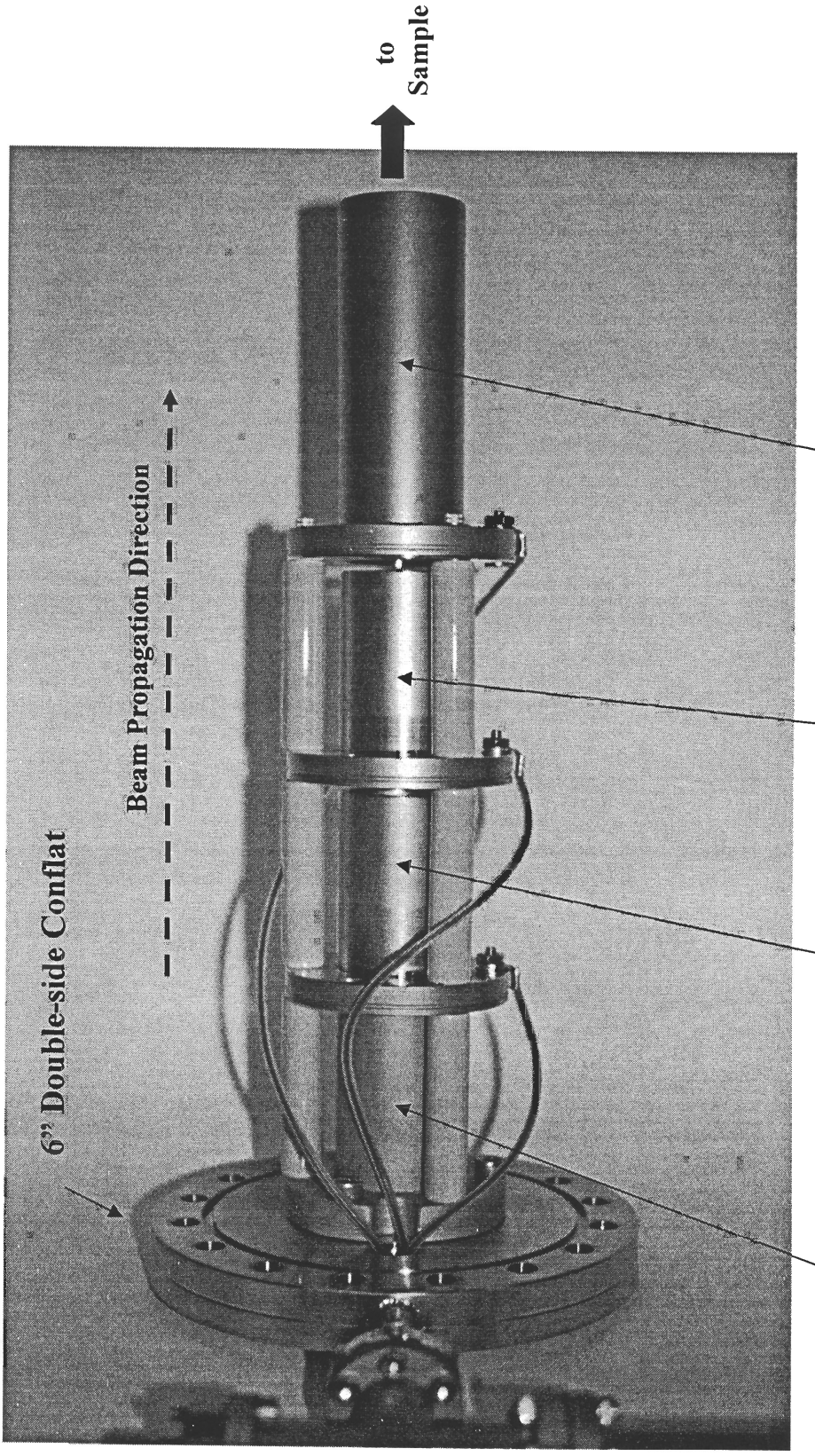

Figure 4.20: Photograph of the decelerator electrode system with individual components specified.

The end cap served as the mounting point for a rotatable beam flag made of tantalum with 2 mm diameter beam aperture. The flag was positioned as close to the target as possible to present a cylindrically symmetric slowing field to the decelerating ions. In this way, the asymmetric field from the 45° target position did not affect the deceleration step in any way. The flag also screens out any stray electrostatic fields near the target that may be seen by charged species leaving the surface. Finally, the beam current to the flag was separately measurable to aid in rough focusing of the ion beam.

Decel lenses #1, 2, and 3 each run from -25 kV DC supplies (Deltona, model 250651) while the quad centerline float is provided by a -20 kV supply (Glassman). The shield used a +3 kV supply (ENI, model 3000R) floating on the quad centerline and each of the quad plates were driven by +2 kV DC modules (EMCO, E-series) also floating on the centerline potential provided by the Glassman supply.

4.10 Scattering Chamber

The scattering chamber which contains the target sample was specially built for this study from an existing 12″ OD long tubular vacuum cross having four 6″ CF port extensions. Extensive modification of this starting chamber was carried out in the Caltech chemistry machine shop to outfit two additional pumping stages for the scattered product detector along with numerous other access ports. At the heart of the chamber is a 5-axis sample goniometer (X, Y, Z, polar, azimuth) built by Thermionics Northwest that was modified to include a floatable sample stage and separately floatable sample platen to measure beam current continuously during bombardment. A twist-lock mechanism was used for in-vacuum transfer of the sample platen between a loadlock chamber and the goniometer dock.

Important features of the sample platen and mounting system are given in Fig. 4.21. As shown in the blown-up view, the target sample is sandwiched between a 0.030″ thick sapphire flat and cover ring for electrical isolation. This sample ″stack″ is held down to the molybdenum transfer platen with a hollow molybdenum cover fixture and four screws. A fine wire K-type thermocouple on the sample face functions as both temperature and sample current readouts.

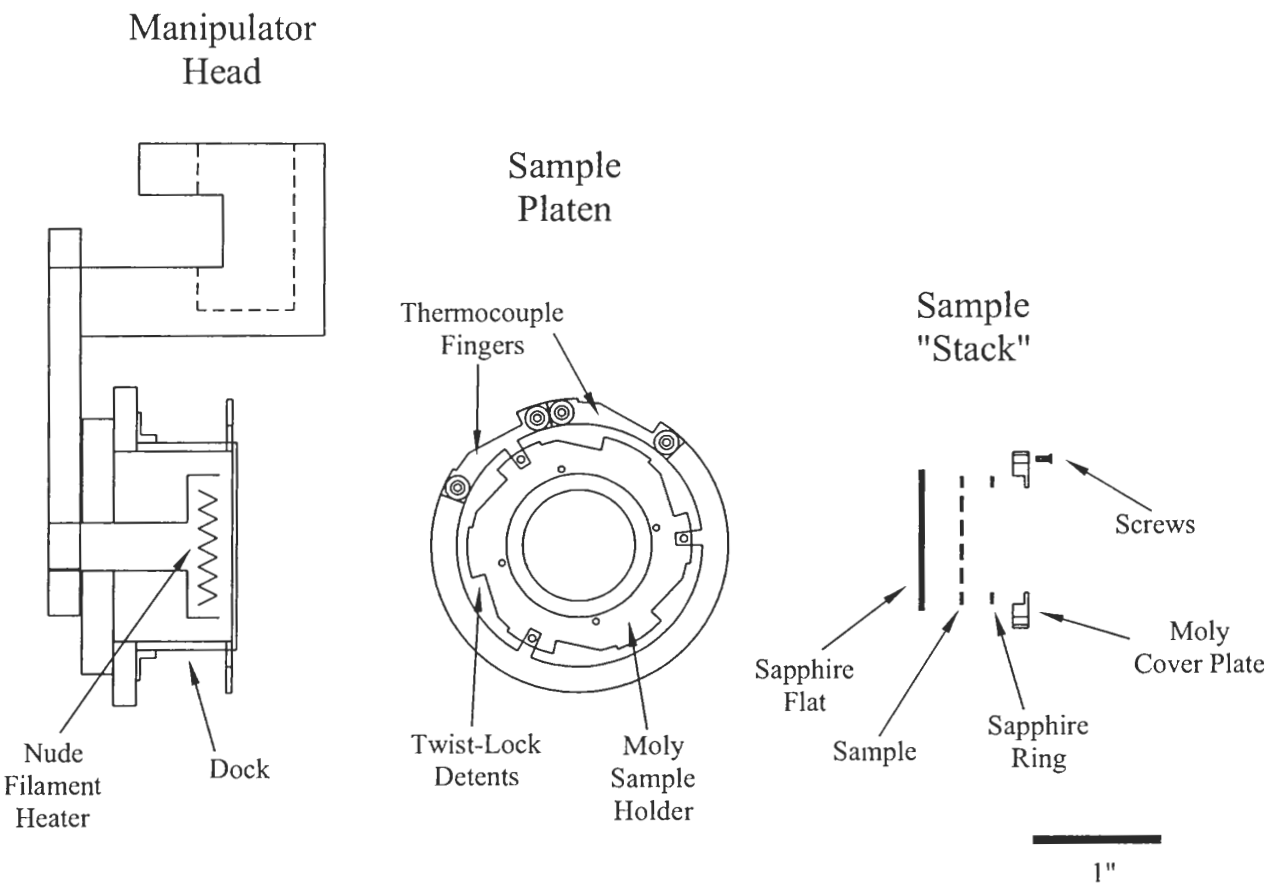

Figure 4.21: Schematic of the sample manipulator and tranfer platen which houses the target between two sapphire insulators.

The thermocouple readout amplifier simply floats on the electrometer circuit used to measure the ion beam current on the sample. Thermocouple leads are brought out and behind the moly platen to an electrically isolated set of thermocouple contacts which travel with the platen. These two contacts mate to a receiving pair of thermocouple fingers on the goniometer dock. The dock on the goniometer head is isolated from ground by sapphire balls and contains a tungsten nude filament element which can be used to heat the sample via radiation (through the sapphire isolating flat) to 700-800 °C max.

The scattering chamber is pumped at one side through a 10″ CF port by two CTI 8 cryopumps through a 10″ CF Tee and sliding gate valve. The tremendous pumping speed (~5000 L/s air speed) of the two cryos keeps the sample interaction region at 1-2•10^{-8} torr during bombardment. There is also a hollow cathode ion sputter gun from VG for sample cleaning and SIMS along with an SRS residual gas analyzer in the chamber.

4.11 Ion Beam Axial Energy Analyzer

A miniature electrostatic sector analyzer that could be moved in and out of the beam path was built to measure the ion beam energy distribution during scattering experiments. After lifting the target with the goniometer stage, the sector could be pushed up using a pneumatic bellows assembly into the beam path, placing the sector inlet aperture directly at the scattering center defined by the target. In this way, beam energy distributions were measured exactly at the target location. Fig. 4.22 shows a schematic of the analyzer. A photograph of the analyzer with one of the side cover plates removed is shown in Fig. 4.23 to give a feeling for the miniature size of the entire system. The theory of the spherical sector will be mentioned later in Section 4.13.2 on the scattered product energy analyzer.

The 180° spherical sectors were constructed from 6061 aluminum in the Caltech chemistry machine shop and later gold plated to avoid any charging problems which could occur in oxygen beam experiments. The mean sector radius was 0.9″ with Herzog corrector plate (see Section 4.13.2) for proper electrostatic field termination. The inlet and exit slits were 2 mm holes on the Herzog plate itself.

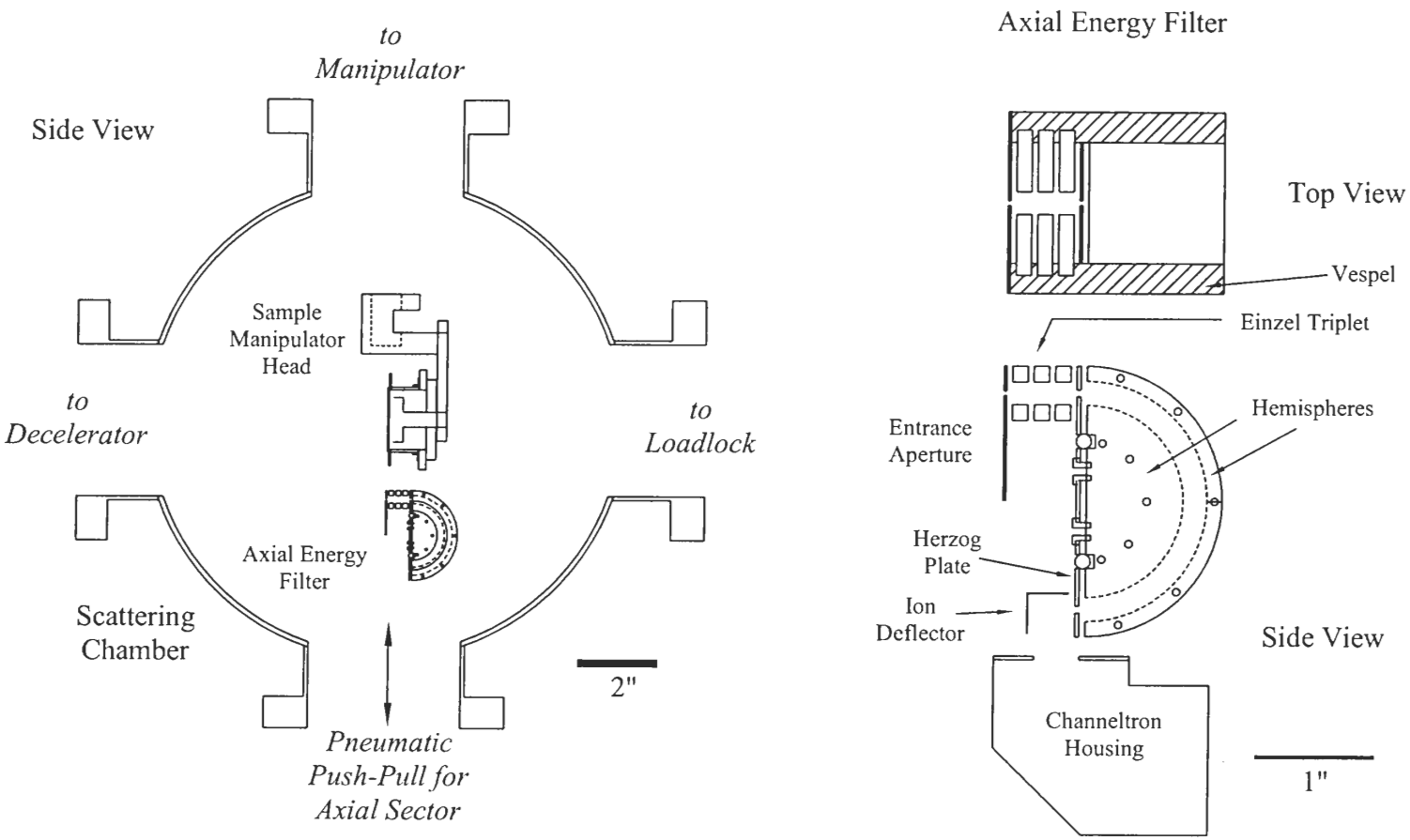

Figure 4.22: Schematic of the 180° axial sector energy filter showing its construction and movement into the ion beam path at the target location. In this way, the ion beam energy distribution is measured directly at the target position.

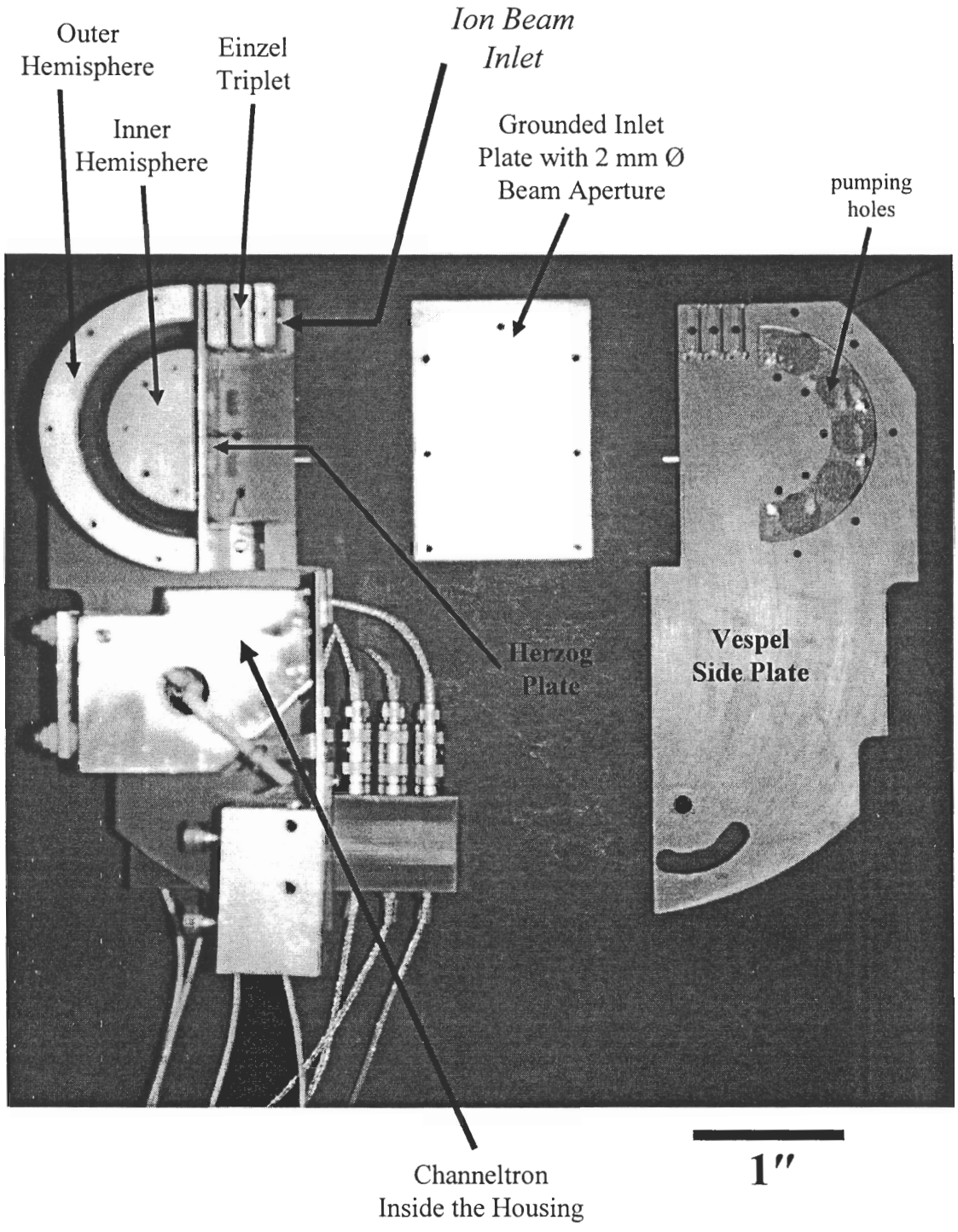

Figure 4.23: Photograph of the 180° hemispherical sector energy analyzer constructed to measure the ion beam energy distribution directly at the target position. In this view, the Vespel housing has been removed from one side of the analyzer to show the internal components.

A grounded analyzer entrance aperture of 2 mm is followed by a short Einzel triplet (gold plated aluminum) to image the beam on the inlet hole in the Herzog plate. As ions exit the sector field, they encounter an L-shaped ion deflector plate which directly opposes the Channeltron ion detector. The entire sector assembly and Einzel lens are aligned with pins and screwed to the two-piece analyzer housing made of Vespel. The assembly was pre-aligned to the scattering center with a HeNe laser from the scattered product detector side. The sector could be moved 2″ downward via pneumatic vacuum bellows during scattering.

The electrostatic control for the analyzer was custom-built with electrical schematic in Fig. 4.24. Modular DC power supplies and trimable divider networks floating on the main sector pass control voltage (retard voltage) were used for the sector and Einzel voltages. The retarding voltage was provided by a +3.5 kV Acopian DC power supply (stepped down with a divider chain) that was controlled remotely from a 16-bit D/A-A/D computer card and LABVIEW. The channeltron operated in analog mode at -2 kV bias with the anode connected to a floating Keithley electrometer. The electrometer chart recorder drive output was fed through a linear isolation amplifier before being digitized at 16 bits. Energy distributions were recorded in the same LABVIEW program by running the analyzer in constant acceptance energy (CAE) mode at 2 or 15 eV pass energy. The retarding voltage was swept via computer from 0-800 eV in 0.5 or 1 eV steps while recording the channeltron output current.

4.12 Scattered Product Detector

As mentioned in Chapter 2, the most idealized scattering experiment would involve the detection of all species leaving the target surface, both ions and neutrals, within the space of mass and energy. This scheme would allow the pure energetics of scattering to be studied along with the *chemistry* of surface processes through the identification of reaction products. A detection scheme which can accomplish both of these goals simultaneously, in the same vacuum system, seems like the obvious choice.

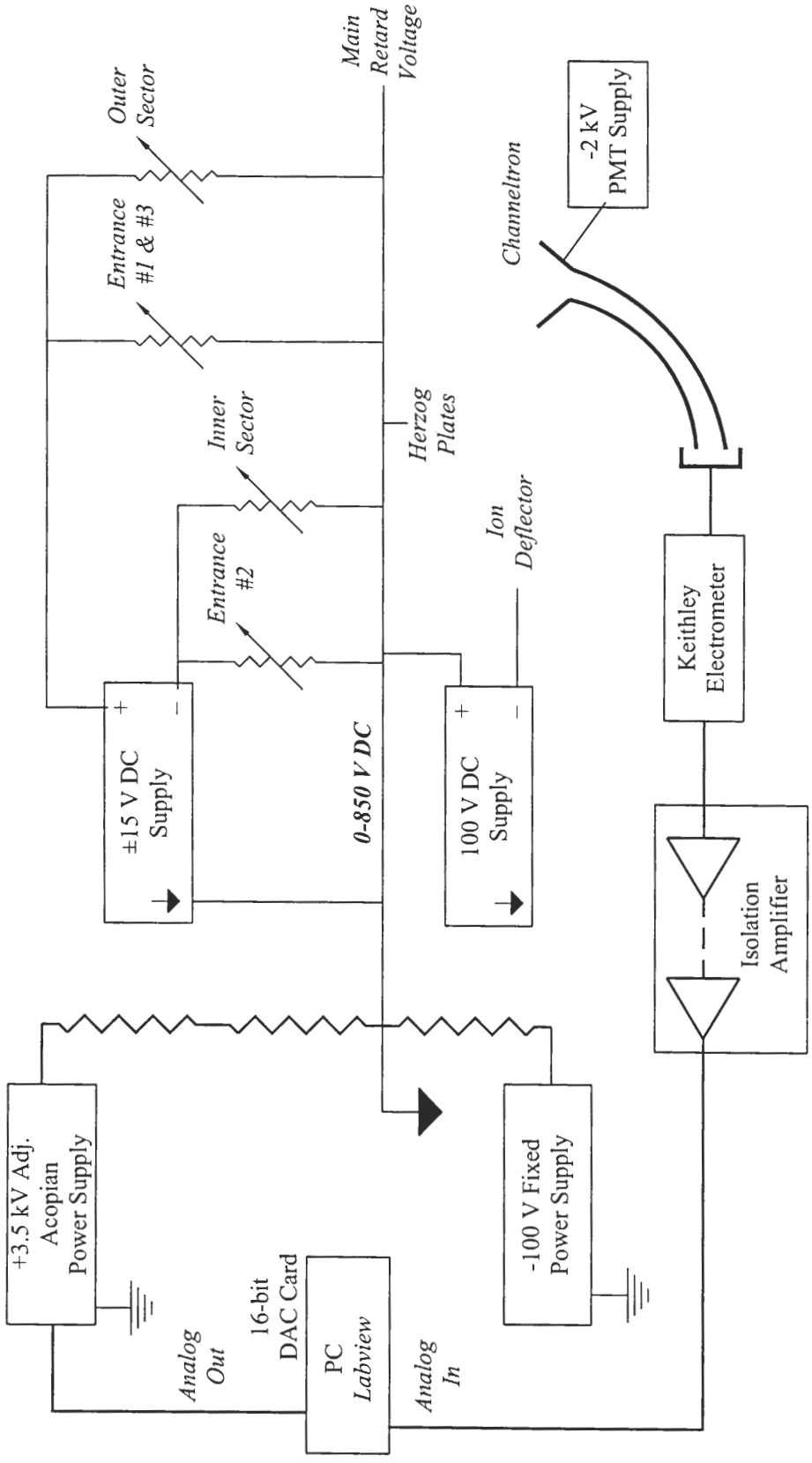

Figure 4.24: Power supply bias scheme for the 180° electrostatic sector energy analyzer located at the target position.

However, history has shown this goal to be exceptionally demanding experimentally to the extent that it has only been accomplished a few times (see Scoles, 1988 for an example).

Our approach has been to combine an electron impact ionizer, electrostatic sector energy filter, and high transmittance RF/DC quadrupole mass filter with an extremely sensitive single ion counting system. We believe that the electrostatic sector with sequential quad mass filter provides several advantages over traditional time-of-flight (TOF) techniques. First, the sector system can be placed very close to the sample surface unlike the TOF situation where a reasonable flight distance between the sample and detector is required for decent energy resolution. Second, the TOF technique requires the incident beam to be chopped to create a ″time zero″ for velocity measurement. For instance, a 1 m path length gives flight times in the microsecond range which in turn, requires beam chopping with a rise time better than 10 ns to obtain an energy resolution of 1%. This is not often achieved (Czanderna and Hercules, 1991). The sector field, on the other hand, can easily give 1% energy resolution and be situated any distance from the sample. The normal mode of operation for the sector is an un-chopped incident beam, but it can be run just as easily in chopping mode to phase-lock particle detection if signal to noise is a problem. The TOF system must always be run in chopped mode because a modulated signal is required for timing. Third, the sector field measures the particle energy directly whereas the TOF technique always requires calibration to convert flight time to energy space. Finally, the TOF approach becomes almost intractable if it is used for both mass and energy detection. Double chopping and multi-step deconvolution of flight time spectra are required to get both the particle mass and energy.

4.12.1 Ionizer and Einzel Triplet

The electron impact ionizer of our detection system is based on an axial ionizer from an Extrel QPS quadrupole mass spec system from 1978. We have modified the design somewhat and added an Einzel triplet lens system to the ionizer rear to provide better extraction and imaging of ions on the inlet slit of the electrostatic sector. A schematic of the ionizer and Einzel setup is shown in Fig. 4.25.

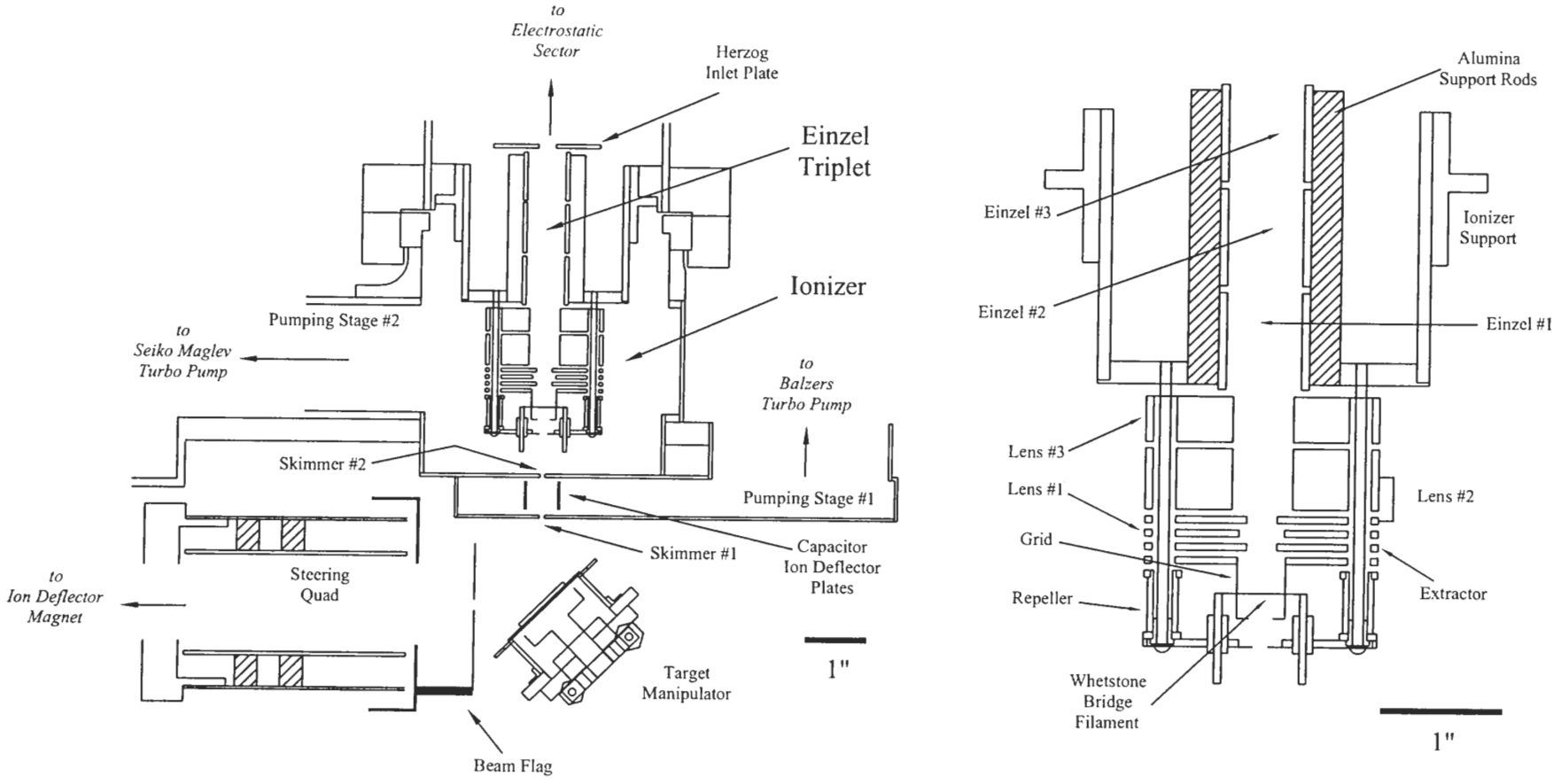

Figure 4.25: Schematic of the target region, differential pumping stages of the scattered product detector, and ionizer. A blow-up view of the ionizer shows the multi-lens extraction system and the Einzel triplet transfer lens. The transfer lens system images the ionized neutrals at the ionizer exit on the inlet slit of the 90° hemispherical sector electrostatic energy filter. The scattered ions from the target pass straight through the ionizer (when its off) and are imaged on the energy filter inlet slit by the same transfer lens setup.

The target region is also given in Fig. 4.26a with annotations on the photograph showing the manipulator head, steering quad exit, and first pumping stage. Fig. 4.26b shows a photograph of the ionizer itself. The ionizer has a Whetstone bridge filament structure with axial entrance and axial ion extraction from the ionizing volume. As shown in the figure, it has five lens elements after the grid which enable many different modes of ion extraction. Specifically, the ionization volume size and ion creation potential variation can be easily changed by tailoring the grid, extractor, and focus plate voltage ratios. This is a very important point because any variation in ion creation potential in the ionizing volume (most ionizers have this problem) causes an artificial line width in the energy spectrum. We made specific intent to minimize this effect by fully characterizing our ionizer system. Experiments with the electrostatic sector show that the ionizer can be sufficiently ″tuned″ to provide ionization at a uniform ion creation potential of narrow energy width (≤1 eV).

All lens elements in the ionizer are fully tunable and emission currents up to 10 mA at 100 eV electron energy are possible. The high emission current capability is critical for measuring small signals of secondary neutrals leaving the target surface. The Einzel triplet was added to transport and focus the ions exiting the ionizer on the sector inlet slit. The triplet lens system floats off the electrostatic sector retard voltage ramp to provide a nearly constant focusing power over all ion energies. SIMION was used to design the lens system and operating voltages to provide uniform transmittance of all ion energies irrespective of retardation level.

The ionizer is positioned directly behind the second skimming aperture (2 mm) on the back of the first differential pumping stage. The Whetstone bridge and ionizing volume are only 3.2″ from the sample surface. Inside the first pumping stage, a parallel plate capacitor electrode set is used to deflect ions and prevent them from passing through the second skimmer aperture. This mode of operation is used to measure only the neutrals leaving the surface by deflecting the ions out of the exit beam before they can get to the detector. When only ions are being detected, the entire ionizer assembly is earthed and the ions pass right through the ionizer where they are subsequently focused by the inlet Einzel on the sector inlet slit.

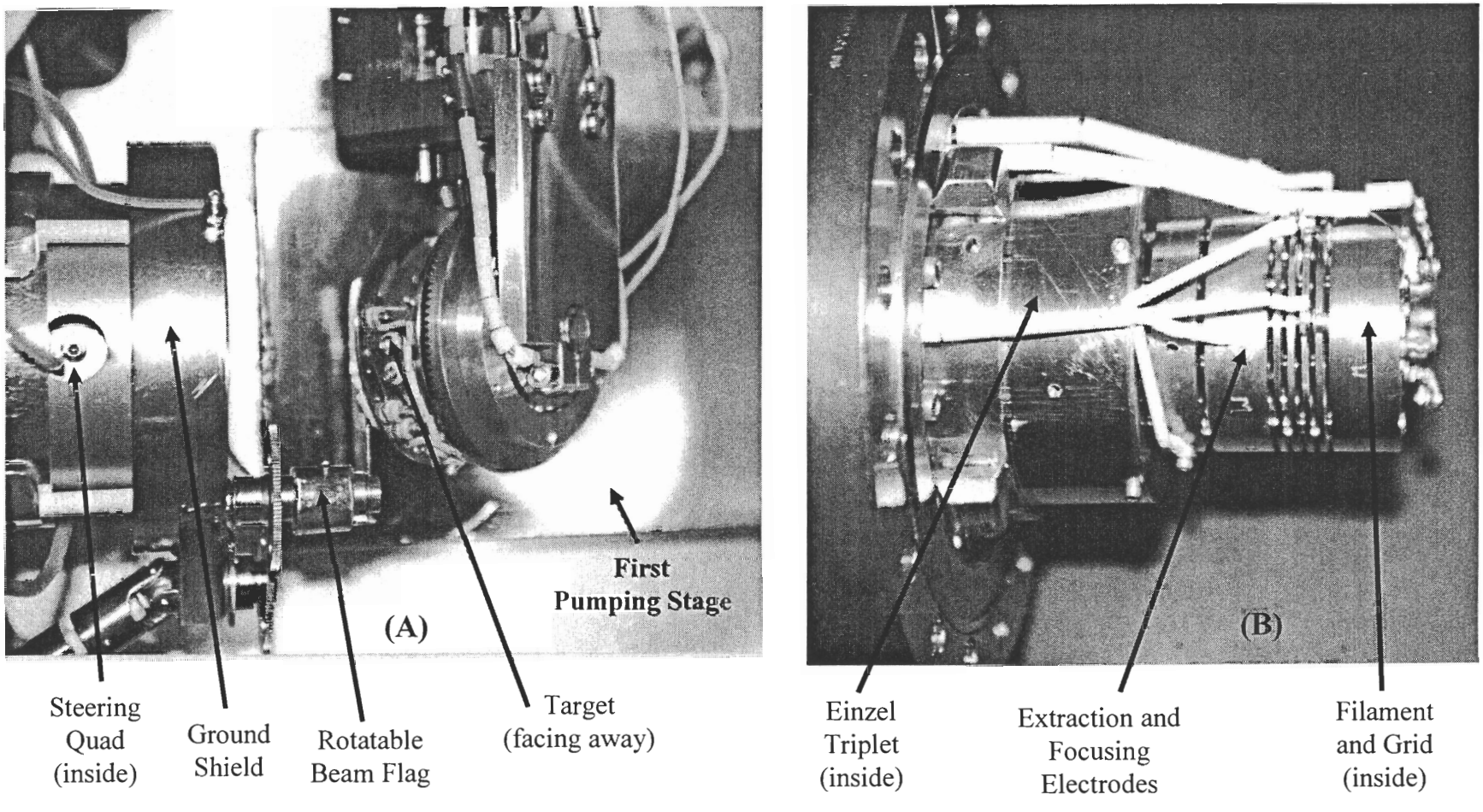

Figure 4.26: Photographs of (A) target manipulator, first differential pumping stage, and ground shield surrounding the steering quadrupole at the decelerator exit; and (B) electron impact ionizer and Einzel triplet transfer lens system (hidden by the ionizer support tube).

A 170 L/s Leybold turbo-pump is used on the first pumping stage and a 300 L/s Seiko Maglev turbo-pumps the ionizer in close proximity. The large ultra-clean Maglev can provide 2-5•10^{-10} Torr in the ionizer region with the ionizer at 5 mA emission current giving an extremely low residual gas background. Both turbo-pumps are backed by an oil-free communal roughing pump stack composed of a roots blower and dry scroll pump from Leybold.

4.12.2 Electrostatic Sector Energy Filter

Electrostatic sector fields (electrostatic prism/condenser) using spherical electrode surfaces have been the mainstay of high-resolution electron spectroscopy for many years. Their well-defined transport and focus characteristics make them ideally suited for ion energy spectroscopy as well. These devices are simple energy band-pass filters which use a variable pre-retardation or pre-acceleration scheme to bring incoming particles into the energy pass band where they pass through the analyzer without striking any electrode surfaces.

In an analogous fashion to the discussion on magnetic sectors (Section 4.7), the motion of a charged particle in an electrostatic sector field is governed by the balance between the centrifugal force and electrostatic force on the ion between the electrodes:

$$\frac{m\mathrm{v}^2}{r_e} = -q\mathrm{E} \tag{4.7}$$

where,

m, q = mass and charge of the particle
v = particle velocity
E = electrostatic force between sector field electrodes
r_e = radius of curvature for particle trajectory in electrostatic sector field

Expressing Eqn. 4.7 for positively charged ions in terms of the particle energy and charge state is more instructive:

$$r_e = \frac{2U}{ze\mathrm{E}} \tag{4.8}$$

where,

$U =$ kinetic energy of the positive ion
$z =$ ion charge state

Since the mass of the particle does not enter into Eqn. 4.8, particles will move along the same trajectory if they have the same mass, charge, and kinetic energy. This demonstrates the well-known fact that an electrostatic condenser acts as an energy-only filter. In addition, we can see that ions with different kinetic energy will be bent through different radii of curvature. A mechanical aperture at the exit of the sector serves as the ″energy-defining″ slit. Doubly charged ions will pass through the sector field at half of their actual kinetic energy.

Our discussion on magnetic sectors included the importance of fringe field effects on ion trajectories and the necessity of their inclusion for proper magnet design. Likewise, the electrostatic condenser exhibits fringing fields at the electrode boundaries which must be corrected. Consider an electrostatic sector field as shown in Fig. 4.27. The physical electrode boundary is represented by a sector angle $\left(\Phi_e\right)$ with spacing $2b$, along with an effective field boundary angle $\left(\Phi_{eff}\right)$ that is *felt* by the ions traveling between the electrodes. Also shown are thin diaphragm plates, known as ″Herzog corrector plates, ″ situated a distance d from the electrode boundaries with holes of diameter $2s$. It can be shown that the relation between the physical sector angle and effective one is given by Eqn. 4.9 using a parameter η, which represents the increase in the sector angle due to fringing fields (Ingram *op. cit.*; Septier, 1967):

$$\Phi_{eff} = \Phi_e + 2\eta \tag{4.9}$$

Nomographs are used to determine the parameter η, which depends on the diaphragm geometry through the ratios $\left(\frac{s}{b}\right)$ and $\left(\frac{d}{b}\right)$. There exist specific values of $\left(s, b, d\right)$ for which η will vanish, making the effective sector angle identically equal to the physical one. This technique was used in our system to design the Herzog corrector plates to yield an effective sector angle equal to the physical one.

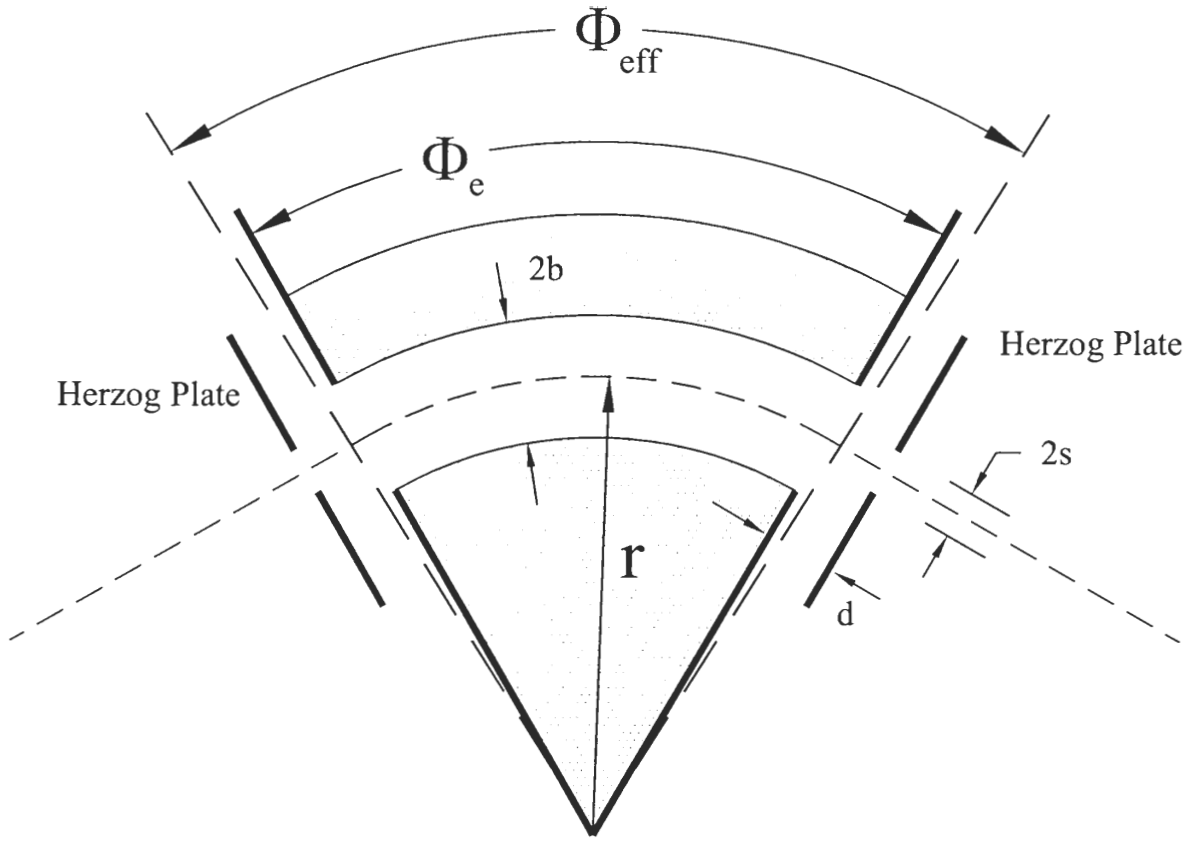

Figure 4.27: Schematic of an electrostatic sector field showing the actual and effective sector field angles. The Herzog plates which terminate the sector field are shown with the important design dimensions specified.

The 90° electrostatic sector in our system was custom-built in the Caltech chemistry machine shop. The spherical electrodes were gold-plated OFHC copper of 50 mm and 65 mm radii, respectively, giving a mean sector radius of 57.5 mm (~2.25″). Herzog corrector plates of 304SS were positioned at the inlet and exit of the sector with sapphire ball standoffs for alignment and electrical isolation. Dimensions of this arrangement are given in Fig. 4.28. After the exit Herzog plate, a four-element Einzel-type cylindrical lens assembly is used to transport and tightly focus exiting ions to the entrance aperture of the RF/DC quadrupole rod set of the mass filter. Fig. 4.29 shows photographs of the unassembled sectors (4.29a) and the entire analyzer in assembled condition with Herzog plates attached (4.29b). The energy filter is positioned inside a custom ″loadlock-type″ cross from MDC Vacuum and pumped with a Varian 60 L/s triode ion pump.

The energy filtering action of the sector is accomplished by slowing down or speeding up ions which enter the sector to the ″pass energy″ of the analyzer (constant acceptance energy or CAE mode). The relationship between the particle kinetic energy, analyzer pass energy, retard voltage, and sector voltages is given in Eqns. 4.10-4.11 (Bertrand *et al*., 1977).

$$U = R + E_{pass} \tag{4.10}$$

$$E_{pass} = H_z \Delta V \tag{4.11}$$

where,

$U =$ particle kinetic energy
$R =$ retarding voltage
$E_{pass} =$ pass energy (kinetic energy of particles passing through analyzer at r_e)
$H_z =$ Herzog constant for analyzer (determined by sector radii)
$\Delta V =$ absolute potential difference between inner and outer sectors

Further, the Herzog constant for the analyzer depends only on the sector geometry (Bertrand *op. cit*.):

$$H_z = \frac{r_{inner}\ r_{outer}}{r_{outer}^2 - r_{inner}^2} \tag{4.12}$$

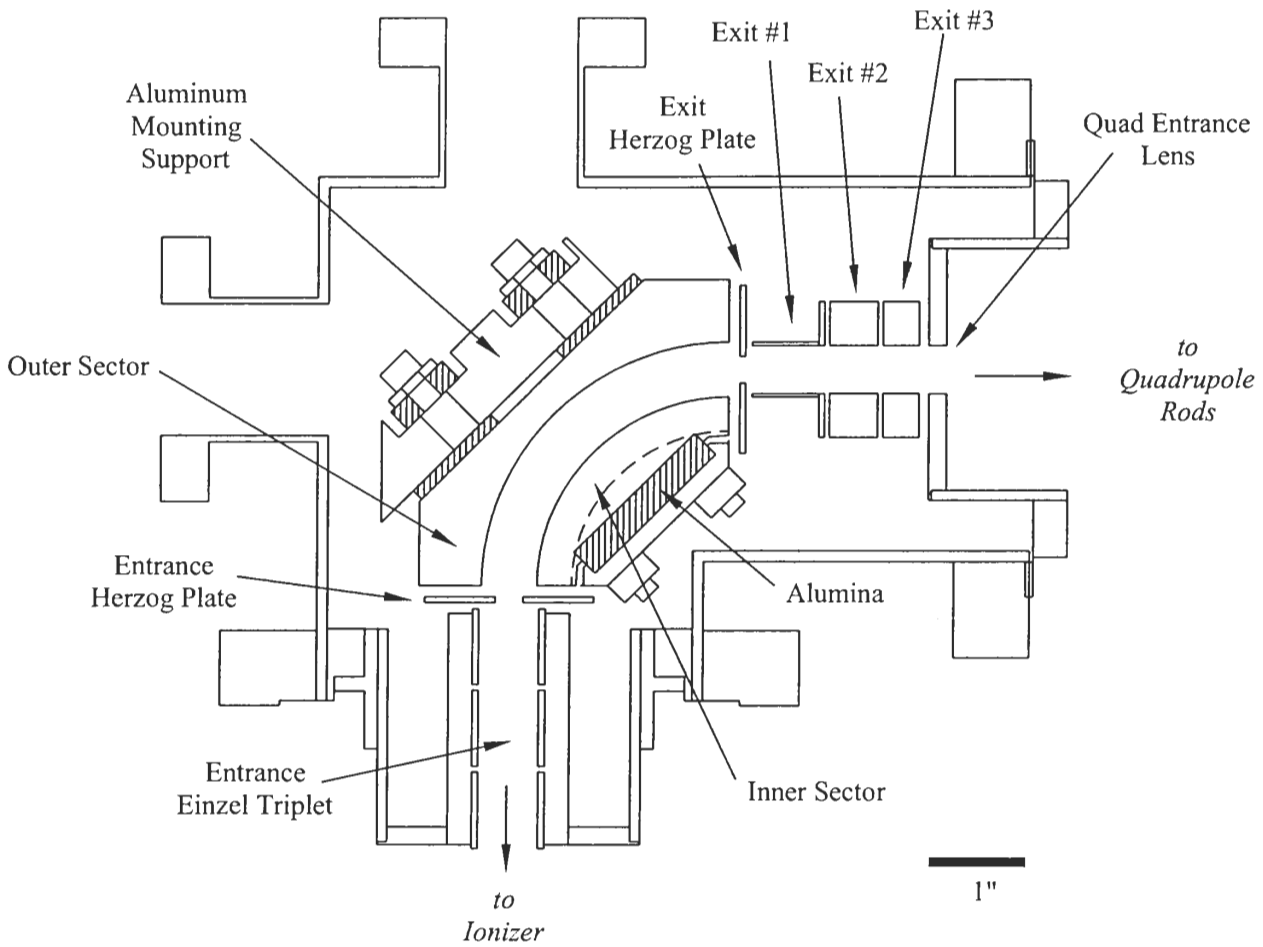

Figure 4.28: Schematic of the 90° hemispherical sector energy filter constructed for the scattered product detector. The sector resides between the ionizer and quadrupole rods with both inlet and exit transfer lens systems.

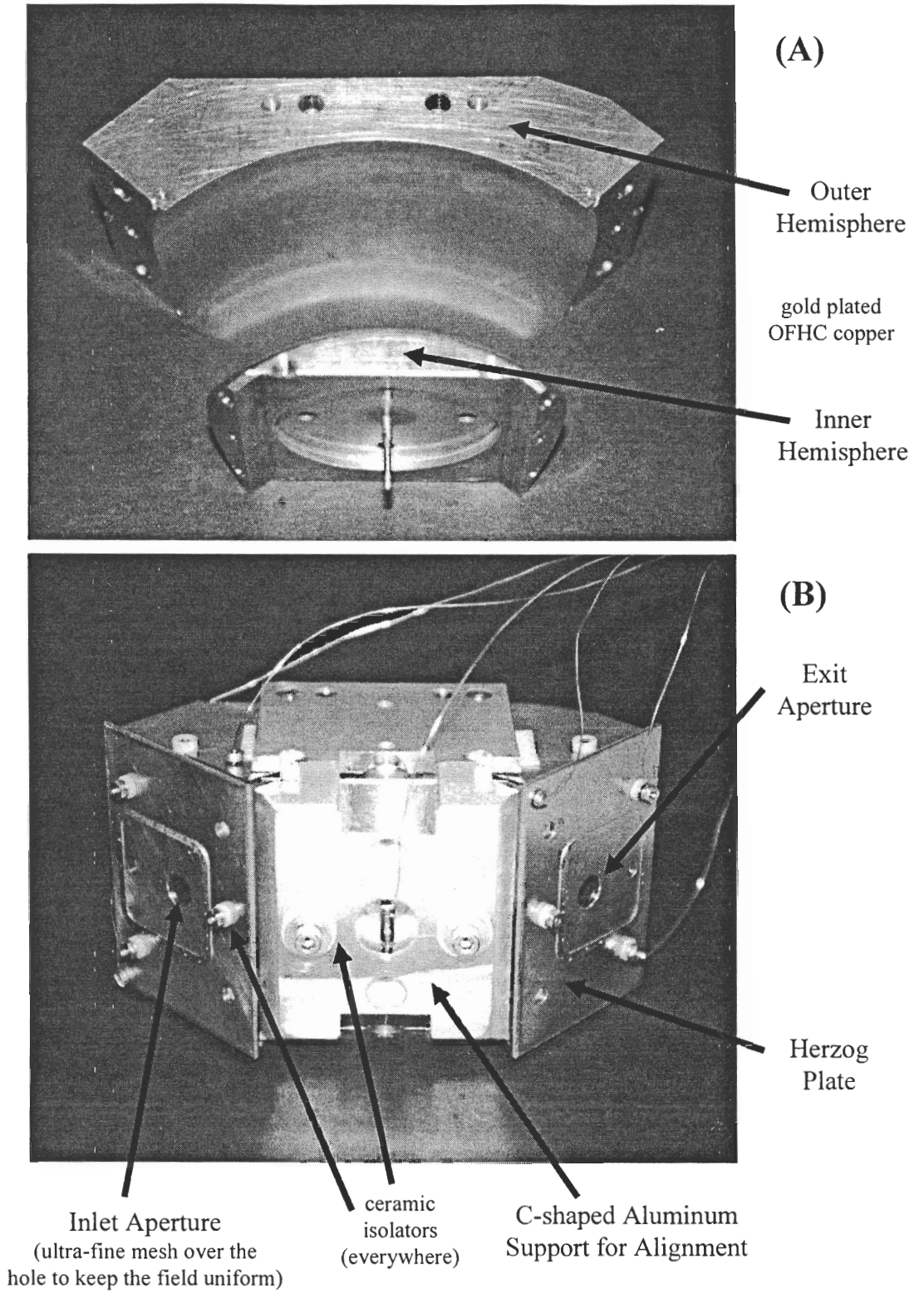

Figure 4.29: Photographs of the scattered product energy filter with individual components specified. (A) unassembled view of the 90° hemispherical sectors and (B) assembled view with Herzog plates in place.

where,

r_{inner} = radius of curvature for inner sector electrode
r_{outer} = radius of curvature for outer sector electrode

The usual mode for sector operation is to fix the pass energy constant (CAE mode) and sweep the retarding voltage from $-E_{pass}$ (zero kinetic energy) up to some maximum scanned energy (see Eqn. 4.10). A pass energy of 15 eV was used for most of our scattering energy experiments because it provided good energy resolution and adequate transport energy through the quadrupole rod set (see next section).

Both the inlet triplet and 4-lens exit system on the sector analyzer were designed through extensive SIMION simulation. An example ion trajectory calculation for a 50 eV ion beam retarded to the 15 eV pass energy of the analyzer is shown in Fig. 4.30. Very specific voltage ratios between the inlet and exit lens elements were required for proper focus over a wide range of ion energies.

A custom, computer controlled power supply system was built for the sector analyzer, inlet, and exit Einzel lenses. An electrical schematic is shown in Fig. 4.31. It utilizes resistive divider networks off two separate bipolar DC supplies floating on the retard voltage for each of the lens bias voltages. The main retard voltage is provided by an extremely stable +1kV PMT tube power supply that was remotely programmed by a 4 channel, 12-bit DAC (IOTech, model DAC 488/4). A LABVIEW program drives the DAC through a GBIP bus to sweep the PMT supply. The sector could be swept from 0-550 eV kinetic energy referenced to ground with a maximum pass energy of 50 eV. The LABVIEW program also controlled several digital output lines from the DAC for timing and channel advance in the counting electronics for the ion detector (see Section 4.12.4).

4.12.3 Quadrupole Mass Filter

The mass filter used after the energy analyzer was based on a ⅝″ diameter x 9.5″ long RF/DC quadrupole rod set from Extrel. The large rod diameter was chosen to maximize the ion acceptance ellipse of the quad and gain the highest ion transmittance possible.

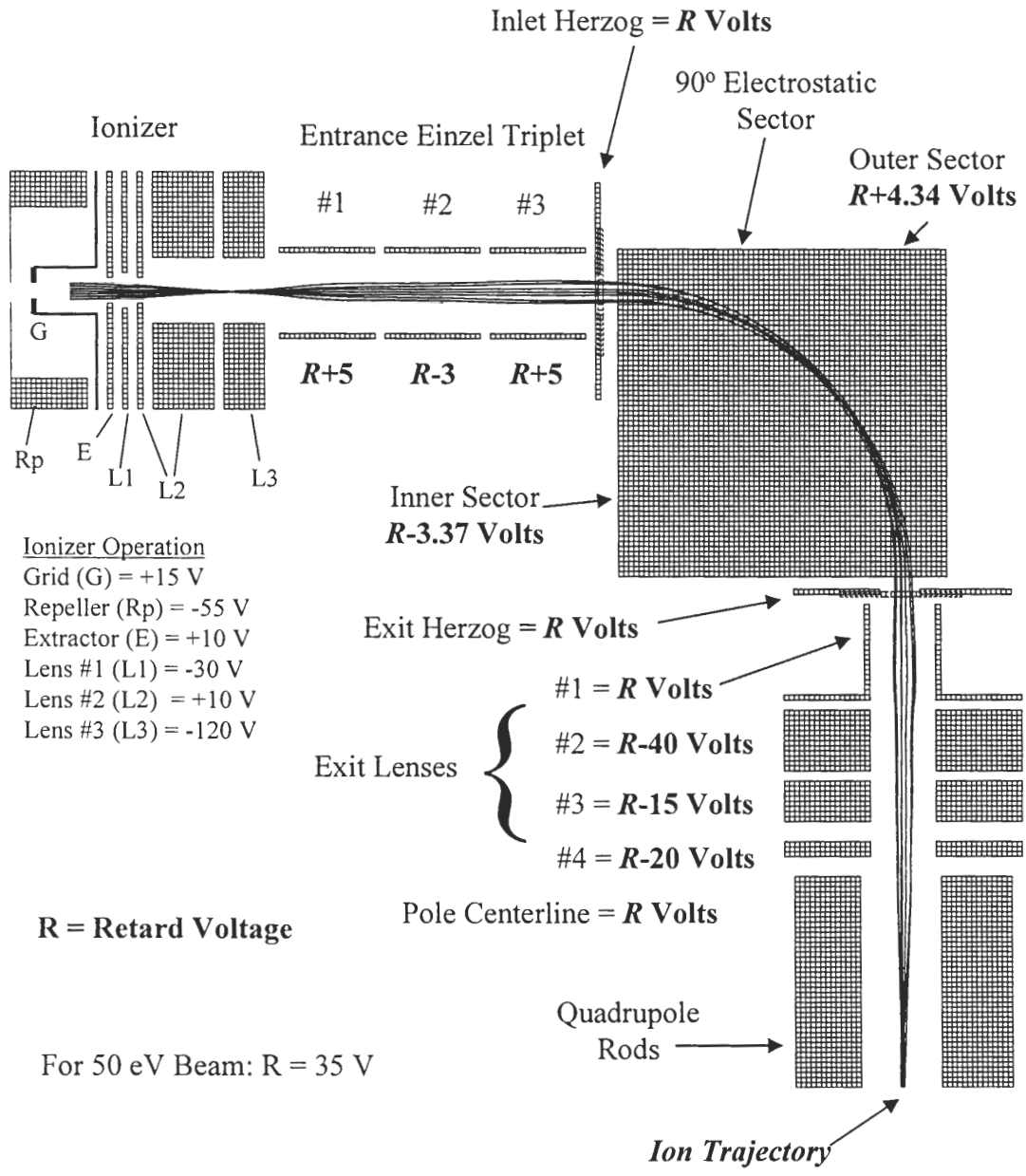

Figure 4.30: SIMION simulation of the scattered product energy filter for a 50 eV Ar^+ beam decelerated to the 15 eV pass energy of the 90° sector energy filter. All the lens voltages, including the centerline potential of the quadrupole rods, are based of the main retard voltage (R). Ion kinetic energies are scanned by ramping the retard voltage. In this way, the energy of ions through the filter and the quadrupole is always the same.

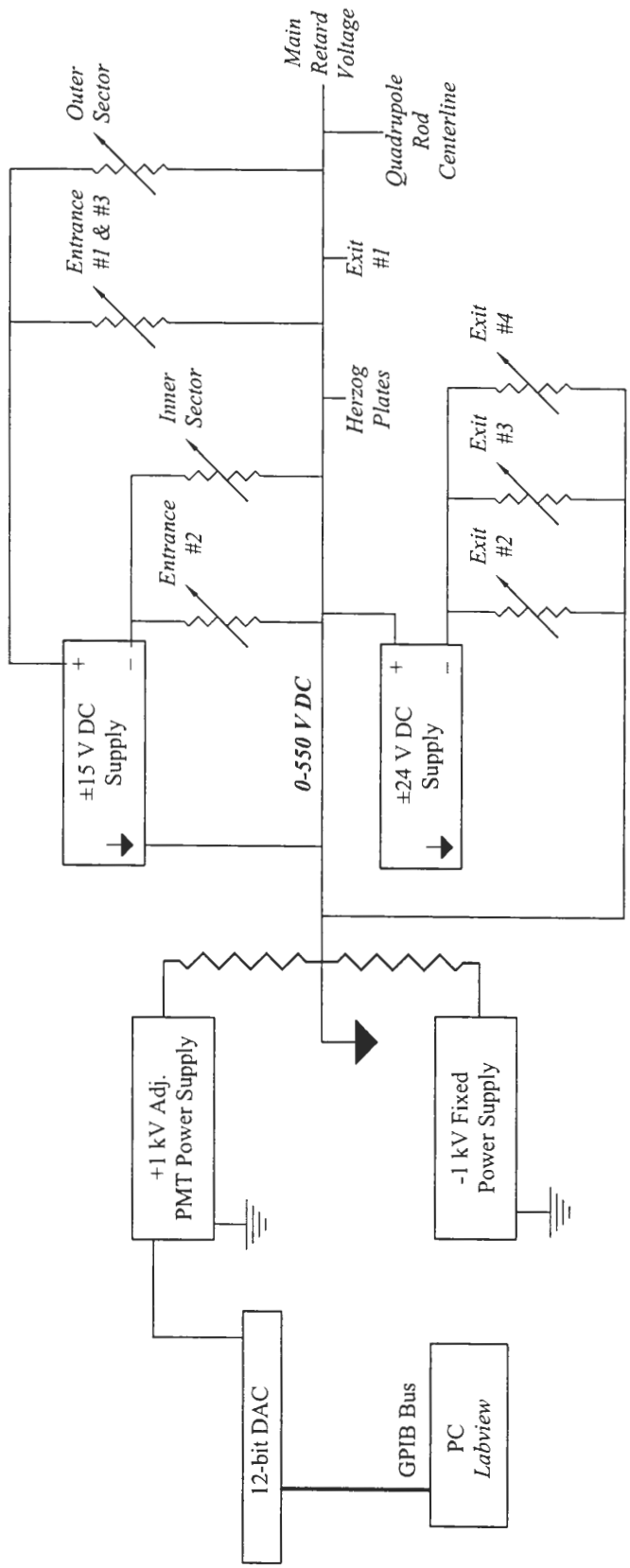

Figure 4.31: Power supply bias scheme for the 90° electrostatic sector energy analyzer in the scattered product detector.

The pole set was driven by a tube-based RF amplifier (Extrel QPS system) and match box with 300W maximum output power at 2.22 MHz. Although built in1978, the stability of the vacuum tube power supply is unequaled and can provide extremely high mass resolution (>500) that is much higher than most other quadrupole mass filters.

In the system, the DC rod voltages are derived directly from the RF drive by vacuum tube diodes. This unique feature allowed the entire rod set and match box circuitry to be floated above ground. The ability to artificially move the quad centerline potential above ground was absolutely necessary because the ion flight energy within the quad must ramp with the energy analyzer retard voltage. The centerline quad potential was attached directly to the main retarding voltage ramp of the energy filter. In this way, ions fly through the quad at exactly the pass energy of the energy filter, irrespective of what kinetic energy is being scanned. This may seem to be a subtle point, but it is critical that the ion energy within the quad be low ($\leq$ 80 eV) for proper mass filtering to occur (Dawson, 1995). High on axis energy means that the ions are not within the quad filtering field for enough RF periods to give adequate deflection and as a result, mass resolution becomes very low (a width of several AMU can get through the analyzer). Our setup was run with 15 eV pass energy on the energy filter and a corresponding 15 eV ion flight energy through the quad even when analyzing 500 eV ions leaving the grounded target. Since all ions are retarded to the 15 eV energy filter pass energy, the subsequent mass filtering step is always carried out with identical focus conditions (made possible by floating the quad centerline).

In an effort to further decrease the residual gas background and prevent ion forming collisions within the quad filter section, a special cryo-cooled shroud was placed around the quad pole set. A copper tube sleeve around the pole set is connected to the refrigerator cold head of a CTI 8F cryopump. This allows the shield to be cooled to 30 K continuously to freeze out any residual gas and capture all the ions deflected by the quad field. The quad vacuum chamber is sealed at both ends by the pole set mounting flanges to provide another differential pumping stage for the Daly ion detector. Finally, there was an auxiliary Varian 60 L/s triode ion pump on the chamber to pump helium and background hydrogen which would not freeze on the 30 K shroud.

4.12.4 Daly Ion Detector

The extremely small ion signals (10^{-15}-10^{-17} Torr effective pressure) that are generated by electron impact ionization of secondary neutrals leaving the target surface require an extremely sensitive, single-ion type counting system. The problem is unavoidable because ionization by electron impact is horribly inefficient. The most well-designed magnetically confined ionizers running in space charge limited mode at 10 mA of emission current can only provide a conversion efficiency of maybe one part in 10^4 (Scoles, 1988). This dictates that the ion detector must be able to count every single ion that is generated. Unfortunately, single ion counting is impossible with the standard electron multipliers used for mass specs because of signal to noise levels. Channeltrons, multi-channel plates, and discrete dynodes can provide a gain of 10^6 to 10^7, but their dark noise is just too high.

However, there is a solution to this dark-noise problem. We first recognize that single photon counting with a properly shielded and/or cooled PMT tube system is relatively straightforward. This is possible for two reasons. First, there are certain photocathode materials for PMT tubes that have very high yield (many electrons per photon). Second, some of these same high-yield photocathodes generate very few thermal electrons (essentially no dark noise). As a result, photon-generated electron pulses can be distinguished from thermal electron pulses with ease. Finally, if we could convert ions to photons somehow, then we could use single photon counting techniques. This approach was first taken in 1959 by Daly who showed that ion signals as low as $1 \bullet 10^{-18}$ Amps could easily be detected with a noise level better than $4 \bullet 10^{-20}$ Amps (Daly, 1959). Such a signal corresponds to just a few singly charged ions per second.

Our ion detection system follows the approach of Daly where ions are first converted to electrons, the electrons are then converted to photons in a scintillator, and the resulting photons are finally detected with a single-photon counting PMT tube system. A schematic of our system is shown in Fig. 4.32. Ions that leave the mass filter are pulled by a huge accelerating field between -15 to -30 kV onto a metal ″conversion″ stub.

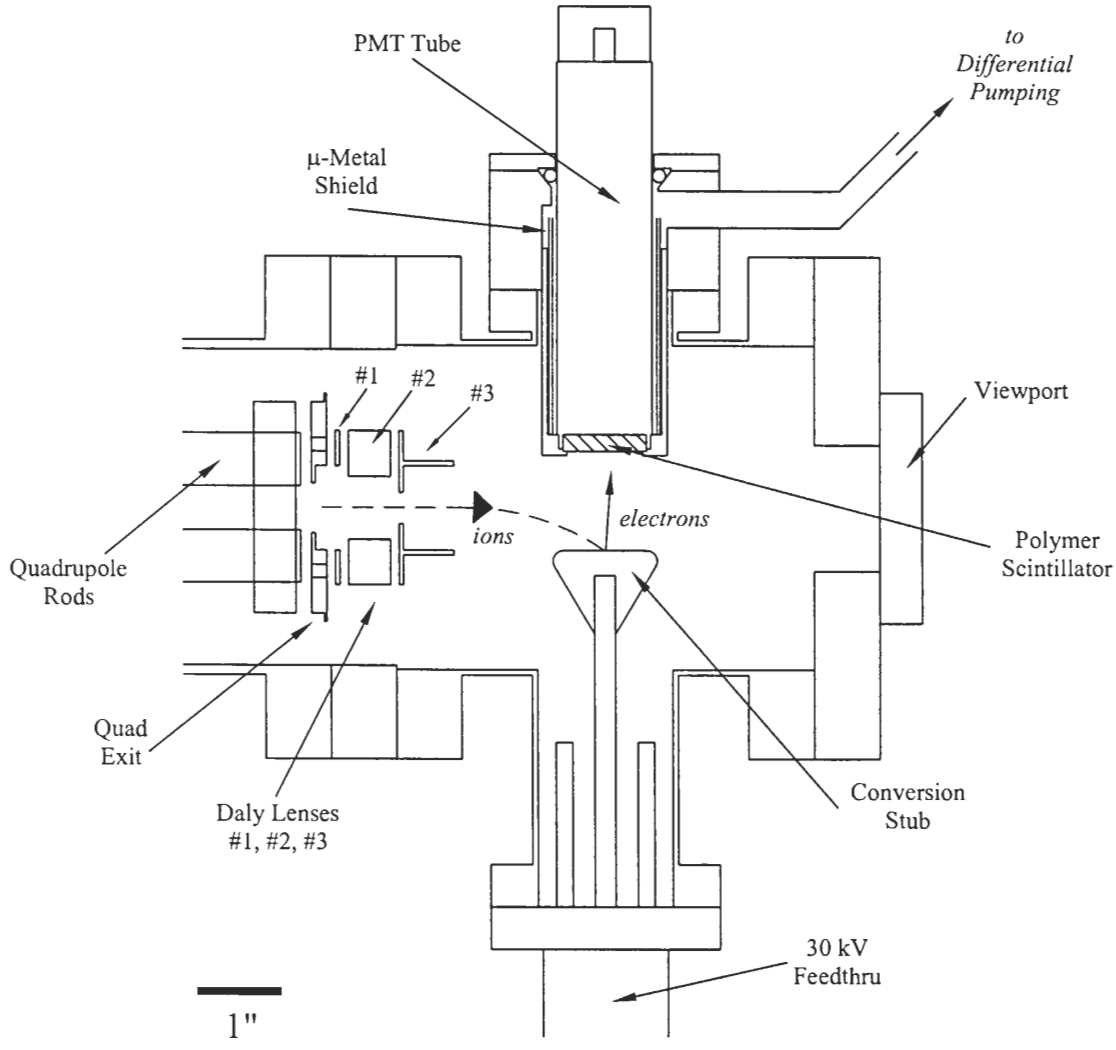

Figure 4.32: Schematic of the Daly-type ion detector constructed for single ion counting in the scattered product detector. Ions exit the quadrupole mass-filtering field and are accelerated by -15 to -30 kV, where they impact the conversion stub and create a shower of secondary electrons. These electrons are accelerated away from the stub at very high energy and are annihilated in the polymer scintillator, where conversion of electron to photon occurs. The photons from the scintillator are then counted with a photomultiplier tube.

Ion impact on the stub at such a high energy creates an avalanche of secondary electrons released from the stub surface (ion-to-electron step). The electrons from the -30 kV stub are accelerated away from the stub surface toward ground where they tunnel through a thin metallized layer on top of an organic scintillator material. As the electrons traverse the scintillator, they are eventually annihilated and converted to photons. A PMT tube at the rear of the scintillator picks up the photons, converts them back to electrons via the photocathode, and amplifies the electrons by 10^6 - 10^8. The electron current at the PMT rear is read as a discrete set of pulses which echo the photon flux. Since the ion arrival at the stub is statistically discrete at such low signal levels, the number of PMT pulses is directly proportional to the number of ions.

The geometry of our Daly conversion system was based on extensive SIMION simulation of ion exit trajectories from the quad rear aperture to design corrector lenses between the quad and stub. When ions of the correct pass mass move through a quadrupole mass filtering field, their trajectories are sinusoidal in nature with hybrid beat patterns having nodes or anti-nodes at the exit of the field (Dawson, *op. cit.*). Ions are usually ejected from the field in an axially symmetric cone pattern expanding outward from the quad exit aperture with 30°-60° solid angle. A three-element hybrid plate lens system was designed to properly pull the ions exiting the quad aperture and pinch them inward to provide a 45° angle of incidence when impacting the stub surface. This impact angle was chosen because the maximum ion-induced secondary electron yield occurs near 45° (Daly, *op. cit.*). Typical operating voltages for these lenses (#1, #2, #3) are +200, -600, and -3000 V, respectively. The stub was made from 304SS in a ″door-knob″ shape and later coated with ~5000 Å of aluminum by DC magnetron sputtering in the Nicolet lab at Caltech. Aluminum provides a low sputter yield with almost the highest secondary electron yield of all metals (Bourne *et al.*, 1955). Such an arrangement provides an additional gain stage of 5-10 electrons per ion.

The organic scintillator was 1″ OD x 5 mm thick BC408 polyvinlytoluene based material from Bicron, sealed in a custom made differentially pumped housing. The organic material was chosen because of its fast rise time (<1 nS), reasonable low-energy yield (several photons per electron at 30 keV), and emission wavelength maximum at 408 nm. The 408 nm emission was matched with a UV glass, counting PMT tube

(Hammamatsu, model R6095) that had a special bi-alkali photocathode giving maximum sensitivity at 400-420 nm. The scintillator was metallized on the stub side by sputter coating with 1500Å of aluminum to provide a good grounded surface. The PMT tube itself was housed inside vacuum with a mu-metal magnetic shield and pressed firmly against the rear of the scintillator. The tube is run in pulse count mode only with the photocathode at positive high voltage (the non-traditional way) to further reduce spurious electron pulses.

Pulses from the PMT tube were amplified by an AC-coupled pre-amp (EG&G Ortec, model 9301) with a fixed gain of 10. The pre-amp output goes to an gated photon counter (SRS) with a tunable discriminator where it is converted to NIM-standard pulses, if above threshold. An EG&G MCS Plus multi-channel scalar card in a PC computer is used to count and bin the NIM pulses from the photon counter. The channel advance and signal gate for the MCS card are provided by the digital I/O from the IOTech DAC used to control the sector energy filter. In this way, the entire counting system is controlled and advanced in sequence with the retard voltage ramp of the sector energy filter. A connection and control diagram for the sector, quad, and ion detector showing the signal paths is given in Fig. 4.33.

The whole Daly detector is housed in a custom 6″ CF Tee chamber that is pumped by another 300 L/s Seiko Maglev turbo for ultra-clean pumping. The turbo exhaust is not backed by a conventional rough pump but directly connects to the turbo-pump used on the loadlock chamber. This double stage of turbos absolutely ensures that the Daly detector chamber is held at the lowest possible pressure without any possibility of contamination or oil backstreaming from roughing mechanical pumps.

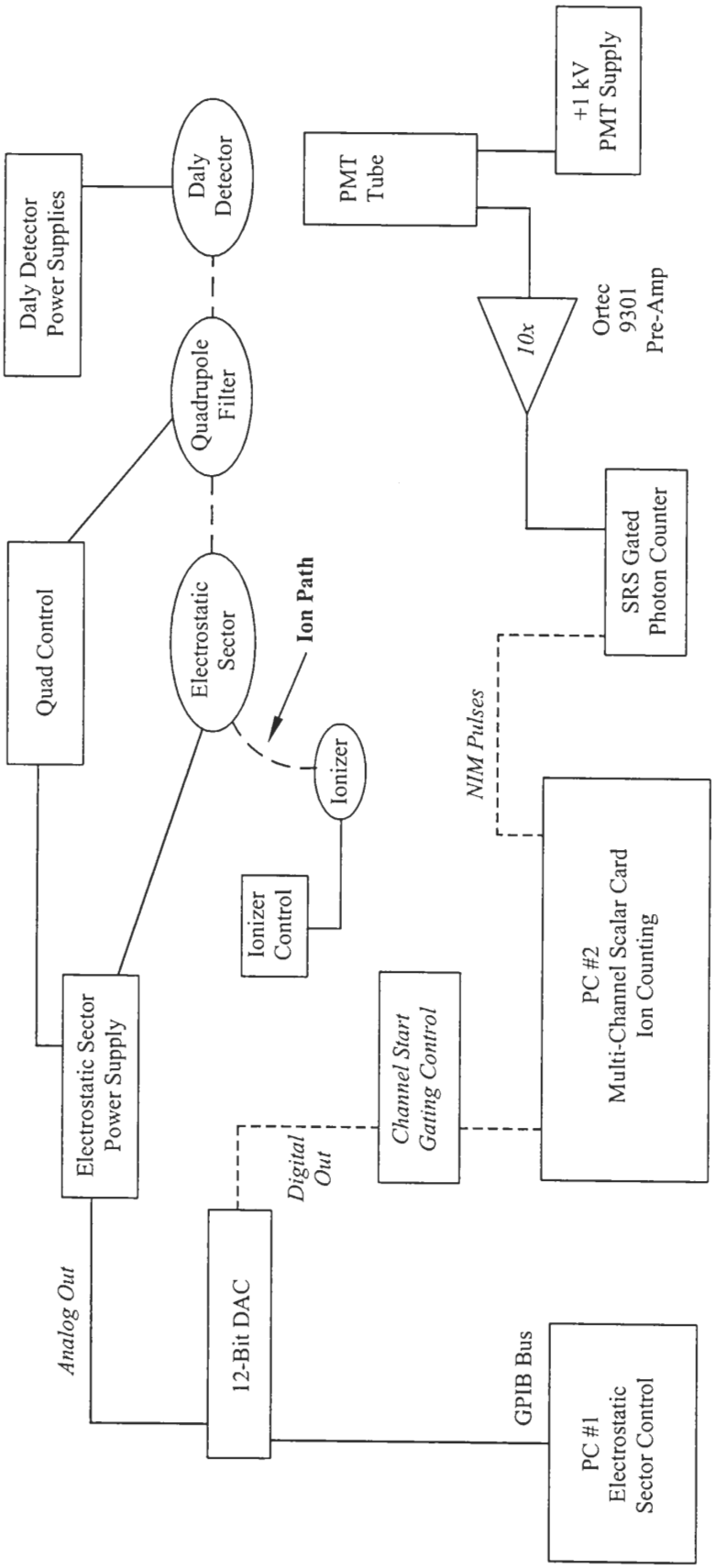

Figure 4.33: Signal connection and control diagram for the scattered product detector along the ion flight path from the ionizer to the Daly detector.

4.13 Beamline Focus Controls

The focusing system of the ion beamline is rather complex because many electrostatic lenses are needed for extraction, steering, and focus correction. Some of these lens components require a very stable, small voltage trimming range (< 1-2 kV) on top of a high voltage of 15-20 kV for the main beamline acceleration and transport. Clearly, a floating power supply scheme, although experimentally more difficult, is the most ideal approach. Our control system utilizes multiple floating power supplies for steering and focus components parked on top of other high-voltage supplies for main sections of the beamline. Small supplies floating on a -15 to -20 kV common also require control schemes that float along with fully isolated AC line power. The problem of floating controls for these small bias supplies were solved in our system by a ″brute-force″ method. Each trim control is fully shielded from the user with >20 kV isolation techniques using isolated plastic control boxes, ceramic standoffs everywhere, and shielded high-voltage control wire throughout.

A schematic representation of the floating power supply scheme for our system is shown in Fig. 4.34. All of the beamline power supplies (except the plasma bias) float on top of a separate DC supply that is ramped up identically with the plasma bias voltage. In this way, exactly the same extraction and focus conditions with respect to earth occur for all beam energies. It is necessary to separate these two voltages because the13.56 MHz noise from the plasma electron oscillation causes havoc in the regulator circuits of all the beamline power supplies. When the plasma bias (final beam energy) is raised, so is the beamline floating supply through a massive AC line isolation transformer that drives *all* the beamline supplies. As shown in the schematic, the vertical bunching plates and quadrupole doublet float on the beamline high voltage. The steering quad supplies and quad shield float atop the steering quad centerline potential. Typical operating conditions for all the electrostatic lenses along the beamline are summarized in Table 4.1.

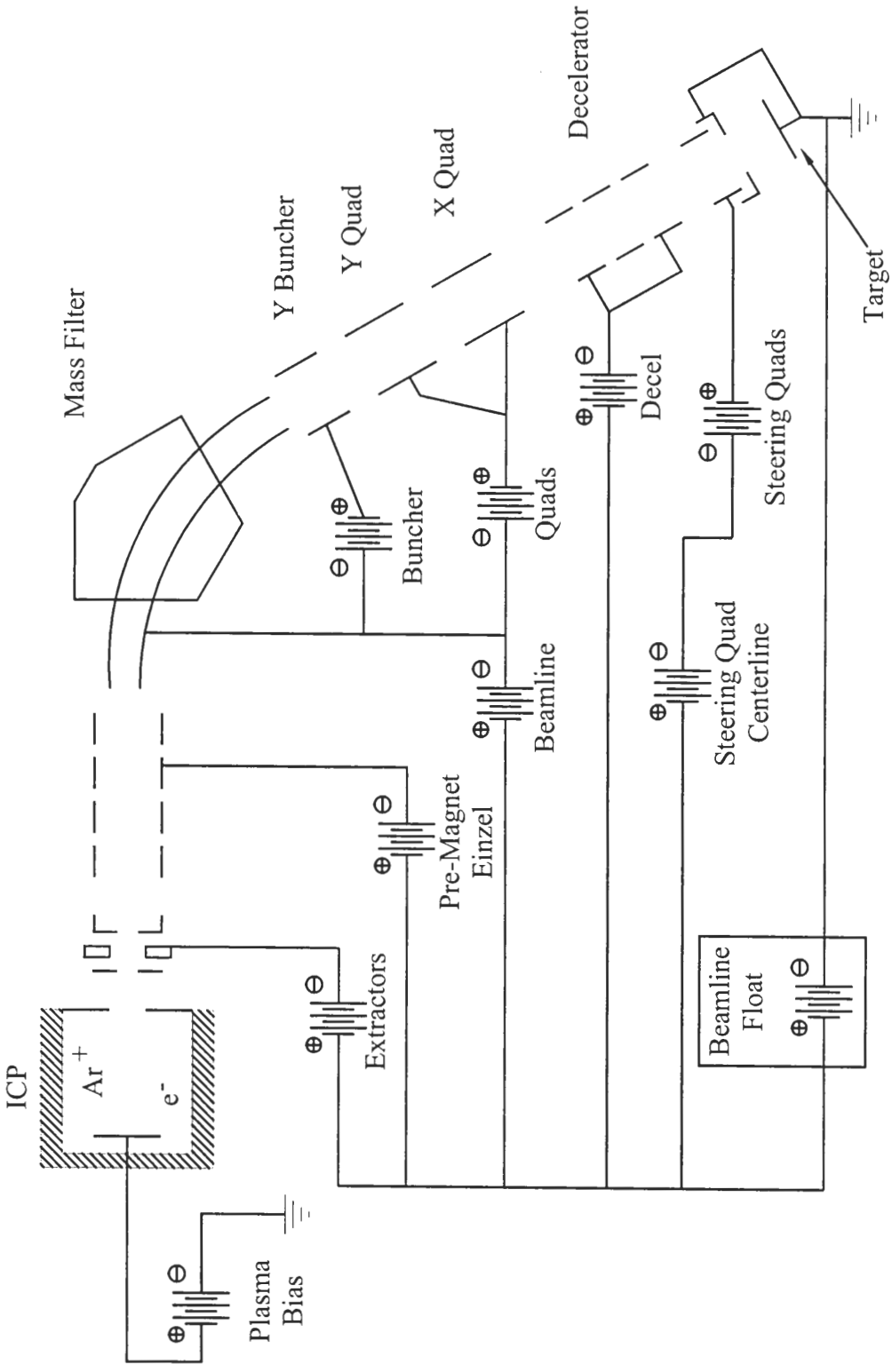

Figure 4.34: Floating power supply scheme for the ion beamline.

Table 4.1: Typical ion beamline electrostatic lens operating voltages.

Electrostatic Lens	Operating Range [Volts]	Typical Setting [Volts]	Supply Common
Plasma Bias	0 → +1500	Beam Energy	Ground
Main Beamline Float	0 → +1000	= Plasma Bias	Ground
Puller	0 → -4500	-900 → -1500	Beamline Float
Buncher	0 → -6000	-2000 → -2500	Beamline Float
Front Beamline Accel.	0 → -25 kV	-10.5 kV	Beamline Float
Pre-Magnet #1	0 → -25 kV	-13.8 kV	Beamline Float
Pre-Magnet #2	0 → -25 kV	-7.2 kV	Beamline Float
Pre-Magnet #3	0 → -25 kV	-6.3 kV	Beamline Float
Magnet Beamline	0 → -25 kV	-14 kV → -16 kV	Beamline Float
Vertical Buncher	0 → +1000	+200	Magnet Beamline
Quad Doublet Plates	0 → +4000	+700→ +1000	Magnet Beamline
Decel #1	0 → -25 kV	-7.7 kV	Beamline Float
Decel #2	0 → -25 kV	-10.9 kV	Beamline Float
Decel #3	0 → -25 kV	-10.0 kV	Beamline Float
Steering Quad Centerline	0 → -20 kV	-6.0 kV	Beamline Float
Steering Quad Shield	0 → +3000 V	+750	Quad Centerline
Steering Quad Plates	0 → +4000 V	+500	Quad Centerline

5. Plasma-Beamline and Scattered Product Detector Performance

This chapter contains the performance details of our scattering system with specific emphasis on the ability of the ion beamline to provide isotopically clean ion beam surface probes at low impact energy. In addition, our broad-based approach to the detection of both the mass and energy spectrum of the scattered particle flux will be discussed. The combined detection of mass and energy will show how the particle signatures coming from the target can be resolved and associated with specific surface collision events and overall scattering processes.

5.1 Beamline Performance

5.1.1 Introduction

The major goal of this project was to design and build a mass-filtered ion beam scattering system to study gas-surface interactions in the hyperthermal energy regime (50-500 eV). As we stated earlier, the 50-500 eV range has largely been ignored because of the experimental difficulties in forming ion beams with sufficient current at these low energies. We have specifically targeted this energy range, so it is essential to highlight the important operational features of our plasma-beamline system which enable scattering experiments at such low energies. Specifically, the following operational aspects were characterized:

1) What are the mass filtering capabilities of the system? Can isotopically pure ion beams be generated from complex plasma gas mixtures?

2) What beam currents can be delivered to the target at low impact energy?

3) What does the ion beam energy distribution at the target look like and is it sufficiently narrow for scattering experiments?

4) Is the ion beam energy tunable? Can the impact energy be tuned successfully by floating the entire ICP plasma source above ground?

Each of these issues will be discussed in the following sections. The performance results of the ion beamline will show that the ICP plasma source, when combined with the *accel-decel* scheme, can be effectively used for low energy scattering studies. We will also see that the system can provide a wide variety of isotopically clean ion beams at low energy with high current and narrow energy width.

5.1.2 Mass Filtering Performance

The mass resolution of our ion beamline system was evaluated by forming isotopically clean ion beams from a complex plasma gas mixture that is typically used for dry etching of SiO_2. This situation represents an extreme case of beam contamination and can be used to test the ability of an ion beam system to give high mass resolution and produce clean, pure beams. Figure 5.1 shows a ″mass sweep″ of the ion beams that can be formed by extracting all the ions from a CF_4 / Ar / O_2 plasma mixture (typical SiO_2 etch mix) running at 500W plasma power. The plot was formed by sweeping the field strength of both the 60° sector and 10° deflector magnets simultaneously via computer control while maintaining the beam energy at 100 eV and beamline acceleration voltage at -12 keV. The mass exit slit on the 60° magnet was set to a 3 mm width and the beam current at the target location was measured with a movable Faraday cup having ~0.5 mm diameter inlet aperture. It can be seen that all the ions in the plasma source are easily resolved by the sector magnet and can be transported to the sample as *individual*, isotopically pure beams for scattering experiments. Higher resolution is possible with smaller exit slit size, but better mass separation is really not needed for most of the beams shown in this plot.

The ability to conduct mass sweeps of this kind with the beamline suggests an ideal way to study the ion concentrations in an ICP discharge. For instance, the gas mix composition or input power can be varied with magnetic field sweeps used to determine the change in ion concentrations of the discharge. In this way, the ion beamline with 60° sector magnet can be used, by itself, as a plasma diagnostic tool. Figure 5.2 shows one such study of how the relative ion concentrations of the CF_x^+ homologous series change with increasing CF_4 content in the gas mixture.

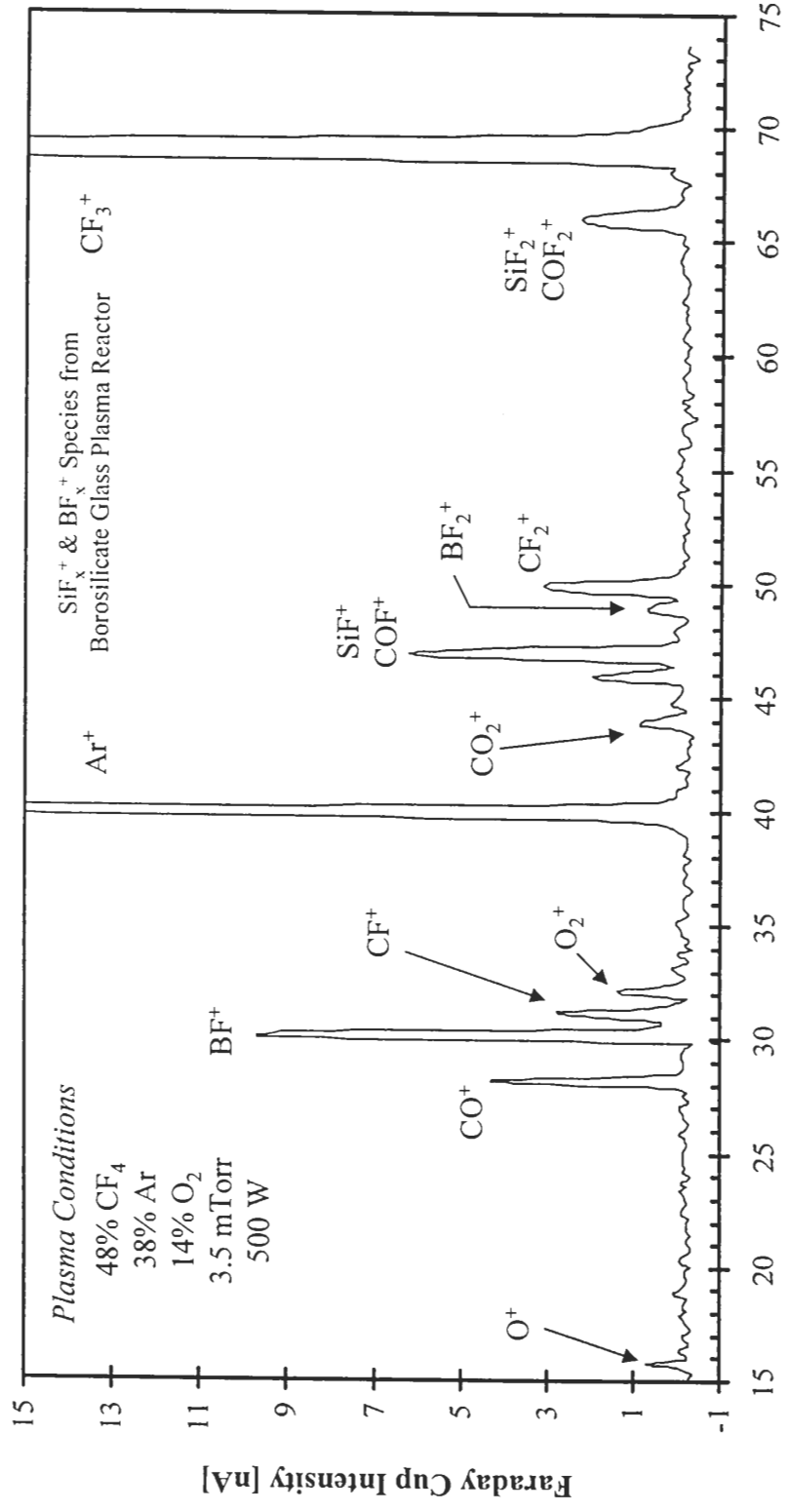

Figure 5.1: Mass sweep for a CF_4 / Ar / O_2 plasma using computer controlled ramping of both beamline magnets. The 60° sector and the 10° ion deflector magnets must be ramped up in field strength simultaneously to keep the ion beam focused on the Faraday cup since the ion transport energy was held constant at ~12 keV.

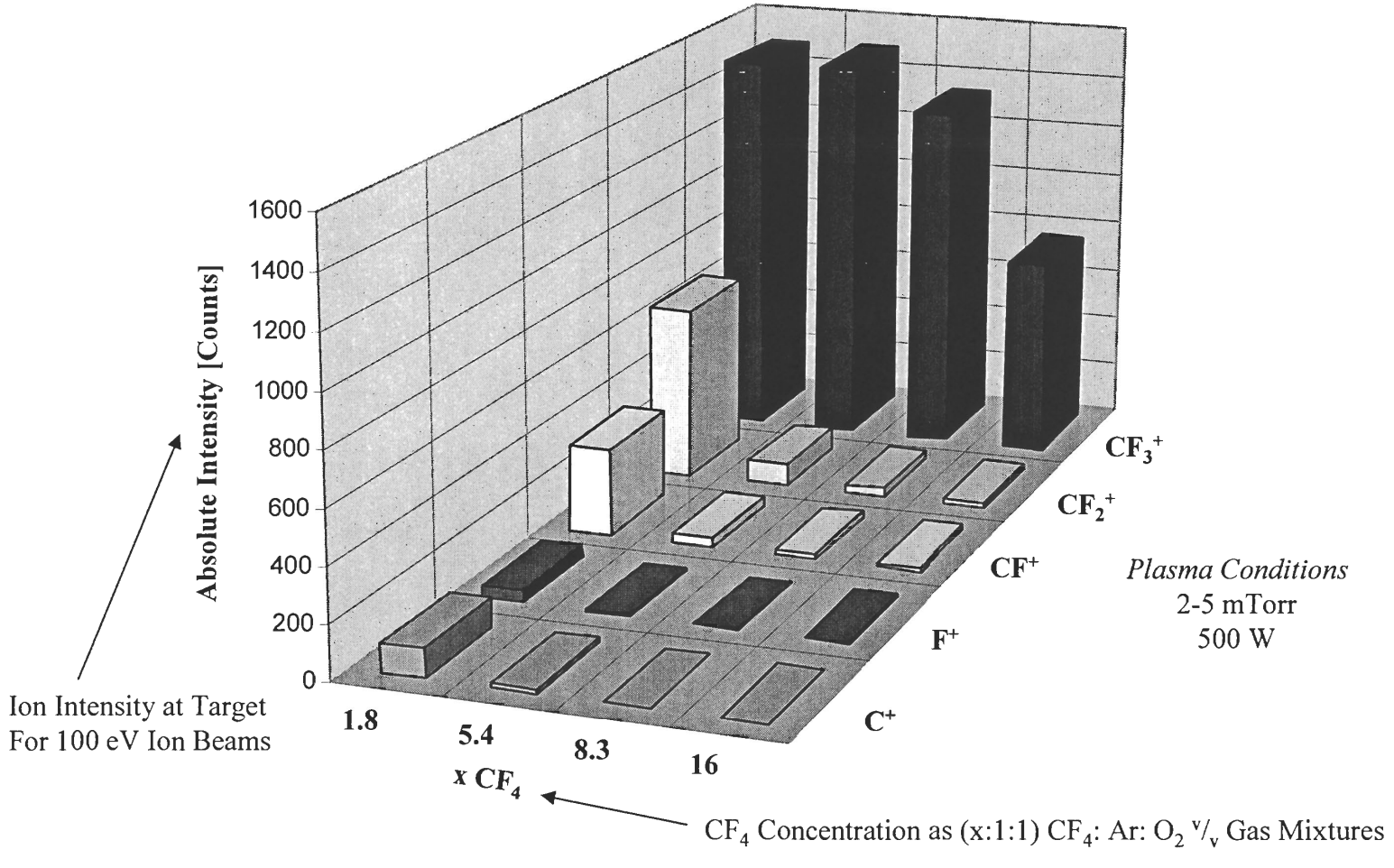

Figure 5.2: Relative ion concentrations of the CF_x^+ homologous series in mixed ion beams extracted from CF_4 / Ar / O_2 plasmas.

This experiment was conducted using different gas mixtures in the plasma source with computer sweeping of both magnets for fixed extraction and transport conditions. The ion beam energy was fixed at 100 eV and the beamline transport energy was 12 keV for all experiments. As shown in the plot, gas mixtures that are rich in CF_4 result in CF_3^+ as the dominant ion species, which could be caused by recombination of unsaturated CF_x^+ ions. Under lean condition, CF_x^+-CF_y^+ ion collisions are much less frequent, so the recombination rate is less and higher concentrations of CF^+ and CF_2^+ are seen. These experiments demonstrate the power of the beamline system for plasma diagnostics as well as a direct feedback mechanism for tuning plasma operation to obtain the highest yield of the ion species of interest.

5.1.3 Sample Currents at Low Energy

One of the most important design criteria for our ion beamline system was high beam current at low impact energy. This is made possible by the *accel-decel* scheme where ions are created in the plasma at the impact energy, accelerated to high transport energy, and then decelerated near the target back to their initial creation potential. The success of such a scheme depends on having high ion density in the plasma, efficient extraction, minimal current loss during transport, and proper focus correction during deceleration. However, the entire system cannot deliver high current at low beam energy unless all of the beamline components function together as a unified system through proper beam transport between each stage. Overall system performance can be evaluated through the amount of beam current available at the target for low impact energies.

The mass-filtered beam current that can be delivered to the target at low impact energy is shown in Fig. 5.3 for our system. The ion arrival rate is represented in terms of raw beam current as well as an areal current density for the 2 mm flag aperture. Current density at the target is more useful for direct comparison with an arrival rate of one monolayer per second (1 ML/s = 320 $\mu A/cm^2$ for Si). Figure 5.3a shows an Ar^+ beam extracted from a pure argon plasma discharge running at 500W of input power.

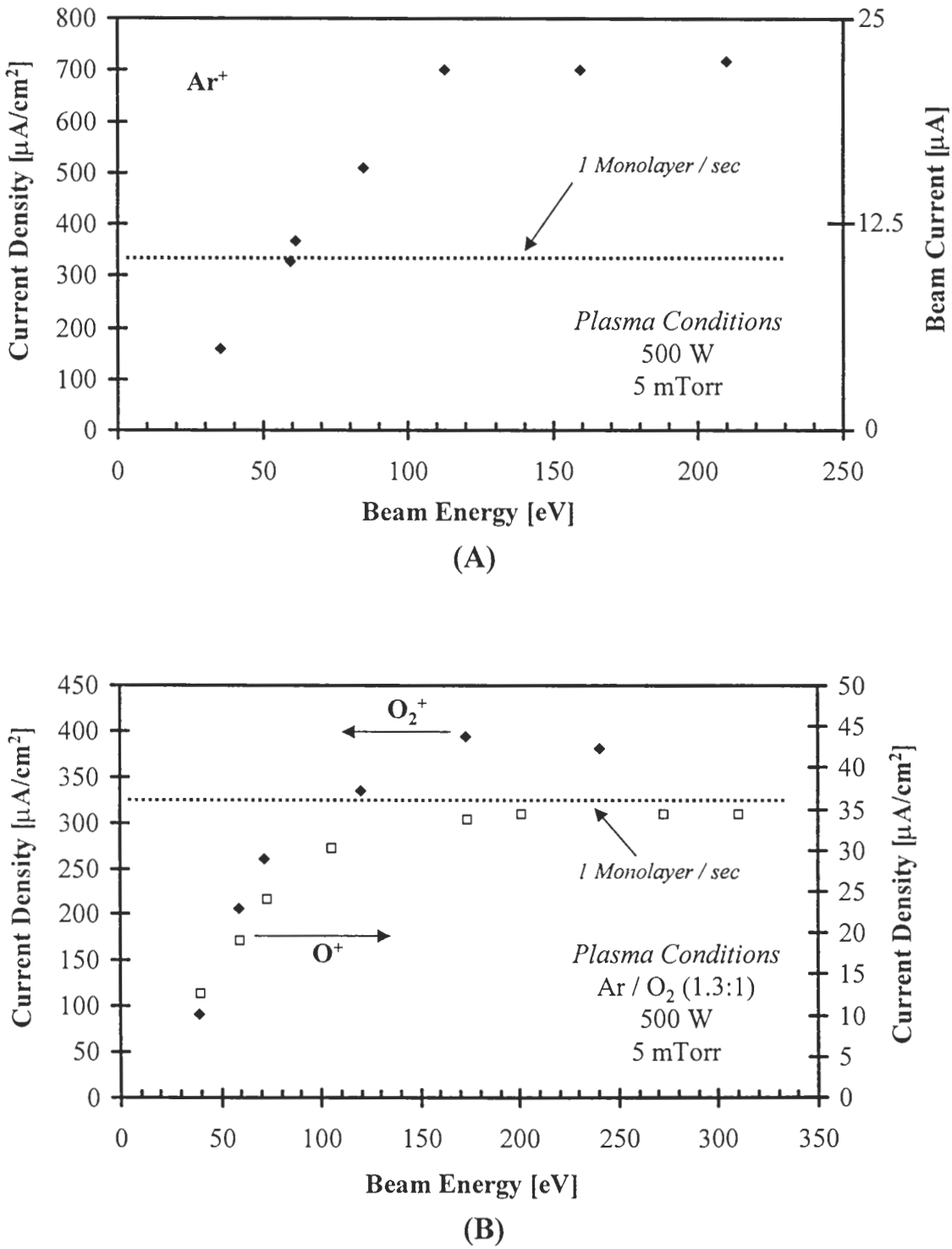

Figure 5.3: Ion beamline current performance at low beam energy.
(A) Ar^+ and (B) O_2^+ and O^+ for 2 mm Ø beam flag aperture.

The atomic and molecular oxygen beams that can be extracted from an Ar / O_2 plasma are given in Fig. 5.3b. Argon was added to the oxygen discharge to act as a good source of electrons for efficient inductive power coupling.

The beam currents on these plots were measured for identical extraction conditions (puller and buncher voltages held constant) over all beam energies with the main beamline transport energy at ~12 keV. As one might expect, the beam current increases with increasing impact energy until a saturation condition is reached. The saturation current depends strongly on the plasma operating conditions and the field strength in the beam extraction region. When the beam energy is lowered below 100-150 eV, the beam current begins to fall off because of excessive space charge spreading during the deceleration step. Higher beam currents overall are possible if the ICP plasma is driven harder and stronger extraction conditions are used. Beam currents below 100 eV can also be increased (up to ~1.5 times) if the decelerator is specifically tuned for stronger focusing action and the steering quad plates directly in front of the target are run significantly positive to pinch the beam inward. The ion fluxes shown for the Ar^+ and O_2^+ beams are at least 1 ML/s (relative to Si) from ~100 eV and up. This current level into a 2 mm spot at such low impact energy represents several orders of magnitude higher arrival rate than any other mass-filtered ion beam source. For reference, electron impact sources typically used for ISS (even without mass filtering) can barely approach 0.01-0.1 ML/s. These sources typically provide up to 100 nA into a beam spot of 1 mm at 1 keV with the spot size becoming significantly larger and beam current smaller as the impact energy is lowered.

High beam currents in the monolayer per second range at low impact energies open up a new realm of experimental possibilities. At these arrival rates, the beam no longer behaves as a passive probe of the surface but can be directly involved in the dynamic evolution of the surface itself. Ion arrival rates are high enough such that the surface can evolve within the time frame of bombardment. These experiments are much more relevant to actual industrial processes like plasma etching or thin film growth than scattering studies conducted at extremely low fluxes. In fact, the development of a dynamic, reactive surface layer (which requires high arrival rate) is the basis of all Si etching technologies (Lieberman and Lichtenberg, 1994). As well, surfaces can behave

very differently at low versus high flux conditions because the turn-over rate of adsorbate species and surface chemical reactions may strongly depend on surface coverage.

5.1.4 Ion Beam Energy Distributions and Energy Tunability

The success of any ion beam scattering experiment relies heavily on a well-defined scattering geometry and incident beams with narrow energy spread if the energy distributions of surface scattered products are to be meaningful. Furthermore, tuning the projectile energy provides a direct means of varying the distance of closest approach (apsis) that occurs during the close encounter between the two colliding nuclei. These two features, tunable energy and narrow width, are fundamental requirements for any ion source and beam system used for scattering studies, especially at low impact energy.

ICP plasma discharges have been shown to have a relatively narrow ion energy distribution function (IEDF) by several different measurement techniques (Edelberg *et al*., 1999; Sobolewski *et al*., 1999). Typical IEDF's are 5-10 eV full width at half maximum (FWHM) with low- or high-energy tails in some cases. However, the ICP plasma has never been used as a beamline ion source before and most of the beamline experience that exists in literature pertains to much higher impact energies (>1-5 keV), where an energy width of 20-50 eV is usually inconsequential. Therefore, we felt that a concrete measure of the beam energy distribution for our plasma-beamline system *at the sample location* was necessary. Just because the ICP can be tuned to give a narrow IEDF, does not mean that the beam hitting the target sample will be narrow as well. Broadening of the distribution due to collisions with background gas atoms during transport or the creation of ions along the beam flight path from collisions with electrode surfaces could potentially pollute the beam hitting the sample. As well, any capacitive coupling in the ICP can cause inherently broad beams because the IEDF in the plasma will become bimodal (capacitive discharges have bimodal distributions). Finally, our technique for adjusting the impact energy, by floating the entire plasma volume above ground with a DC bias, must be tested.

The energy tunability of our ion beamline system was evaluated by measuring the IEDF of the incoming ion beam directly at the target location with the 180° energy sector

analyzer mentioned in Section 4.12.4. A typical energy distribution for both a low and high energy $^{20}Ne^{+}$ beam measured at the target location is given in Fig. 5.4a. The signal intensity represents the output current from the channeltron ion detector in the 180° energy filter as read by a Kiethley electrometer on the channeltron anode. The non-zero quiescent current shown represent the voltage burden on the channeltron bias supply (channeltron is ~5 GΩ). The sector was run in constant acceptance energy (CAE) mode with a pass energy of 15 eV. The ion energy was measured by ramping the retard voltage on the whole analyzer and recording the channeltron output current by computer. This plot shows that the beam energy can be varied easily by increasing the DC voltage on the plasma bias plate. Figure 5.4b gives a blow up of the low energy beam where the measured beam energy width is ~12 eV, showing that the IEDF of the plasma can be transported all the way to the sample without significant broadening. A narrow energy distribution for the incoming ion beam is very important because this ″inherent″ energy width can be comparable to the particle exit energies for the 50-500 eV range. Also, inelastic energy loss mechanisms typically account for <10% of the total loss upon scattering (Rabalais, 2003). Careful measurements of these losses can not be accomplished if the incident beam energy width is too large. Discrete losses during the close encounter may occur but they are overshadowed or ″smeared out″ by an incident energy range that is too broad.

For both beams shown in the figure, the mean ion energy is ~12 eV higher than the DC floating voltage applied to the plasma bias electrode. This floating voltage represents the mean offset from ground of the 13.56 MHz electron oscillation in the plasma. It was measured directly off the bias plate with a calibrated 100X divide oscilloscope probe. The 12 eV difference between the float voltage and beam energy represents the plasma potential for the Ne discharge. Similar plasma potentials in the 10-20 eV range have been measured by other authors with Langmuir probe techniques for inert gas ICP discharges in the 2-5 mTorr range (Hopwood *et al*., 1993). Our beam energy measurement with the axial sector combined with knowing the plasma floating voltage provides an alternate method for estimating the plasma potential.

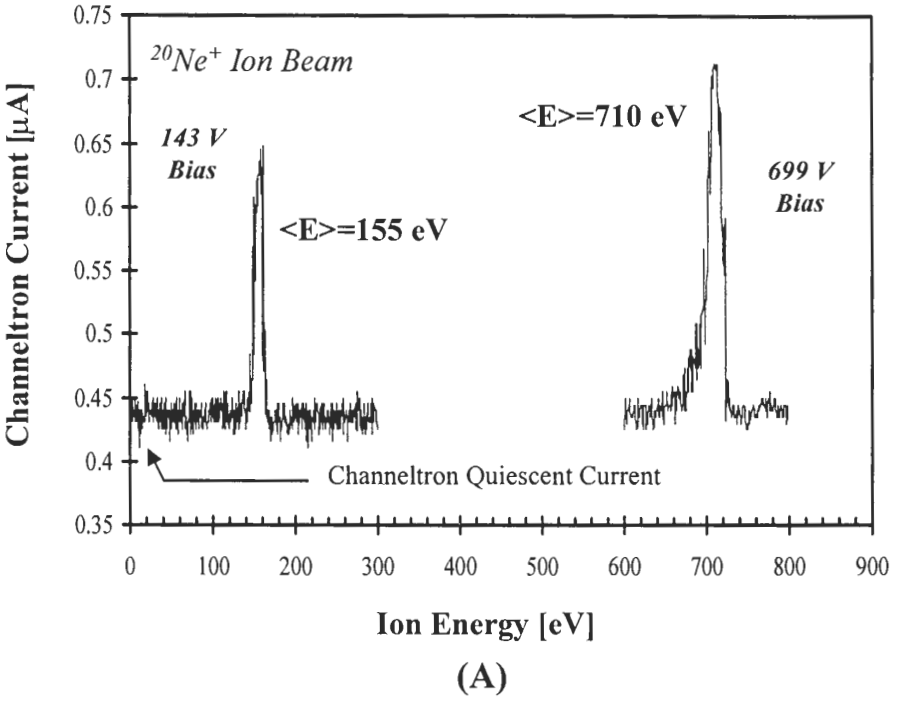

(A)

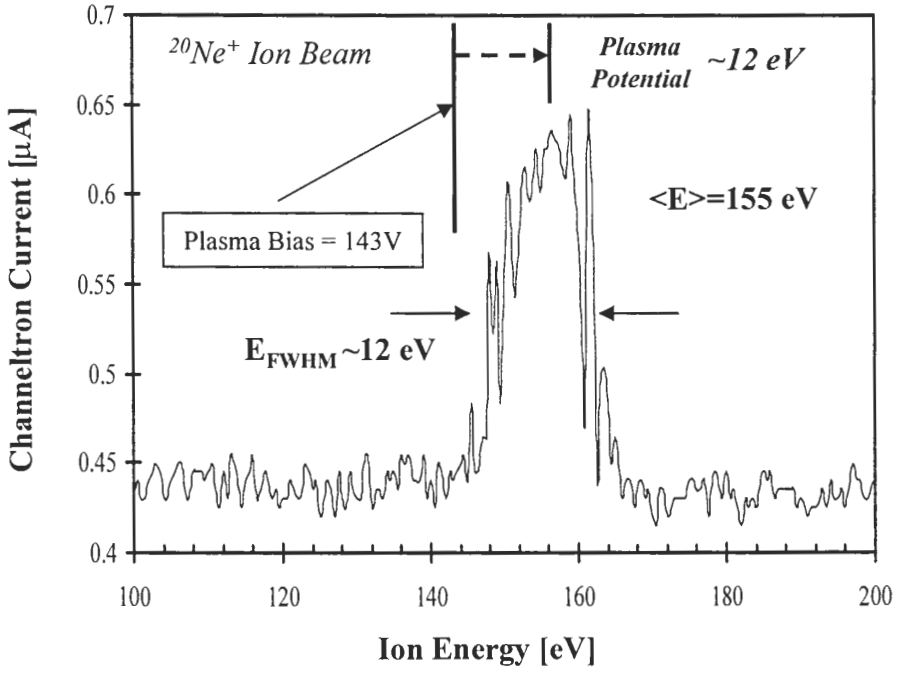

(B)

Figure 5.4: $^{20}Ne^{+}$ beam energy distributions from the axial sector at the target location. (A) low- and high-energy beams and (B) zoom of low energy beam. *Note: Energy scans are raw data from the channeltron running in analog mode with no post-filtering of the electrometer signal. Scans were obtained from a single energy sweep only.*

Other energy distributions measured for Ar^+ and O_2^+ beams are given in Fig. 5.5. These IEDF's are typical for the ion beams used in our scattering studies. Also, the incident beam energies specified in all the experimental plots of our work were directly measured at the target with the 180° sector for each beam scattering condition to provide an absolute energy reference to remove any plasma potential variation. Finally, the presence of high energy species in the beam was ruled out by a simple retarding potential experiment using the target itself at normal beam incidence. The target current was monitored with a floating electrometer and the sample was back-biased with positive voltage. All of the beam current would disappear for bias voltages ~5 V above the mean beam energy as measured by the sector, indicating that no high energy ion species were present in the incoming beam.

5.2 Scattered Product Detector Performance

5.2.1 Introduction

Energetic ion bombardment of a solid sample generates a whole range of particle fluxes leaving the target surface as shown in Fig. 5.6. The major species are sputtered neutrals and secondary ions with kinetic energies of a few eV up to tens of eV. These species are a mix of projectile and target atoms that are generated as result of multiple collisions and sputtering processes. At higher exit energies, surface atom recoils and directly scattered projectiles that survive neutralization or those that are re-ionized on the exit path from the target surface are observed. The energy spectrum of these directly scattered species contains information about single collision processes and the energy losses that can occur during the close encounter between the projectile and target nuclei. The inelasticity in these single collisions can manifest itself as electron excitation of the projectile or target atoms, photon generation, or energetic electron release. A product detection system capable of distinguishing the energy spectrum of many of the species leaving the surface could prove very useful in understanding the fundamental processes occurring on the surface during bombardment.

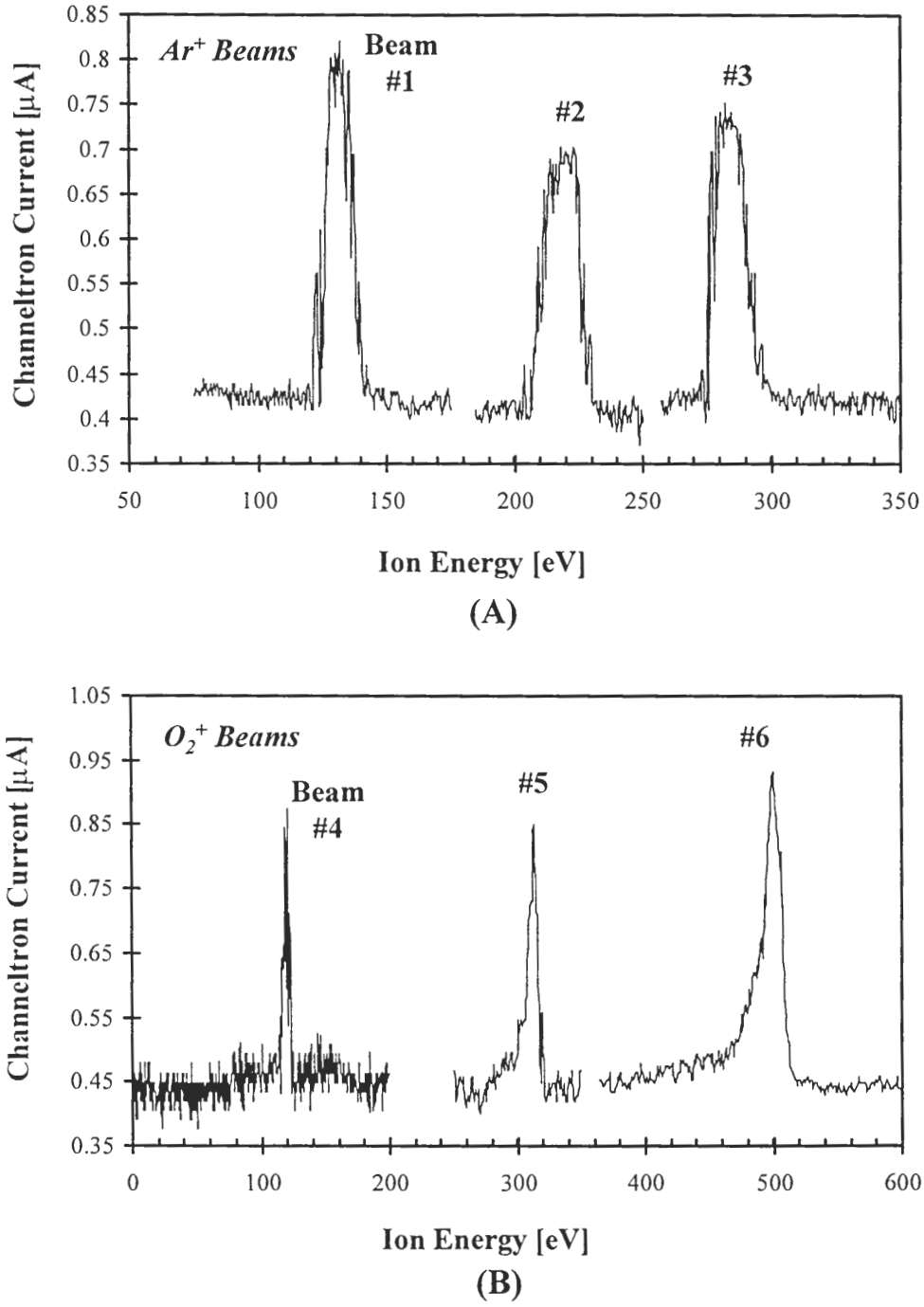

Figure 5.5: Beam energy distributions from the axial sector at the target location for (A) Ar^+ and (B) O_2^+ Beams. *Note: Energy scans are raw data from the channeltron running in analog mode with no post-filtering of the electrometer signal. Scans obtained from one pass only.*

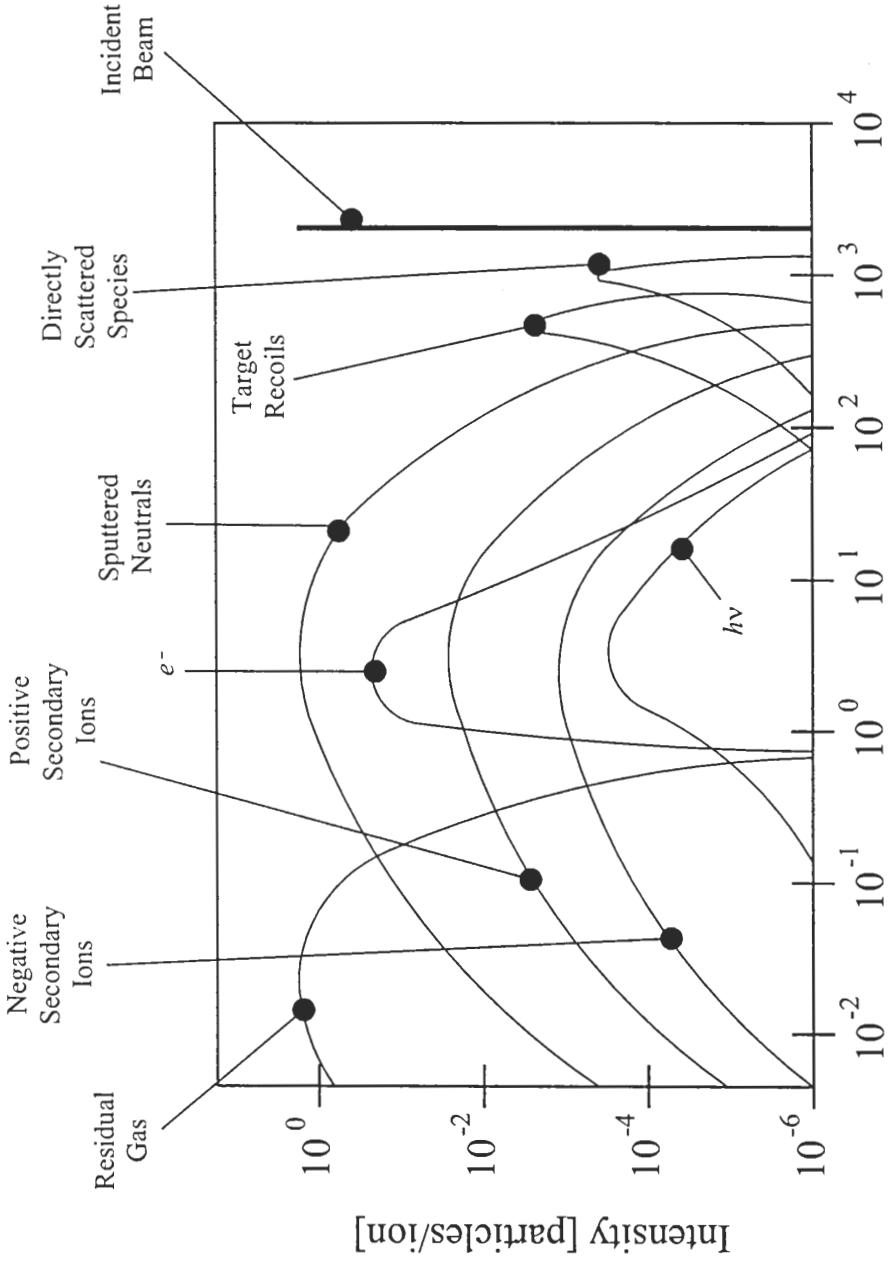

Figure 5.6: Particle fluxes and their representative energies generated by energetic ion bombardment of a solid surface. Adapted from Briggs and Seah, 1992.

We have tried to build such a system to look carefully at the mass and energy spectrum of ion and neutral species leaving the target surface to enable fundamental studies of ion bombardment at low energy. Such broad based detection capabilities required the merging of techniques from energy spectroscopy (like XPS / Auger / ISS) with those of high resolution mass spectrometry into one detection package. As this is very rarely done, some time will be spent here to discuss the operational details of our system. In a later chapter, the necessity of both mass and energy analysis of surface scattered products will be clearly demonstrated in the case study on Ne^+ scattering from light targets (Mg, Al, Si, and Ti).

Our detection system combines an electron impact ionizer, 90° electrostatic sector energy filter, and high transmittance quadrupole mass filter with a very sensitive Daly ion counting system. Its mass and energy resolution depends on the successful mating of the ionizer, sector, and quad through proper electrostatic focusing and ion transport between each section. As well, the linearity and accuracy of the energy scale provided by the sector energy filter must be without question if energy loss measurements are to be made in surface scattering experiments. Specific issues to be addressed include the following:

1) Does the transmittance or peak shape change with ion energy?
2) Can very low energies be measured successfully?
3) Is the energy scale linear and accurate?
4) Is the resolution sufficient for energy loss measurements?
5) How does ionization affect the measurement of kinetic energy for neutrals?
6) Is the detection system sensitive enough to see small neutral signals leaving the target surface?

5.2.2 Ion Transmittance and the Energy Scale

The overall performance of the scattered product detector for ions leaving the target region was evaluated by shooting a K^+ beam with known energy directly into the detector. It has long been known that tungsten wire, when heated above 2000 K, can give

off alkali ions (Craig and Hock, 1980). This occurs because tungsten frequently contains several parts per million (ppm) of alkali impurities (Na, K, Cs) that are difficult to remove in the refining process. At very high temperatures, these alkali ion impurities in the tungsten diffuse out to the surface and ″boil off″ into vacuum with a kinetic energy distribution equal to the filament temperature (~0.1 eV peak at 2000 K).

This technique was used to generate K^+ beams for energy calibration by simply turning the sample heater on the manipulator dock (nude W filament) directly at the first stage skimmer of the scattered product detector. The hot filament acted as a point source of K^+ ions at the target location that effused directly into the detector with a kinetic energy equal to the mean filament potential (plus ~0.1 eV). The kinetic energy of the K^+ beam with respect to ground could be tuned easily by floating the filament power supply common above ground. Figure 5.7 shows the results for the energy scale calibration using three different filament floating voltages of 20, 50, and 80 V. As an added test, a 10 V square wave with 50% duty cycle at 300 Hz was superimposed on the filament floating potential for each case to provide two K^+ beams with an energy separation of 10 eV. For all measurements, the ionizer was off and totally grounded, the sector pass energy was set to a constant 15 eV, and the quad was tuned to K^+ at 39 AMU. The energy analyzer was ramped from 15-45, 45-75, and 75-105 eV in 0.25 eV steps with a counting time of 10 sec per energy step.

As seen in the figure, the K^+ peaks appear exactly where they should on the energy scale with respect to the filament floating voltage and each doublet has a 10 eV peak separation for all three conditions. The shapes of these peaks are symmetric with very narrow (2 eV FWHM) width and full baseline return. Furthermore, the constant pass energy of 15 eV for the sector represents a significantly different retarding field condition for the low versus high energy beams, yet the peak heights and widths are effectively identical. Pushing the K^+ beam energy to several hundered eV gives similar results. The similar peak shape and the nearly equal intensity for low versus high ion kinetic energies show that the retardation lens scheme on the sector inlet provides decent ion transmittance over a wide range of kinetic energies.

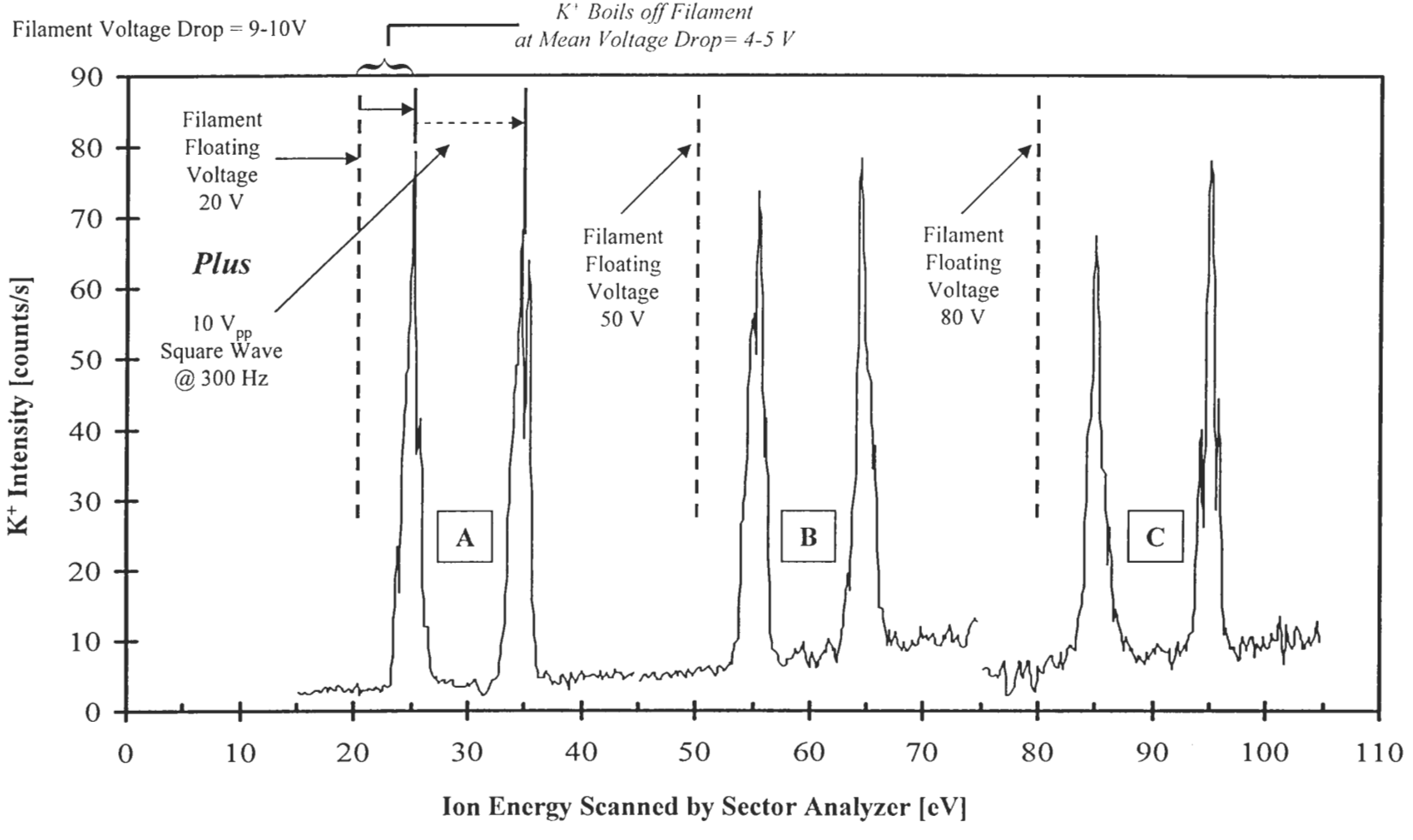

Figure 5.7: Scattered product energy filter performance – K^+ beams from W heater filament on manipulator. Peak sets A, B, and C represent experiments with filament floating voltages of 20, 50, and 80 V.

5.2.3 Neutral Detection

The detection of neutrals leaving a target surface that is under energetic ion bombardment is more demanding than analysis of just the ions. The difficulty arises because neutrals must be post-ionized after leaving the surface and discriminated against residual gas atoms which are ionized as well. The best all-around scheme for post-ionization under UHV conditions is electron impact because it is relatively easy and will always work for any neutral species. Unfortunately, the one drawback to this method is its low efficiency. Even the best electron beam ionizers, running in space charge limited emission mode with 10 mA electron current at 100 eV, can only achieve conversions of about one ion per ~10^4 neutrals (thermal energy neutrals) (Scoles, 1988). Fast neutrals are even harder to detect. Higher velocity results in a lower residence time in the ″active″ ionizing volume where the conversion to ions takes place. Therefore, the detection efficiency for fast neutrals scales inversely with particle velocity, making it more and more difficult as the kinetic energy gets larger.

Fortunately, the inefficiency of ionization can be partially overcome by extremely sensitive ion detection techniques. Also, the preferential sensitivity to neutrals coming from the target surface over residual gas can be accomplished by differential pumping and energy filtering. The signals from residual gas, surface sputtered neutrals, and directly scattered species can be separated based on their very different energy distributions. Residual gas is always present at thermal energies (<1 eV) while sputtered neutrals from the target surface (mostly target atoms) tend to be tens of eV. Directly scattered neutrals (neutralized projectiles) are even higher in energy and occur very near to the energy of directly scattered projectile ions. An effective test of any neutral detection system for surface scattering studies would be the ability to distinguish these three energetically different exit channels.

The neutral detection capabilities of our system were evaluated by looking for directly scattered Ar^0 from Ar^+ bombardment of Ag at 100 eV impact energy. Results of this experiment are shown in Fig. 5.8. Energetic Ar neutrals are formed from single collision binary events of Ar^+ projectiles with Ag target atoms that are neutralized along the incoming or outgoing portion of the trajectory in the near surface region.

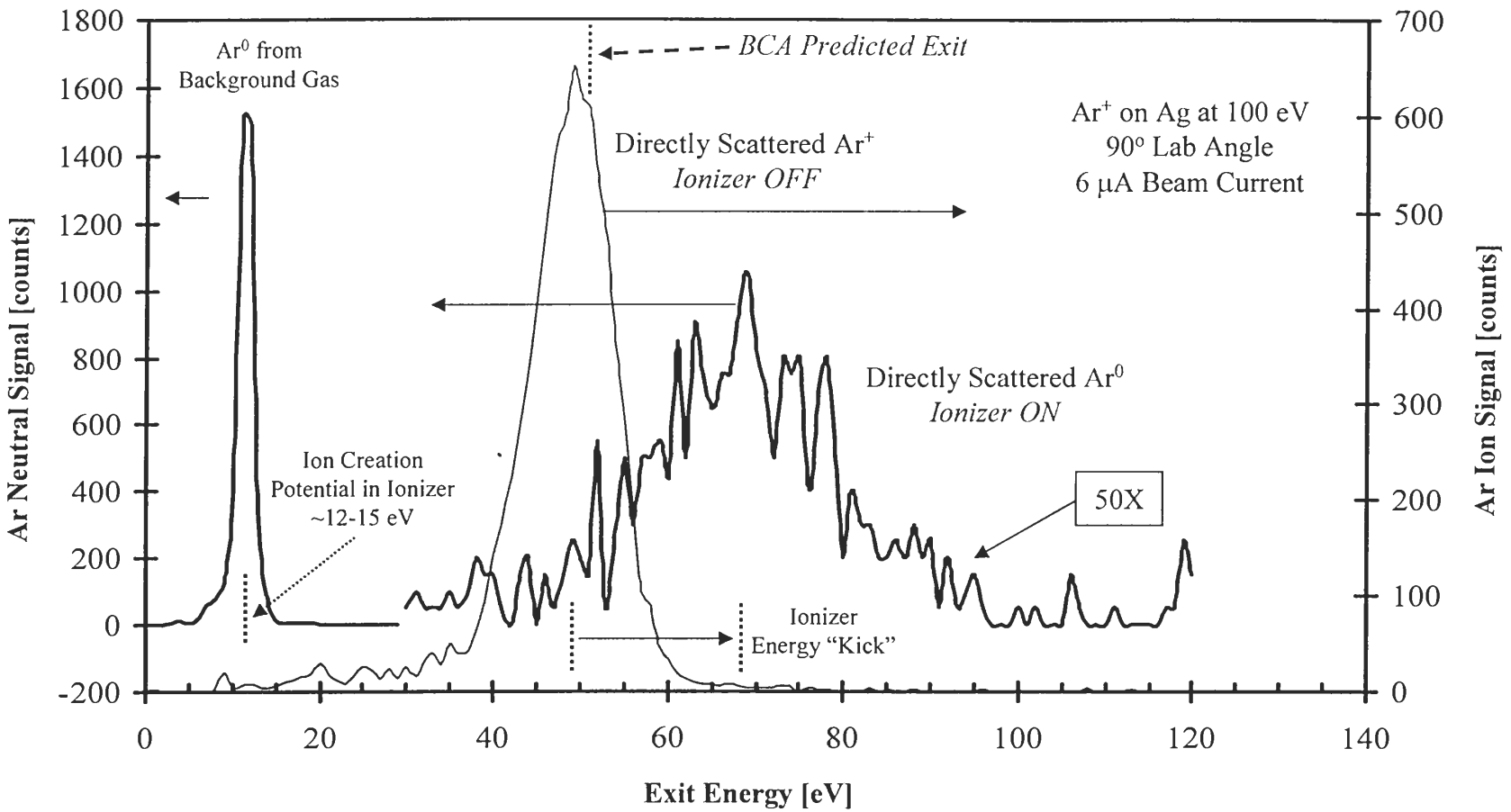

Figure 5.8: Energy scans of Ar^0 and Ar^+ exit channels from Ar^+ scattering off Ag at 100 eV. Neutrals were detected with the ionizer at 2.0 mA emission current with 70 eV electron energy. The capacitor ion deflector in the first pumping stage was set to +200V to deflect all the Ar^+ leaving the target during the neutral scans. Note: The directly scattered Ar^0 scan has been multiplied by 50. Also, the noisiness of this peak occurs because the scan was acquired in only one energy pass.

Two-electron, Auger-type processes are considered the most likely candidates for Ar^+ projectile neutralization. The high ionization potential of the rare gases usually preclude direct resonant tunneling processes, so neutralization usually occurs through Auger events (Rabalais, 2003). The fast ion exit channel most likely comes about from projectiles that are neutralized along the incoming path, followed by re-ionization in the hard collision or exit trajectory. This neutralization followed by re-ionization is believed to be the operative mechanism because rare gas ions have very high neutralization rates on metal surfaces (Rabalais *op. cit.*). Therefore, the majority of energetic projectile species leaving the target surface should be neutral rather than charged (Lipinsky *op. cit.*; Rabalais *op. cit.*). However, the low detection efficiency for fast neutrals (maybe 1 in 10^5-10^6 because they are fast) makes the scattered flux distribution appear as though directly scattered projectile ions are the dominant exit channel.

In Fig. 5.8, single collisions of Ar^+ with the surface result in a large fast scattered ion signal near 44 eV. This energy represents the single scattering events that occur in one binary collision where the energy transfer can be approximated by the BCA framework. The kinematic factor for Ar^+ on Ag for a 90° scattering angle is ~0.46, which would predict a 46 eV exit energy for the 100 eV incident projectile. Also shown are the neutral signals, with one large peak at low energy along with a much smaller, broad Ar^0 peak occurring near 65 eV. All neutral scans were conducted with the capacitor ion deflector in the first pumping stage set to +200 V to prevent any charged species from ever reaching the detector. The ionizer was run at 2 mA electron emission current with 70 eV electrons and the quadrupole was locked at 40 AMU with ~1 AMU pass mass width.

The large Ar^0 peak at low energy represents the residual gas background that is ionized near the 15 V grid potential of the electron impact ionizer. The ~3 eV shift to lower energy occurs because of the space charge potential depression created in the ionizing volume by the high electron emission currents (2 mA) (UTI, 1992). The 65 eV neutral peak can be attributed to directly scattered projectiles that are neutralized along the incoming or outgoing scattering trajectory by the Ag surface. This peak is shifted upward by 15-20 eV from the directly scattered ion peak because the ionizing volume of the ionizer is run 15 V above ground. When fast neutrals enter the ionizer, they are given

a ″kick″ in energy the moment they are converted to ions by electron impact due to the 15 V accelerating field. A question may arise why the Ar^0 exit kinetic energy is not exactly equal the Ar^+ exit energy taking into account the 15 eV kick. The fast neutrals seem to appear ~ 3-5 eV faster than the directly scattered ions. The offset probably occurs because the electron friction associated with the incoming and outgoing trajectories is charge state specific (Neilhus *et al*., 1993). It has also been shown by Xu *et al*. (1998) that the continuous loss, as represented by the Oen and Robinson formula (Eqn. 2.22), depends on the particle charge state. They find that their $Ne^+ \rightarrow Si$ energy loss data requires a larger fitting coefficient in the Oen and Robinson loss formula for the Ne^{++} exit channel than for Ne^+. This suggests that the continuous loss on the +2 ion is greater than that for the +1 ion. Therefore, it is not unlikely to expect that the loss associated with an Ar^0 exit would be smaller than for Ar^+. Thus, the neutral exit (taking into account the ionizer 15 eV kick), should be slightly faster than the ion.

The neutral experiments conducted with our scattered product detector indicate that having an energy filter between the ionizer and the rest of the detection system can be successfully used to separate residual gas neutrals from those originating from the target. In addition, the peak energy positions of both the ion and neutral signals can be identified and make good sense when the operation of the detection system is clearly understood. As well, the detection of neutrals generated at the target surface has been demonstrated, suggesting that scattering experiments with reactive systems (where most of the reaction products are neutral) will be possible.

6. BCA Validity at Low Impact Energy

6.1 Is BCA Valid at Low Energies?

Low energy noble gas ion scattering has been used for many years to determine surface composition and structure (Czanderna and Hercules, 1991). It is based on the model of binary elastic collisions between the projectile ion and target atoms where the energy transfer during the collision can be sufficiently described by the classical principles of energy and momentum conservation. The energy of the observed peaks in the ion scattering spectra can be directly correlated to the mass composition of the surface through the well know scattering relation mentioned earlier in Chapter 2:

$$E_{exit} = \frac{1}{(1+\gamma)^2}\left(\cos\theta_L + \sqrt{\gamma^2 - \sin^2\theta_L}\right)^2 E_0 \qquad (6.1)$$

where,

E_0, E_{exit} = incident and scattered projectile energies
γ = target-to-projectile atomic mass ratio
θ_L = scattering angle in the lab frame

An important fundamental question in ion scattering and the BCA view of collision phenomena is the validity of this relation when the impact energy is lowered. Application of the BCA model to ISS (ion scattering spectroscopy) experiments with He^+ projectiles has been extremely successful for keV energy ranges (Czanderna *op. cit.*; Nielhus *et al.*, 1993). In fact, energy transfer measurements for He^+ scattering off clean metal surfaces under UHV conditions often provides a convenient means of calibrating the energy scale of the product energy filter or accurately measuring the scattering angle (MacDonald and O'Conner, 1983; Neilhus *op. cit.*). Systematic studies of scattering phenomena involving heavier inert ions at lower impact energies have not been widespread. However, a few experiments of Ne^+ and Ar^+ scattering have been performed to specifically test the validity of the BCA model.

Prior Tests of BCA Validity

The following results have been reported for Ne^+ and Ar^+ projectiles on heavy targets in the hyperthermal energy range (<500 eV) for incident angle ϕ and scattering angle θ_L :

Ne^+ on Metals

Studies conducted by Tongson and Cooper (1975) have shown that Ne^+ scattering on polycrystalline Cu for $\left(\phi = 45^\circ, \theta_L = 90^\circ\right)$ follows binary collision theory to a remarkable degree for E_0 values all the way down to 20 eV. The work of Taglauer and Heiland echoes this same behavior for Ne^+ on Ni (100,110) and Ag (poly) at $\left(\phi = 30^\circ, \theta_L = 60^\circ\right)$. The BCA model described these collisions down to 45 eV for Ni (Taglauer and Heiland, 1972) and 100 eV for Ag (Heiland and Taglauer, 1976), respectively. Their data shows scattered ion energy peaks which can be attributed to both single collision events and multiple collision phenomena that yield higher than BCA exit values.

In contrast, the $Ne^+ \rightarrow$Ag (poly) work of MacDonald *op. cit*. shows a ″significant departure″ from BCA predictions at all energies (100-2000 eV) for the $\left(\theta_L = 30^\circ \rightarrow 120^\circ\right)$ range tested. They conclude that there is an inelastic loss mechanism which shows an impact parameter dependence. This energy loss was associated with the ion passing through the electron gas ″selvedge″ at the surface because of the path length dependence of the loss.

Very recent work by Tolstogouzov *et al*. (2001) for Ne^+ on polycrystalline Pt and Au have given ″reasonable″ agreement with BCA values above 200 eV, but the deviation from BCA becomes more and more significant as the impact energy is lowered to 40 eV. In general, lower incident energies resulted in more energy transfer to the target atoms and smaller than expected exit energies.

Ar^+ on Metals

Energy loss measurements for Ar^+ projectiles below 1 keV are very rare. One study of Ar^+ on Ni (110) by Heiland *et al*. (1973) from 300-1200 eV shows a complex mix of scattered projectile energy peaks, both above and below the BCA predicted values. This suggests that the energy of backscattered particles cannot, in general, be interpreted in terms of single binary collisions. The authors go on to say that multiple binary events can only explain *some* of the scattering events observed. It was also found that the intensity of the scattered ion peaks was dose dependent, indicating that the surface must be changing during bombardment. They conclude that sputtering and generation of surface imperfections by binary collisions influence the binding forces and inelastic interactions between the ions and lattice atoms. As a result, BCA events are hard to single out.

Quite the contrary, Ar^+ scattering on Cu (poly) by Hart and Cooper (1979) has shown that there is no systematic deviation from the BCA prediction down to an incident energy of 25 eV. The authors point out an uncertainty of up to 20% in evaluating the kinematic factor for the low energy data near 25 eV, but they do not provide any reasoning for the textbook-like agreement between experiments and BCA predictions. Likewise, Smith and Goff (1969) have stated that the $Ar^+ \rightarrow Cu$ (single crystal and poly) system could be described by the binary model down to 100 eV.

Commentary

In summary, it is not clear from a survey of literature that the applicability of the BCA model to hyperthermal energies has been well established. All of the aforementioned studies were conducted with different scattering geometries, detection techniques (magnetic versus electrostatic sectors), and target samples (single crystals versus polycrystalline). As well, we note that scattering experiments are often lacking when it comes to a convincing treatment of experimental uncertainties. Some of the previous studies offer no solace in this regard. It is well documented from studies at higher impact energies that accurate determinations of projectile energy, scattered ion

exit energy, and scattering angle are difficult ─ energy loss measurements strongly depend on these parameters (Neilhus *op. cit.*). Assessing the errors in these three parameters in low energy work is even more important. Therefore, it is hard to ascertain if the observed deviation between experimental scattering data and BCA predictions in the hyperthermal range is real, specific to each projectile-target combination, instrumental, or a combination of all three.

Specifically, we want to know how our scattering system fairs in the discussion of BCA predictions at low energy. In addition, we must establish how much to trust the BCA model as the platform for later discussions on energy loss measurements and inelasticity determinations. With so many experimental issues involved in making correct inelasticity evaluations (known scattering angle, accuracy of energy measurements for projectile and scattered ion, beam alignment and focusing, analyzer sensitivity, *etc.*), we would like to have an appreciation for how our system performs overall.

We have taken the approach of trying to fill in the gap between 50-500 eV for Ne^+ and Ar^+ projectiles on a variety of target materials. Our ion beamline system and scattered product detector with energy filtering capability seem well suited for such a task. The intent of these experiments will be to compare ion scattering spectra for Ne^+ and Ar^+ projectiles on the same target materials under the same scattering conditions to investigate potential deviations from the BCA model. It is very important to us to examine how well our measurements fit the BCA model or not ─ in an effort to establish how much to trust our scattering measurements in Chapter 7.

We will cast our scattering results in light of a proper assessment of experimental uncertainties to examine BCA predictions at low energy as well as document the performance of our entire scattering system. The experiments in this chapter will focus on Ne^+ and Ar^+ scattering off several heavy targets from Ge to Pb to probe a variety of target-to-projectile mass ratios from 1.8 to 10.3. The results concentrate on those projectile-target systems where single binary collision peaks can be clearly seen in the scattered ion energy spectrum. In addition, since our scattering angle is fixed at 90° with a specular reflection geometry, the importance of changing inelastic losses with different incident angles will be avoided (see Chapter 7 for more discussion). This chapter will

also discuss the experimental conditions used for all scattering studies presented here and in Chapter 8 with respect to beamline operation, sample preparation, and error analysis procedure.

6.2 Experimental Aspects

The scattering studies presented in this chapter and Chapter 8 were conducted in our ion beamline system using pure ion beams of $^{20}Ne^{+}$ and $^{40}Ar^{+}$ projectiles. Experiments were conducted with Mg, Al, Si(100), Ti, Ge(111), Ag, Au, and Pb targets to span a wide range of target-to-projectile mass ratios. The ion beams were generated from Ne plasma discharges (13.56 MHz) at 600W and 5 mTorr or Ar at 500W and 2.5 mTorr. The beamline was operated with ~14 keV ion transport energy and typical beam currents at the target were 0.5-5 μA for $^{20}Ne^{+}$ and ~5 μA for Ar^{+} at impact energies ranging from 50-400 eV. Some of the Ne^{+} data in Chapter 7 on Mg, Al, Si, and Ti targets was pushed to higher impact energies with 1300 eV being the maximum energy tested. The lab scattering angle of our system was fixed at 90°.

All target materials were degreased and ultrasonically cleaned with organic solvents followed by sputter cleaning with Ar^{+} from a hollow cathode ion gun at ~5 keV and 20-30 μA for 5-15 min. Some samples were also annealed during bombardment to 400 °C for extra cleaning power. Cleanliness of the samples was checked periodically by SIMS using the sputter ion gun in a focused mode with the scattered product detector in mass sweeping mode for 5-10 eV secondary ions leaving the target surface. A few alkali impurities (Na, K) were seen on some samples initially which were removed by sputter cleaning. All of the target samples were metal films 0.005” to 0.030” thick with at least 99.9% purity (Mg and Ti). The other metal targets were 99.99% or better and the single crystals were B-doped Si(100) (~10 ohm-cm) and undoped Ge(111) (the undoped Ge was quoted by the manufacturer as n-type with ″low″ resistivity).

The incident beam energy distributions were measured at the target location using the 180° electrostatic sector analyzer for each projectile incident energy. The analyzer pass energy was set to 15 eV for constant acceptance energy (CAE) mode operation. The peak centroids of these energy distributions served as the mean incident beam energy for

calculation and plotting purposes. Scattered ion energy distributions were obtained with the ionizer grounded and electrostatic sector set to 15 eV pass energy for a corresponding 15 eV ion flight energy through the quadrupole over all scanned exit energies. Most distributions were taken with 0.5 or 1 eV energy steps in one pass with 500 ms dwell counting time used for each step.

6.3 Model Predictions and Error Analysis

The applicability of the BCA model to capture experimental trends requires an adequate analysis of experimental uncertainties in any scattering system. Measurement errors in the projectile incident energy, scattered ion energy, and scattering angle can all affect the accuracy of energy loss data and ultimately the interpretation of BCA validity. We have chosen to present our scattering data in a form which clearly shows how BCA model predictions are affected by experimental measurement errors in the three aforementioned parameters. All the scattering data is presented as plots of the scattered projectile exit energy for the single collision peak versus impact energy with their associated error bars. The predictions from the BCA model are shown on the plots as an envelope of expected exit energy values derived from Gaussian error propagation of Eqn. 6.1 based on uncertainties in E_0 and θ_L.

The maximum error in the predicted exit energy given by the BCA model can be derived assuming a normal distribution of measurement errors:

$$\Delta E_{exit} = \sqrt{\left[\Delta E_{exit}\left(\Delta E_0\right)\right]^2 + \left[\Delta E_{exit}\left(\Delta \theta_L\right)\right]^2} \tag{6.2}$$

where,

$\Delta E_{exit} =$ maximum error in exit energy from BCA prediction

$\Delta E_{exit}\left(\Delta E_0\right) =$ partial error connected with uncertainty in incident energy, E_0

$\Delta E_{exit}\left(\Delta \theta_L\right) =$ partial error connected with uncertainty in scattering angle, θ_L

The partial errors are derived directly from the BCA model functional dependency using the standard method of partial derivatives. For our system with 90° scattering angle, these expressions become:

$$\Delta E_{exit}\left(\Delta E_0\right) = \frac{\gamma - 1}{\gamma + 1} \tag{6.3}$$

$$\Delta E_{exit}\left(\Delta \theta_L\right) = \frac{-2E_0\sqrt{\gamma^2 - 1}}{\left(\gamma + 1\right)^2}\Delta \theta_L \tag{6.4}$$

where,

$\Delta E_0 =$ raw measurement error in incident energy, E_0
$\Delta \theta_L =$ raw measurement error in scattering angle, θ_L
$\gamma =$ target-to-projectile mass ratio

Examining Eqn. 6.4 shows that the overall expected error in exit energy depends directly on the incident energy and gets worse with increasing impact energy. The experimental plots for each projectile-target pair include lines representing the BCA prediction errors propagated as above, along with error bars on the experimental data points for ΔE_0 and ΔE_{exit}.

We have taken the approach of conservative estimates for ΔE_0, $\Delta \theta_L$, and ΔE_{exit}. All experimental plots were made with an estimated maximum error in the incident energy of ±10 eV, scattering angle error of ±1° max, and ±5 eV in the exit energy measurement. Values for the energy measurements are certainly much better than ±10 eV and ±5 eV (as shown in the Chapter 5), but we have chosen a maximum upper bound which would cover every one of our scattering experiments. As well, the scattering angle must be better than ±1° because the entire scattered product detector was machined to align properly from the start. In addition, the beam flag with 2 mm aperture in front of the target was laser-aligned with the take-off trajectory defined by the skimmers of the scattered product detector. These values were chosen to give a feeling for how much error is usually associated with scattering measurements and its influence on any model validation. Most authors do not mention the importance of such an analysis, but we think it is warranted in any model validation study.

6.4 Scattering Results

The scattering studies in this section were carried out with $^{20}Ne^{+}$ and $^{40}Ar^{+}$ projectiles on Ge(111), Ag, Au, and Pb. These projectile-target pairs represent systems were the energy spectrum of scattered projectile ions is dominated by single collision phenomena. As such, the scattered energy spectra are quite clean with a clearly identifiable BCA-like peak. For example, a raw energy distribution for $^{20}Ne^{+}$ scattered off polycrystalline Ag at 155 eV is shown in Fig. 6.1. The accompanying incident energy distribution of the Ne^{+} beam measured by the 180° sector at the target location is also shown.

Each of the four targets listed above will be discussed in the following sub-sections to highlight important features seen in the raw scattering spectra. Also, plots of the mean exit energy versus impact energy along with BCA predicted values are given to summarize all the scattered energy distributions on one convenient graph for comparison of Ne^{+} and Ar^{+} on the same target.

6.4.1 Germanium

Scattered ion spectra for low- and a high-impact energies are shown in Fig. 6.2 for Ne^{+} and Ar^{+} scattering off Ge(111) at 90°. The ISS spectra contain only one ion exit peak which tracks upward in energy with increasing projectile incident energy. This peak appears near the location expected for a single collision event that is predicted by the BCA model for a single deflection of the projectile by a Ge target atom. The ion exit peak widths are inherently wide because Ge has five natural isotopes from 70-76 AMU, three of them being major: ^{70}Ge (20.5%), ^{72}Ge (27.4%), and ^{74}Ge (36.5%) with ^{73}Ge and ^{76}Ge at ~7.7% each. This isotope split from 70-76 AMU causes an inherent scattered ion energy line width of no less than 8.2 eV (11.3 eV) for Ne^{+} (Ar^{+}) at 300 eV. The isotopic line width grows significantly to ~28 eV for Ar^{+} at the highest incident energy tested (750 eV). The appearance of clear shifts due to each Ge isotope should be observable if there were no loss mechanisms in the collisions. Indeed, this is not the case, so the isotope effect manifests itself as a ″smearing″ of the fine structure in the exit energy spectrum.

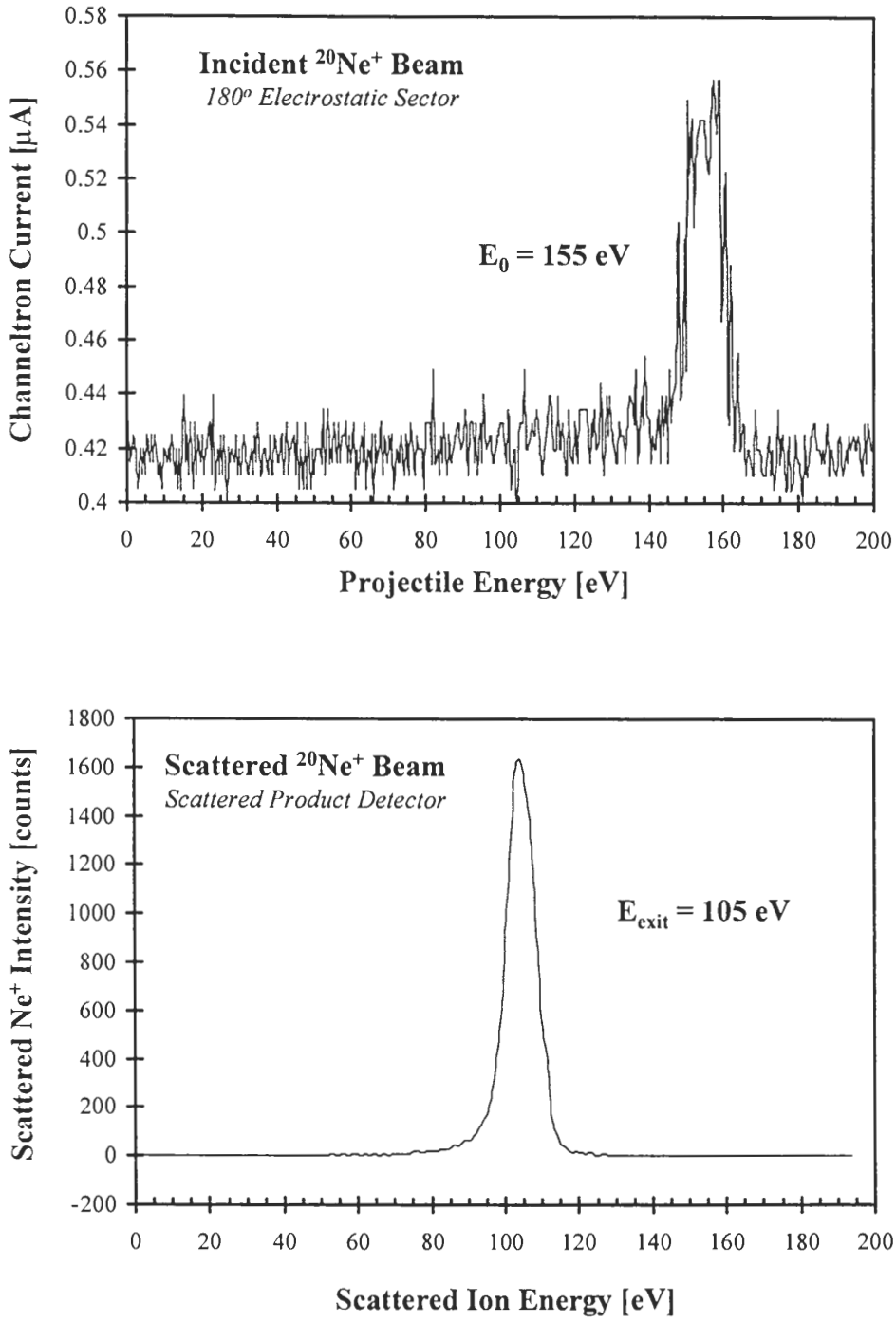

Figure 6.1: Incident and scattered ion energy distributions for 155 eV $^{20}Ne^+$ on polycrystalline Ag at 90° lab scattering angle. Note: the incident beam energy spectrum is choppy due to analog operation of the channeltron detector and no post-filtering of the electrometer signal.

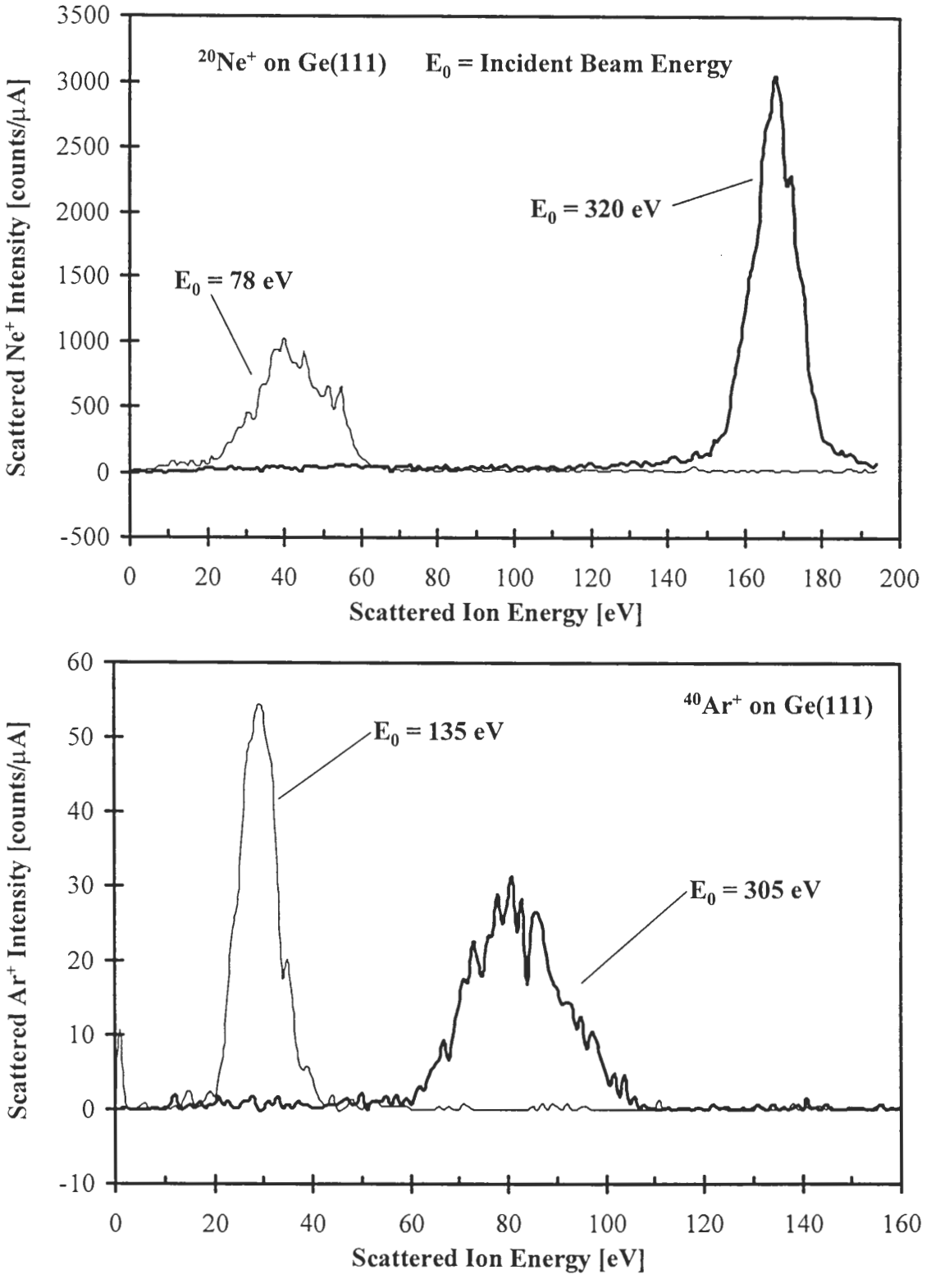

Figure 6.2: Scattered ion energy distributions for Ne^+ and Ar^+ on Ge(111) at different incident beam energies. The Ne^+ scans are for 78 and 320 eV incidence while the Ar^+ scans are shown for 135 and 305 eV incidence.

This issue clearly demonstrates why $^4He^+$ is used at 1-5 keV for surface compositional analysis in ISS. The light He^+ projectile mass causes a much larger kinematic factor difference for nearby isotopes and the shift gets larger for larger target mass. As well, the 1-5 keV impact energy provides better mass resolution because nearby isotopes are separated more in the ISS spectrum.

At low impact energy, Ne^+ scattering is dominated by a rather broad BCA peak of moderate intensity. However, when the impact energy is raised, single collision events become much more well-defined yielding a narrow and more intense Ne^+ exit peak. Scattering of Ar^+ exhibits somewhat the opposite behavior with increasing incident energy, but the Ar^+ peaks will certainly get more broad at higher energies due to the Ge isotope effect. In that case, Ge is not such a good target material for BCA validations, but it is one of the lowest mass, single crystals available which gives BCA-like peaks for both Ne^+ and Ar^+ at 90° scattering angle.

It should be pointed out that the scattered ion intensities for Ne^+ versus Ar^+ are quite different. The ion survival rate for Ne^+ scattering is some 60 times greater than that for Ar^+ as shown in the plot. Depending on the projectile-target pair, higher energy experiments have shown the ion yield can increase with increasing energy as well as decrease (Neilhus *op cit*.). Auger neutralization (AN) of the projectile on the incoming or outgoing trajectory should favor a higher neutralization rate for a slower velocity approach or exit (Rabalias, 2003). The transition rates for AN depend exponentially on the ion-surface distance and the exact electron density distributions of projectile and target (Rabalais *op. cit*.). For the same impact energy, the Ar^+ minimum approach distance is longer and the ion velocity is ~1.4 times slower than for Ne^+, therefore, more neutralization of Ar^+ is expected. The Ne^+ data does seem to echo this trend, but the Ar^+ does not as a general rule. Collisions of Ar^+ are certainly expected to be more violent than for Ne^+, causing more lattice damage and sputtering of Ge target atoms. In fact, the sputtering yield of Ge by Ar^+ is about twice that for Ne^+ in the 100-500 eV range (Wehner *et al*., 1962). Therefore, ion surviving collisions seem more probable in the Ne^+ case with less target damage than for Ar^+.

One subtlety in the Ar^+ spectra should be mentioned. In many of the Ar^+ cases, a small constant energy peak at ~2 eV was seen that did not occur for Ne^+. Although this

peak is rather small, its continued appearance in many Ar^+ spectra suggests that it is real. The low energy peak occurs near 2 eV, irrespective of the incident projectile energy. A peak of this type has been seen before in higher energy scattering (~2.5 keV) of Ar^+ and Kr^+ off Mo and Ti (Wittmaack, 1996) as well as Ne^+ off Al at 1.5 keV (Tolstogouzov *et al*., 2001). Wittmaack has hypothesized that this constant energy peak at 0-2 eV is perhaps caused by two sources. First, the ionization processes leading to this peak occur as a result of collision phenomena between two projectile species (Ar-Ar) or between the projectile and re-emitted Ar atoms from the target. There is evidence that implanted Ar atoms are released from the surface by diffusion (Menzel and Wittmaack, 1985) with energies near 0.2 eV (van Veen *et al*., 1986). These re-emitted Ar atoms participate in charge exchange processes with incoming projectiles. The second potential source of this peak is ionization due to gas phase interaction of two re-emitted gas atoms that are released in an excited state. The low impact energies where the 2 eV peak is observed for Ar^+ seem to suggest that in our system, charge exchange is not the likely culprit, because high impact energies are needed for these processes to occur.

A summary of the scattering results on Ge(111) for Ne^+ and Ar^+ are shown in Fig. 6.3 for comparison to BCA predicted values. The limits of uncertainty in the BCA model predictions as derived in Section 6.3 are shown as dashed lines above an below the solid BCA curve. Error bars are shown on the experimental data points for measurement uncertainties in the incident and exit energy. For the Ge case, it seems as though the experimental data gives a consistently lower exit energy than predicted, as indicated by the negative intercepts of the regression lines through the experimental points. The Ar^+ data begins near the BCA line, but a deviation occurs as the energy is raised above ~150 eV to give a nearly constant offset for higher impact energies.

Lower than BCA values can imply sub-surface scattering as well as a hard collision inelastic loss. The presence of what looks to be a constant offset between the measured exit energy and the BCA predicted value would seem to point more toward a fixed inelastic loss that occurs during the hard collision. The expected exit energy from the BCA prediction, adjusted for inelastic energy losses along the incoming and outgoing trajectory paths as well as a fixed loss during the hard collision was derived earlier in Chapter 2 for 90° scattering angle:

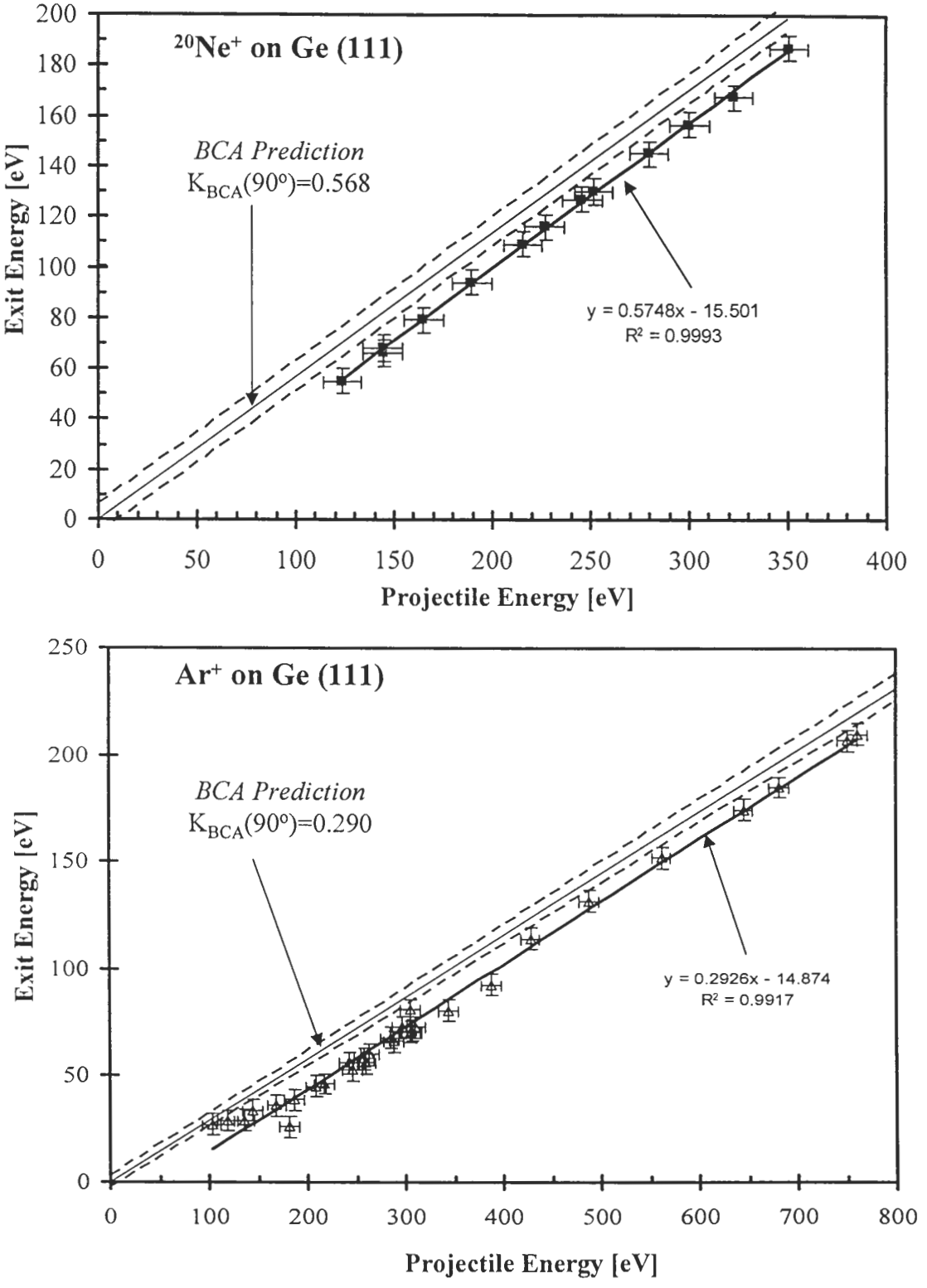

Figure 6.3: Exit energy vs. incident projectile energy for (A) $^{20}Ne^+$ and (B) $^{40}Ar^+$ on Ge(111).

$$E_{exit} = \frac{\gamma - 1}{\gamma + 1}\left(E_0 - Q_1\right) - \frac{\gamma}{\gamma + 1}Q_{bin} - Q_3 \tag{6.5}$$

where,

$E_0, E_{exit} =$ incident and scattered projectile energies
$\gamma =$ target-to-projectile mass ratio
$Q_1, Q_3 =$ energy loss along incoming (1) and outgoing (3) paths
$Q_{bin} =$ inelasticity occurring during the hard collision

Since we are more interested in the magnitude of the binary inelastic loss at this point (we will calculate the continuous loss carefully in Chapter 7), consider an approximation to Eqn 6.5. The energy loss along the incoming path Q_1 is quite small (a few volts maybe) compared to E_0 (at least 100 eV), therefore, Eqn. 6.5 does not change much if Q_1 is simply eliminated. Next, assume that Q_3 is small or at the least does not vary too much over the range of exit energies. Then, the scattering data could be reasonably approximated by a straight line whose slope is equivalent to the BCA kinematic factor and negative intercept which includes an inelasticity in the hard collision:

$$E_{exit} = \frac{\gamma - 1}{\gamma + 1}E_0 - \frac{\gamma}{\gamma + 1}Q_{bin} \tag{6.6}$$

The data in Fig. 6.3 seem to fit this simple model rather well with a slope dependency that is nearly identical to the BCA predicted value, along with a sizable negative intercept. The intercept values are -15.5 eV (Ne^+) and -14.9 eV (Ar^+), which are equivalent to losses of about 19.8 eV (Ne^+) and 23.1 eV (Ar^+) using Eqn. 6.6. These hard collision losses, if anything, are larger that the actual values because we did not remove the continuous straggling loss on the incoming and outgoing paths. The fact that these offsets from the BCA are so discrete suggests that atomic transitions of some kind are involved. However, the low collision energies where the offset begins would tend to

discount such transitions (see the discussion in Chapter 7). We will mention later in Chapter 7 that in many cases, the current picture of ion-solid collisions involves neutralization of the projectile before the hard collision. Therefore, the hard collision loss could be attributed to one-electron transitions of the neutralized projectile (to re-ionize so we can detect the scattered ion) or perhaps electronic excitation of the target atom. We should point out that ~20 eV is close to the range of the first ionization potentials for $Ne^0 \rightarrow Ne^+$ (21.6 eV) and $Ar^0 \rightarrow Ar^+$ (15.8 eV). However, when we compare the Ge scattering data to some of the metals to follow, we become puzzled because no constant offset is typically seen. At this time, we are unsure exactly why the offset occurs for Ge.

6.4.2 Silver

A summary of the scattering data measured for Ne^+ and Ar^+ off polycrystalline silver is given in Fig. 6.4. Silver has an almost equal distribution of two isotopes: ^{107}Ag (51.8%) and ^{109}Ag (48.2%). The agreement of Ne^+ data with pure no-loss BCA predictions is excellent. This same behavior for the Ne^+-Ag system was seen by Heiland and Taglauer, (1976) down to 100 eV impact energies as mentioned earlier. The Ar^+ energy data shows more scatter and it is questionable if a clear deviation from BCA exists. Silver has an extraordinarily large sputtering yield of about 2 atoms per incident Ar^+ at 300 eV impact energy (Wehner *op. cit.*). Perhaps this high yield results in a damaged surface layer which could ″smear″ out the BCA single scattered peak through inelastic processes associated with the ion traversing the damaged layer. The Ar-Ni results of Heiland *et al*. (1973) echo this type of behavior for Ar^+, but we do not see deviations from the BCA model which are that significant.

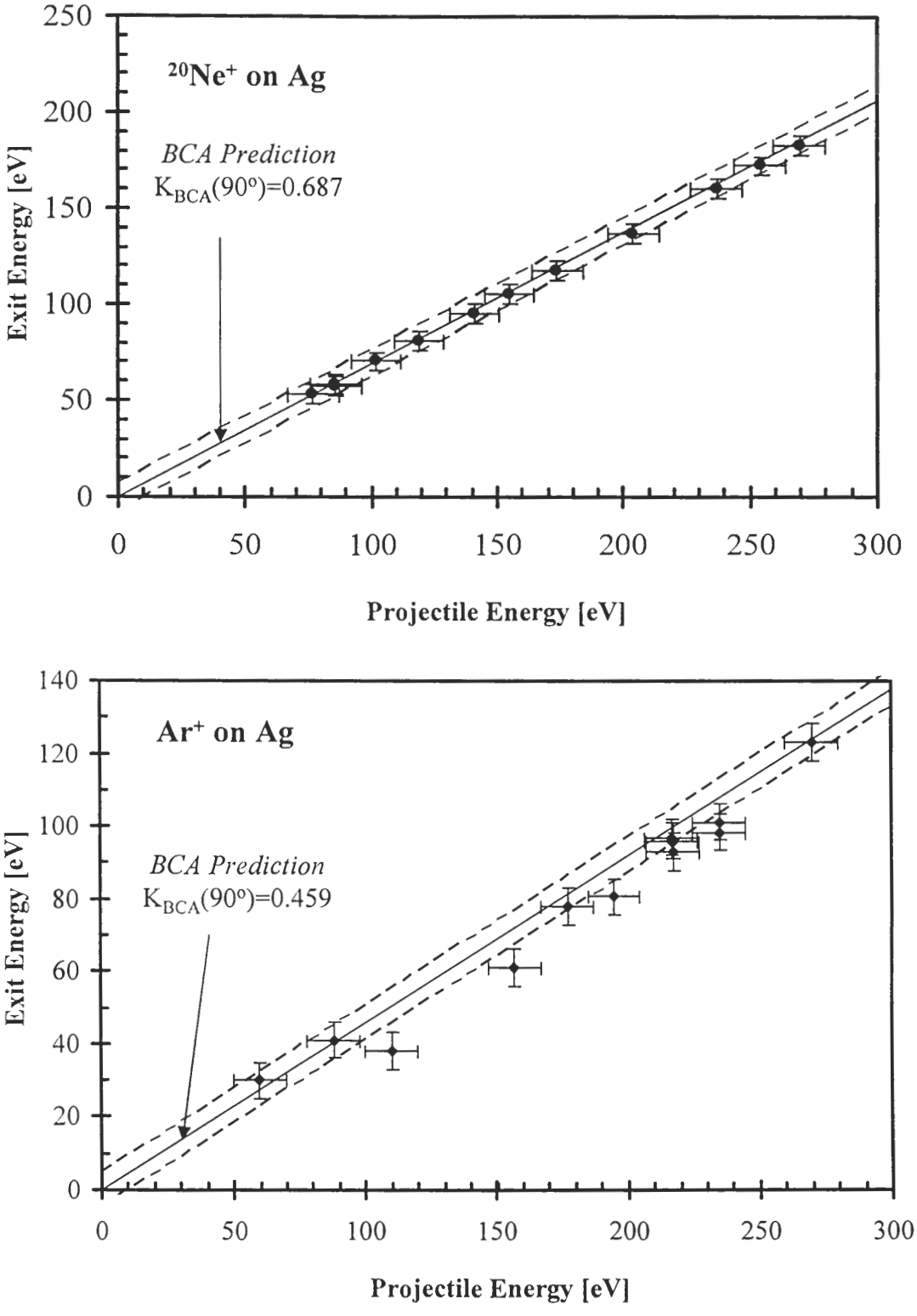

Figure 6.4: Exit energy vs. incident projectile energy for (A) $^{20}Ne^+$ and (B) $^{40}Ar^+$ on Ag.

6.4.3 Gold

Gold is very nice target material for ISS studies with heavier projectiles because it has only one isotope at 197 AMU. This provides a nice, narrow-width scattered ion peak that is not inherently broadened by any isotope effect. A summary of scattering results for Ne^+ and Ar^+ on Au is shown in Fig. 6.5. The agreement of both data sets with no-loss BCA predictions is quite good. However, the Ne^+ exit seems to be a few volts high in most cases while the Ar^+ is slightly lower than BCA values. Both are well within the maximum expected error for BCA predictions.

Gold, like Ag, has an extremely low sublimation heat, making the sputtering yield quite high (~0.7 atoms/Ne^+ and ~1.7 atoms/Ar^+ at 300 eV) (Wehner *op. cit.*). For this reason, ion bombardment above tens of eV will result in efficient sputtering of target atoms and an overall "stirring" of the surface atomic layers. One would expect such a damaged surface layer to scatter incoming ions from the top as well as deeper layers. Such a phenomenon would most likely result in scattering from several layers simultaneously where the incoming projectile could suffer losses as it proceeds through the top layers to eventually scatter from lower layers. As such, the BCA single collision peak should show this ″straggling″ and exhibit tailing on the low energy side. A scattered ion energy distribution for Ne^+ on Au at 215 eV and Ar^+ at 240 eV are shown in Fig. 6.6.

The BCA peak in the Ne^+ spectrum shows a clear, low energy fronting that is indicative of subsurface scattering. This phenomena has been observed before for the Ne^+-Au system at impact energies of 1 keV and up (Tolstogouzov *op. cit.*). The Ar^+ scattered ion spectrum does not show this same low energy fronting to the BCA peak. The very low ion yield of directly scattered Ar^+ (~12 counts/μA) shows that neutralization of the incoming projectile is extremely efficient on the Au surface. As such, any subsurface scattering, if it does occur, most likely results in a neutralized Ar exit which is not registered in ion counting mode. Also consider that the importance of subsurface scattering in the $Ne^+ \rightarrow$Au case is minor, perhaps 1/10th of the peak BCA intensity at the most. A corresponding signal level for any subsurface scattering in the Ar^+ case could very well be below the detection limit.

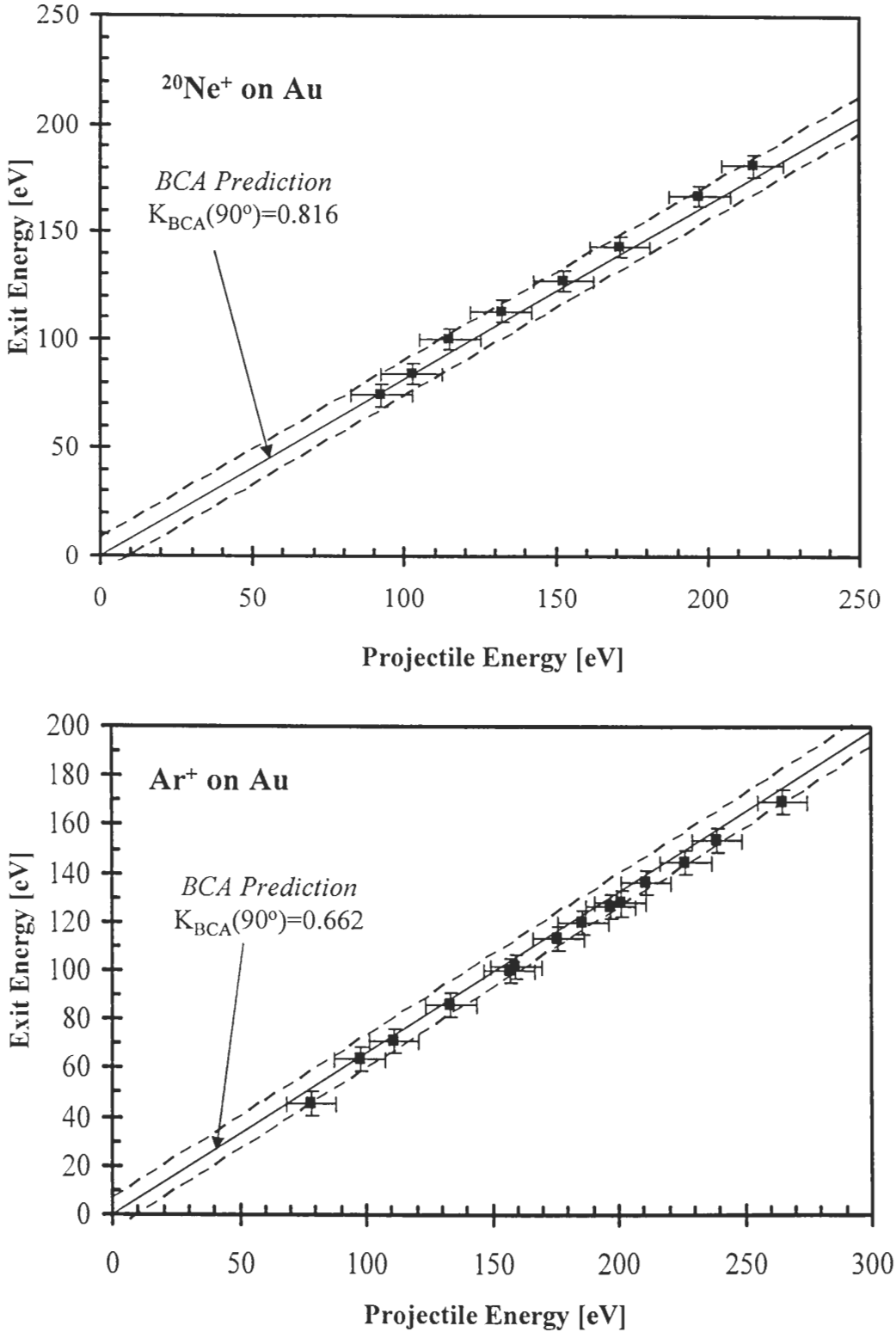

Figure 6.5: Exit energy vs. incident projectile energy for (A) $^{20}Ne^+$ and (B) $^{40}Ar^+$ on Au.

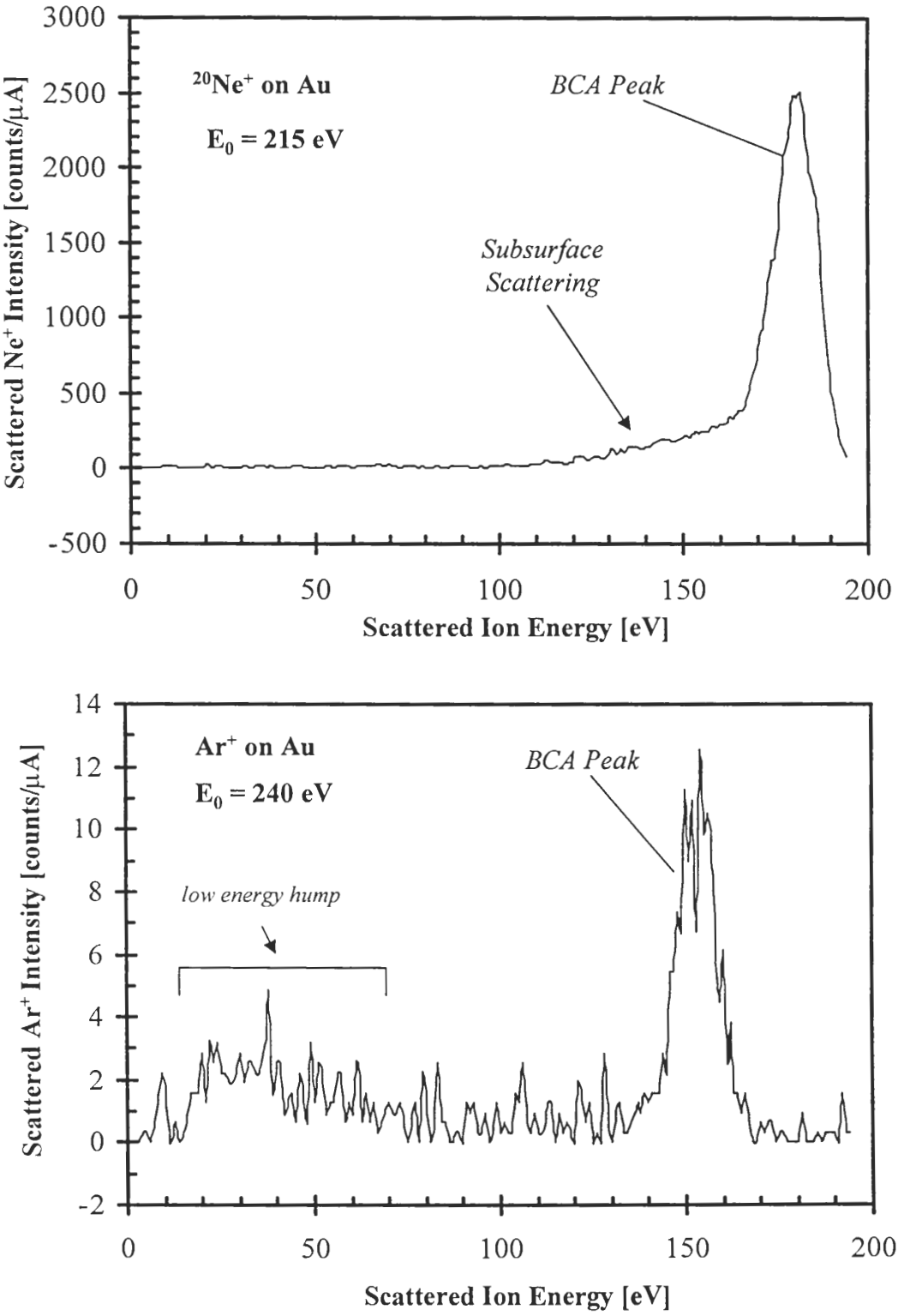

Figure 6.6: Scattered ion energy distributions for $^{20}Ne^{+}$ and $^{40}Ar^{+}$ on Au.

There is one broad, very low intensity ″hump″ in the $Ar^+ \rightarrow Au$ spectrum, whose origin is unknown. Since the center of the hump is near 30 eV, it is doubtful if this peak arises from the same source as the 2 eV Ar^+ peak as discussed in the Ge case. It may be possible that this signal is connected with re-emitted Ar^0 atoms that are sputtered from the surface by the incoming beam, eventually being ionized through a gas-gas collision or by secondary electrons released from the surface.

6.4.4 Lead

Lead was the highest mass target tested in all of the scattering studies. It has four natural isotopes: ^{204}Pb (14.8%), ^{206}Pb (23.6%), ^{207}Pb (22.6%), and ^{208}Pb (52.3%). Summary plots of Ne^+ and Ar^+ are given in Fig. 6.7 with BCA model predictions for comparison. For the Ne^+ case, agreement with no-loss BCA is good with some of the measured exit values on the high side of the BCA line. The huge mass disparity in the collision $Ne^+ \rightarrow Pb$ system results in a projectile exit energy that is nearly equal to the incident beam energy. Ar^+, on the other hand, shows exit energies that are lower than BCA for most incident energies. The sputtering yield of Pb is lower than that of Au, but the energetic Ar^+ projectile most certainly damages the surface. Unpredictable losses associated with the projectile traversing a damaged surface and scattering from several top layers simultaneously may be the culprit for the lower than BCA values. Of course, this possibility would seem to be of much less importance for Ne^+ because of its smaller momentum and size.

As with the $Ne^+ \rightarrow Au$ case, Ne^+ on Pb results in the same subsurface scattering and low energy tailing on the front side of the BCA single collision peak. The Ar^+ data on Pb also shows a slight low energy tailing, in contrast to the Au case. This is apparent in the scattered ion energy spectrum because the ion yield of Ar^+ on Pb is nearly 40 times higher than for Au. A comparison of Ar^+ on Au at 250 eV and Ar^+ on Pb at 225 eV with the ion yield normalized by the incident beam current is given in Fig. 6.8.

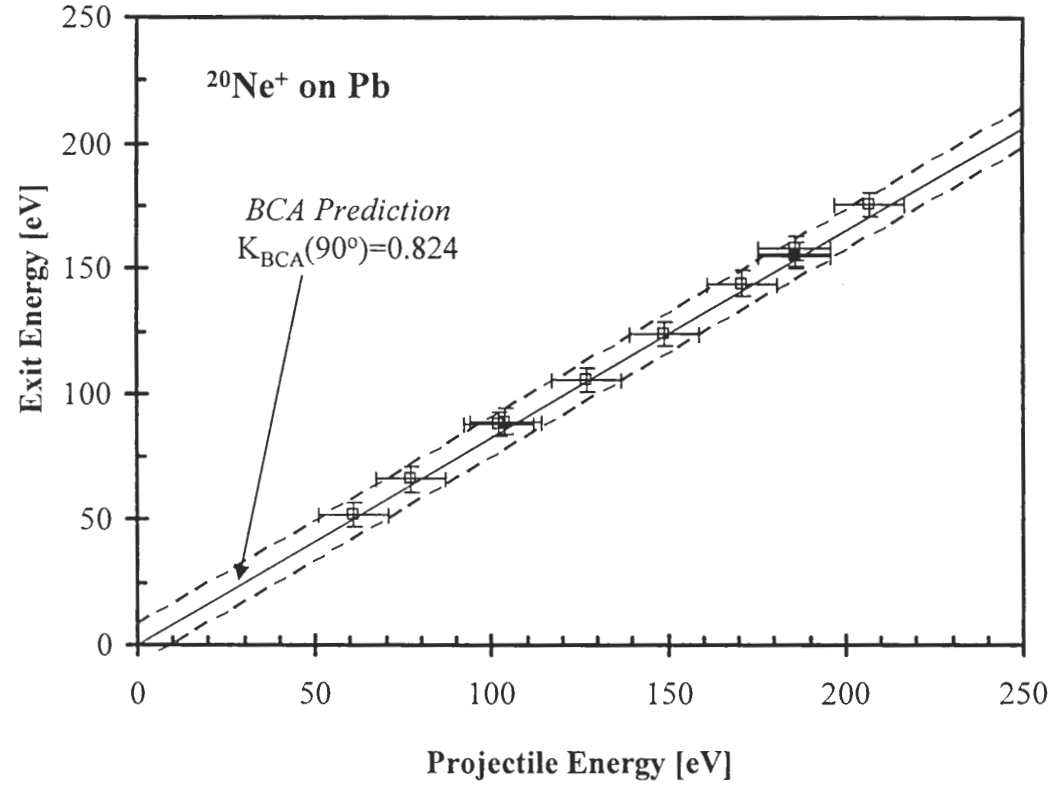

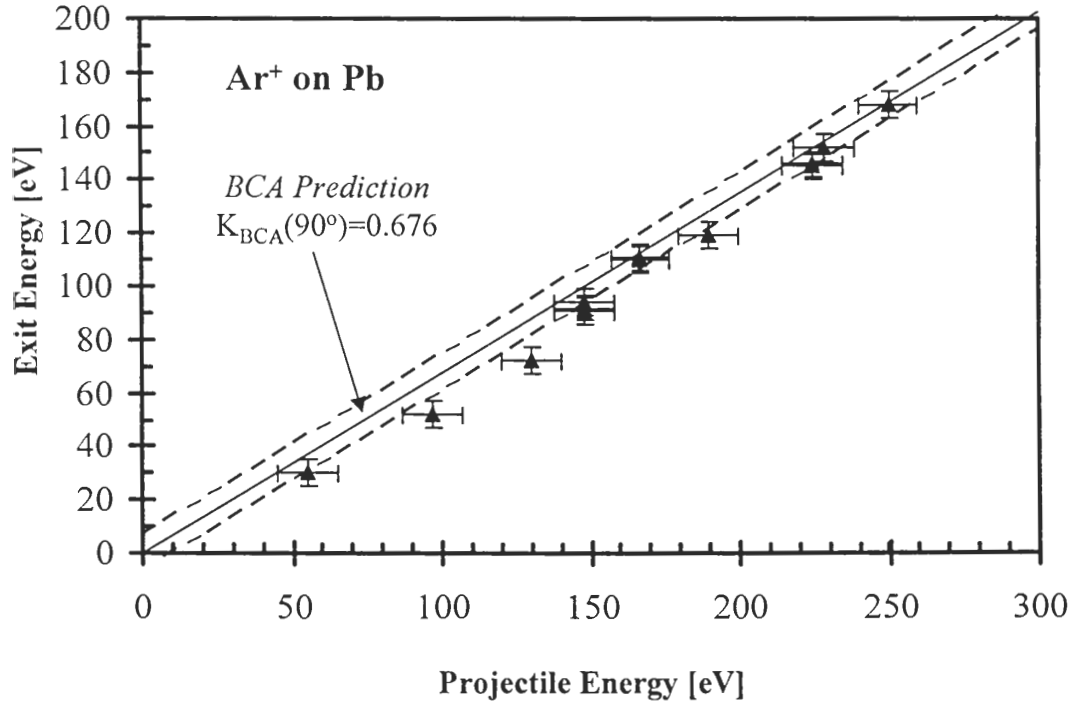

Figure 6.7: Exit energy vs. incident projectile energy for (A) $^{20}Ne^+$ and (B) $^{40}Ar^+$ on Pb.

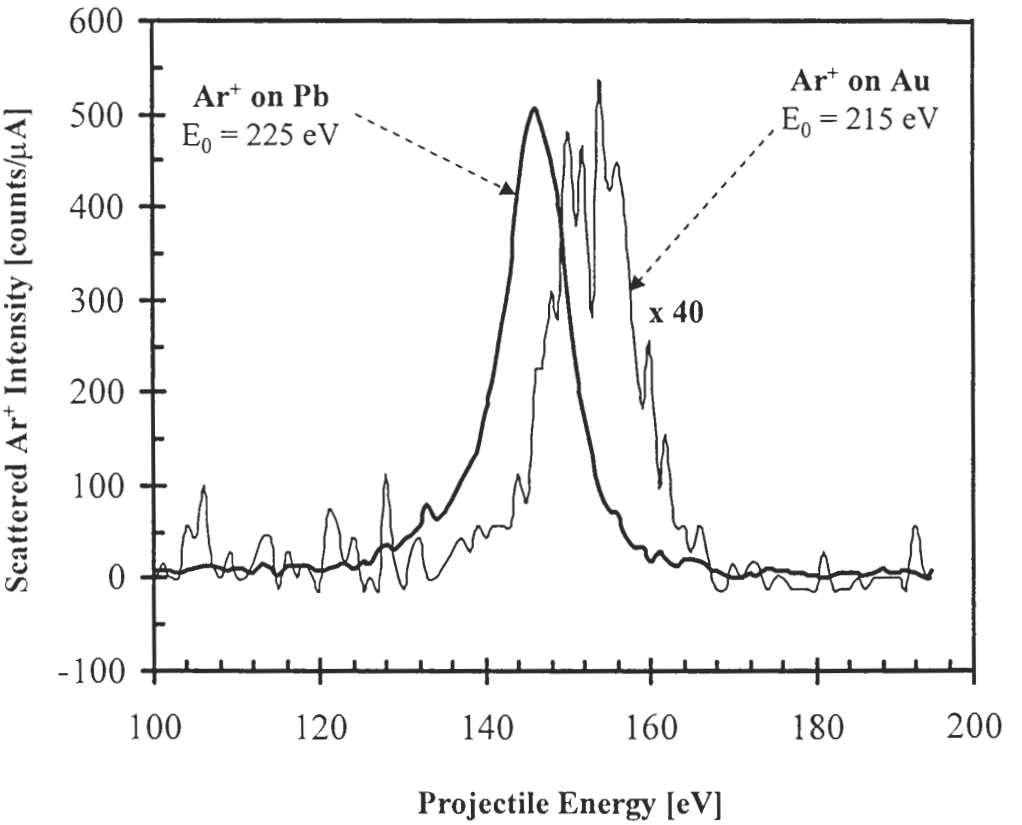

Figure 6.8: Scattered ion energy distributions for Ar^+ off Au and Pb showing the large difference in ion yield. The $Ar^+ \rightarrow$Au data has been multiplied by 40 to show on the same scale as $Ar^+ \rightarrow$Pb.

6.4.5 The Master Curve

A summary of all the kinematic factor (K-factor) assessments for Ne^+ and Ar^+ scattering off the four targets (Ge, Ag, Au, and Pb) is given in Fig. 6.9 as a ″master curve″ of K-factor versus target-to-projectile mass ratio. It is hard to say what the proper way to calculate the overall K-factor for the experimental data would be, given possible inelastic losses. In addition, some of the experimental data show deviations from a linear dependence of exit energy on incident energy which makes it difficult to establish an overall K-factor. In an effort to summarize the data, we have chosen to allow for inelasticity in the hard encounter and ignore electron friction losses on the incoming and outgoing trajectory paths. Therefore, the experimental K-factor is just the slope of the best fit regression line put through the E_{exit} versus E_0 data for each projectile-target combination. All regression lines for the K-factor fits to experimental data have correlation coefficients (r^2) greater than 0.978. The BCA model prediction is shown in the figure as the solid curve. This data presentation method is somewhat misleading because it removes any K-factor dependency on the incident energy for different energy ranges (if there is one). The reader should reference each of the individual E_{exit} versus E_0 plots. The conclusion from such an analysis is that the scattered projectile energy most certainly varies in a linear way with respect to incident energy. In addition, if we lump any inelasticities into the hard collision, the BCA model predicts the energy transfer dependency reasonably well at low impact energies (< 500 eV) for the Ge, Ag, Au, and Pb targets tested.

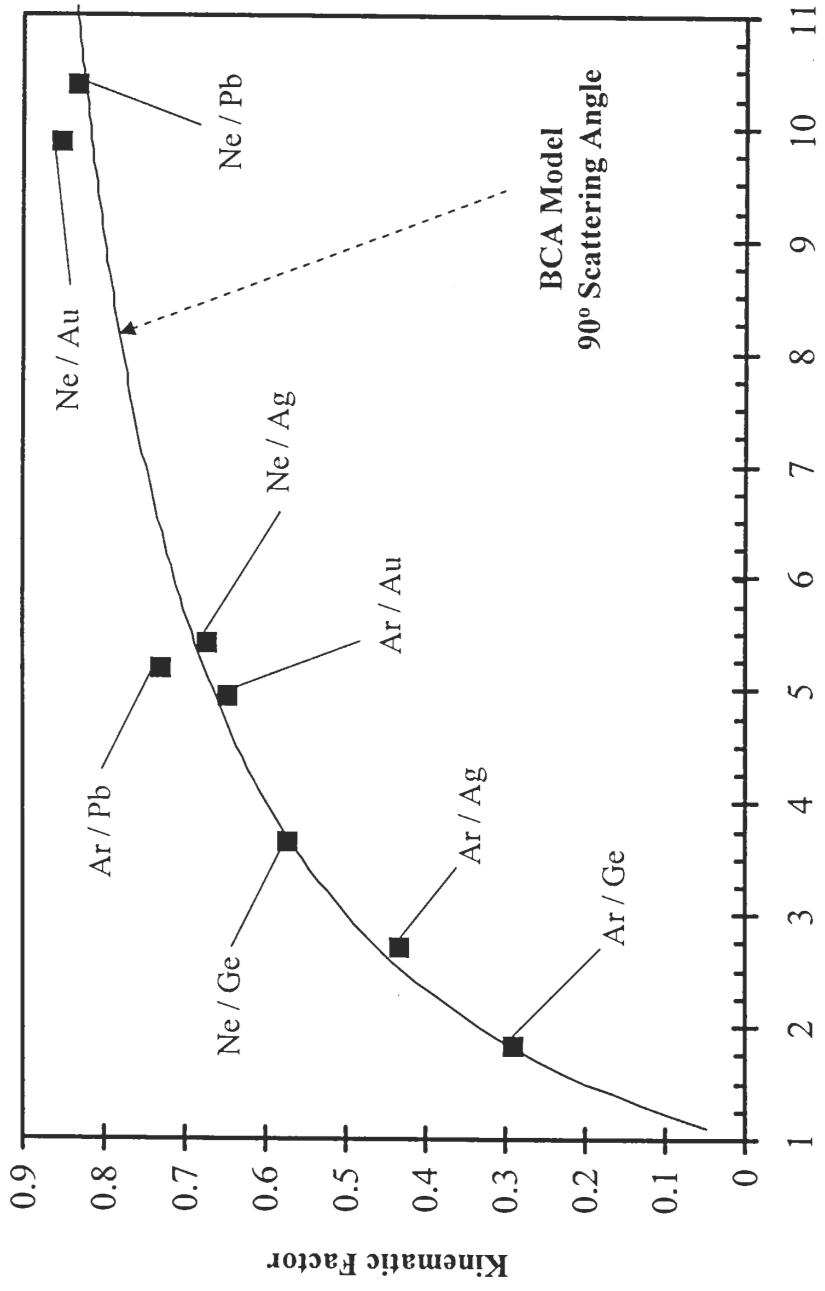

Figure 6.9: Experimental kinematic factors for $^{20}Ne^{+}$ and $^{40}Ar^{+}$ scattering at low energies.

6.5 Summary

One of the main driving forces behind the Ne^+ and Ar^+ scattering studies presented in this chapter was to demonstrate the performance of our ion beamline and scattered product detector system in its entirety. As well, a cursory goal was to perhaps add to the discussion of single collision phenomena at low impact energy where scattering phenomena are more nebulous. Most certainly, a detailed evaluation of BCA model validity with inert ions should be conducted in an ISS system with high resolution energy filter that can be rotated around the target. In this way, the scattering angle can be varied to probe multiple bouncing phenomena and ion neutralization channels which depend on the particle trajectory length in the near surface region. Our ion beamline and scattering system was designed for an entirely different purpose in mind. However, several conclusions about the scattering studies mention in this chapter can be made.

As a general rule, the lighter the projectile, the more closely the experimental data follows BCA predictions under 500 eV. We know that He^+ fits the BCA model exceptionally well (Czanderna *op. cit.*; Nielhus *op. cit.*). Our Ne^+ studies show experimental data with less scatter, more linearity, and better consistency with BCA single collision predictions than Ar^+. This statement is consistent with the picture that Ar^+ damages the target surface more than Ne^+ from momentum arguments alone, making it more probable that the incoming projectile will suffer losses in traversing the upper atomic layers of the target. In addition, Ar^+ and Ar^0 have a much richer distribution of lower energy excited states than Ne^+ or Ne^0, which may favor small losses to electronic excitation in Ar more so than Ne. From a simplistic point of view, the kinetic energy of the projectile seems like it should be more easily accommodated into electronic excitations of Ar^0 or Ar^+ due to the availability of more energetically lower electron states.

Next, the measured exit energies for single collision scattering events are quite close, but slightly less than BCA values in most cases. This implies that the collisions in the 50-500 eV range are indeed quite binary in nature for ion exit channels. Multiple bouncing phenomena, giving a higher than BCA exit energy, were not seen in any of our scattering experiments at 90° lab angle for the Ge, Ag, Au, and Pb targets. Also, the

scattered ion yield at 90° for Ne^+ was usually much greater than Ar^+ for most impact energies and targets tested.

Finally, we have seen mixed results for Ar^+ scattering which puts our scattering work somewhere in the middle of the debate on BCA validity for Ar^+. As mentioned earlier, both textbook-like agreement as well as significant deviations from single collision phenomena have been documented for Ar^+ below 500 eV. In some cases, like Au and Ge (with inelasticity offset), the BCA predictions are right on for our experimental data, while other targets give more data scatter and less than BCA values on average. Perhaps single collision events with Ar^+ are mediated by damage to the target surface which affects the incoming or outgoing ion trajectory. This phenomenon would, of course, depend on the specific target material and how easy the target is to sputter.

From an equipment standpoint, the entire ion beamline and product detector system have demonstrated their performance in an actual ion scattering experiment. Noble gas ion scattering on metals at low energy is dominated by high neutralization rates (at least Ar^+) for the projectile ion because Auger transition rates depend exponentially on the ion approach or exit velocity perpendicular to the surface (Neilhus *op. cit.*). Low impact energy greatly increases the probability for ion neutralization. Our product detector system has shown clean spectra, easily identifiable BCA-like scattering peaks, and high signal to noise for these low ion survival rate surface collisions. The system has also shown that mass-filtering, in addition to energy analysis of the ion flux leaving the target surface, can significantly clean up the scattered ion spectrum so that peak assignments are easy and subtle features like sub-surface scattering can be seen.

7. Ne^+ Scattering off Light Targets

7.1 Historical Perspective of Ne^+ Scattering

Collision studies and cross-section measurements with energetic Ne^+ projectiles on static or molecular beam gas targets were first conducted 30-40 years ago (see Barat *et al*., 1970). In many cases, the scattered ion energy spectrum exhibited a remarkable richness which could be attributed to discrete electronic excitations of the collision partners during the close encounter. For instance, the ion energy spectrum for the $Ne^+ \rightarrow Ne$ system at 2.5 keV and 3° lab angle from Barat *op. cit* shows multiple inelastic peaks below the BCA value which can be directly identified with specific electronic excitations of the collision partners. As an example, excited neutrals and ions, as well as singly and doubly excited autoionizing states, can be formed during the collision through one- and two-electron transitions:

$$Ne^0 \rightarrow Ne^*\left(2p^5 - 3s, 3p\right) \text{ at 16-19 eV loss} \tag{7.1}$$

$$Ne^0 \rightarrow Ne^{**}\left(2s^2 2p^4 - 3s^2, 3s3p, 3s3d, 3p^2\right) \text{ at 45-52 eV loss} \tag{7.2}$$

$$Ne^+ \rightarrow Ne^{+*}\left(2p^4 - nl\right) \text{ or } Ne^{+**}\left(2s2p^4 - nln'l'\right) \text{ at 40-60 eV loss} \tag{7.3}$$

This type of behavior served as the experimental basis for charge exchange processes that are commonly understood in terms of the quasi-molecular mechanism known as the Fano-Lichten-Barat theory discussed in Chapter 2 (Fano and Lichten, 1965; Barat and Lichten, 1972).

Many systems such as $Ne^+ \rightarrow$Ne, Na, Mg, and Al have been investigated in the gas phase along with the reverse collisions Na^+ and Mg^+ on static Ne in the keV impact energy range (for a review, see Massey and Gilbody, 1974). Clear inelastic losses and multiple peaks in the energy spectrum can be seen in many instances that are attributable to specific electronic excitations. Since these phenomena were seen in the gas phase, experimenters turned to ion-solid scattering studies to probe whether or not the same

behavior could be seen off a surface. The same type of behavior was indeed shown to occur in ion-solid collisions, along with a few surprises.

In general, surfaces tend to ″spoil″ some of the inelastic loss channels, resulting in a less rich scattered ion energy spectrum. However, clear losses are observable. In the case of Ne^+ collisions with light target materials (Mg, Al, Si), two perplexing phenomena have been seen. First, the ion yield for Ne^+ scattering off some surfaces was found to greatly increase with increasing impact energy ─ much greater than that expected for a rare gas ion (Ar^+ ion yields are very small). In some cases, ion yields as high as ~70%, comparable to alkali ions, have been seen for keV collisions with Ne^+ on certain metals (Rabalais *et al*., 1985a; Rabalais, 1988). Such a high ion yield did not make sense in the standard view of ion-solid collisions because Ne^+ should be Auger or resonant neutralized with high probability as it approaches a metal surface. Interestingly, the Ne^+ scattered ion energy was seen to be smaller than the BCA predicted value, which implied that an inelastic loss could be occurring during the hard collision.

The second peculiar observation was a peak in the ISS spectrum at slightly less than half of the Ne^+ exit energy. This ″mystery″ peak was attributed to Ne^{++}. Since most ISS systems utilize energy dispersion rather than momentum, the peak for Ne^{++} occurs in the spectrum at half of its actual energy. However, when the +2 charge state is taken into account, the actual Ne^{++} exit energy is noticeably lower than the inelastic Ne^+ exit. This energy difference between the Ne^+ and Ne^{++} exit channels implies that two separate processes are responsible: one for the inelastic Ne^+ with very high yield and the other associated with generation of Ne^{++}. Surprisingly, the first attempts to study these issues on surfaces did not focus on the ion energy loss, but rather on low-energy electrons released from Auger transitions in the projectile and/or target atoms.

There is much more prior art in Auger electron spectroscopy (AES) for Ne^+ collisions with surfaces than for ISS energy loss measurements. The reason for this lies in the difficulty with properly quantifying ISS losses and the ambiguity that comes with multiple charge states and multiple ion species overlapping one another in ISS spectra. In this sense, AES measurements are much ″cleaner″ because electron kinetic energies can often be assigned directly to the initial and final states of the atomic transitions involved. Since our measurements focus on ion scattering, it is important to establish

some of the issues involved in making ISS energy loss evaluations for the Ne^{+} and Ne^{++} exit channels.

7.2 ISS Measurements and the Utility of Energy and Mass Dispersion

We are interested in probing the electronic excitation mechanisms that occur during the close encounter when a short-lived quasi molecule is formed between the two collision partners (Ne^{+}→Al, Si, Mg, and Ti). Evidence for electronic excitation and charge exchange processes will be measured through energy losses associated with the BCA single collision peak as seen in the scattered ion energy spectrum. Our scattered product detector, because it has both mass and energy dispersion, will enable easy and unambiguous separation of the Ne^{+} and Ne^{++} energy distributions. Separating the Ne^{+} and Ne^{++} channels (even if inelasticities are not evaluated) can be difficult and not often conclusive with standard ISS systems (both TOF and electrostatic sector). For example, consider the results of Grizzi *et al.* (1990) (Fig. 7.1a ─ TOF machine) and Souda *et al.* (1995) (Fig. 7.1b ─ electrostatic sector only) for Ne^{+} scattering on Mg.

The TOF and electrostatic-only techniques do not have mass dispersion. As such, the scattered ion spectrum contains a mix of *all* charged species leaving the target surface in *any* charge state. This means that the ISS spectrum for TOF and electrostatic-only machines contains

(1) directly scattered projectile ions (any + charge state)
(2) direct recoil target atoms (any + charge state)
(3) sputtered target atoms (the standard SIMS signal)
(4) any contaminant species sputtered or directly recoiled off the target surface
(5) photons ─ TOF only
(6) electrons ─ TOF only

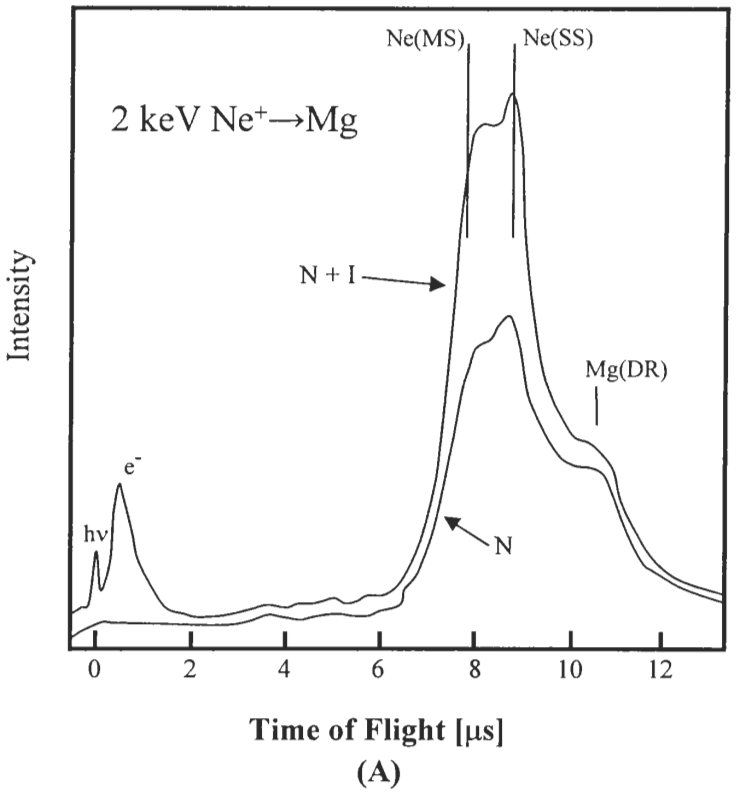

(A)

SS= single scatter, MS= multi-scatter, DR= direct recoil
N= neutrals only, N+I= neutrals and ions

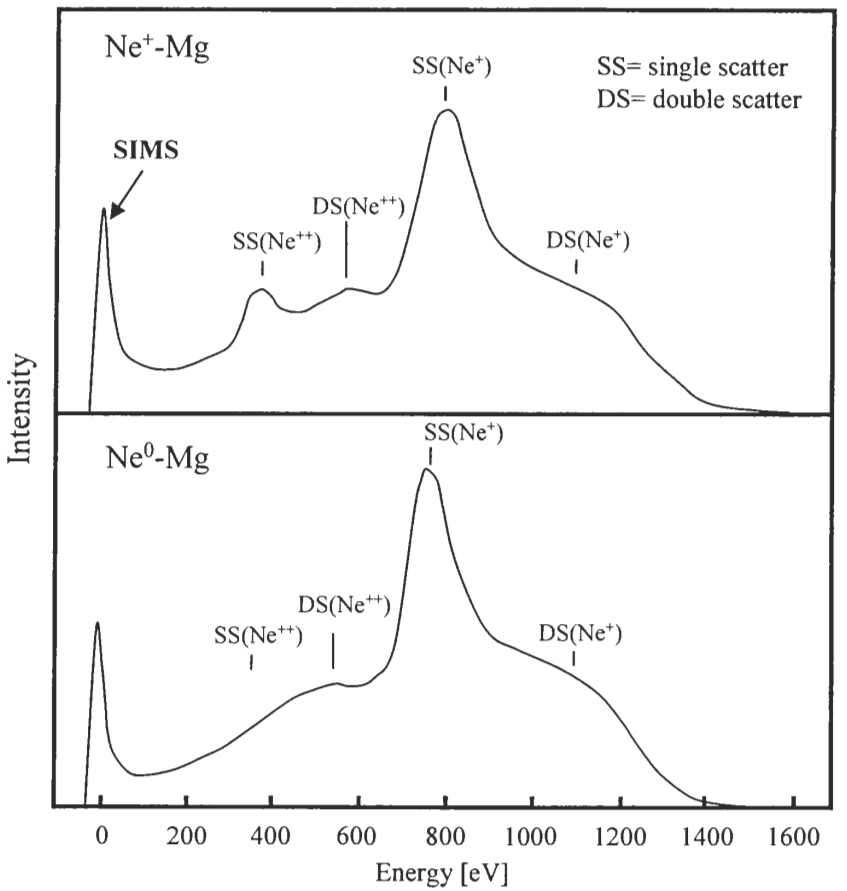

(B)

Figure 7.1: (A) TOF data for Ne^+ on Mg at 2 keV from Grizzi *et al.* (1990).
(B) Electrostatic sector data for Ne^+ on Mg at 2 keV (upper panel) from Souda *et al.* (1995).
Overlap of Ne and Mg signals can be seen in (A) – no indication of Ne^{++} (probably beneath Ne^+ peaks). Electrostatic sector scan in (B) shows Ne^{++} and low energy SIMS ion signal (annotated).

As shown in Fig. 7.1, the individual energy distributions of each of these species are convoluted in the overall ISS energy scan (or time scan for TOF). Peaks are identified with a specific ion mass or charge state through a process of elimination based on where one ″thinks″ a certain peak ought to appear in the spectrum. For more than one ion mass, a mix of charge states, or multiple bounce phenomena (single and double bounce give different exit energies), it is easy to see that the identification process can be difficult and ambiguous. As well, overlapping energy distributions make it impossible to extract the energy distribution for just one ion species alone. In this case, subtle phenomena such as sub-surface scattering (indicated by peak fronting on the low-energy side) are entirely missed.

As seen in the TOF neutral scan (Fig. 7.1a), the single-bounce Mg recoil (Mg-DR) overlaps with both the single scattered Ne (SS) and the multi-bounce Ne (MS). Another important aspect about TOF measurements should be mentioned. The TOF technique requires a modulated projectile beam (on-off, on-off) to establish a ″time-zero″ for particle velocity measurement. This means that ions with the same kinetic energy, but different charge states, will have the same flight time because they have the same velocity ─ therefore, no separation of the two charge states will occur. In Fig 7.1a, it is unknown from the TOF scan if Ne^{++} is generated (hidden beneath the Ne^{+}?), whereas, the electrostatic sector (Fig. 7.1b) does show a small peak where one might expect the Ne^{++}. This comparison between the two detection techniques for the same system ($Ne^{+}\rightarrow Mg$ at 2 keV) shows the detriment of overlapping signals. Neither technique can give a crystal-clear picture of the scattering phenomena. The TOF method allows both ion and neutral detection (fast neutrals *only* – above about 30-50 eV), but cannot disperse in mass or charge state; the electrostatic sector does disperse in charge state, but cannot detect neutrals or disperse in mass.

In contrast, a detection system with mass *and* energy dispersion (like ours) can easily separate Ne^{+}, Ne^{++} and Mg^{+}. The individual energy distributions for each of these species can be measured separately because the quadrupole mass filter disperses the ions based on mass-to-charge ratio after the energy filtering step: Ne^{+} at 20 AMU, Ne^{++} at 10 AMU, and Mg^{+} at 24 AMU.

For example, the scattered ion energy distributions measured with our system for Ne^+, Ne^{++}, and Mg^+ are shown in Fig 7.2a-c for $Ne^+ \rightarrow Mg$ at 844 eV impact. Our system also has an electron impact ionizer *before* the energy filter, so neutrals can be energy analyzed and detected as well as ions.

Finally, our goal is to investigate the near threshold processes (100's of eV) involved in the Ne^+ inelastic scattering channel and the mechanism for Ne^{++} generation. These experiments are in contrast to previous Ne^+ loss measurements conducted at much higher energies (1-2 keV and up). The ability of our detector to clearly separate Ne^+ and Ne^{++} from one another, as well as from other ion species, will prove helpful in separating Ne^+ inelastic losses from Ne^{++} generation.

The next section will briefly discuss some of the various experimental approaches to Ne^+ scattering off surfaces and the subtleties associated with ISS loss measurements. In addition, literature results of AES and ISS for Ne^+ scattering off light targets are presented in the subsequent sections to outline the current understanding of Ne^+ and Ne^{++} loss mechanisms.

7.3 Collision Studies of Ne^+ with Solid Targets

The main body of scattering work with Ne^+ has been on light materials (Na, Mg, Al, and Si) along with a few experiments on heavy targets like Cu, Ag, Pt, and Au. The majority of these studies are conducted at 1 keV or above and do not specifically examine the validity of BCA predictions. Quite often, the scattered ion energy distribution is not even measured. Instead, these experiments focus on the total ion yield with respect to the scattering angle and/or impact energy, so that neutralization phenomena and cross-sections can be measured. As mentioned earlier, bombardment induced Auger emission from the projectile or target atoms is also studied to more clearly understand excited state formation and charge exchange processes that occur during the hard collision.

Many measurements have been conducted in the keV range for a few fixed projectile energies using variable scattering angle at or near the specular reflection geometry.

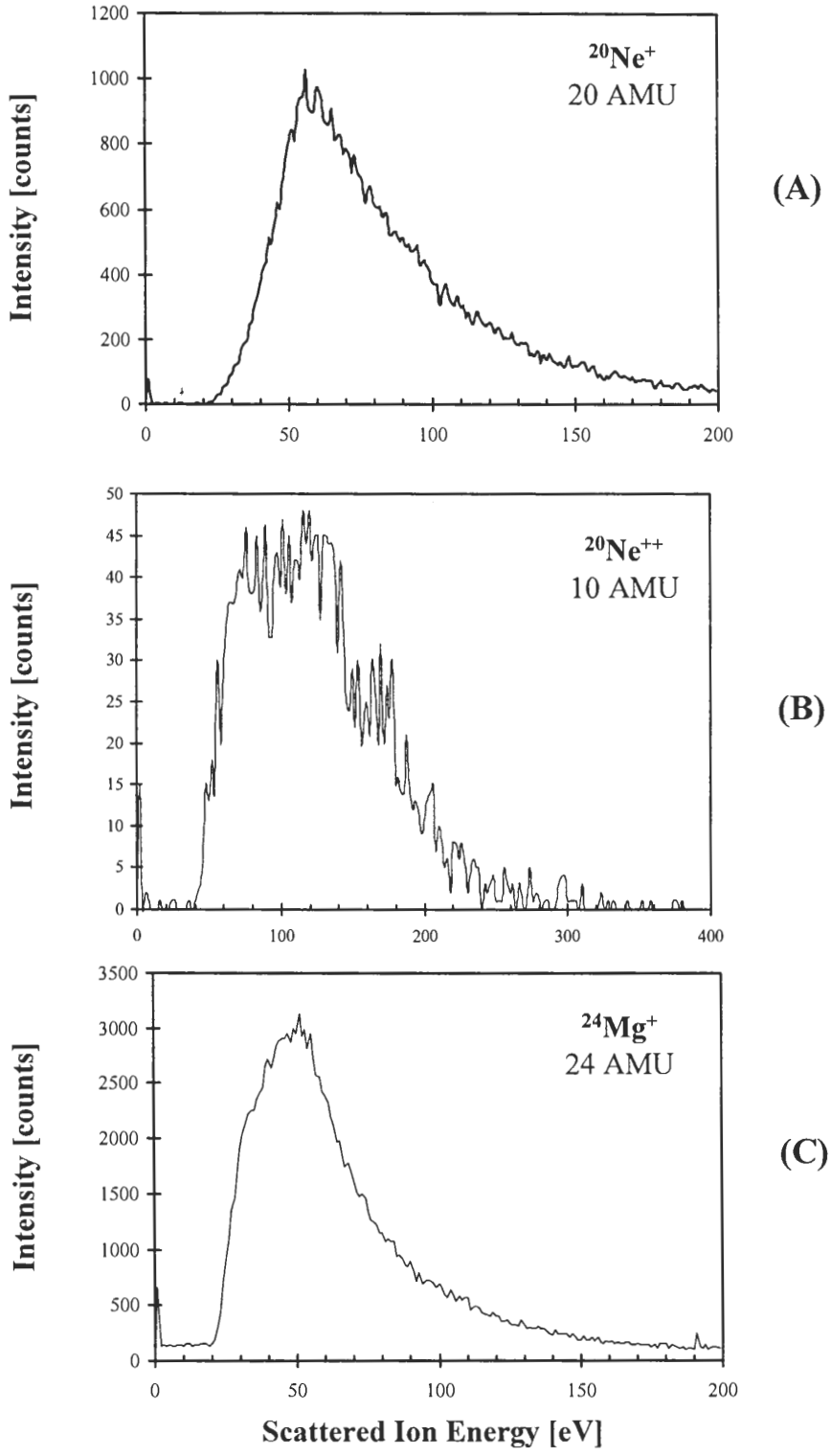

Figure 7.2: Scattered ion energy distributions for Ne^{+} impact on Mg at 844 eV. (A) Ne^{+} exit, (B) Ne^{++} exit, and (C) Mg^{+} exit. Note: the energy axis for the Ne^{++} scan is expanded to 0-400 eV, which makes the peak appear much narrower than Ne^{+}—which it is not.

A variable angle of incidence or takeoff results in a large variation in the contact time that the projectile spends in the near-surface region during the incoming and outgoing portions of the trajectory. Multiple collision events and high neutralization rates become more pronounced for smaller scattering angles (Niehus *et al*., 1993). As such, these experiments are ideally suited to examine ion neutralization phenomena at surfaces by monitoring the total ion yield with respect to angle or energy. The ion yield can often be correlated with the approach and exit velocities of the projectile because the Auger transition probability for neutralization depends on the time that the projectile spends in the near-surface region (Niehus *op. cit*.).

Inelastic loss mechanisms associated with electron straggling (electron friction) of the projectile in the near-surface region can change character with angle. This occurs because the trajectory length of the projectile in the near-surface region changes greatly with both the incident angle and scattering angle. Straggling losses that depend on projectile velocity(v), projectile energy, or even v^3 have been seen for different projectile-target combinations, energy ranges, and scattering angles (Niehus *op. cit*.). These studies serve as useful tests of neutralization theory and straggling models, but they make single collision events ─ where inelastic losses may be present ─ difficult to compare to the BCA model. The inelastic losses which can vary with angle as well as impact energy must be properly accounted for and ″removed″ from energy loss measurements to extract inelasticities associated with the hard collision only. This is not often easy and as such, it is not done in most cases.

Alternatively, variable incident energy at large, fixed scattering angle provides a means of keeping the trajectory length short while directly probing the distance of closest approach in the violent collision. Inelastic losses are also important for these experiments, but can often be treated with an impact-parameter dependent energy loss after the method of Oen and Robinson (1976) mentioned in Chapter 2. The functional dependence of the straggling loss should not change character at fixed angle, so these losses can be evaluated by calculating the impact parameter dependent loss for each collision energy.

7.4 Ne^+ Scattering: Auger Results

Low-energy Auger electron release has been studied by many authors for Ne^+ scattering in the low keV range as an indicator of excited state production during the hard collision. In the low-energy region of the electron spectrum, two distinct peaks at ~22 eV and ~25 eV can be clearly seen for most light target materials (Na, Mg, Al, and Si). The nominal transition energies for these peaks are assigned as 20.35 eV and 23.55 eV. The observed energy offset is due to kinematic effects of the electron release. When electrons are ejected from a fast-moving excited Ne traveling away from the target surface, a considerable Dopper shift occurs in the measured electron energy which requires a subsequent correction (Pepper, 1986; Gallon and Nixon, 1992). The two electron peaks seen in the 20 eV range are associated with autoionization of doubly excited Ne atoms that decay to Ne^+ in vacuum far away from the target surface:

$$Ne^{**}\left({}^3P \text{ core}\right)\left(2p^4 3s^2\right) \rightarrow Ne^+\left(2p^5\right) + e^- \text{ at 20.35 eV} \tag{7.4}$$

$$Ne^{**}\left({}^1D \text{ core}\right)\left(2p^4 3s^2\right) \rightarrow Ne^+\left(2p^5\right) + e^- \text{ at 23.55 eV} \tag{7.5}$$

As an example of the rich Auger phenomena, the electron spectra taken during 5 keV bombardment of Al with Ne^+ from Gallon *et al*. is shown in Fig. 7.3a-b. A summary of the initial Ne states which produce these electron peaks is also given.

Intense electron emission from autoionization decay of the Ne^{**} with the ^{1}D core has been seen for Ne^+ impact on Na, Mg, Al, and Si (Guillemot *et al*., 1996a and references therein; Lacombe *et al*., 1995). At slightly higher energies between 25-32 eV, smaller structures associated with higher lying autoionizing states with $2p^3$ and $2p^4$ cores are also seen:

$$Ne^{**}(2p^4 - nl \text{ or } 2p^4 - nln'l') \rightarrow Ne^+ \tag{7.6}$$

$$Ne^{+**}(2p^3 - nl \text{ or } 2p^3 - nln'l') \rightarrow Ne^{++} \tag{7.7}$$

$$Ne^{***}(2p^3 3s^2 - nl) \rightarrow Ne^{++} \tag{7.8}$$

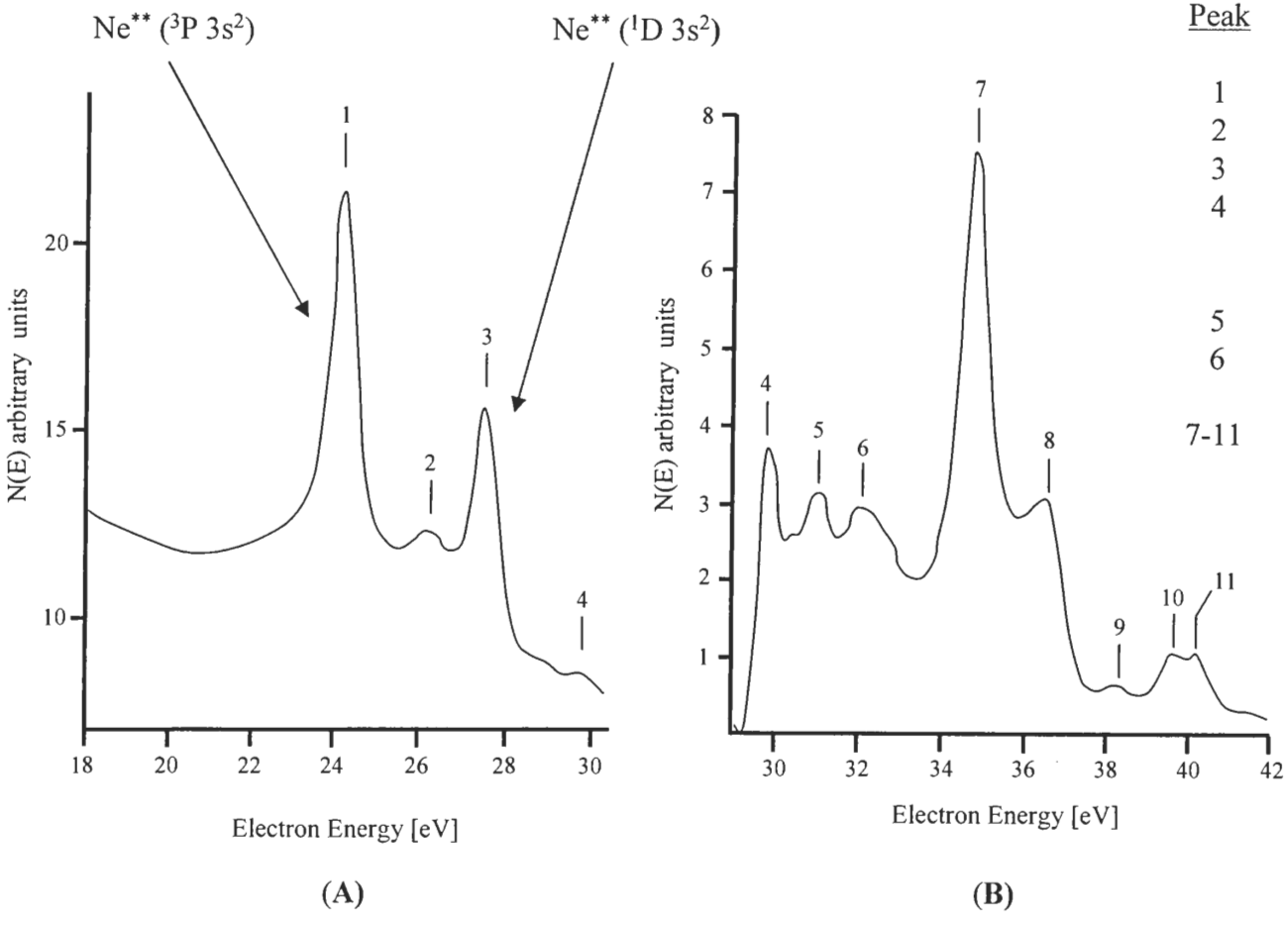

Peak	Initial Ne State
1	$(^3P)\ 3s^2\ ^3P$
2	$(^3P)\ [3s3p(^3P)]\ ^3D, ^3P$
3	$(^1D)\ 3s^2\ ^1D$
4	$(^3P)\ [3s4s(^3S)]\ ^1P$
	$(^1D)\ [3s4p(^3P)]\ ^3F$
5	$(^3P)\ [3p^2(^3P)]\ ^1D, ^1P$
6	$(^1D)\ [3s3p(^1P)]\ ^1F, ^1P, ^1D$
7-11	unknown, possibly Ne

Figure 7.3: Auger spectra obtained for 5 keV Ne^+ on Al. (A) lower energy and (B) higher energy.
Data from Gallon and Nixon (1992). Peak identifications are from the cited work.
Annotations shown for the two most common Ne^{**} autoionizing electron lines seen for Mg, Al, and Si targets.

A summary of the major autoionization decay lines for Ne^+ collisions on Mg and Al is given in Table 7.1 along with their respective transition energies. The two main autoionizing lines that have been seen for most light targets (Eqn. 7.4-7.5) are shown in bold. The mix of excited neutral and ion states that are listed (initial states for Auger transitions) give a good feeling for the inelastic losses that one may see in ISS spectra for the Ne^+ and Ne^{++} exit channels. The energies required to pump the excited state transitions fall in the ~40-100 eV range depending on the starting state (Auger line energy + the corresponding ionization potentials for $Ne^0 \rightarrow Ne^+$ (21.5 eV), $Ne^0 \rightarrow Ne^{++}$ (62.5 eV), or $Ne^+ \rightarrow Ne^{++}$ (40.96 eV)). Some of these autoionizing energy levels will be revisited later in the discussion of ISS data from the literature as well as our measurements for Ne^+ scattering off Al, Si, and Mg targets.

An electron loss and capture scheme between the various Ne, Ne^+, and Ne^{++} states for the $2p^4 3s^2\ {}^3P$ core state of Ne^{++} has been hypothesized by Lacombe *et al.* using Auger data and gas-gas scattering data as a guide. A block diagram of this scheme is shown in Fig. 7.4. The formation of excited particles and ions is the result of a series of electron capture, loss, and de-excitation processes that occur as the particles fly away from the surface. This complex scheme gives a flavor for the richness which can be seen in Ne^+ scattering and the potential for inelastic loss processes.

Xu *et al.* (1994) have gone a step further and monitored the Auger line intensities for the three strongest autoionizing transitions for the $Ne^+ \rightarrow Al$ system as a function of impact energy and angle. Threshold collision energies for the three transitions are shown in Table 7.2. Due to the overlap at ~30.5 eV, it is unknown which transition (IIIa or IIIb) is responsible.

Table 7.1: Auger lines for autoionization decay of excited Ne^0 and Ne^+ states for Ne^+ bombardment of Mg and Al in the keV collision energy range. Data from Guillemot *et al.* (1996).

Initial State Ne^{**} or Ne^{+**}	Final State Ne^+ or Ne^{++}	Transition Energy [eV]
$\left[2p^4\left(^3P\right)3s^2\right]^3P$	$2p^5\left(^2P\right)$	**20.35**
$\left[2p^4\left(^1D\right)3s^2\right]^3P$ or $\left[2p^4\left(^3P\right)3s3p\right]^3P$	$2p^5\left(^2P\right)$	22.9
$\left[2p^4\left(^1D\right)3s^2\right]^1D$	$2p^5\left(^2P\right)$	**23.55**
$\left[2p^4\left(^1D\right)3s3p\left(^3P\right)\right]^3P/^3D$	$2p^5\left(^2P\right)$	25.95
$\left[2p^4\left(^3P\right)3p^2\left(^3P\right)\right]^1D/^1P$	$2p^5\left(^2P\right)$	26.7
$\left[2p^4\left(^1S\right)3s^2\right]^1S$ or	$2p^5\left(^2P\right)$	27.7
$\left[2p^3\left(^2D\right)3s^2\right]^2D$	$2p^4\left(^3P\right)$	27.7
$\left[2p^3\left(^2D\right)3s3p\left(^2P\right)\right]^4F$	$2p^4\left(^3P\right)$	30.56
$2p^3\left(^2P\right)3s^2\left(^2P\right)$	$2p^4\left(^3P\right)$	30.66
$\left[2p^3\left(^2D\right)3s^23p\left(^2P\right)\right]^4F$	$2p^4\left(^3P\right)3p\ ^2F$	31.7
$\left[2p^3\left(^2D\right)3s^23p\left(^2P\right)\right]^4F$	$2p^4\left(^3P\right)3p\ ^2D$	32.0
$\left[2p^3\left(^2D\right)3s^23p\left(^2P\right)\right]^4F$	$2p^4\left(^3P\right)3p\ ^4D$	32.3

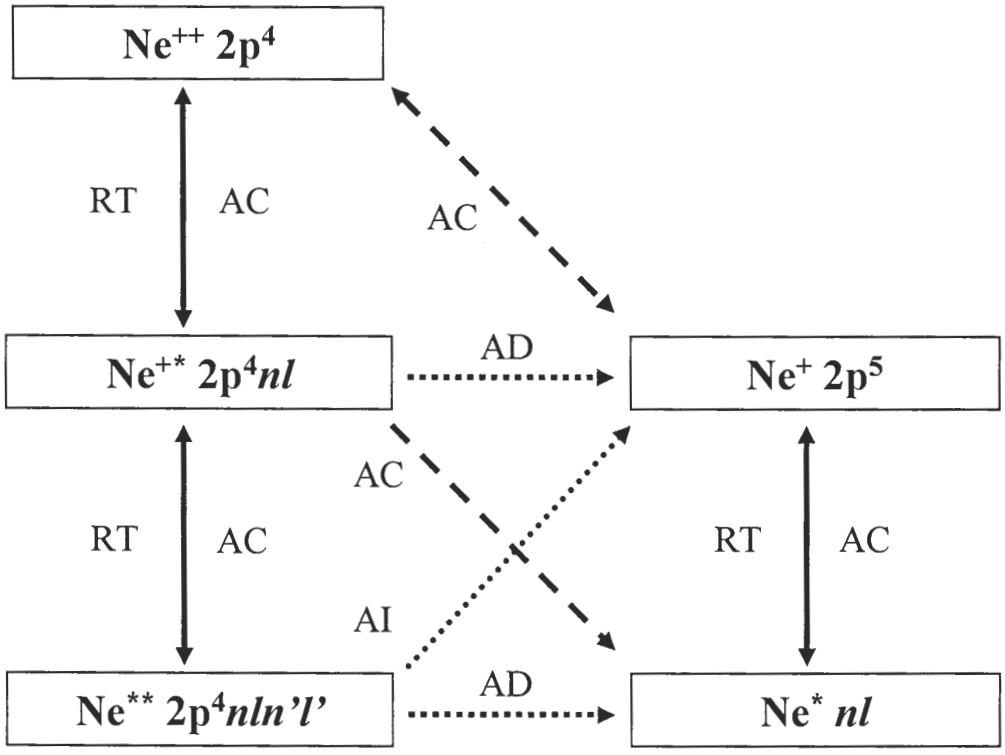

AC = Auger Capture
AD = Auger De-excitation
RT = Resonant Transfer
AI = Auto-ionization

Figure 7.4: Electron loss and capture scheme for the Ne^{++} (^3P $2p^4$) core state, after Lacombe *et al.* (1995).

Table 7.2: Auger transitions and threshold impact energies for the three strongest autoionizing Ne lines occurring for $Ne^+ \rightarrow Al$. Data from Xu *op. cit.*

Peak	Transition	e^- Energy [eV]	Threshold Impact Energy [eV]
I	$Ne^{**}\left(2p^4\left(^3P\right)3s^2\right)^3P \rightarrow Ne^+\left(2p^5\right)^2P$	20.35	230
II	$Ne^{**}\left(2p^4\left(^1D\right)3s^2\right)^1D \rightarrow Ne^+\left(2p^5\right)^2P$	23.55	230
IIIa	$Ne^{+**}\left(2p^3\left(^2D\right)3s3p\right)^4F \rightarrow Ne^{++}\left(2p^4\right)^3P$	30.56	440
IIIb	$Ne^{+**}\left(2p^3\left(^2D\right)3s^2\right)^2P \rightarrow Ne^{++}\left(2p^4\right)^3P$	30.66	440

The Auger intensity data for these three lines with respect to impact energy is reproduced in Fig. 7.5 for the Ne^+ beam at 50° incidence from the target normal. The data for other incident energies is nearly identical to the 50° case. Xu *et al.* attributed the initial states for peak IIIa-b with two-electron excitations of the Ne^+ ion which had survived neutralization prior to the hard collision. The decay of these states in vacuum far from the surface, where re-neutralization is unlikely, was hypothesized as the formation mechanism for the Ne^{++} exit channel.

Commentary about Auger Measurements with Impact Energy

Auger measurements of Ne and Ne^+ autoionization decay that are made with respect to impact energy can be deceiving. The Auger measurements of Xu *et al*. were done with a fixed angle between the Ne^+ incident beam and the electrostatic analyzer (70°) by rotating the sample. Their electrostatic analyzer has approximately 50° solid angle acceptance, meaning that most of the electrons released from the target (many angles) are collected as well as those electrons released by autoionizing Ne traveling away from the surface at many angles. Consider for a moment the geometrical implication of this measurement as represented in Fig. 7.6.

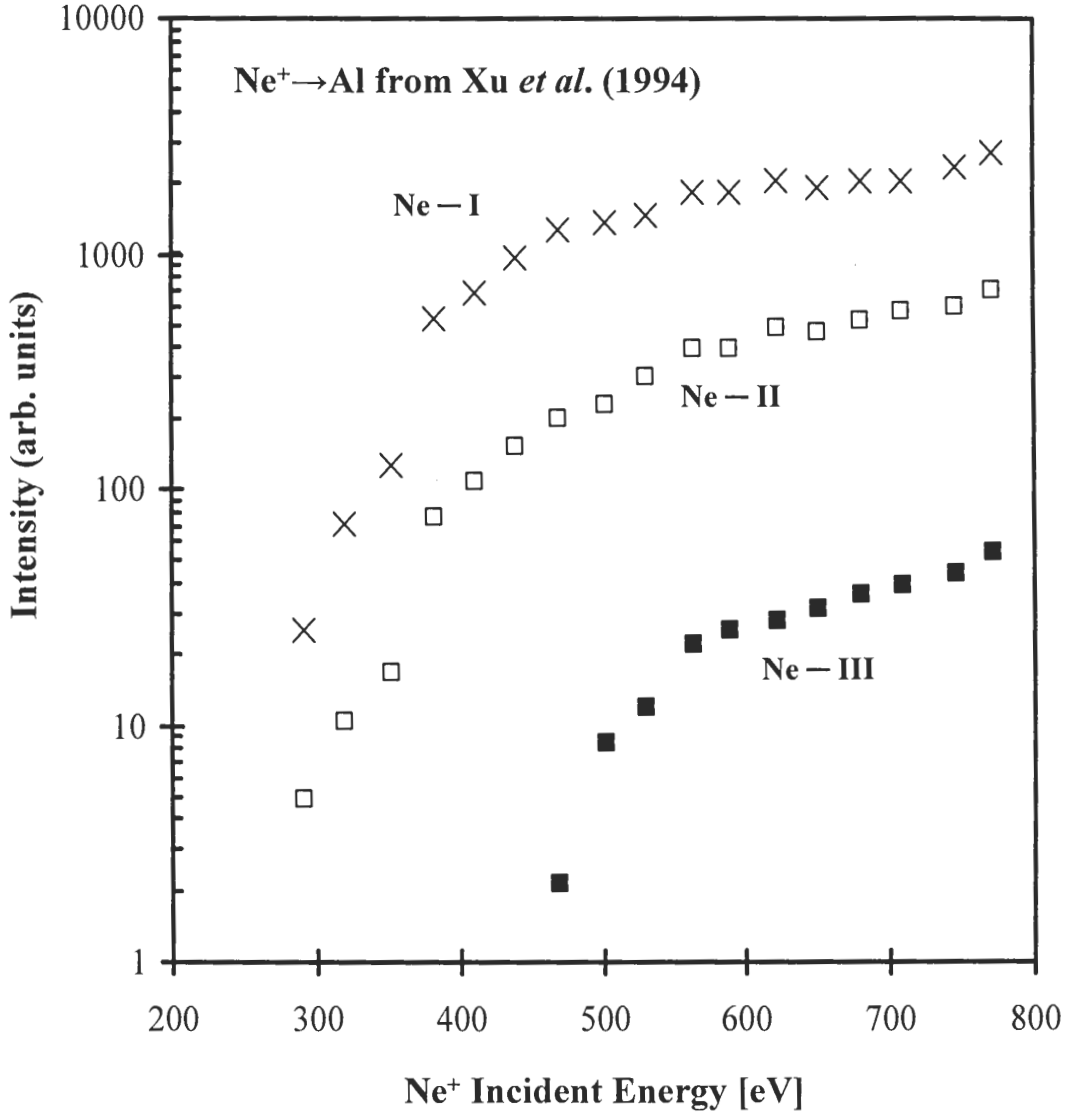

Ne — III:

$$Ne^{+**}\left(2p^3\left(^2D\right)3s3p\right)^4F \rightarrow Ne^{++}\left(2p^4\right)^3P \qquad \text{with 30.56 eV } e^-$$

or

$$Ne^{+**}\left(2p^3\left(^2D\right)3s^2\right)^2P \rightarrow Ne^{++}\left(2p^4\right)^3P \qquad \text{with 30.66 eV } e^-$$

Figure 7.5: Auger line intensity for peaks I, II, and III (see text) for $Ne^+ \rightarrow Al$ at 50° incident angle. Data from Xu *et al.* (1994).
Peak III has been identified as the transitions listed. The peak III electron release should result in Ne^{++} generation. Note that peak III turns on between 400-500 eV.

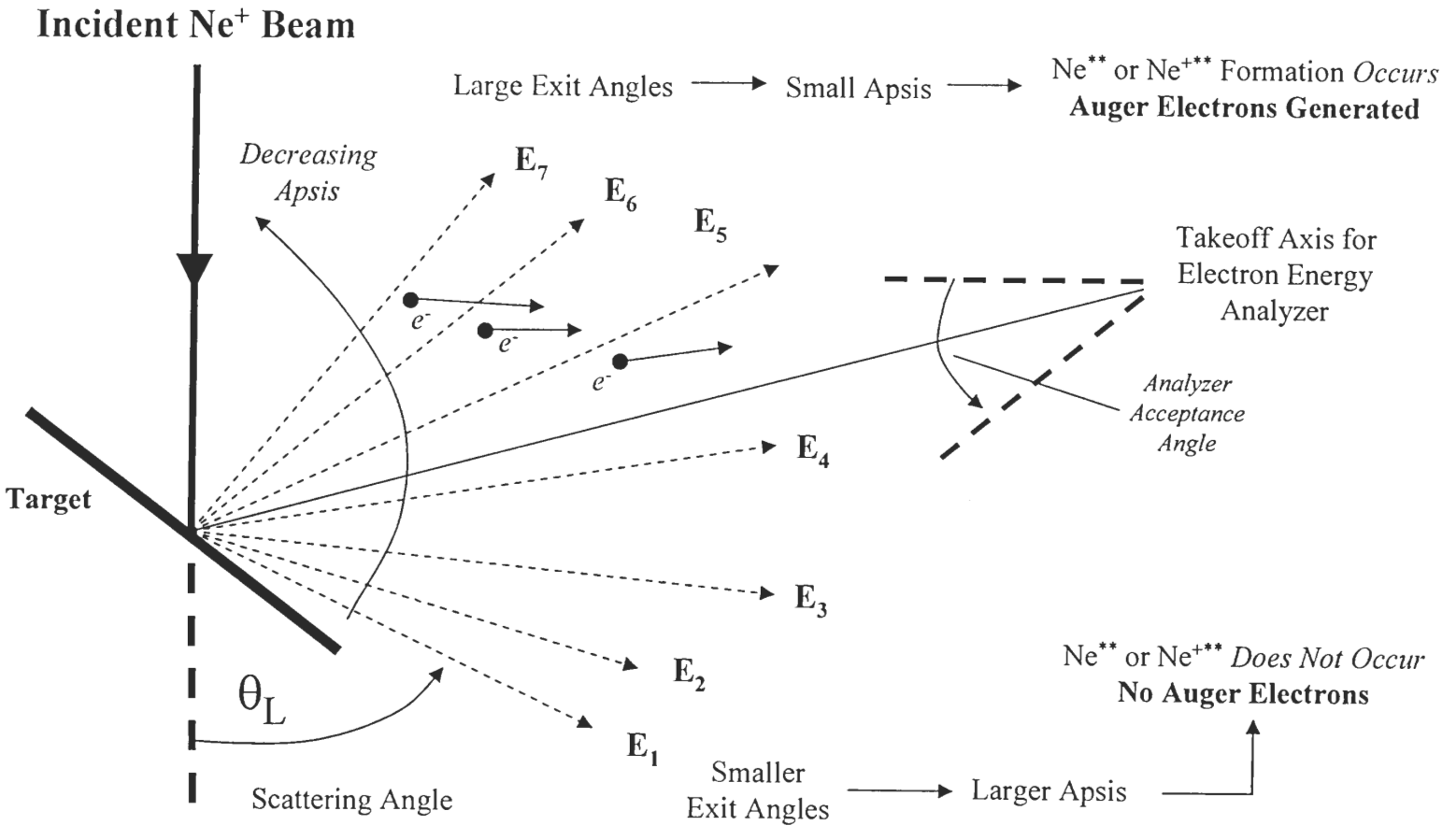

Figure 7.6: Geometrical implications of Auger measurements for autoionizing Ne^{**} and Ne^{+**} states. Note that the excited state exit channels have a strong angular distribution. As the the impact energy is raised, the angular spread for Ne^{**} and Ne^{+**} release gets larger and larger – tending toward smaller and smaller lab angles. $\mathbf{E_i}$ are the different scattered projectile energies.

Remember that projectile species are scattered by the target into all lab angles with an exit energy predicted by the BCA model (single collisions only) ─ if we assume no inelastic losses. As shown in the figure, small lab scattering angle probes a large apsis distance, whereas, a large lab scattering angle probes smaller apsis distances. The ambiguity with the Auger peak turn-on with impact energy (Fig. 7.5) comes from the fact that small lab scattering angles (collisions with large apsis) do not generate projectile excitations (like Ne^{**}). Larger scattering angles where the apsis is small do generate the Ne^{**} states, which decay and give the Auger electrons. This means that the scattered projectiles in the Ne^{**} state have a strong angular dependence. The angular dependency of the Ne^{**} exit channel (and the resulting Auger electron release) makes it difficult to put any real meaning to the threshold impact energy which generated the Ne^{**} state in the beginning. One can only say that above the threshold impact energy, Ne^{**} is generated at *some* exit angle. Most likely, the Ne^{**} state is first generated for projectiles that are strongly backscattered (lab scattering angle → 180°) at the threshold impact energy. As the impact energy is raised, Ne^{**} is generated over a greater angular width starting from the full backscattering direction and tending toward more forward directions (smaller lab angle).

Target Excitations

Auger decay of excited state target atoms has also been seen for Ne^{+} collisions with light targets. For example, excitations of the form Mg^{*} and Mg^{+*} (30-50 eV) and Na^{*} (25-30 eV) have been observed for Ne^{+}→Mg and Na collisions (Guillemot *et al*., 1996a, 1996b; Lacombe *op. cit*.). This indicates that target atoms excitations occur during the hard collision *simultaneously* with the excitation of Ne projectile species.

Summary

The existence of very favorable excitations to form autoionizing states in the hard collision is usually invoked to explain the high ion yield for Ne^{+} scattering at keV energies. This mechanism is plausible because the lifetime of the Ne^{**} precursor state

(~1.5x10^{-14} s) (Morgensten *et al*., 1980) is long enough that the particle can travel far away from the surface, where it subsequently decays to Ne^+. For example, Ne at 1 keV will travel ~15 Å in 10^{-14} seconds and be out of reach of the valence band electron states of the target. The near-surface trajectory is over too quickly, so that the Ne^{**} can not be quenched before it gets far away from the surface.

Auger results clearly show that Ne^+ collisions with light targets can create a rich spectrum of excited projectile states which can decay to Ne^0, Ne^+, and Ne^{++}. In addition, target atom excitations occur simultaneously with projectile excited state formation during the hard collision. The presence of target excitation adds yet another dimension to the inelastic loss processes that may be important in the scattered ion energy spectrum for Ne^+ and Ne^{++} off light targets. We can also see that ISS loss measurements must be cast in the light of the extensive body of Auger data for Ne^+ collisions.

7.5 Ne^+ Scattering: ISS Results

7.5.1 Inelastic Ne^+ Exit Channel

Energy loss measurements of Ne^+ scattering off light targets has lagged behind electron spectroscopy measurements. Grizzi *et al.* (1990) have studied $Ne^+ \rightarrow$Mg in the keV range for small incident angles and lab angles between 10-50°. They have observed a steep rise in the ion yield for distances of closest approach (apsis) below 0.7 Å. Their time-of-flight (TOF) experiments show raw ion energy losses of ~12 eV for small scattering angle (larger apsis) and ~30 eV for the violent collisions when the apsis is less than 0.7 Å. Taking into account the energy partitioning in the $Ne^+ \rightarrow$Mg collision, a binary inelasticity of ~45 eV (from the 30 eV raw loss) was obtained for apsides <0.7 Å. Given the ionization potential for $Ne^0 \rightarrow Ne^+\left(2p^5\right)^2P$ (ground state) at 21.56 eV (Weast *et al*., 1988) and the first few Auger decay lines from Table 7.1 for $Ne^{**} \rightarrow Ne^+\left(2p^5\right)^3P$ at 20-23 eV, the ~45 eV inelasticity in the Ne^+ exit seems totally consistent with the $Ne^0 \rightarrow Ne^{**}$ pump scheme. The authors make the point of wondering why a one-electron Ne 2p excitation (direct ionization) does not occur giving an inelasticity of ~20 eV in the

ion energy spectrum. They suggest that, due to fast transition rates, the Ne^+ from the 20 eV excitation is resonantly neutralized by the Mg $3s$ valence band to form $Ne^*\left(2p^5 3s\right)$. They believe that the Ne^+ is formed by the direct route (but neutralized), because resonant photons at 73.6 and 74.4 nm from the Ne^* decay are seen (Rabalais *et al*., 1985b).

Ascione *et al.* (1997) and Manicò *et al.* (1997) (the Italian group) have conducted Ne^+ scattering studies at 1950 eV off Al and Si with variable lab angle. They report an inelasticity value of ~45 eV for Ne^+ on both target materials. The 45 eV loss was explained through the $Ne^0 \rightarrow Ne^{**}$ transition which occurs via a two-electron promotion involving the Ne 2p orbital. In looking at their data, we note that the inelasticity determination for $Ne^+ \rightarrow$Al has a good fit at small apsis (<0.38 Å), but the scatter in their data for larger apsides is much greater, making the 45 eV fit more questionable for weaker collisions. The Si data seem to fit the 45 eV inelasticity model much better (however, they only probe apsides < 0.41 Å).

Later, the same Italian group (Xu *et al*., 1998) conducted an extensive investigation of the Ne^+ and Ne^{++} exit channel inelasticities for Ne^+ collisions with Si in the 500-1950 eV range. Their study reveals that for small incident energy (500 eV), Ne^+ loses about 5-6 eV in the interactions with the surface and that the inelasticity steadily increases up to ~45 eV. The rise in the Ne^+ inelastic loss begins when the apsis distance reaches 0.59 Å. For apsides less than ~0.47 Å, a constant inelasticity of 45±4 eV is measured for the binary encounter. This energy loss was assigned to the $Ne\left(2p^6\right) \rightarrow Ne^{**}\left(2p^4\left(^1D\right)3s^2\right)$ transition at 45.15 eV (Olsen *et al*., 1976) because it matches one of the main Auger autoionization lines (Eqn. 7.5) seen in $Ne^+ \rightarrow$Si collisions. The authors say that two-electron processes ($Ne^0 \rightarrow Ne^{**}$) appear more important at the higher collision energies rather than one-electron excitations. The inelastic losses at lower impact energy (500 eV) are explained as excitations of the Si valence band. The discussion for why the Ne^+ inelasticity increases from 5-6 eV at 500 eV impact to 45 eV at 1400-1950 eV impact is generally avoided. They do mention that one-electron processes could be operative in the lower energy regime.

Other work on $Ne^+ \rightarrow Al$ and $Ne^+ \rightarrow Si$ by Tolstogouzov *et al.* (1999) for 122° scattering angle at 1.5-5 keV has given inelasticities of 45±5 eV for Al and 55±5 eV for Si. Their ion beam source did not have mass filtering so the beam was composed of both major isotopes of Ne: ^{20}Ne (90.9%) and ^{22}Ne (8.8%). Inelasticites were measured for $^{22}Ne^+$ and found to be 60±5 eV for Al and 65±5 eV for Si. These results do not seem to make sense. There should not be such a difference in inelasticity values for ^{20}Ne versus ^{22} Ne. The authors point this fact out, but do not provide any thoughts on the matter.

An interesting study by Souda *et al.* (1995) was conducted with Ne^+ and Ne^0 incident on Mg, Al(111), and Si(100) from 0.1-2 keV. Fast Ne^0 was generated in a charge exchange cell with Ne gas at 10^{-3} Pa. Their results show that the Ne^+ scattered energy spectra (however, not the Ne^{++} exit) are almost identical for Ne^+ and Ne^0 incidence. This indicated to the authors that the incoming projectile ions must be neutralized very efficiently on the incoming path and that the hard collision occurs mostly between Ne^0 and the target atom (rather than Ne^+). Therefore, it would seem that excitation mechanisms which occur in the hard collision must originate most of the time from an Ne^0 state rather than excitation from an Ne^+ state. In contrast with the Italian group, Souda, *et al.* explain their results in light of one-electron mechanisms where the neutralized projectile is re-ionized in the hard collision involving a single Ne 2p electron. Inelasticity values were unfortunately not reported in the Souda *et al*. work.

7.5.2 Ne^{++} Exit Channel

Collisions of Ne^+ with Mg, Al, and Si surfaces at keV energies have been shown to generate Ne^{++} and Ne^{3+} exit channels (Hird *et al*., 1994; Souda *et al*., 1995, 1996). Hird *et al*. have detected Ne^{++} and Ne^{3+} for Ne^+ impinging on Si surfaces at threshold energies of 800 eV and 11.1 keV, respectively. They attribute the formation of multiply charged Ne ions to a two-electron *transfer* mechanism involving an electron movement from the $4f\sigma$ to $3s\sigma$ or $3d\pi$ MO's and $3d\sigma$ to $3s\sigma$ or $3d\pi$ MO's, followed by an Auger process to fill the $3d\sigma$ vacancy. The electron *transfer* mechanism between the correlated MO's involves transfer of electrons between the collision partners

(Si 3s to Ne 2p). This mechanism is distinctly different from the curve-crossing approach where the Ne 2p electrons are just *promoted* to higher MO states (no transfer between the partners).

Ascione *et al.* (1997) have studied the inelastic effects in Ne^+ scattering off Al and Si at 1950 eV to try to understand the excitation mechanism involved in producing the Ne^{++} exit channel. Their studies indicate that an inelasticity of ~86 eV occurs in the hard collision which results from a hypothesized two-electron promotion of Ne^+ that occurs in the quasi molecule at the curve-crossing. The excited state involved in this transition was thought to be $Ne^{+**}\left(2p^3 3s\right)$ with a ^{2}D or ^{2}P core at 85 or 87 eV. Their hypothesized excitation scheme is summarized below:

$$Ne^{+}\left(2p^5\right) \rightarrow Ne^{++*}\left(2p^3 3s\right)\left({}^2D \text{ or } {}^2P \text{ core}\right) + e^- \quad \text{requiring 85-87 eV pump} \qquad (7.9)$$

then

$$Ne^{++*}\left(2p^3 3s\right)\left({}^2D \text{ or } {}^2P \text{ core}\right) \rightarrow Ne^{+**} \quad \text{help from surface?} \qquad (7.10)$$

followed by

$$Ne^{+**} \rightarrow Ne^{++} + e^- \quad \text{autoionization} \qquad (7.11)$$

This multi-step mechanism has been suggested because their inelasticity value of 86 eV does not match the more direct route to the doubly excited ion (by-passing the Ne^{++*} state):

$$Ne^{+}\left(2p^5\right) \rightarrow Ne^{+**} \rightarrow Ne^{++} + e^- \quad (\sim 71\text{-}72 \text{ eV pump}) \qquad (7.12)$$

Evaluating the energy of the doubly excited ion (Ne^{+**}) is difficult because the Grotrian diagrams do not contain such states. However, one could make a rough estimate of ~72 eV for the pump energy requirement to convert Ne^+ to the Ne^{+**} state ($Ne^+ \rightarrow Ne^{++}$ at 41 eV plus the Auger line for $Ne^{+**} \rightarrow Ne^{++}$ at ~30.5 eV (peak IIIab – Table 7.2) = 71-72 eV). Further, we note that they have chosen the multi-step scheme involving Eqns. 7.9-7.11 to make the ISS inelasticity (86 eV) consistent with the Auger results (Table 7.2) ─ Auger shows that the Ne^{+**} autoionization (Eqn. 7.12) occurs for impact energies >440 eV.

They also mention that the Ne^{++} could originate from direct decay of Ne^{++*}. If the latter statement is the mechanism, we then wonder what brings about the Auger line for Ne^{+**}.

The authors explain the Ne^{++} formation from an $Ne\left(2p^3\right)$ core state that is created in the hard collision via two-electron promotion of Ne^{+} that survives Auger neutralization along the incoming path. In the work mentioned earlier, Xu *et al.* (1998) (with Ascione) detected Ne^{++} off Si for apsides less than 0.59Å only (1000 eV at 38° lab scattering angle), indicating the existence of a threshold distance. They explain the Ne^{++} inelasticity at high energy using the same 86 eV excitation required for two-electron promotion in Ne^{+}.

Inelasticity measurements by Tolstogouzov *et al.* (1999) on the Ne^{++} generation channel for Ne^{+} on Al and Si from 1.5-5 keV have given results of 100±10 eV and 110±10 eV, respectively. The authors do not appear to have corrected their data for the continuous loss on the incoming or outgoing trajectory and do not offer any prediction of excitation mechanisms.

Finally, Souda *et al.* (1995) state that they have seen the Ne^{++} exit channel at 400, 600, and 800 eV for Ne^{+} impact on Mg, Al, and Si at 60° lab angle. Another important result comes from this work when we consider Ne^{+} versus Ne^{0} incidence. Refer back to Fig. 7.1b. They find that the Ne^{++} exit channel (off Mg and Si) depends strongly on the projectile charge state for 2 keV impact. When Ne^{+} projectiles are used, Ne^{++} is formed above a specific threshold impact energy. However, Ne^{++} is *not* formed for Ne^{0} projectiles at any energy tested. This charge state sensitivity implies that the Ne^{++} generation channel most likely comes from surviving Ne^{+} that is not neutralized on the incoming path. Souda *et al*. attribute the Ne^{++} formation to one-electron excitation of Ne^{+}. However, no mention of inelasticity values is given in their work. In a later paper, Souda *et al.* (1996) showed that a small amount of Ne^{++} *was* generated off Al(111) for Ne^{0} at 2 keV, but only at the double scattering peak position. They attributed the Ne^{++} formation in this case with two consecutive collisions where one electron was transferred in each step: $Ne^{0}\rightarrow Ne^{+}$ (first collision) then $Ne^{+}\rightarrow Ne^{++}$ (second collision).

7.5.3 Gas-Gas Scattering Data and Direct Transitions

Similar trends in gas-gas and ion-solid collisions suggest that the same *primary excitation mechanisms* are operative (Lacombe *et al.*, 1995). Gas phase excitations are explained in terms of the molecular orbital promotion model of Fano, Lichten, and Barat. In most cases, Ne^{+} excitation to Ne^{**} during the hard collision is considered in terms of electron promotion of the $4f\sigma$ molecular orbital, which is correlated with the outermost $2p$ orbital of Ne. Excited state production results from one or two-electron transitions from the $\left[...3d\pi^4 4f\sigma^2...\right]$ core states of the quasi molecule. This curve-crossing of the atomic orbitals (AO) of the projectile and target nuclei to form a hybrid molecular orbital (MO) is invoked to explain the strong excitation of Ne^{**}. Experimental and theoretical studies of gas phase collisions of Na, Mg, and Al with Ne indicate that the $4f\sigma$ promotion occurs at internuclear distances on the order of those shown in Table 7.3.

Table 7.3: Experimental and theoretical predictions of $4f\sigma$ MO promotion from gas-gas scattering. Compiled from the references shown.

System	$4f\sigma$ Promotion Distance [Å]	Reference
Na ─ Ne	0.77	Ostgaard *et al*. 1979
Mg ─ Ne	0.64	Fayeton *et al*. 1976a; 1976b
Al ─ Ne	0.45	Dowek 1978

From a qualitative point of view, this means that the excitation cross-section should decrease from Na to Al. The Auger experiments from Lacombe for Na, Mg, Al, and Si suggest that this trend also occurs for ion-solid collisions.

Inelastic losses associated with direct ionization of Ne through one and two-electron transitions have been seen in gas-gas scattering (autoionization state formation is seen too). For example, in the work of Ostgaard *et al.* (1979) (the Barat group) for the $Na^{+}\rightarrow Ne$ collision, direct ionization of Ne has been seen for violent collisions (large

scattering angle). Energy loss measurements of the Na^+ exit indicate that single and double ionization probably occur:

$$Na^+ + Ne^0 \rightarrow Na^+ + Ne^+ + e^- \quad (7.13)$$

$$Na^+ + Ne^0 \rightarrow Na^+ + Ne^{++} + 2e^- \quad (7.14)$$

These transitions roughly equate to inelasticities given simply by the first and second ionization potentials of Ne^0 (data from Weast *et al*., 1988):

$Ne^+ \rightarrow Ne^{++}$ requiring 40.96 eV (between ground states) (7.15)

$Ne^0 \rightarrow Ne^{++}$ requiring 62.5 eV (between ground states) (7.16)

The gas-gas data for the $Na^+ \rightarrow Ne$ collision also show that the elastic scattering cross-section drops dramatically at an apsis of 1.7 Å. Single-electron excitation is found to be the main process for energy loss in the 1.39-1.63 Å range. A switchover to two-electron excitation seems to occur for smaller apsis ranges (higher collision energies). Therefore, it seems that both one and two-electron excitations are important in Ne^+ collisions with lighter solid target materials; the dominant mechanism would appear to depend on the collision apsis range.

The one- and two-electron direct routes (rather than promotion) have not received much attention from the ISS community because the inelasticities that have been measured at high impact energies, at least for Ne^{++}, are larger (80-100 eV) than the ionization potentials listed above. As well, there seems to be an unspoken desire in the ISS literature to favor autoionizing channels (which one can measure with Auger) over the more simple direct routes. Undoubtedly, the direct routes would result in very slow electron ejection (to the target and to vacuum), which would most likely not be discernible in Auger spectra. Any slow electrons from direct ionization would be overshadowed by the low-energy secondary electron background (a few eV) that comes from the target during ion bombardment. However, we should not discount these direct transitions when we look at our loss measurements for Ne^+ and Ne^{++} in the threshold

impact energy range below 1 keV. Single-electron processes, at larger distances, could be important for the threshold region.

7.5.4 Ne^+ Scattering Summary

Although it is generally accepted that electronic excitation must occur in the hard collision, leading to the formation of an Ne $2p^4$ or $2p^3$ core configuration, a detailed description of the excitation channel and the mechanism involved in Ne^+ scattering from light targets still remains controversial. Several mechanisms for Ne^+ energy loss and Ne^{++} generation have been proposed ─ single-electron excitations as well as two-electron processes related to electron transfer (between the partners) or promotion of Ne 2p electrons.

Auger electron measurements of autoionizing Ne states and target atom excitations are very telling about the charge exchange phenomena that occur during the close encounter of the two colliding nuclei. It is clear that excitation of singly and doubly excited, autoionizing Ne neutrals as well as ions are formed in keV collisions. In addition, target atom excitation occurs simultaneously with projectile excited state formation.

ISS results must be scrutinized more carefully than Auger data because many hard collision inelasticity values reported for the Ne^+ and Ne^{++} exits have not been corrected for the continuous energy loss on the incoming and outgoing trajectories. At keV collision energies, these losses can be significant (several eV up to a few tens of eV) depending on the scattering angle. Loss data aimed at identifying discrete electron transitions in the collision partners must be corrected for this effect, otherwise the raw energy shifts of scattered ion peaks may give erroneous identifications. It is clear from the mix of literature inelasticity data (i.e., 86 eV versus 100-110 eV for Ne^{++}), that some authors may not have done this correction. The disparity in Ne^{++} inelasticity values could also signify that Ne^{++} formation is caused by multiple phenomena, depending on the exact experimental scattering setup (incident beam angle and lab scattering angle). In addition, threshold information about the inelastic Ne^+ exit channel has only been studied

in detail for Si (Xu *et al*., 1998). The Ne^{++} inelasticity in the threshold creation region has not been measured.

It is generally believed that the autoionization decay of Ne^{**} is responsible for the high ion yield of Ne^{+} at energies of ~2 keV and up. The experimental scattering data available suggests an inelasticity of ~45 eV for Ne^{+} associated with the formation of Ne^{**} from the $Ne^{0} \rightarrow Ne^{**}$ pump scheme. It certainly seems as though two-electron processes are more important at the upper energies where inelasticities are large. However, it is unknown what processes lead to Ne^{+} inelasticity and Ne^{++} generation at lower collision energies. Gas-gas scattering work suggests that one-electron transitions are more important at larger apsides (lower impact energy) than two-electron processes. We believe that loss measurements at low collision energies may help to extend the current understanding of Ne^{+} and Ne^{++} inelastic loss mechanisms as well as suggest whether one-electron excitations are more dominant in the threshold region in ion-solid systems.

7.6 Ion Neutralization at Surfaces

Before embarking on our energy loss measurements for Ne^{+} scattering, we must discuss the neutralization of ions at surfaces. When an ion approaches a solid surface, electrons can be exchanged from the valence band (Fermi sea) of the solid to the ion through one-electron, resonant capture transitions or two-electron, Auger-type events. These two processes are depicted in Fig. 7.7. Resonant capture (RC) occurs at larger internuclear distances in the 5-7 Å range when the energy level of the ion vacancy is equal to the energy level of an electron in the solid valence band. If RC is energetically allowed, an electron tunnels from the occupied valence band of the solid to the vacancy in the ion ─ causing neutralization. One electron is transferred in this case.

More often, however, the energy of the ion vacancy is lower than the Fermi sea of the solid. In this situation, a two-electron Auger neutralization (AN) transition can occur. One electron from the Fermi sea transfers to the lower energy vacancy in the ion (neutralization occurs) and a second electron is ejected from the solid valence band to vacuum to maintain energy conservation. AN processes take place at smaller interatomic distances in the 1-3 Å range.

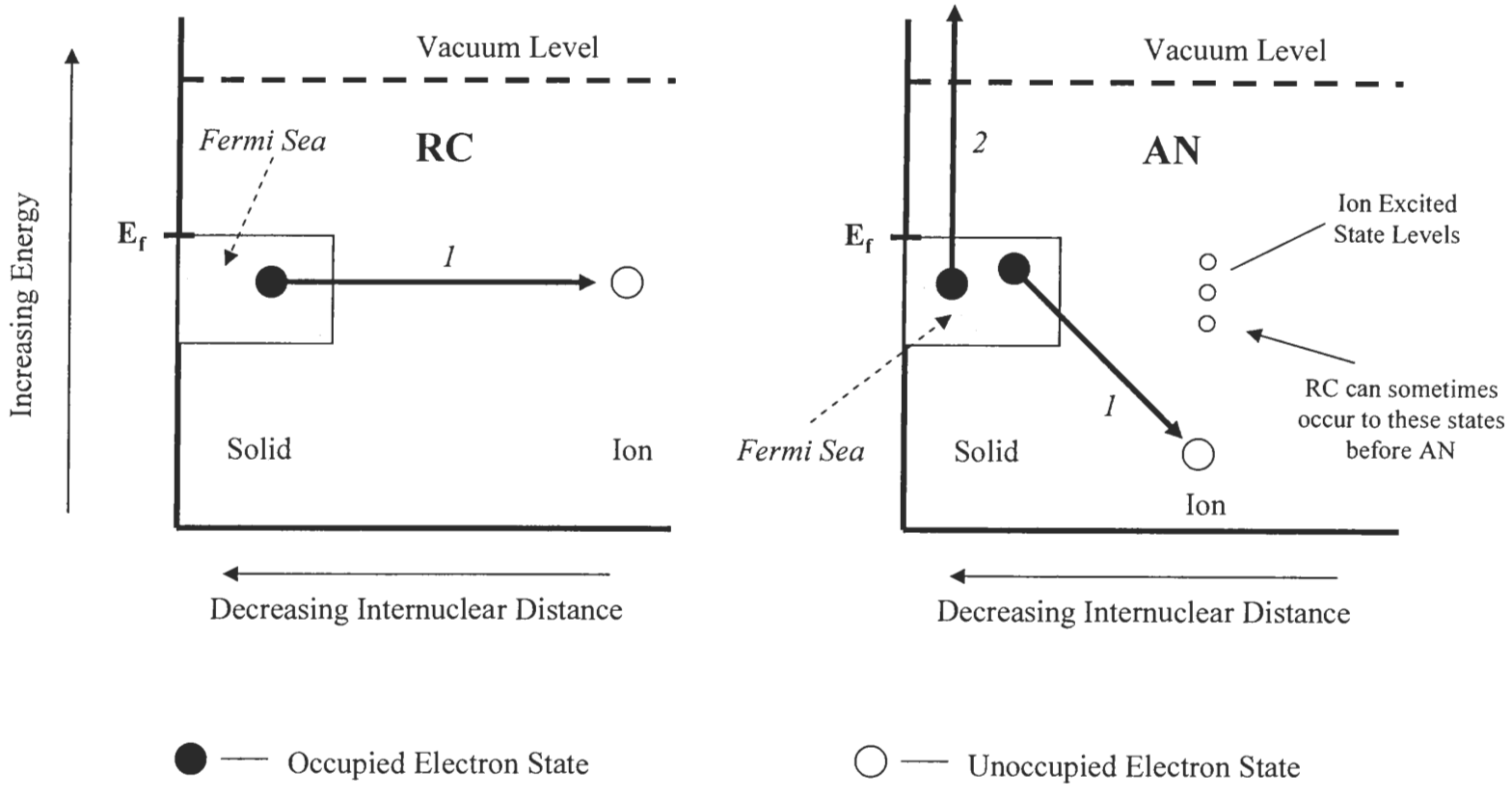

Figure 7.7: Depiction of the electron transfer processes that can occur between an ion and solid. (A) resonant electron capture by the ion – RC is a one-electron transition and (B) Auger neutralization – AN is a two-electron process where the extra potential energy from the initial electron movement causes a second electron to be ejected from the Fermi sea (valence band) of the solid out into vacuum $\mathbf{E_f}$ is the Fermi energy level.

For noble gas ions where ionization potentials are large, neutralization occurs most often by Auger events rather than direct RC transitions. However, AN transitions can be preceded by RC events between the Fermi sea and highly excited levels of the ion as shown in Fig 7.7.

The probability for electron exchange between an ion in the vicinity of a surface and the solid valence band is known as the electron exchange rate (or the transition probability per unit time along the incoming and outgoing trajectories). Note that the outgoing portion of the trajectory is quite important as the ion may not be neutralized along the incoming path or during the hard collision. The transition probability per unit time can be expressed as a function of the distance between the ion and the surface. Since atomic and molecular orbitals have a spatial dependency that decays exponentially, the transition rate also depends exponentially on the ion-surface distance. Therefore, we can write the following expression for the exchange rate (Rabalais, 2003):

$$\Gamma(z) = \Gamma_0 \exp\left(-\frac{z}{d}\right) \tag{7.17}$$

where,

$\Gamma(z) =$ electron exchange transition probability vs. distance
$\Gamma_0 =$ maximum bulk transition rate at zero distance
$z =$ distance between the ion and the surface (normal to the surface)
$d =$ characteristic decay length for the coupling between electron states

When a particle approaches or recedes from the surface, the probability that neutralization occurs within a time interval ∂t is just $\Gamma(z)\partial t = (\Gamma/\mathrm{v}_\perp)\partial z$, where $\mathrm{v}_\perp$ is the particle velocity perpendicular to the surface. We can then write a differential equation for the probability that an ion will reach a distance, z, from the surface along the incoming path without changing its charge state:

$$\frac{\partial P_{in}}{\partial z} = -\frac{\Gamma_{in}}{\mathrm{v}_{\mathrm{in}}} P_{in} \tag{7.18}$$

where,

P_{in} = probability that the ion survives along the incoming path
Γ_{in} = transition rate along the incoming path
v_{in} = ion velocity *perpendicular* to the surface on the incoming path

An analogous differential equation can be written for the outgoing path. Both of these differential equations can be integrated in turn from z to $+\infty$ to yield (Rabalais *op. cit*.):

$$P_{in} = \exp\left[-\frac{d \bullet \Gamma_{in,0}}{v_{in}} \exp\left(-\frac{z}{d}\right)\right] \tag{7.19}$$

$$P_{out} = \exp\left[-\frac{d \bullet \Gamma_{out,0}}{v_{out}} \exp\left(-\frac{z}{d}\right)\right] \tag{7.20}$$

where,

P_{in} = probability that the ion survives along the incoming path
P_{out} = probability that the ion survives along the outgoing path
v_{in} = ion velocity *perpendicular* to the surface on the incoming path
v_{out} = ion velocity *perpendicular* to the surface on the outgoing path

The overall probability for ion survival (both paths) is just the product of the probabilities for survival along the incoming and outgoing regions. Also, it is common to assume that the transition rates on the two path lengths are equal $\left(\Gamma_{in,0} = \Gamma_{out,0}\right)$ and that the charge interaction takes place at some distance of closest approach $\left(z_0\right)$. This allows z in Eqns. 7.19-7.20 to be set equal to z_0. Finally, we just lump all the constants in Eqns. 7.19-7.20 into one characteristic velocity leaving an expression for the overall survival probability of the ion:

$$P = \exp\left[-v_n\left(\frac{1}{v_{in}} + \frac{1}{v_{out}}\right)\right] \tag{7.21}$$

where,

P = overall survival probability for the ion (both path lengths)
v_n = characteristic ″neutralization″ velocity

Equation 7.21 is the take-home message for RC and AN events on metal surfaces. It says that the ion yield should exponentially increase as the incident and exit velocities get larger. Higher ion velocity means lower transition rate and more ion survival along both paths. Characteristic velocities have been evaluated for several collision systems and typical values are in the ~10^7 $^{cm}/_s$ range for metals (Rabalais *op. cit.*). We will revisit Eqn. 7.21 in our data analysis for Ne^+ scattering off surfaces to show that ion survival is responsible for the Ne^+ exit channel in a particular region of collision energies only.

7.7 Our Results of Ne^+ Scattering off Light Targets

We have conducted $^{20}Ne^+$ scattering studies on Mg, Al, Si(100), and Ti surfaces using our ion beamline system to investigate the near threshold behavior for inelastic collisions yielding directly scattered Ne^+ and Ne^{++} exit channels. Collision energies were varied from ~150-1300 eV at 90° scattering angle with scattered ion energy spectra recorded for 10 AMU (Ne^{++} only) and 20 AMU (Ne^+ only). In this way, absolutely no interference between charge states could occur in our system because the Ne^+ and Ne^{++} exits are measured separately. All ISS spectra were taken with a constant sector pass energy of 15 eV, giving a corresponding 15 eV quad mass filter flight energy for all cases. The quad was locked at 10 or 20 AMU with the resolution set for about 1 AMU pass width. Scans at 10 AMU were taken at every incident energy to make a definite determination of the energy threshold for Ne^{++} creation.

The scattering results for each of the targets will be discussed in the next few sections in light of BCA single collision predictions in the same manner as Chapter 6. The BCA model is represented as a set of straight lines which reflect the maximum predicted error in the exit energy, given the uncertainties in the projectile energy and scattering angle by the method discussed in Chapter 6. Scattering on Al and Si will be

discussed first to outline some of the phenomena that can be clearly seen in the scattered ion energy spectrum. Later, Mg and Ti will be addressed in light of the Al and Si results.

7.7.1 Adjustments for the Differential Scattering Cross Section

The intensity of scattered species from a surface is the result of collisions from a large number of particles which sample many different impact parameters. This ″multiple″ nature of the scattering process must be taken into account when comparing intensity data for scattered species at different projectile impact energies. It is common to introduce the differential scattering cross-section to account for this effect. Consider a target bombarded by a constant flux of ion species at the same incident energy. The differential scattering cross-section is defined as the fraction of incident particles scattered into a specific solid angle where observation of the scattered flux occurs:

$$\frac{dN_{d\Omega}}{N} = \sigma_{diff} \bullet d\Omega \tag{7.22}$$

where,

$dN_{d\Omega}$ = number of incident particles (ions and neutrals) scattered into solid angle $d\Omega$
N = number of incident particles impinging on the target per unit area
σ_{diff} = differential scattering cross-section
$d\Omega$ = solid angle for sampling the scattered flux

The differential scattering cross-section represents the relative angular intensity of scattered particles and can be calculated from the ″classical scattering integral″ presented in Chapter 2 using the following relation (Rabalais 2003):

$$\sigma_{diff} = \frac{b}{\sin\chi}\left|\frac{db}{d\chi}\right| \tag{7.23}$$

where,

$b =$ impact parameter
$\chi =$ center-of-mass frame scattering angle

The derivative $db/d\chi$ is obtained by direct differentiation of the classical scattering integral (Eqn. 2.18) after the method given in Ioup and Thomas, (1969). Evaluation of the cross-section at each projectile energy is required to account for the variation of scattered flux intensity (at different impact parameters) with the collision energy. The experimental intensity data (ion yields) presented in the rest of this chapter have been normalized using the differential scattering cross-section. This procedure is required to properly calculate the ″ion yield″ or ″ion fraction″ from the scattered ion intensity measured by the detector. The scattered ion yield or ion fraction $\left(Y^+\right)$ is defined as the fraction of incident projectile species that are not neutralized in the scattering process:

$$dN^+_{d\Omega} = \sigma_{diff} \bullet Y^+ \bullet N d\Omega \tag{7.24}$$

where,

$dN^+_{d\Omega} =$ intensity of scattered ions measured in the lab frame
$Y^+ =$ fraction of projectile ions surviving neutralization upon scattering

Proper comparison of the ion yield for different projectile impact energies requires that the cross-section dependence be ″normalized-out.″ Examining Eqn 7.24, the ion yield scales as

$$Y^+ \sim \frac{dN^+_{d\Omega}}{\sigma_{diff} N} \tag{7.25}$$

Therefore, all the intensity data has been scaled according to the relation below, to remove the cross section effect:

$$I\left(E_i\right) = \frac{\sigma_{diff,\max}}{\sigma_{diff,i}} \bullet dN^+_{d\Omega,i} \tag{7.26}$$

where,

$I(E_i)$ = scattered ion intensity (cross-section corrected) for projectile energy E_i

$\sigma_{diff,\max}$ = maximum cross-section for the data set (lowest impact energy)

$\sigma_{diff,i}$ = cross-section for impact energy E_i

$dN^{+}_{d\Omega,i}$ = scattered ion signal measured at the detector for impact energy E_i

The differential cross-sections were calculated through numerical integration of the expressions in Ioup and Thomas (1969) for the derivatives of the classical scattering integral at each collision energy.

7.7.2 Ne^{+} on Aluminum

The behavior of Ne^{+} scattering off polycrystalline Al exhibits a wonderful richness where a clear deviation from no-loss BCA can be seen along with a rapid turn-on for Ne^{++} generation. The raw scattered ion energy spectrum for Ne^{+} off Al at 315 eV impact energy is shown in Fig. 7.8a. The single collision peak is very close to the no-loss BCA predicted value. Also shown is a small higher energy hump that appears near the BCA location for a double bounce exit from two consecutive 45° deflections. It is not surprising that the double bounce is barely visible because the ion must survive two collisions without being neutralized. Recall that most multiple bounce phenomena occur for glancing incidence, rather than 45° incident angle as in our experiments (Neilhus *et al.,* 1993). An Ne^{++} exit channel was not detected at the 315 eV impact energy. On the other hand, Fig 7.8b shows scattered energy spectra for both Ne^{+} and Ne^{++} for an incident Ne^{+} energy of 875 eV. Clear shifts in the exit energies from the BCA model are seen for the Ne^{+} and Ne^{++} exits. The different sizes of these energy shifts give an indication of the inelastic losses in the hard collision along with a minor contribution from the continuous electron slowing for the incoming and outgoing trajectories.

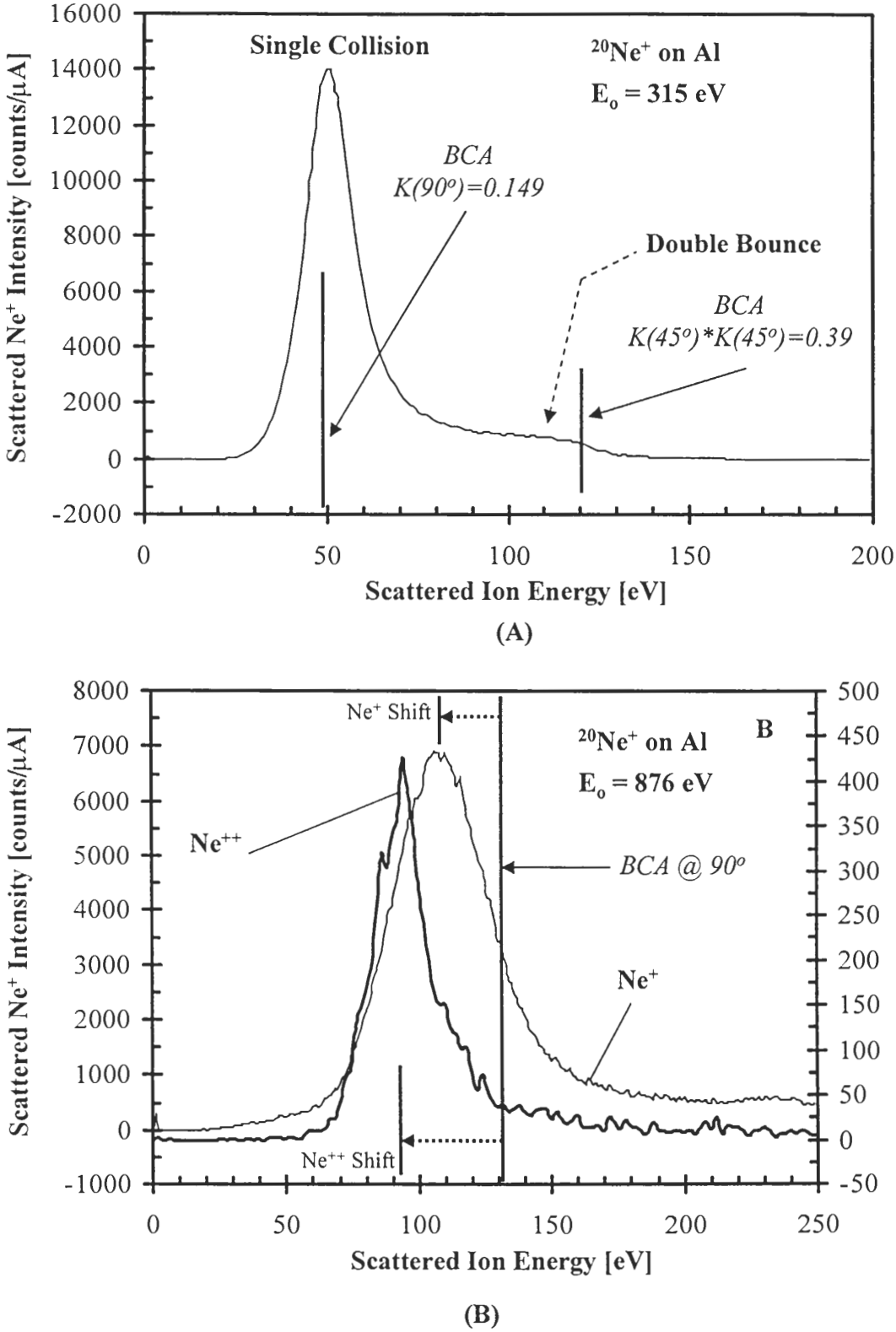

Figure 7.8: (A) Scattered Ne^{+} spectrum off Al showing single and double bounce. (B) Ne^{+} and Ne^{++} exit energy spectra off Al showing inelastic losses.

A summary plot of the measured exit energies for the Ne^{+} and Ne^{++} scattering channels along with the Ne^{+} and Ne^{++} intensity (integrated counts / μA incident beam current, normalized by the differential cross-section) is given in Fig. 7.9 for Ne^{+} scattering off Al from 150-1300 eV. Error bars on the scattering data are shown for the data below 500 eV only to avoid cluttering the plot. Future graphs have error bars that are the same size $\left(\Delta E_0 = \pm 10\ eV,\ \Delta E_{exit} = \pm 5\ eV\right)$, but they are left off for clarity. Also, only one data set for the Ne^{+} and Ne^{++} intensities is shown to avoid clutter as well.

Below about 400 eV, the experimental data for the Ne^{+} exit energy follow the no-loss BCA prediction very well. At 400 eV, the experimental data begins to scatter and a few lower-than-BCA exit energies for Ne^{+} are registered. Around 500 eV, a clear offset of ~13 eV from the BCA value is observed for the Ne^{+} exit which grows larger to ~33 eV as the impact energy is raised to 1300 eV. Remember that raw losses occur in the lab frame, but the total collision inelasticity is calculated from the center-of-mass (CM) frame energy loss. For our setup at 90°, the conversion from lab to CM frame amplifies the raw loss data by ~1.74 for Ne on Al (see Chapter 2).

Of particular interest at ~500 eV is the sudden appearance of Ne^{++} in the scattered ion energy spectrum along with a decrease in the Ne^{+} intensity. In the ″inelastic″ range above 500 eV, a linear response in the Ne^{+} and Ne^{++} exit energies is seen with very different offsets (inelasticities) from the BCA model. It is noteworthy that the Ne^{+} and Ne^{++} exit energies track upward with increasing impact energy with *identical* slopes (note the regression lines) which are different from the BCA predicted kinematic factor. The clear offset behavior of the Ne^{+} and Ne^{++} exits signifies a definite inelasticity which occurs during the hard collision. Also, the Ne^{++} signal intensity grows with increasing impact energy indicating that the Ne^{++} generation mechanism becomes more and more favorable as the impact energy is raised.

The sharp onset of the Ne^{++} channel near 500 eV indicates an excitation mechanism which is dependent on the apsis distance. There seems to exist a minimum distance in the close encounter which allows for specific atomic orbitals of projectile and target atoms to overlap enough that some excitation process is turned on.

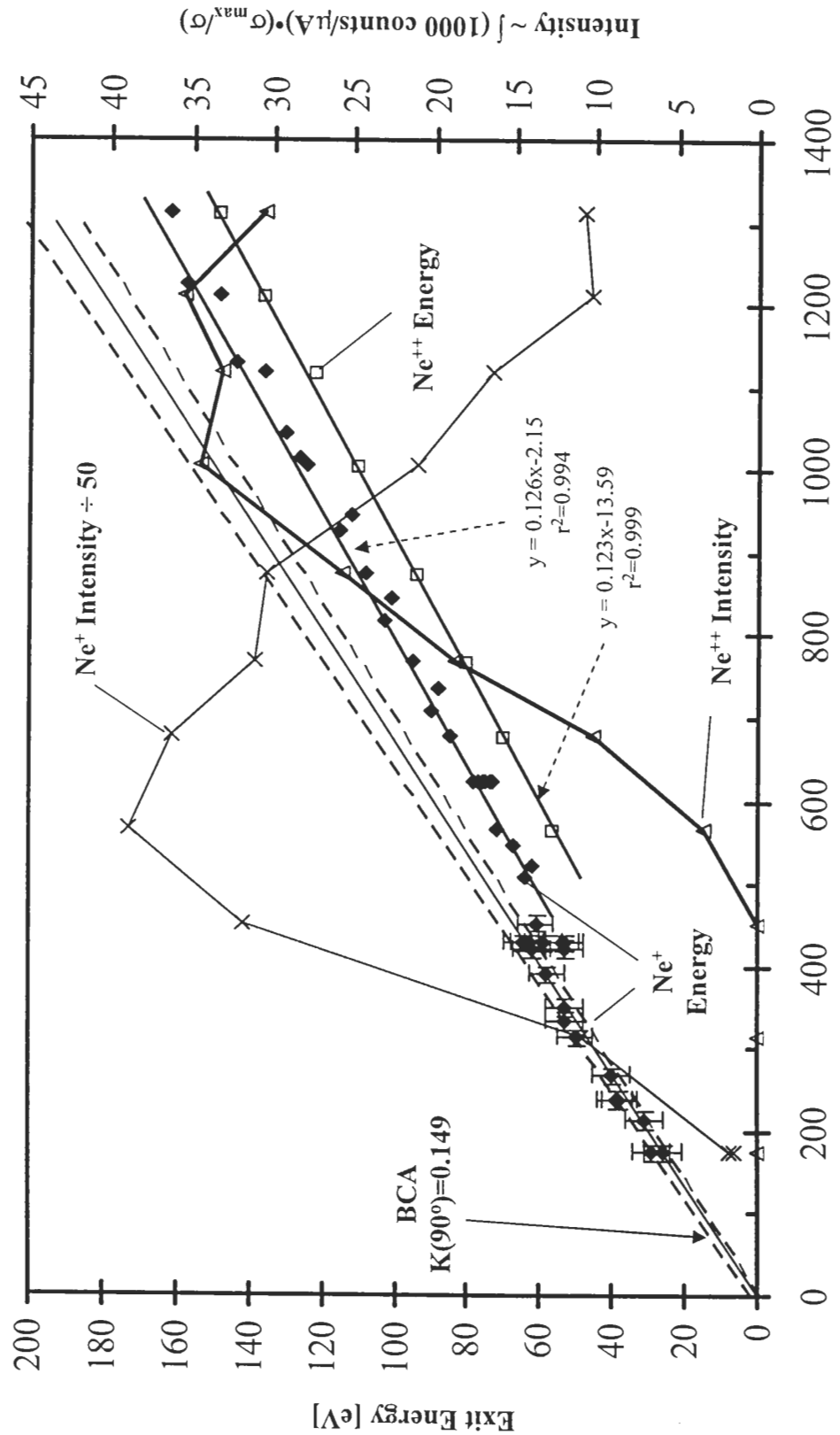

Figure 7.9: Ne^+, Ne^{++} exit energy and Ne^+, Ne^{++} signal intensity for Ne^+ bombardment of Al at 90° lab angle.

The projectile, either Ne^+ or Ne^0 from Auger neutralization along the incoming path, is excited to the Ne^{++} state or an excited precursor state which decays to Ne^{++} away from the target surface. The identical slope dependence of the Ne^+ and Ne^{++} as well as the absolute offsets from BCA may provide clues to possible Ne^{++} generation mechanisms.

Ion Survival

The Ne^+ intensity data in Fig. 7.9 rises considerably in the elastic region (obeying BCA) up to ~450 eV, where it then begins to dive downward. This increase in Ne^+ intensity is suggestive of an increased ion survival rate as the impact energy is raised. To evaluate the ion survival hypothesis, the intensity data can be analyzed in the framework of an Auger neutralization rate that is mediated by the approach and exit velocities. In Section 7.6, we mentioned that the ion survival probability depends exponentially on the time that the ion spends in the surface region (inversely dependent on the approach and exit velocity perpendicular to the surface). We can evaluate this dependence for our Ne^+ intensity data by plotting the logarithm of the intensity (intensity ~ ion yield ~ survival probability) against the inverse approach and exit velocities ($1/v_{in} + 1/v_{out}$) as given by Eqn. 7.21. In this way, a linear dependency (if it is linear) will give a slope that is equal to the ″characteristic″ neutralization velocity $\left(v_n\right)$. This evaluation is presented in Fig. 7.10 for the scattered Ne^+ intensity off Al for impact energies < 450 eV (the scattered Ne^+ counts/μA beam current was normalized by the maximum intensity to force the log scale to go to zero at the maximum intensity).

As shown in Fig. 7.10, the relation is linear, giving a characteristic neutralization velocity of $6.0 \bullet 10^{6}$ $^{cm}/_{s}$ for Ne^+ on Al. Rabalais *et al.* (1985a) has reported a value of $4.9 \bullet 10^{6}$ $^{cm}/_{s}$ for Ne^+ on Mg. This linear dependency in our Ne^+ intensity data and the very reasonable value for the neutralization velocity of Ne^+ on Al show that ion survival, with no inelastic losses, is most probably the mechanism for the scattered Ne^+ signal below ~ 450 eV. Inverting the neutralization velocity gives an Auger transition rate on the order of $2\text{-}5 \bullet 10^{14}$ sec^{-1} for 1-3 Å, which is similar to the results presented by Hagstrum (1954), for rare gas ions on tungsten ($6.4 \bullet 10^{14}$ sec^{-1}).

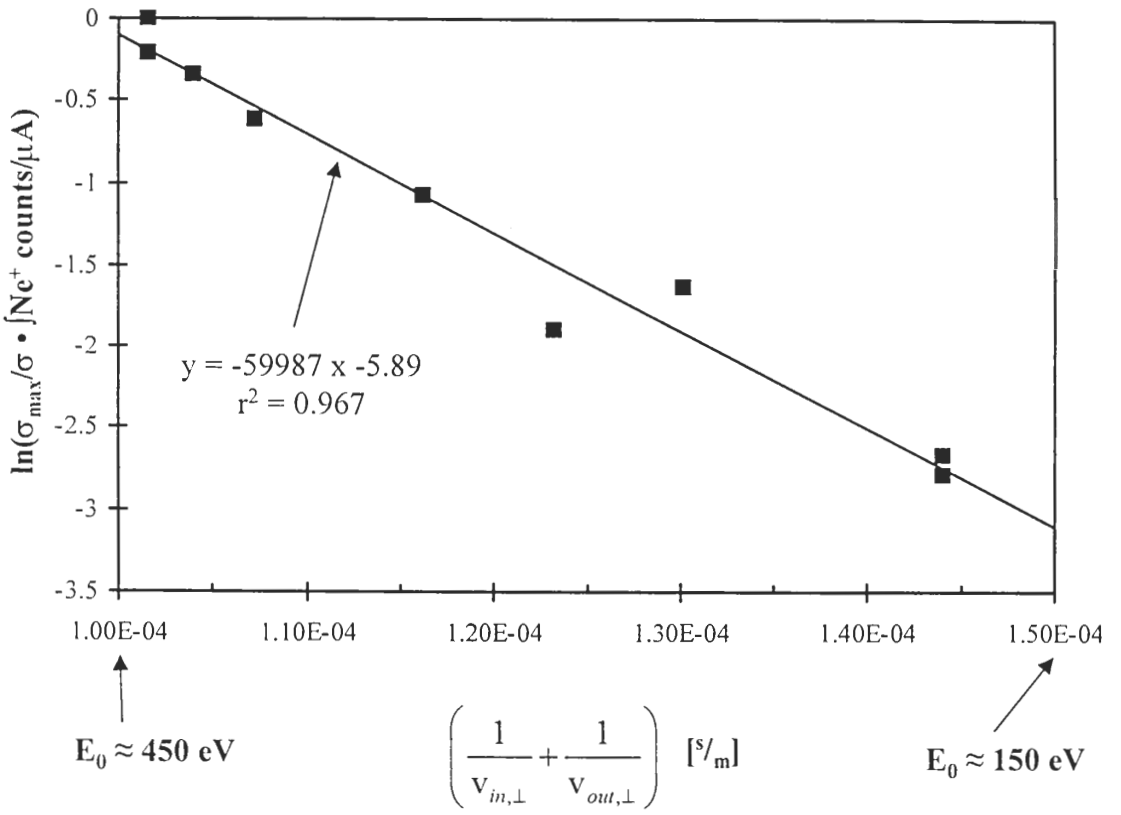

Figure 7.10: Determination of the characteristic neutralization velocity for Ne^+ on Al. The logarithm of the scattered Ne^+ intensity (~ ion yield) for $Ne^+ \rightarrow Al$ below 450 eV shows a correlation with the effective time that the ion spends in the near-surface region along the incoming ($1/v_{in}$) and outgoing ($1/v_{out}$) paths. The regression line gives a characteristic neutralization velocity of $6.0 \cdot 10^6$ $^{cm}/_{s}$ and an Auger transition rate of $2\text{-}5 \cdot 10^{14}$ sec^{-1} for 1-3 Å (typical Auger neutralization distance). See text for explanations.

Near the 450-500 eV region, the ″opening-up″ of inelastic loss channels occurs, which causes a reduction in the Ne^{+} scattered ion intensity along with the formation of Ne^{++}.

Inelasticities

Ascione *et al.* (1997) have fit their energy loss data for the $Ne^{+}\rightarrow Al$ system using the Oen and Robinson method for the continuous loss as represented by

$$Q_i = c_i\left(\frac{A\sqrt{E_i}}{\pi a_F^2}\right)\exp\left(\frac{-0.3R_{\min}}{a_F}\right) \tag{7.27}$$

where,

$Q_{1,3} =$ continuous energy loss along incoming (1) or outgoing (3) path
$c_i =$ fitting parameter
$A =$ screening parameter from the LSS theory (Lindhard and Sharff, 1961)
$E_i =$ particle energy along path (1) or (3)
$a_F =$ Firsov screening length
$R_{\min} =$ apsis or distance of closest approach

For the $Ne^{+}\rightarrow Al$ system, $A = 0.0283$. The fitting parameters were determined as $c_1 = 0.55$ and $c_3 = 0.6$ for their fixed energy study at 1950 eV impact energy with variable scattering angle measurements to give an inelasticity of 86 eV for the Ne^{++} exit. The apsis distance was calculated using the familiar Molière approximation to the Thomas-Fermi (TFM) screened potential with a Firsov screening length (Eqn. 2.10 gives ~0.131 Å).

We have used these same fitting parameters for the Oen and Robinson formula to remove the continuous loss from our scattered ion energy measurements. The apsis distance for each impact energy tested in our study was calculated by numerical integration of the classical scattering integral for the TFM potential with analogous use of the Firsov screening length. Particulars of this calculation are mentioned in Chapter 2.

Recall the expression derived in Chapter 2 (Eqn. 2.23) for the exit energy associated with the BCA prediction including the continuous straggling loss (through

Eqn. 7.27) and binary inelasticity occurring in the hard collision (for 90° lab scattering angle):

$$E_{exit} = \frac{\gamma - 1}{\gamma + 1}\left(E_0 - Q_1\right) - \frac{\gamma}{\gamma + 1}Q_{bin} - Q_3 \tag{7.28}$$

where,

$E_0, E_{exit} =$ incident and scattered projectile energies
$\gamma =$ target-to-projectile mass ratio
$Q_1, Q_3 =$ energy loss along incoming (1) and outgoing (3) paths
$Q_{bin} =$ inelasticity occurring during the hard collision

Incorporating the Oen and Robinson expression for the continuous loss, the exit energy becomes

$$E_{exit} = \frac{\gamma - 1}{\gamma + 1}E_0 - \frac{A}{\pi a_F^2}\exp\left(\frac{-0.3R_{\min}}{a_F}\right)\left(\frac{\gamma - 1}{\gamma + 1}c_1\sqrt{E_0} + c_3\sqrt{E_3}\right) - \frac{\gamma}{\gamma + 1}Q_{bin} \tag{7.29}$$

This expression includes the energy E_3, which is the energy of the particle directly after the hard collision, but before the continuous loss occurs on the outgoing path, as the particle travels away from the target nucleus. This energy, E_3, is not known *a priori*. One could assume that E_3 is nearly equal to E_{exit}, measured in the lab frame. This is not a bad assumption because the Q_3 loss is a few volts compared to at least a 100 eV for E_{exit} and that the square root dependency decreases the error even further. Therefore, we arrive at an expression that can be used to determine the binary inelasticity Q_{bin}, including the continuous losses:

$$E_{exit} = \frac{\gamma - 1}{\gamma + 1}E_0 - \frac{A}{\pi a_F^2}\exp\left(\frac{-0.3R_{\min}}{a_F}\right)\left(\frac{\gamma - 1}{\gamma + 1}c_1\sqrt{E_0} + c_3\sqrt{E_{exit}}\right) - \frac{\gamma}{\gamma + 1}Q_{bin} \tag{7.30}$$

Using expression 7.30 and the c_i values of Ascione *et al.* for the $Ne^+ \rightarrow Al$ system ($c_1 = 0.55$ and $c_3 = 0.6$), the binary inelasticity can be calculated for the Ne^+ and Ne^{++} exits, provided that the apsides are calculated at every incident energy. Results for this determination are shown in Fig. 7.11a-b for our energy loss data. The inelasticity values of Ascione *et al*. for $Ne^+ \rightarrow Al$ at 1950 eV are indicated by arrows with the transitions listed. In addition, several other energy loss values associated with direct transitions as well as the $Ne^+ \rightarrow Ne^{+**}$ pump requirement (Auger data - peak III mention earlier) are indicated.

<u>Ne^+ Results</u>

Our experimental data at low energy shows a nearly constant (within data scatter) inelasticity of zero for Ne^+ until 400-500 eV. The Ne^+ inelasticity begins to take off and rises continually until a saturation-like value is reached in the 40-50 eV range. It is interesting that the jump in the exit energy data in Fig. 7.9 corresponds to an inelasticity between 20-25 eV ─ this range is very near the direct transition for simple ionization of $Ne^0 \rightarrow Ne^+$ at 21.5 eV as well as $Ne^+(2p^5) \rightarrow Ne^{+*}(2p^4 3s)$ at ~27-28 eV (Grotrian diagrams). A turn-on of the Ne^+ exit inelasticity in the 20 eV range seems consistent initially with the picture that Ne^+ is neutralized to Ne^0 on the incoming path and then the Ne^0 is directly ionized in the hard collision back to Ne^+. This is a one-electron excitation process.

Souda *et al.* (1995) showed that the Ne^+ exit is insensitive to the incoming charge state at 2 keV impact, therefore, the ~20 eV required to remake the Ne^+ ion in the hard collision seems consistent. However, the decrease in the Ne^+ signal at the turn-on point is concomitant with the Ne^+ inelasticity onset. If $Ne^0 \rightarrow Ne^+$ by direction ionization were the cause of the Ne^+ inelasticity, why would the Ne^+ intensity suddenly drop instead of rise? We will discuss this point at length in the commentary section. Finally, our data do appear to approach the 45 eV value of Ascione *op. cit*., in the high energy limit where the $Ne^0 \rightarrow Ne^{**}$ transition (two electrons), followed by autoionization to Ne^+ is hypothesized to occur.

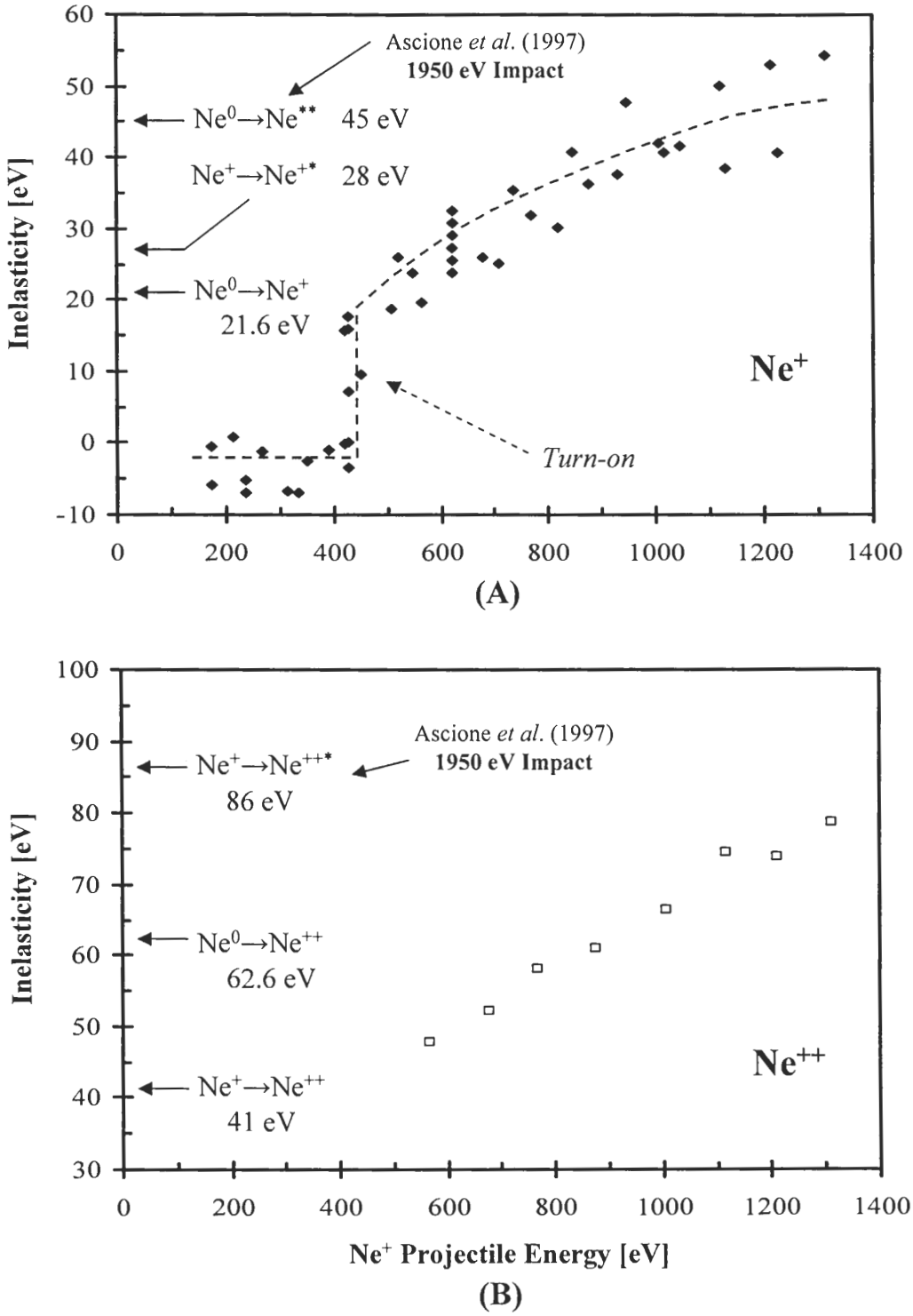

Figure 7.11: Measured inelasticities for (A) Ne^+ and (B) Ne^{++} for Ne^+ bombardment of Al. The 45 eV and 86 eV excitation schemes shown have been hypothesized by Ascione *et al.* (1997) for 1950 eV Ne^+ impact on Al. Energies for one and two-electron direct transitions are shown. Note: line provided in (A) is only intended to guide the eye.

Note, however, that the ~20-30 eV initial inelasticity is too small for a two-electron process on the neutral state in the hard collision for our measurements at 90° lab angle in the low-energy range. The lowest energy requirement for a two-electron transition from the neutral is $Ne^0(2p^6) \rightarrow Ne^{**}(2p^4 3s^2)$ at ~45 eV.

<u>Ne^{++} Results</u>

The Ne^{++} inelasticity data begins near 50 eV and increases up to nearly 80 eV at the highest energy tested. The 86 eV transition proposed by Ascione *et al.* (1997) is given along with the direct routes. The 50 eV loss at the onset of Ne^{++} generation is bracketed by the two direct ionization process for $Ne^+ \rightarrow Ne^{++}$ at 41 eV and $Ne^0 \rightarrow Ne^{++}$ at 62.5 eV. The process proposed by Ascione *op. cit*. for 1950 eV impact seems much too high for our threshold measurements, however, our Ne^{++} inelasticity data do seem to approach the 86 eV value in the high energy limit. Since Souda *et al.* (1995) showed that Ne^{++} was generated for Ne^+ but <u>not</u> for Ne^0 impact, the direct transition from Ne^+ to Ne^{++} (requiring at least 41 eV) seems more plausible. The 50 eV initial inelasticity is enough to pump the $Ne^+ \rightarrow Ne^{++}$ transition (one electron), but not enough for two-electron transitions such as $Ne^0 \rightarrow Ne^{++}$ (63 eV) or Ne^{++} from the autoionization decay of an initial Ne^{+**} state (we estimate $Ne^+(2p^5) \rightarrow Ne^{+**}(2p^3 3s^2)$ at ~70-75 eV). The 50 eV is more consistent with Ne^{++} generation from a surviving Ne^+ (requiring less pump energy).

► There are many questions which come to mind at this point, but we must digress for a moment to look at the $Ne^+ \rightarrow Al$ collision from a slightly different perspective:

The Orbital Overlap Picture

Back in 1960, Slater (1960) completed calculations on the effective size of the individual electron shells for many light atoms. He used the self-consistent field method to determine the radial distance at which the individual atomic orbital (AO) wavefunctions exhibited a maximum value in charge density. These calculations give a

good feeling for the size of the electron shells in an atom. His results for Ne and Al are shown in Table 7.4.

Table 7.4: Distance of maximum radial charge density for atomic orbitals (in Å). Data taken from Slater (1960).

Atom	1s	2s	2p	3s	3p
Ne	0.055	0.37	0.32		
Al	0.042	0.27	0.23	1.16	1.21

This table provides clues about possible excitation channels when we compare AO sizes with the distance of closest approach reached during the hard collision between the Ne^+ projectile and Al target atom. For example, adding up the combined distance for individual AO's from the table and comparing it with the apsis can help to picture the AO overlaps which may occur in an $Ne^+ \rightarrow Al$ collision. Locations of the various permutations of levels in the above table with our apsis calculation and experimental scattering data for the $Ne^+ \rightarrow Al$ system are shown in Fig. 7.12. Our scattering studies from 150-1300 eV at 90° are equivalent to apsides from ~0.9 Å down to ~0.4 Å for Ne^+ on Al.

As seen on the graph, the Ne^{++} creation channel begins to occur around an apsis distance of 0.6-0.64 Å. From a naïve point of view, the Ne^{++} is generated in the region where the maximum charge densities of the 2s and 2p states of the projectile and target atoms begin to overlap. The hypothesis is that the excitation process requires an overlap of these orbital states for the mechanism which generates the Ne^{++} exit channel to occur. This simple idea suggests that overlap of the Ne 2s or 2p with the valence band of Al (3s and 3p states) at distances greater than 1 Å *cannot* result in excitation of the Ne^{++} precursor state. Furthermore, the sudden take-off in the Ne^+ inelasticity at <0.65 Å also seems concomitant with a required Ne 2s or 2p overlap with more than just the target valence band (the 3s valence states are off the graph).

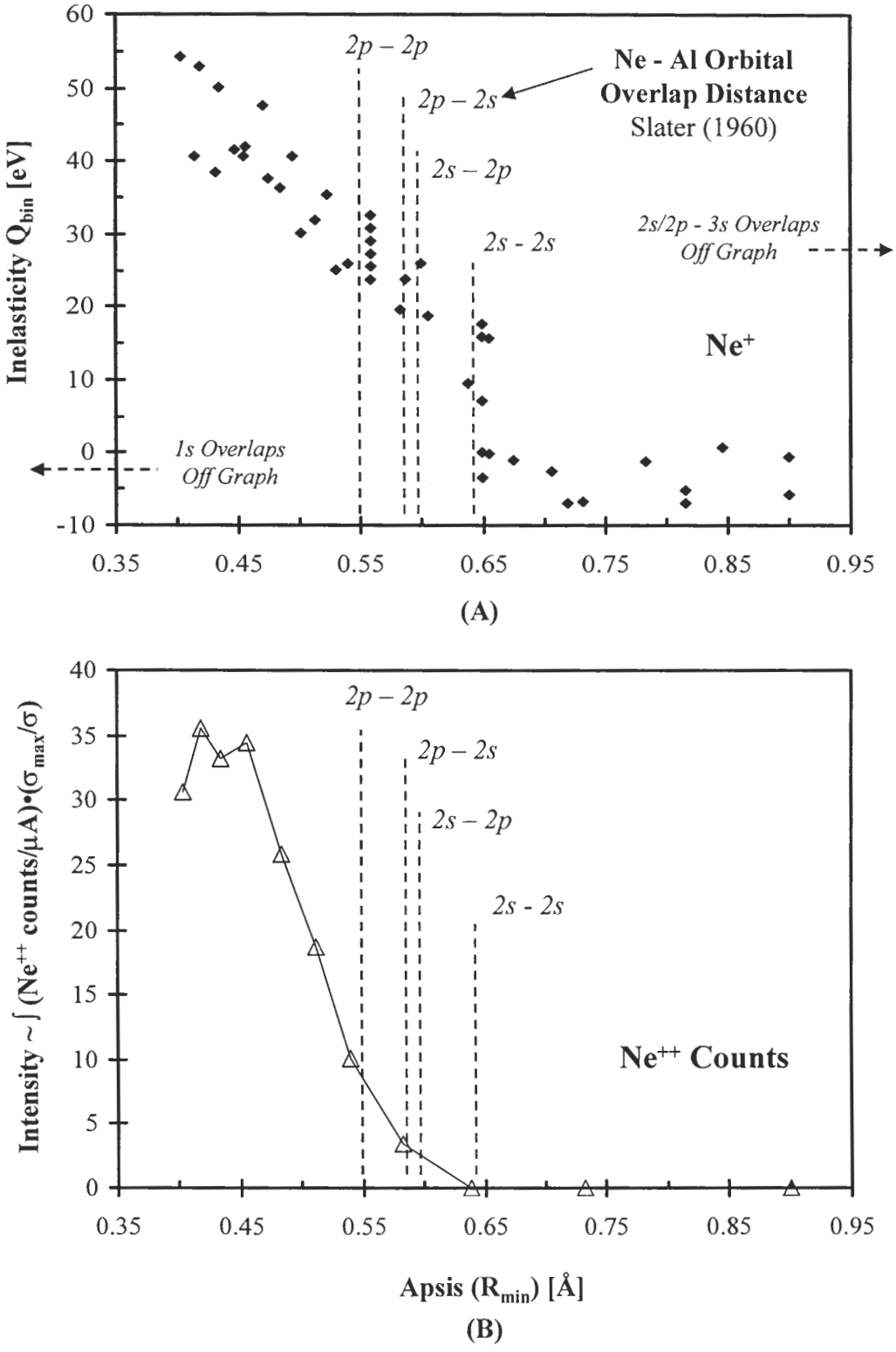

Figure 7.12: (A) measured inelasticity for Ne^+ and (B) Ne^{++} signal intensity for Ne^+ on Al. Collision apsides calculated using the TFM potential for Ne^+ on Al at 90°. Also shown are calculated overlap distances for atomic orbital states of the collision partners using the data of Slater (1960).

Let us summarize our data in light of the AO overlap picture:

1) The Ne^+ exit channel follows no-loss BCA very well below 420 eV.

2) The Ne^+ signal intensity below 420 eV follows the expected trend of more ion survival at higher approach and exit velocities given by Eqn. 7.21. We have determined a characteristic Auger neutralization velocity of $6.0 \bullet 10^{6\ cm}/_{s}$ for Ne^+ on Al which is very close to the measurements for a similar collision system ($Ne^+ \rightarrow Mg$).

3) At 420 eV, the Ne^+ exit channel begins to scatter. Between 500-600 eV, the Ne^+ is clearly inelastic by 20-30 eV, which steadily increases to ~45 eV for 1300 eV impact. The ~20-30 eV inelasticity is near the range for direct ionization of $Ne^0 \rightarrow Ne^+$ (21.5 eV) as well as $Ne^+(2p^5) \rightarrow Ne^{+*}(2p^4 3s)$ at ~27 eV. The Ne^+ inelasticity onset corresponds to an apsis at 0.6-0.65 Å.

4) Ne^{++} generation ″turns on″ at 500 eV, simultaneously with the Ne^+ inelasticity onset.

5) The binary inelasticity for Ne^{++} starts off at ~50 eV for 500 eV impact and rises to ~80 eV for 1300 eV impact. Direct ionization of $Ne^+ \rightarrow Ne^{++}$ requires 41 eV.

6) In the high energy limit *only*, our Ne^+ and Ne^{++} inelasticity data approach the values which Ascione *et al.* (1997) have reported for $Ne^+ \rightarrow Al$ at 1950 eV: (a) $Ne^0 \rightarrow Ne^{**}$ at 45 eV, autoionizing to Ne^+ and (b) $Ne^{++*} \rightarrow Ne^{++}$ at 86 eV.

7) The Ne^+ inelasticity and Ne^{++} generation ″turn-on″ seem to occur when the 2s or 2p AO's of the projectile Ne and target atom overlap (when L-L shell overlap occurs).

Commentary

It seems that our measurements in the threshold region for Ne^{+} and Ne^{++} are quite different from what has been reported for $Ne^{+}\rightarrow Al$ at 1950 eV impact by Ascione *et al.* (1997). However, in the high energy limit, our inelasticity data do seem to approach their values for both Ne^{+} and Ne^{++}. The proposed loss mechanisms for Ne^{+} and Ne^{++} at 1950 eV require more pump energy (45 eV and 86 eV) than we see available in the threshold region of 500-1300 eV ─ as evidenced by smaller deviations in the exit energy from the no-loss BCA single collision values. It does not seem that the two-electron loss mechanisms proposed at higher energies are operative at lower energy. In addition, their Ne^{++} generation mechanism from $Ne^{+}\rightarrow Ne^{++*}$ (requiring 86 eV) seems unlikely to be responsible for Ne^{++} generation at lower energies where the inelasticity is much too small (~50 eV). A smaller inelasticity would tend to favor a one-electron process for Ne^{++} generation.

Careful inspection of the data of Tolstogouzov *et al.* (1999) for Ne^{+} on Al does show a downturn in the inelasticities from 45 eV (Ne^{+}) and 100 eV (Ne^{++}) below 1500 eV impact. This falloff at lower energy lead the authors to quote the 45 and 100 eV values for collision energies of 1500 eV and up *only*. Unfortunately, they did not push the beam energy much below 1 keV.

Our measurements indicate a threshold impact energy for the Ne^{++} generation channel between 400-500 eV for a 90° exit. It is interesting that the data from Souda *et al.* (1995) mentions a threshold energy of ~600 eV for Ne^{++} generation at 60° exit for $Ne^{+}\rightarrow Al$. Considering that our 90° observation angle will probe a smaller apsis distance than their work at 60° exit ─ for the *same* impact energy ─ the lower threshold energy seen in our data makes good sense. The threshold energy at 90° exit must be smaller than that for 60° because the collision is more violent at 90°. From this perspective, our threshold for Ne^{++} generation is totally consistent.

Although it may be slightly out of place, a discussion about ISS trends in the $Ne^{+}\rightarrow Si$ system is instructive at this point. Xu *et al.* (1998) have made measurements in the threshold region for the $Ne^{+}\rightarrow Si$ system. They mention an Ne^{+} inelasticity of 5-6 eV at 500 eV impact which *increases* steadily to ~45 eV for 1950 eV impact. This

observation of an increasing inelasticity for the Ne^+ exit from the $Ne^+ \rightarrow Si$ collision is echoed in our $Ne^+ \rightarrow Al$ data. Xu associates the 5-6 eV loss at 500 eV to valence band excitation of the Si. They do not provide any explanation for the inelasticity increase, but simply say that the Ne^+ inelasticity at 1400 eV and 1950 eV impact is caused by the Ne^{**} excitation scheme mentioned earlier. This explanation for high energy impact does not provide any help for what may be happening at lower energies. What also does not make sense with their picture is how the collision evolves from a simple valence band loss at low energy to a clear 45 eV loss at 1950 eV that is attributed to the $Ne^0 \rightarrow Ne^{**}$ pump scheme. Some obvious questions now arise:

Question: Why is there Ne^+ that follows no-loss BCA below 420 eV?

We have shown in our Ne^+ intensity data that the ion survival rate below 420 eV follows the expected trend of an exponential dependence of the yield on the time that the ion spends in the near-surface region (as measured by the reciprocal velocities on the incoming and outgoing paths – Eqn. 7.21). Therefore, the no-loss Ne^+ exit most likely originates from ions which have survived neutralization along the incoming path, go through the hard collision as ions with no inelastic losses, and survive neutralization on the outgoing path. Then, at 450-550 eV, the Ne^+ intensity turns downward, the Ne^+ exit shows a ~20-30 eV hard collision loss, and Ne^{++} begins to form with ~50 eV hard collision loss. It is surprising that all three of these events occur simultaneously ─ indicating that a common excitation mechanism or precursor state may be involved.

Questions: Why does the Ne^+ intensity begin to decrease?
What mechanism causes the Ne^+ inelasticity onset?
What mechanism generates the Ne^{++} at low energy?
Why does the inelasticity increase?

In an effort to answer these questions, it is instructive to introduce the MO correlation diagram for the Ne-Al system that has been calculated by Souda *et al.* (1996). A reproduction of Souda's MO diagram is given in Fig. 7.13 along with a ″shifted″ energy scale on the right side of the figure. The vacuum level and approximate locations for the valance and conduction bands are also shown. The 4fσ MO, which is correlated with the Ne 2p AO, is strongly promoted when the internuclear distance in the hard collision reaches ~0.65-0.7 Å. The 4fσ crosses both the valence and conduction bands as well as the vacuum level within a narrow apsis range once the apsis ″threshold″ of ~0.65 Å has been reached.

We shall use the curve-crossings of the 4fσ MO with the valance band (VB) and vacuum level to qualitatively explain our experimental observations: (1) Ne^+ signal decrease, (2) Ne^+ inelasticity, and (3) Ne^{++} generation at the ″threshold″ region near 0.65 Å. Although the MO diagram in Fig. 7.13 was calculated for the quasi molecule $(NeAl)^0$ (Ne^0 at ~-20eV (shifted scale on the right) to Ne^+ at the vacuum level), the MO diagram is similar for an Ne^+ ($2p^5$) projectile (near -41 eV) with Ne^{++} at the vacuum level. The promotion of the 4fσ formed from an Ne^0 projectile, versus an Ne^+ projectile, should occur at nearly the same internuclear distance, so the curve-crossings with the VB and vacuum level are analogous for both projectile cases. The 4fσ MO promoted from Ne^+ should be slightly more repulsive than from the Ne^0, so curve-crossings of the 4fσ correlated with Ne^+, if anything, should occur at slightly *larger* apsides than for Ne^0.

If the hard collision occurs with an apsis distance larger than ~0.65 Å, the 4fσ is not promoted ─ resulting in no curve-crossings. Therefore, scattering should be purely elastic with no losses at lower projectile incident energies…..which it is in our experimental data for apsides >0.65 Å (refer back to Fig. 7.12). Several other authors have seen this ″collision-induced neutralization″ (CIN) phenomenon that suddenly causes the scattered ion yield to decrease once a threshold apsis has been reached. In an identical fashion to our $Ne^+ \rightarrow$Al data, $Ne^+ \rightarrow$Ga and $Ne^+ \rightarrow$In from Tolstogouzov *et al.* (2003) and $He^+ \rightarrow$Al from Draxler *et al.* (2002) show good agreement with Auger neutralization at low projectile energy (increasing ion yield with energy), followed by a sudden decrease in the yield at a threshold collision energy.

When the hard collision becomes more violent and the apsis decreases below ~0.65 Å, the 4fσ becomes increasingly promoted. If the quasi molecule in the collision develops in a $3d\pi^4 4f\sigma^1$ configuration (the Ne 2p vacancy is promoted up in the 4fσ, rather than being demoted in the 3dπ), the 4fσ vacancy can be filled by resonant capture (RC) from the VB of the target as soon as the 4fσ is promoted above the bottom of the VB edge (< 0.65 Å). In this case, the projectile has been neutralized in the hard collision ─ causing the Ne^+ scattered ion yield to decrease (as seen in our data for apsides < 0.65 Å). A block diagram for the $3d\pi^4 4f\sigma^1$ quasi molecule state is given in Fig. 7.14, showing electron movements into and out of the 4fσ MO, depending on how strongly the MO state is promoted.

If the neutral core state with the newly filled vacancy is promoted even further, it can be seen from the figure (7.14) that an electron can be irreversibly lost to an empty conduction band state or promoted all the way to vacuum. When this loss to vacuum occurs, the electron can be ″kicked out″ with a significant kinetic energy. Referring back to the MO correlation diagram (Fig. 7.13), we can see that the 4fσ is promoted to higher and higher energies above the vacuum level, where the excess energy of promotion could be carried away from the collision in the kinetic energy of the electron ejected to vacuum ─ possibly explaining the increasing Ne^+ inelasticity.

The newly formed Ne^+ ($3d\pi^4 4f\sigma^1$) core state at the vacuum level would descend on the same potential energy (PE) curve, where the vacancy may be re-filled by resonant capture from the valance band (analogous to the vacancy filling on the PE curve ascent). If the vacancy is filled, a neutral Ne exits the collision. However, if the vacancy is not filled as the Ne^+ core descends the PE curve, an inelastic Ne^+ exit species will be seen. One might think that the energy loss required to pull off the electron from the Ne^0 precursor is ~21 eV (ionization potential for Ne^0), but we must remember that the electron transferred to fill the initial vacancy (which made the Ne^0 from Ne^+ on the ascent) is provided by the valence band of the target (at higher potential energy).

The qualitative formalism given in Fig. 7.14 is based on the MO picture of electron promotion during the hard collision. However, the above argument can only explain the Ne^+ yield decrease and Ne^+ inelasticity.

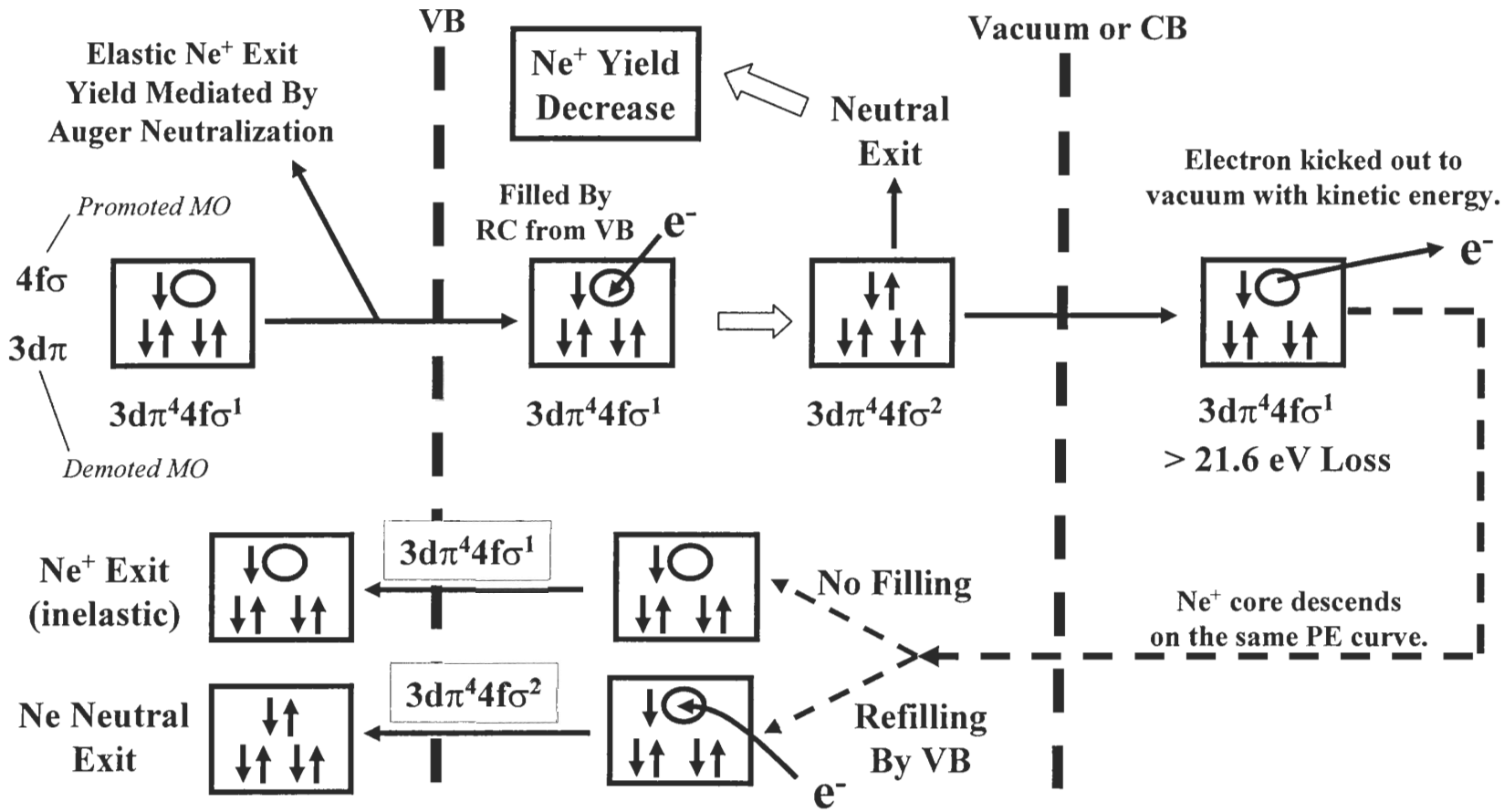

Figure 7.14: Block diagram showing the various outcomes of the hard collision for the $3d\pi^4 4f\sigma^1$ quasi-molecule state. If the apsis is large and the promoted 4fσ never reaches the VB, an elastically scattered Ne^+ exit results. The Ne^+ yield decrease is mediated by resonant capture (RC) from the filled valence band states, at slightly smaller apsis (higher collision energy). Finally, the 4fσ MO can be promoted all the way to the vacuum level, where an electron is irreversibly lost. The Ne^+ core descends on the same potential energy (PE) curve and may be re-filled by RC from the VB.

Creation of Ne^{++} at the same turn-on apsis threshold must therefore result from a different quasi molecule state in the hard collision. Consider the block diagram shown in Fig. 7.15. If the Ne^{+} vacancy is demoted into the 3dπ MO, the collision occurs with a quasi molecule configuration of $3d\pi^3 4f\sigma^2$. The MO correlation diagram shows that the 3dπ MO is always demoted and never crosses the valence band or vacuum level. Therefore, the vacancy in the demoted 3dπ can never be filled by resonant capture from the VB. However, if the 4fσ promotion is strong, one electron can be lost irreversibly to vacuum, yielding a core state with two vacancies ($3d\pi^3 4f\sigma^1$) — as a result, Ne^{++} leaves the collision. The energy deficit required to pull the electron from the Ne^{+} projectile to form Ne^{++} must be equal to at least the second ionization potential ($Ne^{+} \rightarrow Ne^{++}$ requires 41 eV). As we mentioned earlier for Ne^{+}, the increasing inelasticity for the Ne^{++} exit could be explained by more energetic electron release (electrons ejected with increasing kinetic energy) as the projectile energy (and 4fσ promotion) increases.

The explanation we have given here for Ne^{+} scattering off Al is based on an MO promotion model that is mediated by electron transfers from the valence band of the target and electron ejection to vacuum. Although this mechanism is complex, it seems to fit all the peculiarities in the experimental data which suddenly turn on, once a threshold apsis distance has been reached. Indeed, the presence of the surface, particularly the wealth of electrons in the valence and conduction bands, should change the scattering behavior for Ne^{+} compared to the gas-gas case. Many authors have said that the same underlying mechanism is at work for both gas-gas and gas-surface scattering. Our explanation echoes this sentiment because electron promotion through the development of the 4fσ MO seems to be ultimately responsible. At the fundamental level, the L-L shell overlap of the projectile and target atoms is the necessary and sufficient condition for Ne^{+} inelasticity, Ne^{+} yield decrease, and Ne^{++} formation. The atomic orbital overlap of the collision partners at a critical L-L shell overlap distance is manifest as a ″strong enough″ promotion of the Ne 2p AO into the 4fσ, which enables multiple de-excitation channels and direct electron ejection to vacuum. For apsides greater than the L-L shell overlap distance, simple elastic scattering occurs because no loss channels exist.

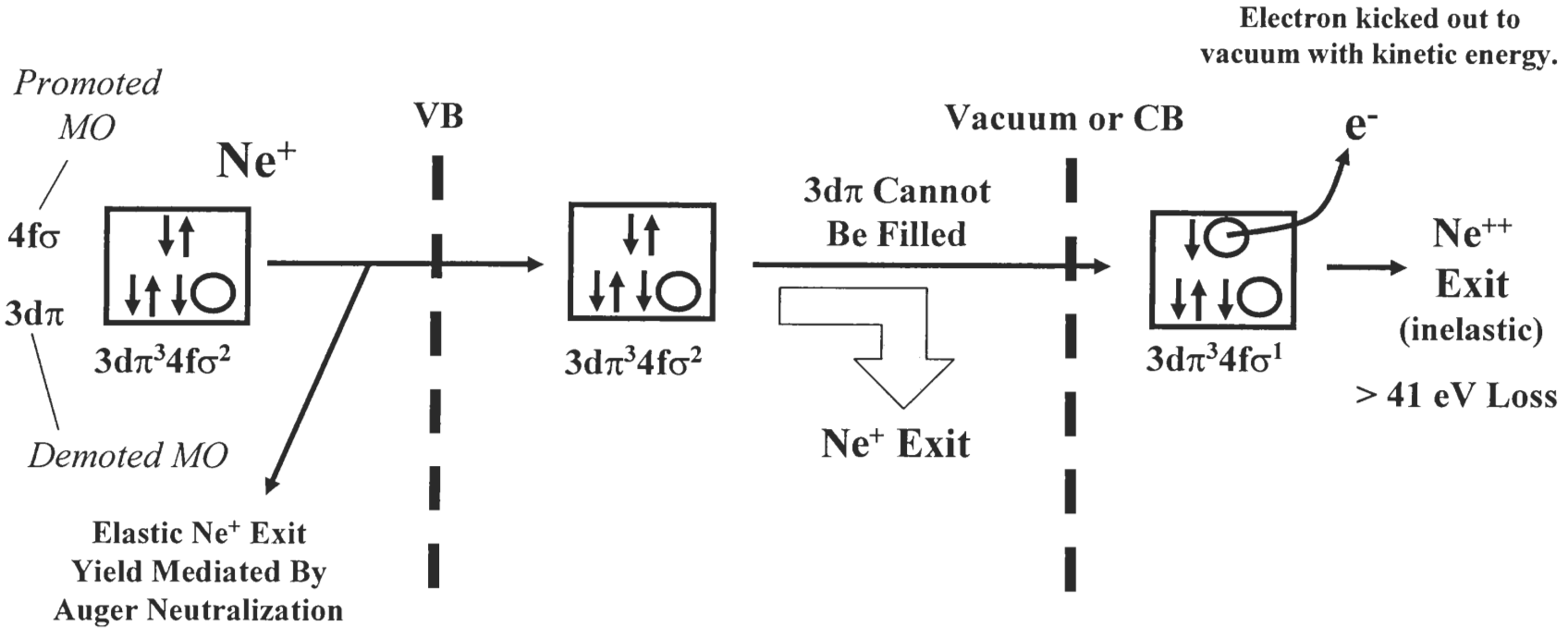

Figure 7.15: Block diagram showing the various outcomes of the hard collision for the $3d\pi^3 4f\sigma^2$ quasi-molecule state. Since the $3d\pi$ MO is demoted and does not cross into the valence band (VB) at any apsis, the vacancy in the $3d\pi$ can never be filled. However, when $4f\sigma$ promotion occurs all the way to the vacuum level, and electron can be irreversibly lost. When the second vacancy is created ($4f\sigma^2 \rightarrow 4f\sigma^1$), Ne^{++} formation occurs with an inelastic loss of at least 41 eV (second ionization potential).

Question: Where does the extra energy go (i.e., more than the excitation requirement to pump the transition)? (or)
Why does the inelasticity increase?

Discussion of this question has been generally avoided in the literature and as yet, there has not been a satisfactory answer put forth. The smooth increase in the inelasticity suggests a ″continuum″ of states, and we have put forth the idea that the extra energy loss can be accommodated in energetic electron release to vacuum. If the ejection of electrons with appreciable kinetic energy (10's of eV) is responsible for the increasing inelasticity, why do we not see a broad distribution of Ne^+ exit energies (starting at the BCA prediction and going to lower energy)? One would suppose that the electron release should occur over a distribution of energies as the promoted 4fσ MO rises above the vacuum level to the final MO energy at the collision turning point on the PE curve. Ultimately, electron release is a rate process. Therefore, electrons should be released to vacuum with highest probability along the promoted 4fσ PE curve where the projectile is the slowest. The slowest part of the trajectory is the turning point on the 4fσ PE curve ─ the apsis. As the collision gets more violent at higher impact energy, the apsis becomes smaller and the turning point on the PE curve goes to higher and higher energies. If the electron release occurs at the turning point with higher probability (because the projectile is the slowest), the electrons are released with greater and greater kinetic energies ─ hence, the inelasticity for Ne^+ should continually increase. The same effect should hold for the Ne^{++} exit as well. We understand that this picture is merely conjecture, but it seems to capture the ″continuum-like″ nature of the ever-increasing Ne^+ and Ne^{++} inelasticities.

Additionally, we note that a multitude of Auger lines from Ne^{+*} and Ne^{+**} are seen for Ne^+ scattering on Mg and Al. Perhaps the extra energy loss could be explained through higher excitation of the Ne^{+*} above the ($2p^4 3s$) state. There are many Rydberg states of Ne^{+*}, all the way from $2p^5 3s$ at 27 eV up to ~ 40 eV (near the ionization potential for Ne^+ to Ne^{++}) above $Ne^+(2p^5)$. Excitation to these higher states would not seem immediately explainable through the Fano-Lichten theory (MO promotion) without help from a ″smearing″ of energy level provided by the valence and conduction bands of

the target. However, it is clear from the Auger decay spectra that some of these excited ion states are formed (how?). In addition, target atoms are excited in the collision simultaneously with the Ne projectile to states such as Mg^{*} and Mg^{+*}, as evidenced by the same Auger spectra. Perhaps target excitation can explain the increased energy loss for both Ne^{+} and Ne^{++}. It would seem to us that the VB or CB of the solid could dissipate the extra collision energy above the transition threshold in more of a continuum-like fashion. The projectile might function as a shuttle for electrons from the valence band (at lower energies) to the conduction band or vacuum (at higher potential energies). Electrons picked up in the valance band by RC to fill the 4fσ vacancy could be deposited at higher energy by resonant ionization into the conduction band or vacuum. Indeed, the binding energy of the 4fσ electrons, under strong promotion, is only a few volts.

Question: Are two-electron processes important for Ne^{++}?

This question is hard to answer. The Ne^{++} generation channel in our data turns on in the 500-600 eV range for Al at 90° scattering angle. The apsis range for this collision energy is quite close to the AO overlap distances involving the L-shells of both the projectile and target. We have also seen that the Ne^{++} generation occurs with an initial inelasticity of ~50 eV which rises in the same manner as that seen for Ne^{+}. We note that the direct transition route from Ne^{+} to Ne^{++} requires only 41 eV. All the other probable excitation schemes ($Ne^{0}\rightarrow Ne^{++}$, 62.5 eV; $Ne^{+}\rightarrow Ne^{+**}$, ~72 eV; and $Ne^{+}\rightarrow Ne^{++*}$ from Ascione *et al.* (1997) and Xu *et al.* (1998), ~86 eV) require much more pump energy. Such a large energy loss is not reflected in the scattered Ne^{++} spectrum for the threshold region near 500 eV where the Ne^{++} channel first appears. Process of elimination and simplicity seem to favor the direct ionization route from $Ne^{+}\rightarrow Ne^{++}$ mentioned earlier, which is a one-electron transition. The inelasticity does not seem to reflect the needed energy for moving two electrons.

Finally, the Auger data from Xu *et al.* (1994) in Table 7.2 says that Ne^{+**} is produced for Ne^{+} impact on Al at energies greater than ~440 eV. The autoionization of the Ne^{+**} state to Ne^{++} is very appealing because the turn-on energy for Ne^{+**} formation (as evidenced by the Auger decay line) is near the impact energy where we see Ne^{++}

begin to appear in the ISS spectrum. Unfortunately, the $Ne^{+} \rightarrow Ne^{+**}$ transition requires a $2p^3$ core and at least 72 eV, which is not echoed in the Ne^{++} inelasticity data (~50 eV). We surmise that Ne^{+**} is probably formed in the 500-600 eV range for our system (Auger data says it should), but the Ne^{++} exit that is associated with the Ne^{+**} autoionization decay must be strongly backscattered and not observable at 90° lab angle ─ otherwise, one should see the 72 eV loss in the Ne^{++} exit energy spectrum. Refer back to Section 7.4 for the details of why the Auger results should be used with caution.

Conclusions for $Ne^{+} \rightarrow Al$

Our loss measurements in the threshold region for the Ne^{+} and Ne^{++} exit channels off Al raise some questions. It seems that the threshold processes which result in Ne^{+} inelasticity and Ne^{++} formation in the 500-600 eV range for Al are clearly very different from those proposed for much higher collision energies. The inelasticities in our measurements and the sudden turn-on for the Ne^{++} channel at the same threshold apsis distance (0.65-0.7 Å) are more consistent with a common underlying cause. We have invoked a hybrid mechanism involving MO promotion that is mediated by electron exchange with the valence band of the target to explain all our experimental observations.

The formation of Ne^{+*} from Ne^{+} and direct ionization of Ne^{+} to Ne^{++} are within reach of the measured exit energy offsets from the BCA model. The Ne^{+} to Ne^{++} seems a bit easier to believe because the direct route is only 41 eV (our Ne^{++} inelasticity starts at 50 eV). The lower inelasticities that we see tend to favor one-electron type excitation processes. The other more esoteric mechanisms (especially Ne^{++}) which involve autoionizing states and ~70-90 eV pump energies do not seem to be immediately applicable to the threshold region. The more direct routes must be favored because they are simpler and fit the lower inelasticity values we see for 500-1000 eV collisions for Ne^{+} with Al. The increasing inelasticity with impact energy is still somewhat mysterious, but could possibly be explained through energetic electron release to vacuum.

The Ne^{+} inelasticity onset and threshold energy for Ne^{++} formation are concommitant with an apsis distance in the 0.6-0.65 Å range. This apsis agrees quite well with the internuclear distance calculated for the (NeAl) collision system by Souda *et*

al. (1996) for strong 4fσ MO promotion. The simple picture of atomic orbital distances indicates that overlap of the Ne 2s or 2p AO's with the target atom AO's may be the common denominator for both the Ne^+ inelasticity onset and threshold distance for Ne^{++} generation. The L-L shell overlap model may just be our simple interpretation of the Fano-Lichten-Barat model for 4fσ MO promotion.

Finally, we note that the gas-gas literature suggests a 4fσ MO promotion distance of 0.45 Å (Table 7.3) for the reverse $Al^+ \rightarrow Ne$ collision. Our apsis distance at 0.6-0.65 Å, if indeed it signifies 4fσ MO promotion (as evidenced by Ne^{++} generation), is larger than the gas-gas data. Our calculation for the collision apsides is based on the TFM potential with Firsov screening length. Perhaps the surface can displace the electron levels enough, unlike the gas-gas case, such that the 4fσ MO forms at a slightly larger internuclear distance. Rabalais, (2003) has mentioned that the image potential from the surface can cause an electron level shift in the incoming ion. In addition, our selection of the TMF potential and perhaps, more importantly, the screening length we have used to calculate the collision apsides may explain the slight disparity. Ultimately, the determination of the collision apsis is only as accurate as the scattering potential used for the calculation.

7.7.3 Ne^+ on Silicon

Scattering studies on Si(100) were carried out in an analogous fashion for direct comparison with $Ne^+ \rightarrow Al$ results. Figure 7.16 shows a summary of the Si scattering data. Identical qualitative trends occur in the $Ne^+ \rightarrow Si$ system as for $Ne^+ \rightarrow Al$, except that the exit energy for Ne^+ in the threshold inelasticity region does not jump as abruptly for Si as it does for Al. Below about 600 eV, the exit energy of Ne^+ agrees fairly well with no-loss BCA. However, above 600 eV, the Ne^{++} generation channel turns on along with inelasticites in the Ne^+ and Ne^{++} exit channels. As in the Al case, the exit energy data for Ne^+ and Ne^{++} have almost identical slope dependence on the impact energy. The same qualitative behavior in $Ne^+ \rightarrow Si$ and $Ne^+ \rightarrow Al$ is not surprising in view of the similarities in the Auger data.

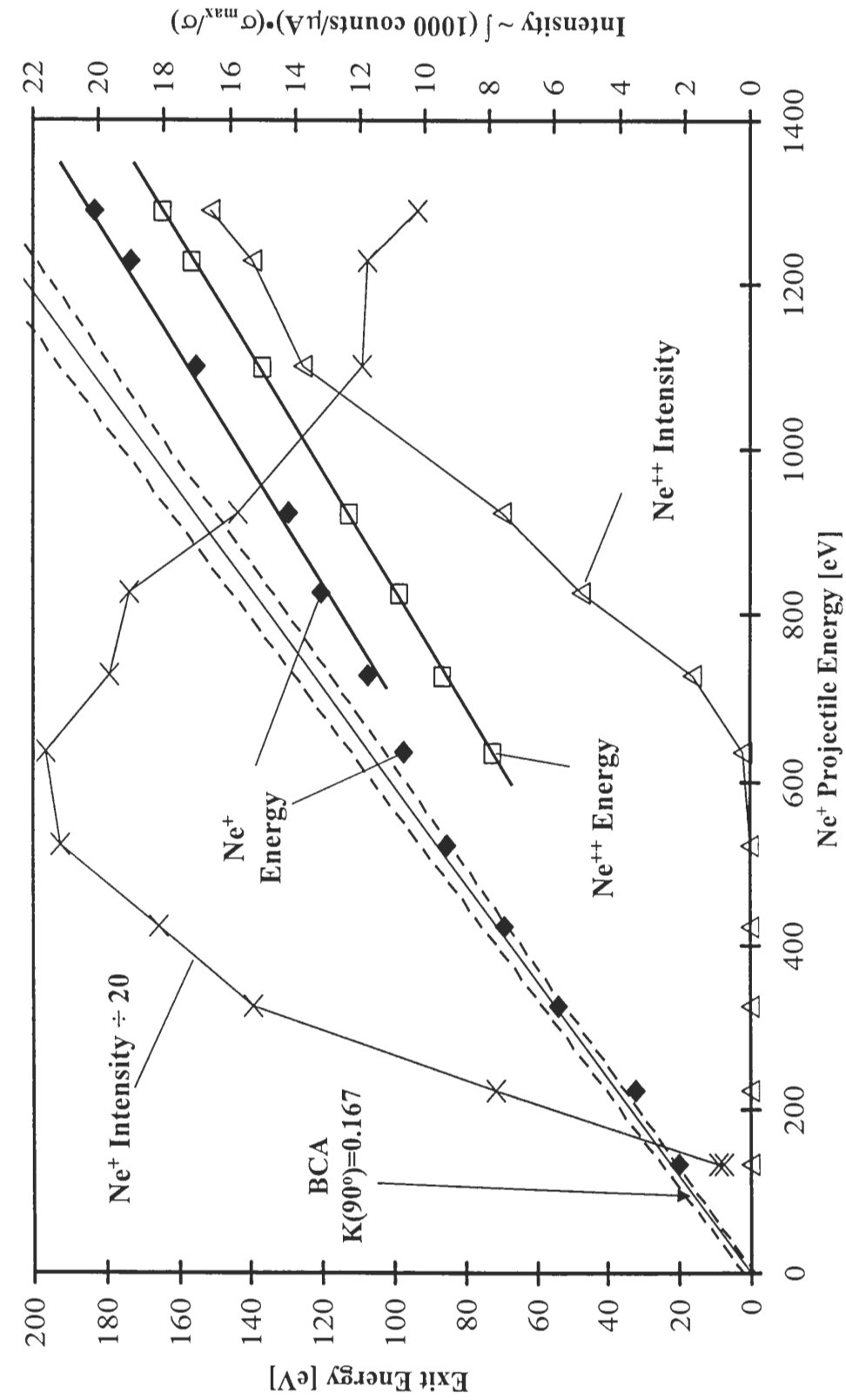

Figure 7.16: Ne^+, Ne^{++} exit energies and Ne^+, Ne^{++} signal intensity for Ne^+ bombardment of Si(100) at 90° lab angle.

It is worth noting that the Ne^{++} channel on Si turns on at a higher energy than for Ne^{+} on Al. This is consistent with a decrease in the required apsis distance for the Ne^{++} formation channel since the 2s and 2p AO states of Si are closer to the nucleus than for Al. As a general rule, increasing the number of electrons as we move down the periodic table does not make an atom considerable larger, but rather, the inner electron shells are pulled closer to the nucleus. For example, consider the maximum charge distribution for the individual AO's from Slater (1960) as mentioned earlier. See Table 7.5.

Table 7.5: Distance of maximum radial charge density for atomic orbitals (in Å). Data taken from Slater (1960).

Atom	1s	2s	2p	3s	3p
Ne	0.055	0.37	0.32		
Al	0.042	0.27	0.23	1.16	1.21
Si	0.040	0.24	0.21	0.98	1.06

If Ne^{++} generation requires the Ne 2p to overlap with the target 2s or 2p (causing the 4fσ MO to form), this overlap will occur at a closer internuclear distance for $Ne^{+}\rightarrow$Si than $Ne^{+}\rightarrow$Al. Hence, the threshold energy should be higher for Si than Al, which it is in our data to the tune of ~100 eV. In addition, Fastrup *et al.* (1971) showed that 2p vacancy production in (P^{+}, S^{+}, Cl^{+}, Ar^{+}, and K^{+}) collisions with static Ar gas requires a smaller apsis distance as the projectile ion gets heavier (higher Z). Our system of a fixed Ne^{+} projectile and increasing target mass from Al to Si is analogous to their ″reverse″ collision. At the fundamental level, Ne^{++} generation is just 2p vacancy production in Ne^{+}, so the scaling argument of a smaller required apsis for a heavier target mass should be the same ─ which it is in our experimental data. Our Ne^{++} intensity data versus apsis for Al and Si are given in Fig. 7.17 along with the data from Fastrup for comparison.

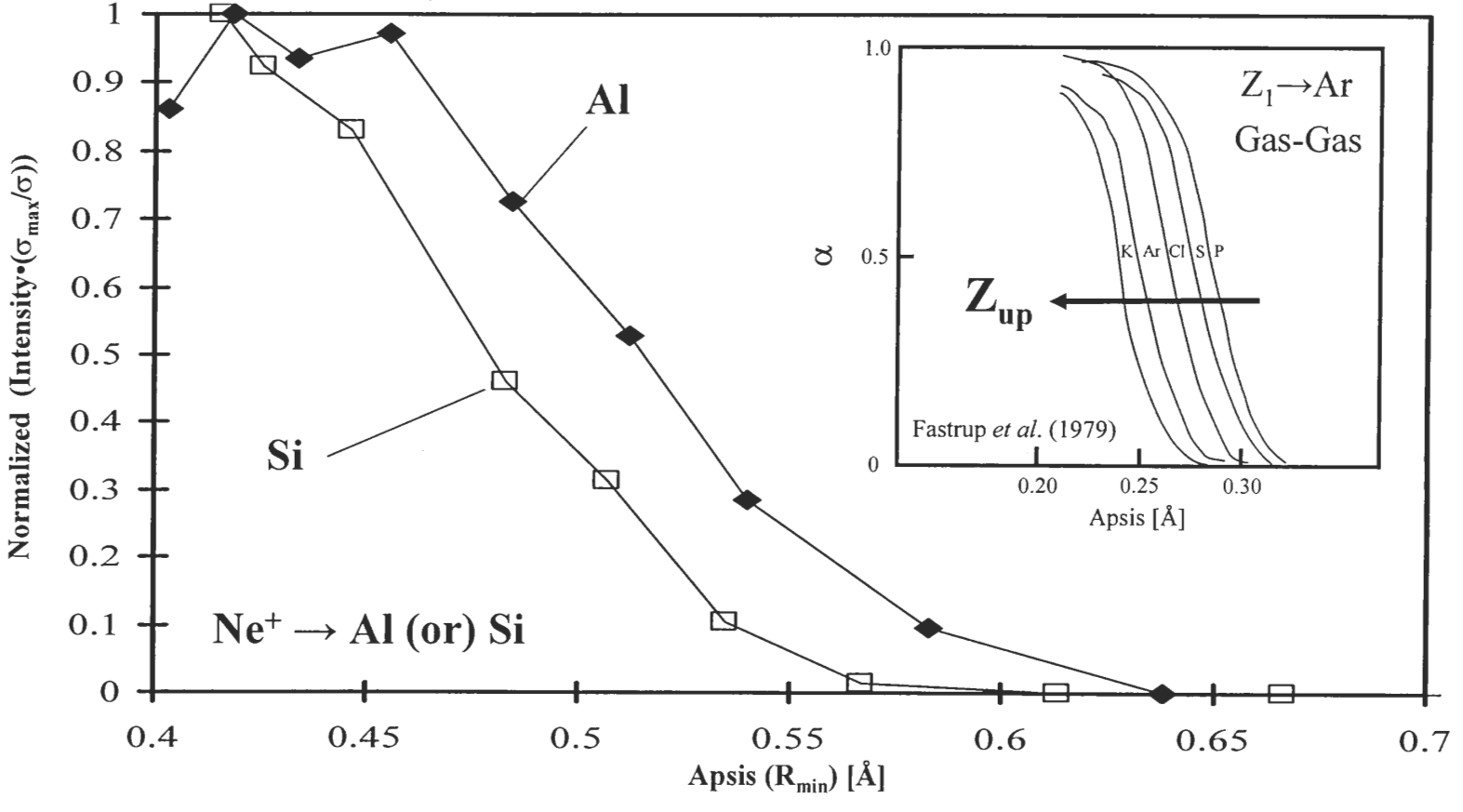

Figure 7.17: Comparison of collision apsides for Ne^{++} generation off Al and Si targets. The apsides were calculated using the TFM potential with Firsov screening length. The inset shows the probability (α) for 2p vacancy production in "reverse" collisions (variable projectile ion, P^+ through K^+, on static Ar) in the gas phase from Fastrup *et al.* (1979). Both plots show that multi-charged ions are formed at smaller apsides as one of the collision partners becomes heavier (higher Z).

Evaluating the inelasticity requires removing the continuous loss via the Oen and Robinson formula. Xu *et al.* (1998) found that their $Ne^{+} \rightarrow Si$ inelasticity data were better fit if different c_i values were used for specific ranges of apsides. Their values are given in Table 7.6.

Table 7.6: c_i values for continuous loss. Data taken from Xu *et al.* (1998).

Charge State	c_1 (Incoming)	c_3 (Outgoing)	Apsis Range
Ne^{+}	0.45	0.68	$R_{min} \geq 0.53$ Å
Ne^{+}	0.45	0.45	$R_{min} < 0.53$ Å
Ne^{++}	0.68	0.74	all

Perhaps such an analysis is needed in their case for variable lab angle measurements from 40° to 100°. We have used their c_i values as specified, but note that changing c_3 from 0.45 to 0.68 makes less than 1 eV absolute difference in the correction for our data at 90°. A plot of the calculated inelasticities for Ne^{+} and Ne^{++}, with the continuous loss removed, is given in Fig. 7.18 as a function of the collision apsis. The data from Xu *et al.* (1998) is also shown for comparison along with the same transitions mentioned earlier for the $Ne^{+} \rightarrow Al$ data.

<u>Ne^{+} Results</u>

In the same fashion as $Ne^{+} \rightarrow Al$, the Si scattering data for the Ne^{+} exit begins to show a binary collision loss that increases as the apsis becomes smaller. The turn-on for this process is between 0.55-0.6 Å, which is the exact point where we begin to see the Ne^{++} exit channel. The agreement between our Ne^{+} inelasticity data and Xu *et al.* is quite good for the Ne^{+} exit.

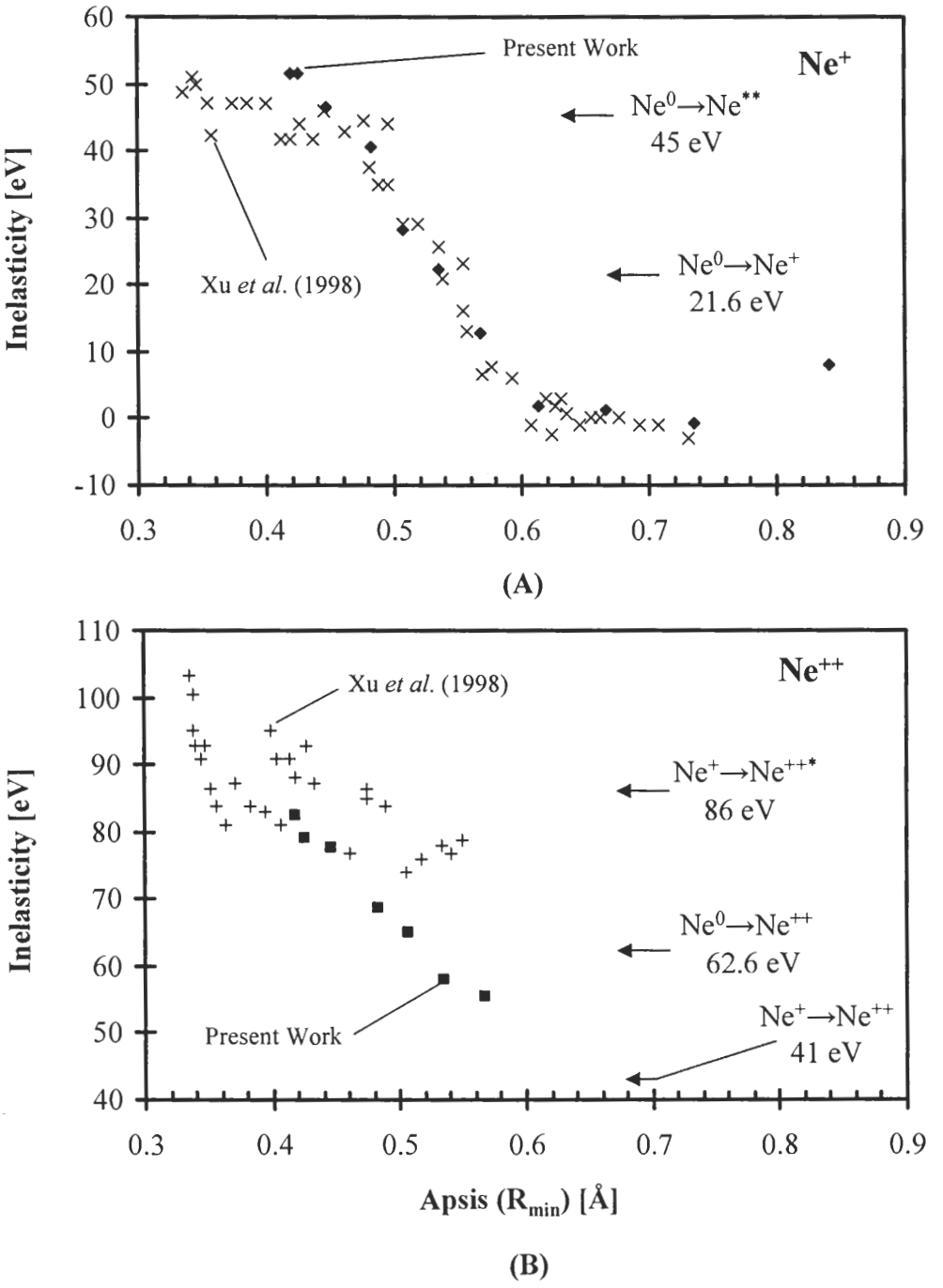

Figure 7.18: Measured inelasticity for (A) Ne^+ and (B) Ne^{++} for Ne^+ on Si. Collision apsides calculated using the TFM potential for Ne^+ on Si at 90°. Also shown are the inelasticity data from Xu *et al.* (1998) for $Ne^+ \rightarrow Si$. The autoionizing transitions at 45 eV and 86 eV from Ascione *et al.* (1997) are shown along with the direct transitions. Note: Xu *et al.* (1998) quote an inelasticity of 86±4 eV for Ne^{++} using the data as shown with the autoionizing transition indicated.

What is strange in the $Ne^+ \rightarrow Si$ case is the lazy turn-on for the Ne^+ inelasticity ─ this slow turn-on is in contrast to the $Ne^+ \rightarrow Al$ case, where a jump appears in the Ne^+ exit energy. The slowly increasing deviation from BCA seen in Fig. 7.16 manifests itself as a correspondingly slow increase in the Ne^+ inelasticity from near zero up to 40-50 eV at smaller apsides.

$\underline{Ne^{++}}$ Results

Our data definitely show a deviation from Xu *et al*. for the Ne^{++} inelasticity measurements on Si. The turn-on for the Ne^{++} exit in our data occurs with an inelasticity of 55-60 eV as opposed to 70-80 eV for Xu *et al*. It is interesting to consider the scatter in the Xu *et al*. data from the perspective that they assign the Ne^{++} generation to the ~86 eV process mention earlier:

$$Ne^{+}\left(2p^{5}\right) \rightarrow Ne^{++*}\left(2p^{3}\left({}^{2}D, {}^{2}P\right)3s\right) \tag{7.34}$$

Xu *et al*. quote a binary inelasticity of 86±4 eV. This assignment with such little error seems, in our opinion, much too generous for the data shown. It is not totally clear to us that the above process has been convincingly shown as the Ne^{++} generation pathway. The scatter in their inelasticity data and our observation that their inelasticity values get larger as the apsis gets smaller ─ which our data shows as well ─ suggests that some other processes may be important. The Tolstogouzov *et al.* (1998) measurements give even higher values of 110 eV for Ne^{++} off Si (correcting for the continuous loss, the 110 eV value should decrease somewhat ─ but probably not all the way down to 86 eV).

Commentary

The Ne^+ inelasticity at the Ne^{++} turn-on (600 eV) is ~5 eV, while the Ne^{++} inelasticity at the turn-on is large (55-60 eV). These observations for Si are qualitatively very similar to the Ne^+ on Al results. However, the slowly increasing Ne^+ inelasticity for Si, with no discernible jumps, is somewhat different than for $Ne^+ \rightarrow Al$. We note that the

MO promotion picture with electron transfer mediated by the target valence and conduction bands should be analogous for the $(NeSi)^+$ and $(NeAl)^+$ quasi molecules. Therefore, the same explanations given for the Al target can be used for Si.

We mentioned that the lazy increase in the Ne^+ inelasticity is somewhat different for the two targets. Examining the AO energy levels may give a clue to the origin of this difference. First, the 2p AO state of Ne has a binding energy of ~21.6 eV. Second, the 3s states of Al and Si (first AO states above Ne 2p on the MO diagram) are located at 11.3 eV and 15 eV, respectively (Slater, 1960). The 3s level gives a feeling for the bottom of the valence band with respect to the Ne 2p level. Since the bottom of the valence band for Si reaches much closer to the Ne 2p state than Al, it is possible that the Ne^+ inelasticity data off Si should not show as much jump (or no jump at all), due to the closer proximity of energy levels. The Al target has a larger energy separation between the bottom of the valence band (VB) and the Ne 2p, so an inelasticity jump is more likely. This observation is only conjecture on our part. However, it is clear that electrons in the promoted 4fσ MO will encounter the VB of Si (at lower potential energy) before the VB of Al on the PE curve ascent. It appears from our threshold ISS data as well as Xu e*t al*. that some process or processes are definitely consuming a reasonably portion (30-40 eV) of the Ne^+ exit energy during the hard collision. Energetic electron ejection to vacuum, as the 4fσ MO rises in potential energy, may be the mechanism for increasing inelasticity as we mentioned earlier for Ne^+ on Al.

The standing question of how Ne^{++} is generated at lower impact energies, with inelasticities less than 86 eV (Xu's hypothesis of Ne^{++*} formation through a two-electron transition), is answered more satisfactory by vacancy production in the quasi molecule $3d\pi^3 4f\sigma^2$ state to $3d\pi^3 4f\sigma^1$ at the vacuum level (refer back to Fig. 7.15). The Ne^{++} turn on in our data is accompanied by ~60 eV inelasticity which gets larger to ~80-85 eV at 1300 eV impact. The direct conversion of $Ne^0 \rightarrow Ne^{++}$ takes 62.5 eV, and it has been mentioned several times earlier that the hard collision might occur between Ne^0 and the target atom. This Ne^{++} generation scheme seems like it can not be ruled out as a potential candidate. However, we remark that the Ne^0 initial state for Ne^{++} production seems very unlikely because the data from Souda *et al.* (1995) does not show an Ne^{++} exit for an Ne^0 projectile. This necessarily means that the $Ne^+ \rightarrow Ne^{++}$ transition needing 41 eV is still a

better candidate than a two-electron excitation (requiring more energy loss). However, 60 eV is a decent bit larger than the 41 eV for direct ionization. As we said before, the extra energy could possibly go into energetic electron release or it could be spent in target excitations of some kind.

The Xu *et al*. Ne^{++} inelasticity data for 0.5-0.6 Å apsides were obtained for 1000 eV impact at about 40-80° lab angle (read directly off their graph). They comment that they did not see Ne^{++} at any of the lower incident energies tested (500 and 700 eV) for scattering angle from 30-120°. This is a bit surprising. Souda *et al.* (1995) has seen Ne^{++} generation on Si at 800 eV for 60° lab angle. Our data gives ~600-700 eV for 90° scattering which is totally consistent with Souda *et al*. because the collision is more violent in our case.

Our results at lower energy point to the possibility of different excitation mechanisms compared to those hypothesized for higher collision energies. In our view, the picture of Ne^{+} and Ne^{++} inelastic losses in the threshold region are likely to be the same for Si and Al; both involve 4fσ MO promotion and electron exchange through RC with the target valence band, along with energetic electron ejection to vacuum. The lower inelasticity values in the threshold region seem to favor one-electron excitation rather than two. The orbital overlap picture for the Ne^{+}→Si collision is shown in Fig. 7.19. The lazy rise in the Ne^{+} inelasticity appears to occur during 2s/2p orbital overlaps. In contrast, the Ne^{++} signal suddenly turns on in conjunction with the AO overlap as shown in Fig. 7.19b. Our simple picture of L-L shell overlap of the projectile and target atoms is the prerequisite for ″enough″ 4fσ MO promotion to cause all three events: Ne^{+} inelasticity onset, Ne^{++} formation (with inelastic loss), and the decrease in Ne^{+} yield. Also, the ~100 eV greater impact energy (smaller apsis) required for Ne^{++} formation off Si, compared to Al, is consistent with the gas-gas scattering trend for 2p vacancy production with increasing projectile mass (nuclear charge ─ Z). Refer back to Fig. 7.17. The mechanism we proposed for Ne^{+} on Al in the previous section could equally explain all the experimental observations for the Ne^{+}→Si system. The same underlying mechanism of 4fσ MO promotion and electron transfers from the target valence band point to one-electron type transitions, rather than two.

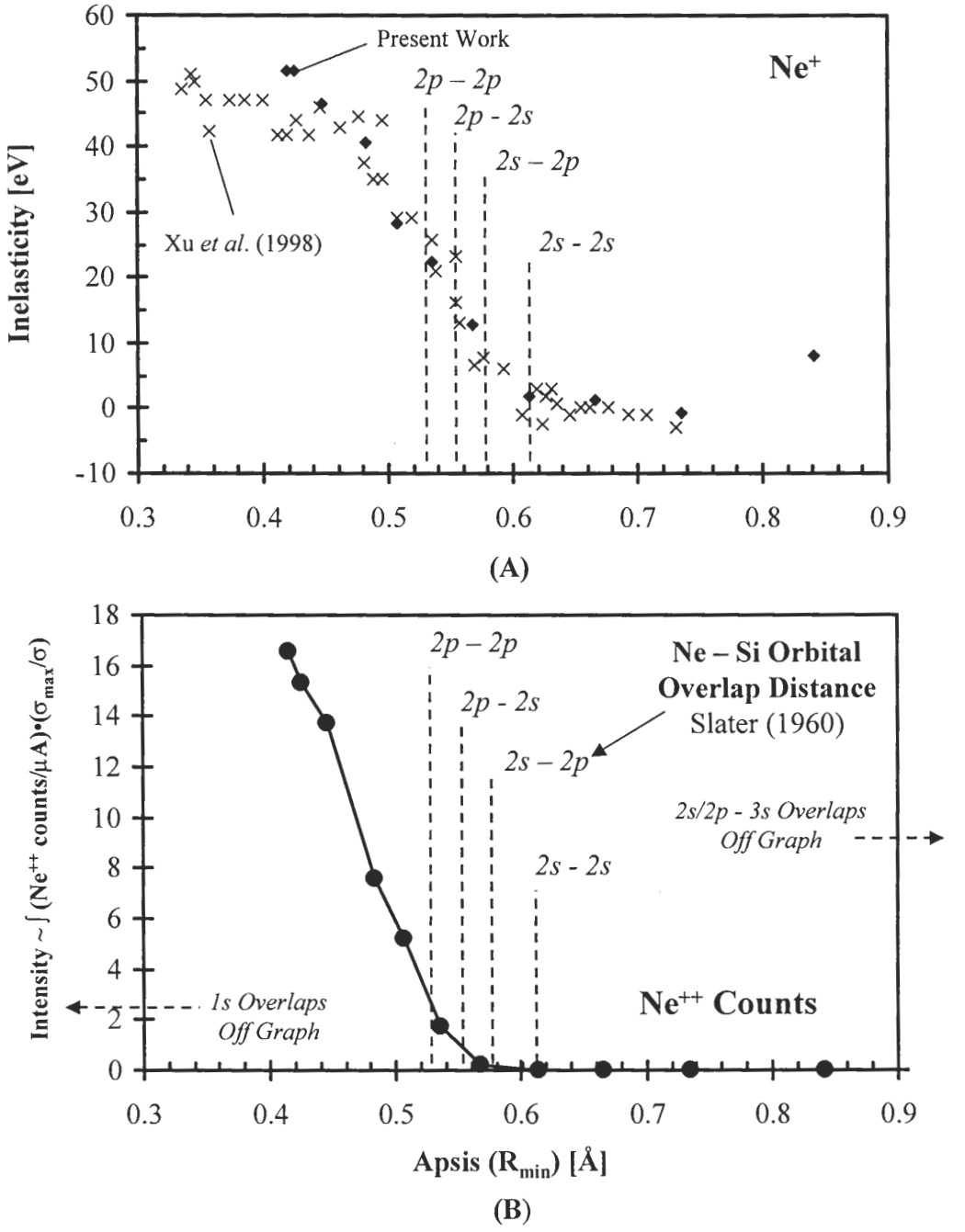

Figure 7.19: (A) measured inelasticity for Ne^+ and (B) Ne^{++} signal intensity for Ne^+ on Si. Collision apsides calculated using TFM potential for Ne^+ on Si at 90°. Also shown are the inelasticity data from Xu *et al.* (1998) for $Ne^+ \rightarrow Si$ and calculated overlap distances for atomic orbital states of the collision partners using the data of Slater (1960).

7.7.4 Ne^+ on Magnesium

The $Ne^+ \rightarrow Mg$ collision is almost symmetric so excitation of both the projectile and target atoms can be expected. Mg^* and Mg^{+*} lines are commonly seen for Ne^+ impact (see Section 7.4). Figure 7.20 shows a summary of our $Ne^+ \rightarrow Mg$ scattering studies. Immediately, one sees different behavior in the very low-energy regime. The Ne^+ exit energy is much higher than the BCA predicted values at low impact energy (<400 eV) and lower than BCA for higher impact energies. The Ne^{++} exit energy has been left off the graph intentionally. This will be discussed later as very broad Ne^{++} energy distributions were measured which makes the actual exit energy difficult to determine.

Considering the kinematics of the $Ne^+ \rightarrow Mg$ collision (Chapter 2), an Mg recoil can not exist for 90° lab scattering angle for a single collision BCA event. In fact, it can be easily shown that BCA single collision recoils are always forward scattered into lab angles less then 90°. Therefore, the Mg^+ recoil spectra at 90° lab scattering angle must result from multiple collisions. Raw scattered ion energy distributions for the directly scattered Ne^+ and Mg^+ exit (not a BCA recoil) are shown in Fig 7.21 for 208 eV and 844 eV Ne^+ impact.

Immediately one can see that the Mg^+ exit is more intense and broader than the directly scattered Ne^+. The Mg^+ exit moves up in energy from ~38 eV to ~50 eV as the impact energy is increased from 208 eV to 844 eV. Although this peak is not BCA, it should logically move upward with impact energy because multiple collisions at higher energies should result in higher exits. As mentioned before, multiple collisions must be responsible for the Mg^+ exit at 90° lab angle. The fact that multiple collision phenomena may be important is echoed by the long high energy tails for the Ne^+ (multiple bounce is higher than BCA). We can also see that peaks near 2-5 eV are observed for both Ne^+ and Mg^+, which are independent of the Ne^+ impact energy. These peaks are just the sputtered secondary ions that one would see in a standard SIMS spectrum.

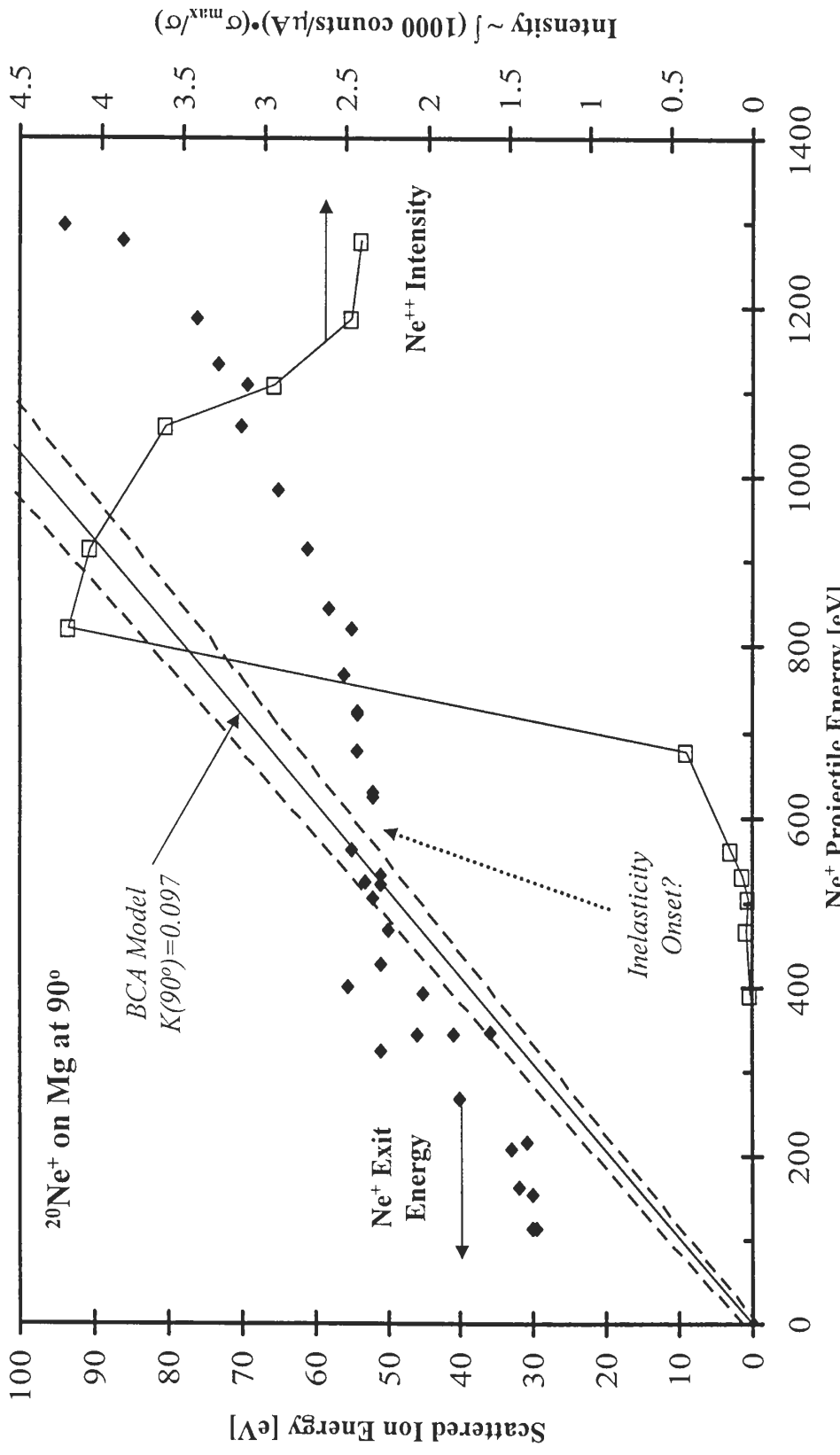

Figure 7.20: Ne^+ exit energy and Ne^{++} signal intensity for Ne^+ bombardment of Mg at 90° lab angle.

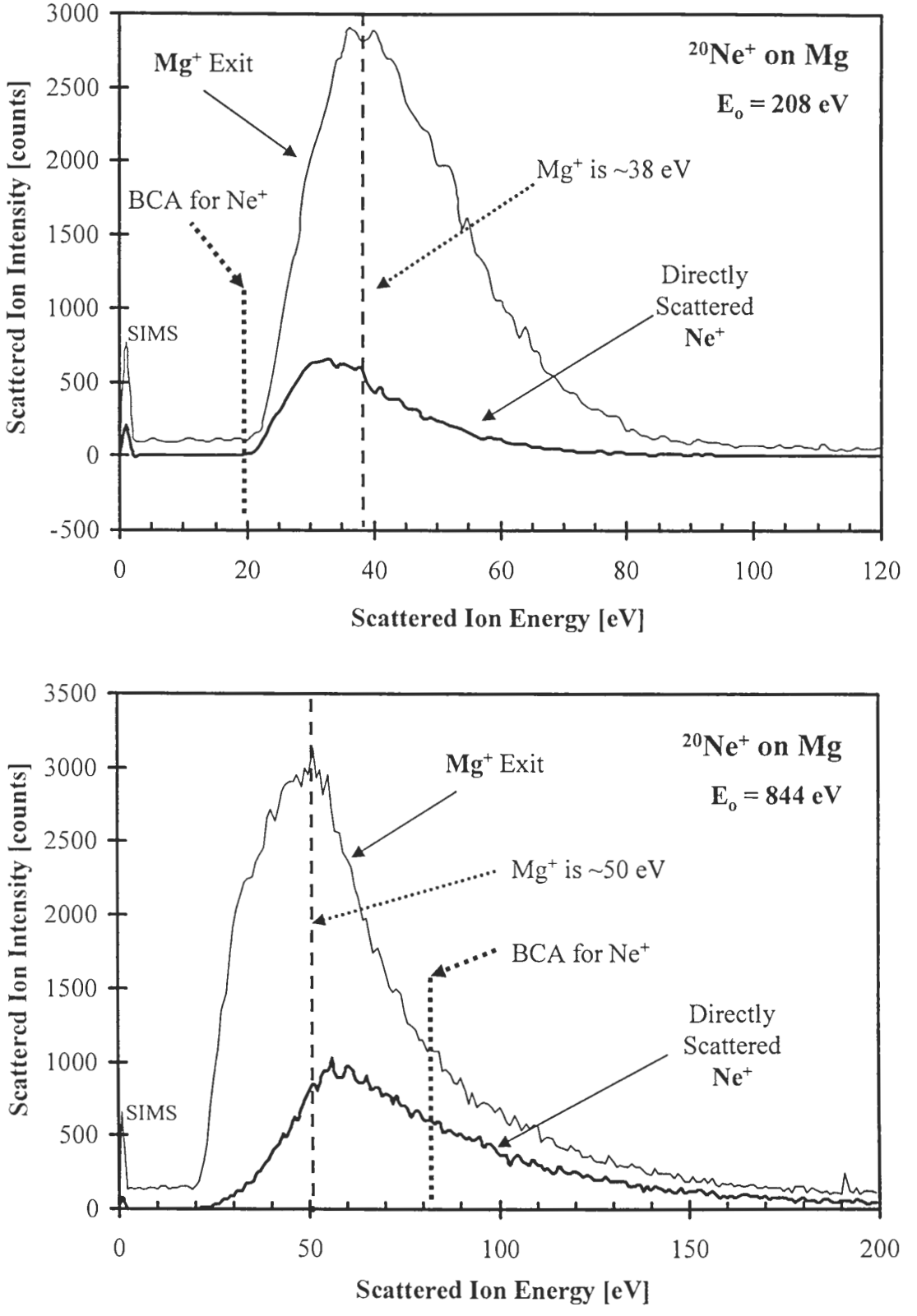

Figure 7.21: Scattered Ne^+ and Mg^+ exit energy spectra for Ne^+ on Mg at 90°.

A raw energy spectrum for the Ne^{++} exit is shown in Fig. 7.22 for 820 eV impact. The Ne^{++} energy distributions are extremely broad, making any useful assessment of the Ne^{++} exit energy difficult. This is in contrast to the Ne^{+} on Al and Si, where the Ne^{++} exit shows a narrower peak with a well defined maximum. The Ne^{++} generation channel onset is a bit more ambiguous with respect to the impact energy for our $Ne^{+}\rightarrow$Mg data. As most of the Ne^{++} data off Mg showed broad exit energy features, it was deemed that determining the Ne^{++} inelasticity with any certainty was not warranted. However, the impact energy for Ne^{++} generation and the Ne^{+} inelasticity were evaluated.

ISS inelasticity measurements for Ne^{+} or Ne^{++} on Mg have not been published and as such, the c_i's for the Oen and Robinsen formula are unknown. We noted earlier in our $Ne^{+}\rightarrow$Si discussion that increasing $c_3 = 0.45 \rightarrow 0.68$ only changed the continuous loss term by ~1 eV for our scattering setup. This fact is echoed by Xu *et al.* (1998), who mention that changing the c_i values only causes a few volts difference in the inelasticity evaluation. In addition, this effect should be even less important for Mg because the Ne^{+} exit off Mg is even slower than that off Si. Therefore, we believe that the c_i values for Mg in our system are not too important in determining the overall size of the binary inelasticity and thus, using the values for Al, should be an approximation as good as any other.

The calculated inelasticity for our Ne^{+} data and Ne^{++} intensity are shown in Fig. 7.23 for the collision apsides calculated from the TFM potential. Also included on the plot are the orbital overlaps calculated from the AO distance data mentioned earlier. In the low-energy region where the Ne^{+} exit is faster than the BCA prediction, the inelasticity is negative (apsides > 0.7Å). In this range, the inelasticity is rather meaningless. However, once an apsis of 0.7 Å is reached, the Ne^{+} exit channel begins to show a binary loss which rises steadily to ~60-70 eV at the smallest apsis (1400 eV). The turn-on of the Ne^{++} generation channel surely occurs by 0.6 Å, but we did detect some Ne^{++} counts in one of the experimental runs at ~6 counts/μA for 391 eV impact energy — which is equivalent to an 0.67 Å apsis distance.

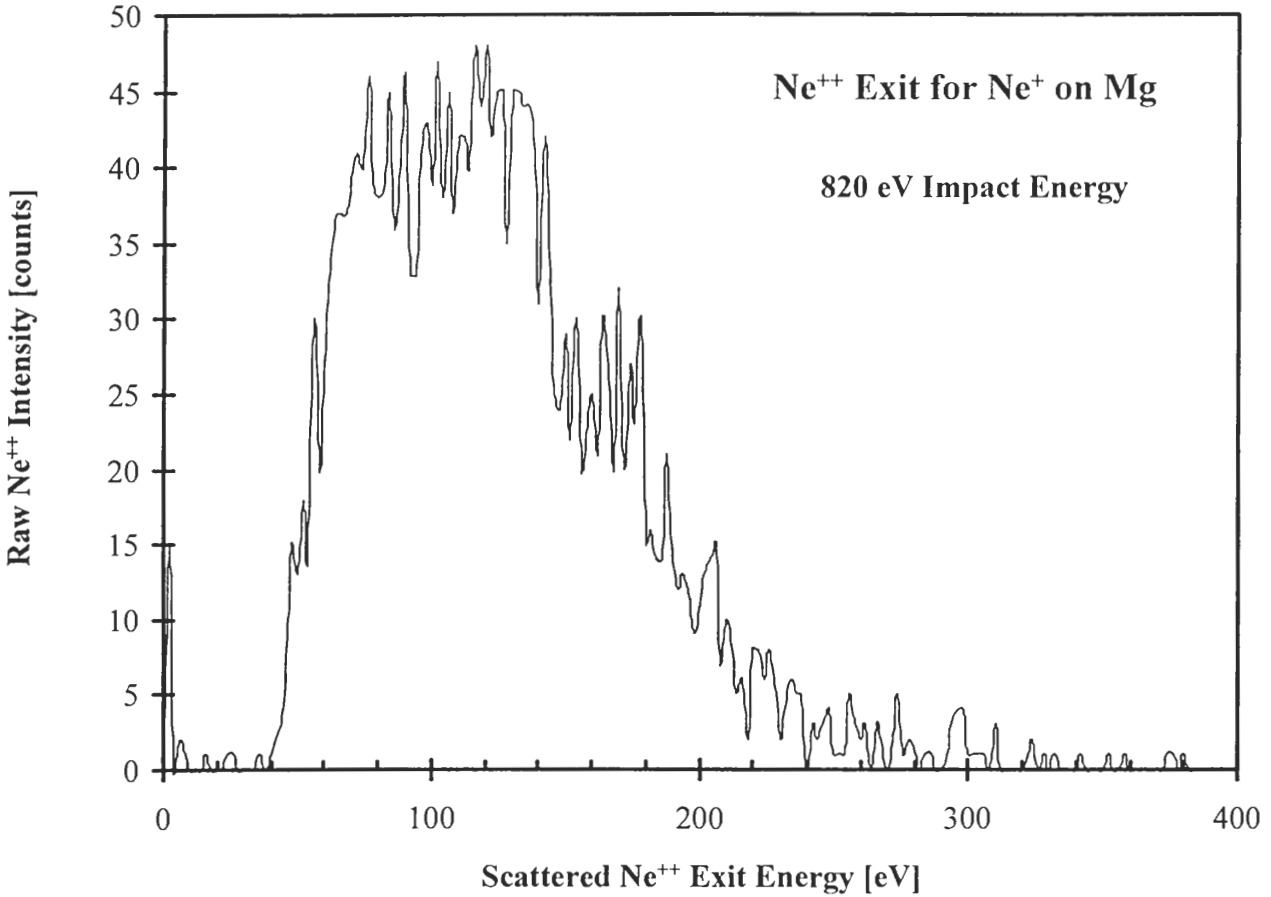

Figure 7.22: Ne^{++} exit channel raw energy spectrum for Ne^{+} on Mg at 820 eV impact energy.

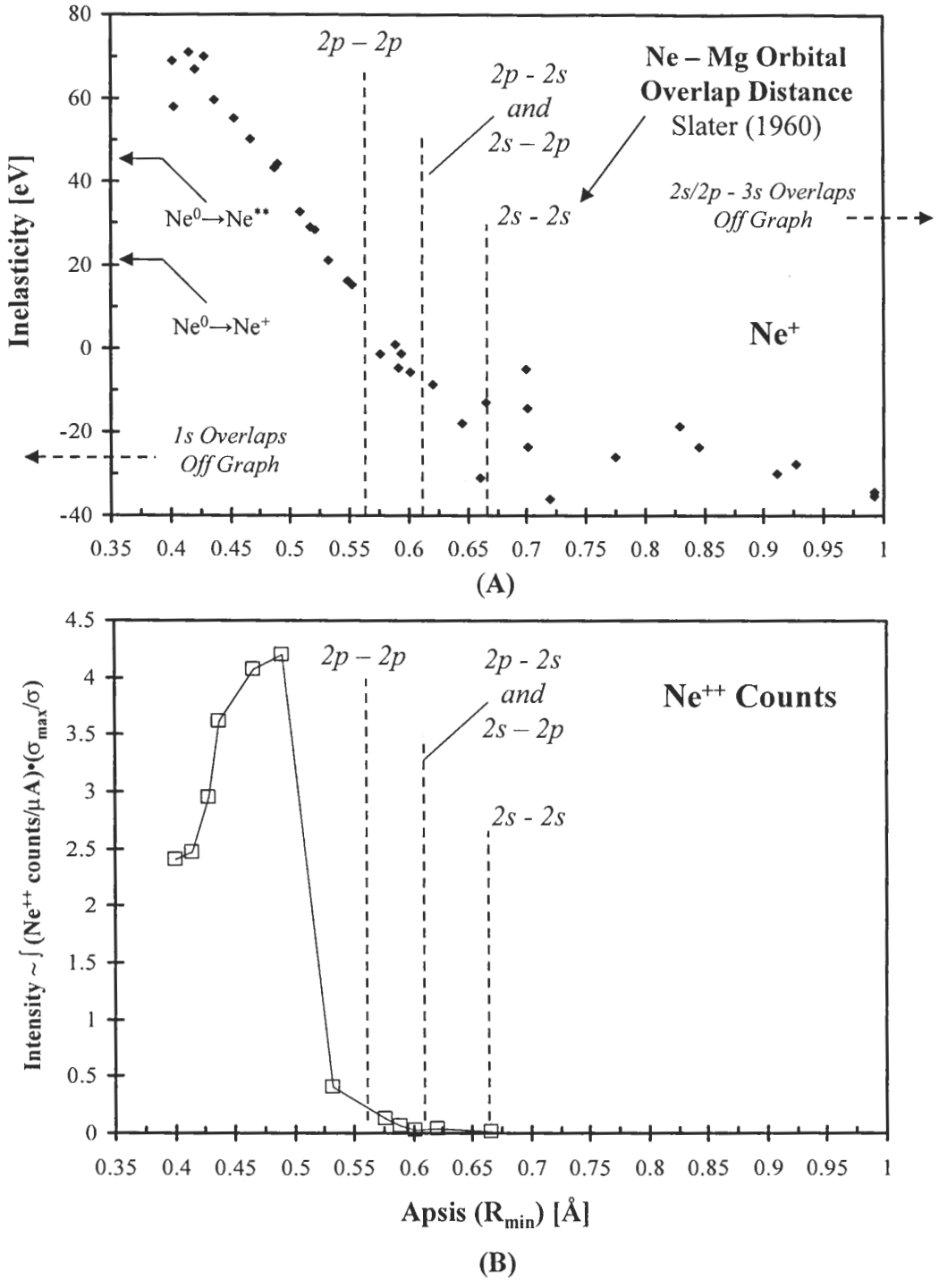

Figure 7.23: (A) measured inelasticity for Ne^+ and (B) Ne^{++} signal intensity for Ne^+ on Mg. Collision apsides calculated using the TFM potential for Ne^+ on Mg at 90°. Also shown are calculated overlap distances for atomic orbital states of the collision partners using the data of Slater (1960). The direct and autoionizing transitions are indicated as well.

The work of Grizzi *et al*. for Ne^+ on Mg shows (1) a dramatic increase in the Ne^+ yield with $R_{min} \sim 0.55$ Å, (2) ~18 eV inelasticity (12 eV raw loss) for large apsis, and (3) ~45 eV inelasticity once a critical R_{min} in the 0.4 Å range is reached. Our results seem to agree with their work for the 0.4-0.5 Å range.

While conducting Ne^+ scattering on Mg, we noticed a very intense green fluorescence from the target that occurred for the higher energies tested. The fluorescence was also seen for Ar^+ impact, suggesting that it comes from radiative decay of some excited target atom state. Both Mg^* and Mg^{+*} have transition lines in the green (Striganov and Sventitskii, 1968). Auger lines from Mg^* and Mg^{+*} have been seen for both Ne^+ and Ar^+ impact at keV energies (Guillemot *et al*., 1996). This says that target atoms are definitely excited during bombardment, so the fluorescence we see could very well originate from target atoms quenching to near-by electron states by dipole-allowed transitions. Although our experimental setup did not include analysis of visible radiation leaving the target, the green fluorescence suggests that some information about target atom excited states might be obtained with a simple monochromator and PMT setup.

Critical approach distances on the range of 0.64 Å (Table 7.3) have been mentioned in the gas-gas literature for 4fσ MO promotion in the Mg^+-Ne system. This promotion should allow for population of higher electron states involving the 2p orbital of Ne. This promotion, if it occurs, should come about with an inelasticity in the hard collision. It is interesting that we begin to see the Ne^{++} exit channel occur for apsides below 0.6-0.65 Å. In addition, our simple orbital overlap scheme with the Slater *op. cit*. AO data shows consistency with the requirement of overlap of the 2p AO of Ne with the 2s or 2p of the target atom. L-L shell overlap seems to promote the 4fσ MO enough for Ne^+ to lose an electron to vacuum, forming Ne^{++} (provided the quasi molecule is in the $3d\pi^3 4f\sigma^2$ configuration ─ the initial Ne^+ vacancy is demoted in the 3dπ).

7.7.5 Ne^+ on Titanium

.

Given what we suspect about orbital overlap requirements for Ne^{++} production, we conducted scattering studies of Ne^+ off Ti. One would expect from the previous observations for Mg, Al, and Si, that much higher energies are required to allow the Ne

2p AO to penetrate deep enough into the target inner electron shells for 4fσ MO promotion and Ne^{++} generation. Consider the following AO distances shown in Table 7.7.

Table 7.7: AO distances for several atoms (in Å). Data taken from Slater *op. cit*.

Atom	1s	2s	2p	3s	3p	3d	4s
Ne	0.055	0.37	0.32				
Mg	0.046	0.32	0.25				
Al	0.042	0.27	0.23	1.16	1.21		
Si	0.040	0.24	0.21	0.98	1.06		
Ti	0.025	0.15	0.122	0.48	0.50	0.55	1.66

The values in this table show that as more electrons are added to an atom, the AO's pull closer to the nucleus rather than making the atom much larger overall. This is important in the context of how deeply can the Ne 2p penetrate into the target atom inner shells at low collision energy. As an example, the apsides that were sampled in our Ne^{+}→Ti scattering study at 90° are given in Fig. 7.24 using the TFM potential. Also shown are various permutations of the Ne 2p AO with the AO's of Ti to give a rough idea of possible orbital overlaps. This plot would seem to indicate that if overlap of Ne 2p with the 2s or 2p is required for 4fσ MO promotion, then this process should not occur for impact energies less than 1000 eV at 90° scattering angle. Next, if the 4fσ MO promotion is responsible for Ne^{++} generation, then an Ne^{++} exit should not be seen below 1000 eV either. This is indeed what we find.

A summary plot of the Ne^{+} scattering off Ti is given in Fig. 7.25. First, the Ne^{+} exit off Ti follows the BCA model upward in energy with no clear jump (inelasticity) that is apparent in the Ne^{+}-Mg, Al, and Si cases. Also, we specifically looked for the Ne^{++} exit channel and it was not observed up to the maximum beam energy tested at 1000 eV.

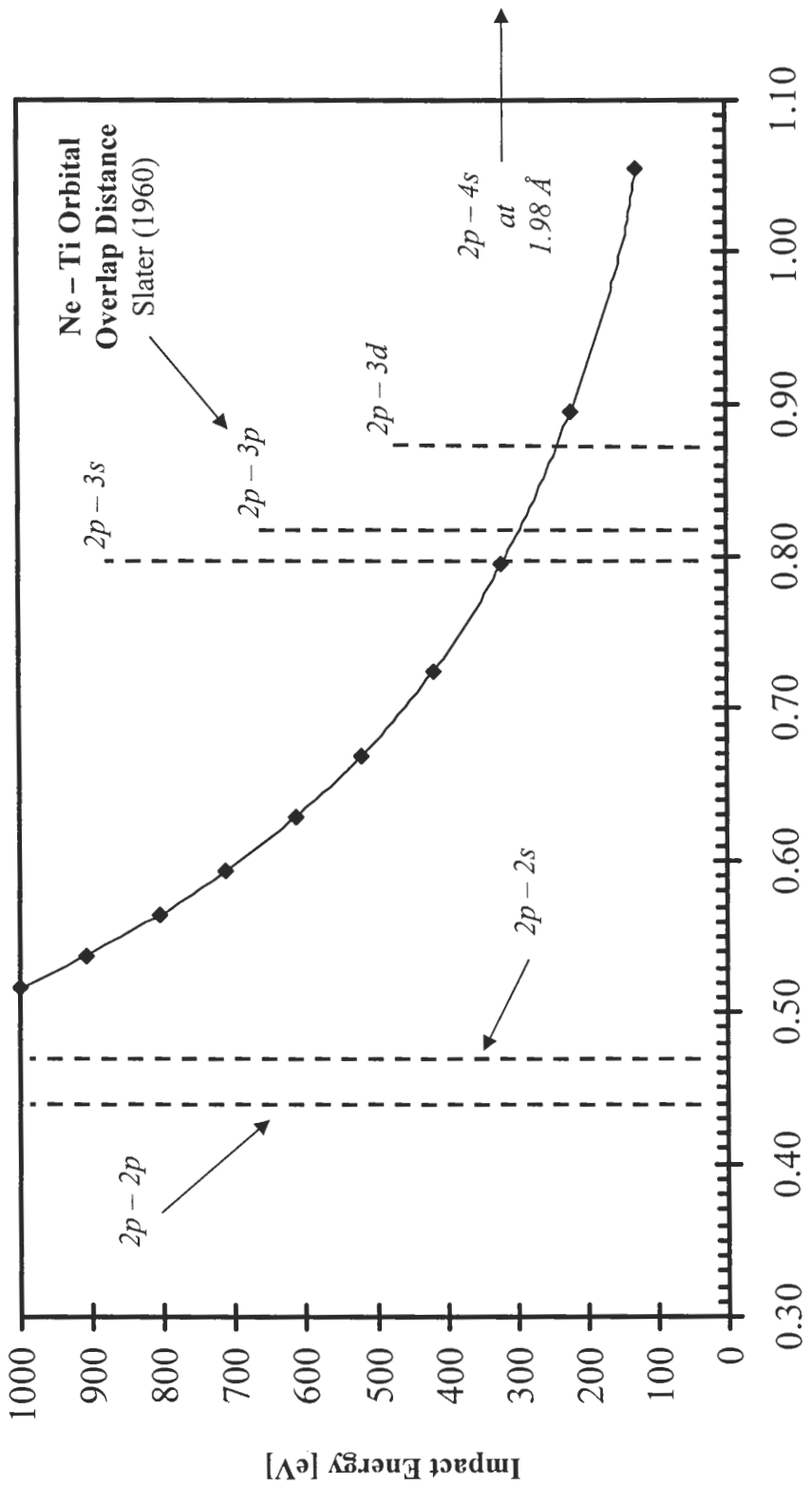

Figure 7.24: Apsides that can be sampled for Ne^+ on Ti at 90° lab angle from the TFM potential. Also shown are calculated overlap distances for atomic orbital states of the collision partners using the data of Slater (1960).
Note: The Ne 2p orbital cannot reach the Ti inner electron shells, even at 1000 eV impact energy.

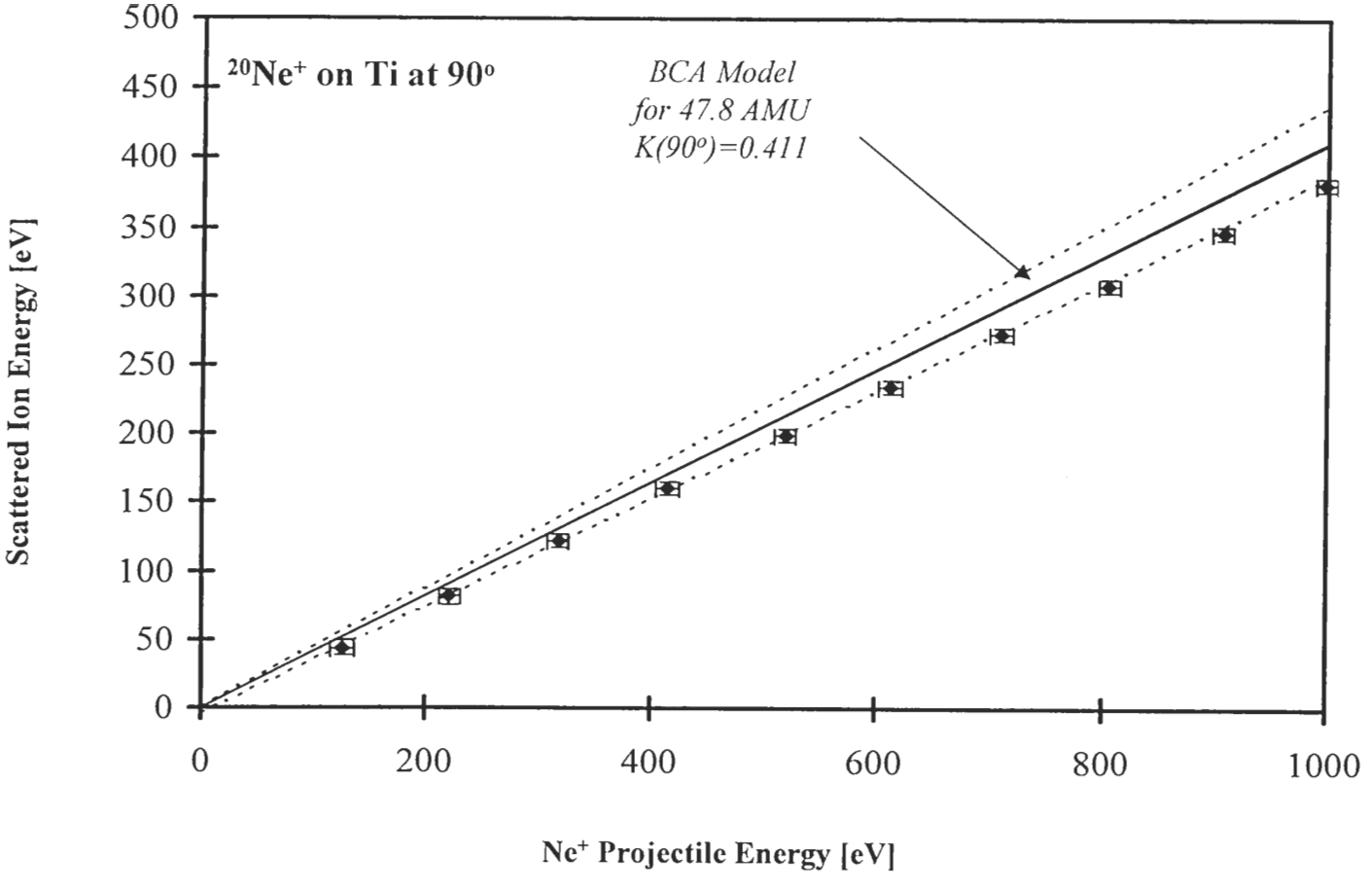

Figure 7.25: Ne^+ exit energy for Ne^+ bombardment of Ti at 90° lab angle. Note: Ti has a bad target nucleus for ISS because it has isotopes at 46, 47, 48, 49, and 50 AMU. The BCA max-min error lines have been calculated for the 46 and 50 AMU isotopes to show the maximum possible error range.

The deviation of the Ne^+ exit from BCA at the upper energies occurs because the raw loss data has not been corrected for the straggling. Since the c_i fitting parameters for the Oen and Robinson loss formula have not been published, it is a bit unclear how we should handle the inelasticity determination for our data.

We note that the high exit energy for Ne^+ off Ti, because the K-factor is much larger than for Mg, Al, or Si, will give a larger Q_3 loss term for the outgoing trajectory. This effect would tend to give more correcting power at higher impact energies for Ti than the other targets (with lower Ne^+ exit energies), and bring the data closer to the BCA model. We have not calculated the Ne^+ inelasticitiies for the $Ne^+ \rightarrow$Ti collision simply because we need more information about the straggling loss to make a proper assessment.

The intent of our $Ne^+ \rightarrow$Ti scattering experiment was to show that Ne^{++} could not be formed for the impact energy range which we could test. The highest energies available in our system, at least from the simple orbital overlap picture, do not allow for Ne 2p overlap with the inner electron shells of Ti. The fact that we do not see Ne^{++} generation suggests that Ne 2p overlap with the inner electron states of the target is a requirement for Ne^{++} generation. Overlap of the Ne 2p with the 3s/3p and 4s states of Ti are not enough to produce the Ne^{++} exit.

7.8 Summary

Collisions of Ne^+ projectiles with surfaces is an ongoing research topic as more is learned about the complex and rich charge exchange processes involved. Studies presented in the literature (~2 keV impact) are somewhat split as to whether one-electron or two-electron processes are responsible for the hard collision inelastic losses. The inelastic loss of Ne^+ at higher collision energies (2 keV) is usually explained by two-electron excitation of $Ne^0 \rightarrow Ne^{**}$, requiring 45 eV. The Ne^0 is formed from neutralization of the Ne^+ projectile along the incoming trajectory path before the hard collision occurs. The Ne^{**} state lifetime is thought to be long enough that autoionization to Ne^+ can occur far away from the surface. Inelasticity measurements for the Ne^+ exit channel off Al and Si typically show 40-50 eV hard collision loss for 2 keV Ne^+ impact energy. Only one

study has been published in the threshold region for inelasticity onset (Xu *et al*., 1998 ─ Ne^+ on Si), which showed a small inelasticity of 5-6 eV at 500 eV incident energy which increased steadily to 40-50 eV for 2 keV impact. Losses at low impact energy were explained as valence band excitations of the Si target. Unfortunately, the increasing inelasticity question was not addressed.

The formation of Ne^{++} is much more controversial, however. Some claim that Ne^{++} is formed from one-electron excitation of Ne^+ directly or even sequential collisions with one-electron excitation in each step (Souda *et al*., 1996): $Ne^0 \rightarrow Ne^+$ (collision #1) then $Ne^+ \rightarrow Ne^{++}$ (collision #2). This latter hypothesis was invoked to explain the Ne^{++} signal at the double scattered position (but not the single scattered position) for an Ne^0 projectile at 2 keV on Al(111).

The other side explains Ne^{++} formation through a two-electron excitation scheme on a surviving Ne^+ (not neutralized on the incoming path) to form Ne^{++*}, requiring 86 eV. The Ne^{++*} is thought to decay directly to Ne^{++} or convert to Ne^{+**} with help from the surface. The Ne^{+**} state would then autoionize far away from the surface to form Ne^{++}. Inelasticiy measurements for the Ne^{++} exit channel on Al and Si have given values in the 75-100 eV range for 1.4-2 keV impact energies.

We have conducted experiments at lower energies to investigate the near-threshold loss processes. We see a small Ne^+ inelasticity which increases to a saturation-like value as the impact energy is raised for Mg, Al, and Si targets. The low value for the Ne^+ inelasticity in the threshold region suggests mechanisms that are different from those published for larger impact energies. The smaller inelasticities we measure in the threshold region favor one-electron excitation processes rather than two-electron transitions. However, our measured inelasticity values approach the literature findings for both Ne^+ at ~45 eV and Ne^{++} at ~ 86 eV in the high energy limit for Al and Si, but slightly higher values for Ne^+ off Mg are seen.

We find that the turn-on for Ne^+ inelasticity appears to move to lower energy as the target gets lighter. This is consistent with Ne 2p AO overlap requirements with the target atom 2s or 2p AO states, which get further away from the nucleus as the target atom gets lighter. L-L shell overlap appears to be a prerequisite for the simultaneous turn-on of inelastic losses, Ne^+ yield decrease, and Ne^{++} generation.

We have also seen that the onset of Ne^{+} inelasticity, as a deviation from the single collision BCA no-loss model, occurs in conjunction with the Ne^{++} generation channel turn-on. This coincidence suggests a common underlying mechanism for excitation. Inelasticities for Ne^{++} in the threshold region are on the order of ~50-60 eV and increase to 80-90 eV at the highest energies tested. The low Ne^{++} inelasticity (50-60 eV) is inconsistent with the proposed mechanism in literature for Ne^{++} production through the Ne^{++*} state that requires ~86 eV hard collision loss.

We have presented an alternative mechanism for the threshold region which combines the MO promotion framework with electron exchange from the target valence band and irreversible electron loss to vacuum. This hybrid picture seems to explain all our experimental observations for Ne^{+} on Al and Si (see the conclusions for $Ne^{+}\rightarrow$Al in Section 7.7.2 for details). The major points are summarized below (reference Figs. 7.14 and 7.15).

Apsides larger than the critical internuclear distance (lower projectile energy)

(1) Elastic Ne^{+} scattering at low projectile energy.

At low collision energies, the AO's of the collision partners do not inter-penetrate enough to promote the 4fσ MO significantly. As a result, there are no inelastic loss channels available because the weakly promoted 4fσ MO does not cross the valence/conduction bands of the target or the vacuum level. The Ne^{+} ($2p^5$) projectile never reaches the point where the 4fσ and 3dπ MO's split on the PE diagram (Fig. 7.13).

(2) Scattered Ne^{+} yield increases exponentially with increasing projectile energy.

Below the threshold apsis for significant 4fσ MO promotion, we saw that the increase in Ne^{+} yield could be well explained by the Auger neutralization (AN) model of Hagstrum. This model predicts an exponential rise in the ion survival rate with decreasing contact time in the near surface region (as measured by the reciprocal velocities of the projectile, perpendicular to the target surface, along the incoming and

outgoing paths). Our experimental data for the Ne^+ yield on Al provided a characteristic neutralization velocity of $6.0 \bullet 10^{6\ cm}/_{s}$. When this velocity is inverted for a 1-3 Å neutralization distance, an Auger transition rate of $2\text{-}5 \bullet 10^{14}\ sec^{-1}$ is obtained ─ in excellent agreement with AN rates for other rare gas ions on metals.

Apsides smaller than the critical internuclear distance (higher collision energies)

(3) Ne^+ yield decrease at the turn-on point.

Higher collision energy and smaller apsis cause significant 4fσ MO promotion. If the entering Ne^+ 2p (with one vacancy) evolves as the $3d\pi^4 4f\sigma^1$ quasi molecule, the 4fσ vacancy can be easily filled by resonant capture (RC) of an electron from the filled valence band (VB) of the target ─ neutralizing the projectile. As a result, the Ne^+ yield decreases with increasing collision energy, once the threshold energy needed to promote the 4fσ MO (enough to cross the filled VB states of the target) has been reached.

(4) Ne^+ inelasticity onset.

If the 4fσ MO is promoted all the way to the vacuum level, the $3d\pi^4 4f\sigma^1$ quasi molecule can be filled by RC from the VB on the PE curve ascent (to form $3d\pi^4 4f\sigma^2$), and lose an electron to vacuum ─ re-making the $3d\pi^4 4f\sigma^1$ state. On the PE curve descent, the $3d\pi^4 4f\sigma^1$ state may not be re-filled by RC from the VB. The end result is an inelastic Ne^+ exit from the descending $3d\pi^4 4f\sigma^1$ state, which shows ~20 eV hard collision loss.

(5) Ne^{++} formation.

In contrast to (4), the hard collision can also evolve as $3d\pi^3 4f\sigma^2$, where the Ne^+ vacancy is demoted in the 3dπ MO (which never crosses the VB or vacuum levels). If the filled $4f\sigma^2$ MO is strongly promoted up to the vacuum level, an electron can be

kicked out to vacuum, creating a second vacancy ─ thus, Ne^{++} is formed. The Ne^{++} exit would show an inelastic hard collision loss of at least 41 eV, the second ionization potential ($Ne^{+} \rightarrow Ne^{++} + e^{-}$).

(6) Increasing Ne^{+} and Ne^{++} inelasticities.

Although we have not specifically answered this question, we put forth the idea that the increasing inelasticity might be accommodated as energetic electron release (electrons ejected to vacuum with ″some″ kinetic energy) at the turning point on the 4fσ MO PE curve. We argued that the 4fσ MO is promoted to ever higher energies as the apsis gets smaller, and that the electron release would most likely occur at the slowest point along the projectile trajectory (the turning point on the PE curve). Such an idea allows electron ejection into a ″continuum,″ which could explain the smooth increase in inelasticity that is seen for both Ne^{+} and Ne^{++}. Finally, we also admit that target atom excitation might be responsible for the increasing inelasticity. However, discrete electronic excitations of target atoms would seem to manifest themselves as finite jumps in the inelasticity data, which is not seen in our work or the work of others.

8. Future Work

This chapter contains a mix of ideas for future experiments with inert projectiles on light targets and some preliminary results for the $CF_x^+ \rightarrow Si$ system, where surface chemical reactions occur during scattering. Scattering experiments with Ne^+ will be outlined which may shed more light on the rich charge exchange processes that occur on lighter target materials. Specifically, energy loss measurements of the neutral Ne component could give more clues about the excitation mechanisms involved in the threshold region of inelasticity onset and perhaps give more ideas about the Ne^+ and Ne^{++} exits. The CF_3^+ ion scattering on Si is served as a demonstration of our ion beamline scattering system in all its splendor as well as the first step in getting a detailed understanding of Si dry etching processes that are used today industrially for pattern transfer on Si / SiO_2.

8.1 Rare Gas Ion Scattering

8.1.1 Ne^+ Projectiles

The most obvious scattering studies to be conducted next with inert projectiles should be Ne^+ on lighter targets like Na, K, and Ca. The trends which we saw for the Ne^+ inelasticity onset with projectile energy and the sharp turn-on for Ne^{++} generation through charge exchange with target atoms should be extended. The hypothesis that $4f\sigma$ MO promotion involving the Ne 2p orbital is the operative generation mechanism for Ne^{**} and perhaps Ne^{++} should be tested for more target materials.

Our experiments showed that the threshold impact energy for Ne^+ inelasticity onset and Ne^{++} generation increases as we go from Mg to Al to Si. This behavior is totally consistent with a required threshold apsis distance for the $4f\sigma$ MO formation that decreases as the target gets heavier. We noted that the 2s and 2p AO states of the target atom pull closer into the nucleus for increasing target mass, and this AO shrinking fits the picture of higher impact energy required for Ne 2p overlap with the target 2s or 2p AO states. We also saw that $Ne^+ \rightarrow Ti$ did not show any Ne^{++} generation below 1000

eV impact energy. The Ti 2s and 2p states lie too close to the nucleus for overlap with the Ne 2p for 1000 eV at 90° lab angle. Na, K, and Ca should be tested to demonstrate the utility of the overlap hypothesis in the Ne^{++} generation channel. Calculations with the TMF potential suggest that the overlap trend for Ne^{++} generation should occur at 400 eV or less for Na, near 1000 eV for the K surface, and Ca being borderline for the highest energy we can test (1400 eV).

The ″opening-up″ of inelastic loss channels (Ne^{+} inelasticity, Ne^{++} generation) with increasing impact energy signals an excitation process which requires a threshold distance between the colliding nuclei. As an example, consider the $Na^{+}\rightarrow Ne$ system which has been well studied in the gas phase (Ostgaard *et al*., 1979). We can directly compare the excitation schemes seen in the $Na^{+}\rightarrow Ne$ system with our reverse system of Ne^{+} on a solid Na target. A molecular orbital (MO) correlation diagram from the Ostgaard data is given in Fig. 8.1 for the $(NaNe)^{+}$ system. This diagram shows the relative energy levels and hybrid MO's that are formed from the overlapping of atomic orbitals (AO) of the collision partners as the nuclei approach one another.

The potential energy of the MO states (3sσ, 4fσ, 4dσ, *etc*.) with respect to the internuclear distance is represented along with how the MO's are correlated to the individual AO states of the collision partners (Ne─2p with 4fσ, Na─3s with 3sσ, *etc*.). According to the Fano-Lichten-Barat model, excitation can occur through electron promotion between the hybrid MO states of the quasi-molecule when the MO states ″cross″ in potential energy (indicated by circles). Electron transfer can also occur between filled and empty levels through rotational couplings such as $4p\sigma\rightarrow 3p\pi$ (rectangle indications). When the collision partners approach, electrons can be excited to higher MO states at the ″curve-crossings.″ As the collision partners recede from one another, the excited electrons become trapped in higher states which decay to higher lying AO states of the receding atoms.

The charge exchange reactions which can occur between the collision partners depend on which atoms provide the electrons for excitation and which atoms take them. The collision partners can effectively (1) give and take back their own Rydberg electrons ─ a direct promotion of the atom's own electrons (Direct – D) or (2) exchange the electrons to the other atom (Exchange – E).

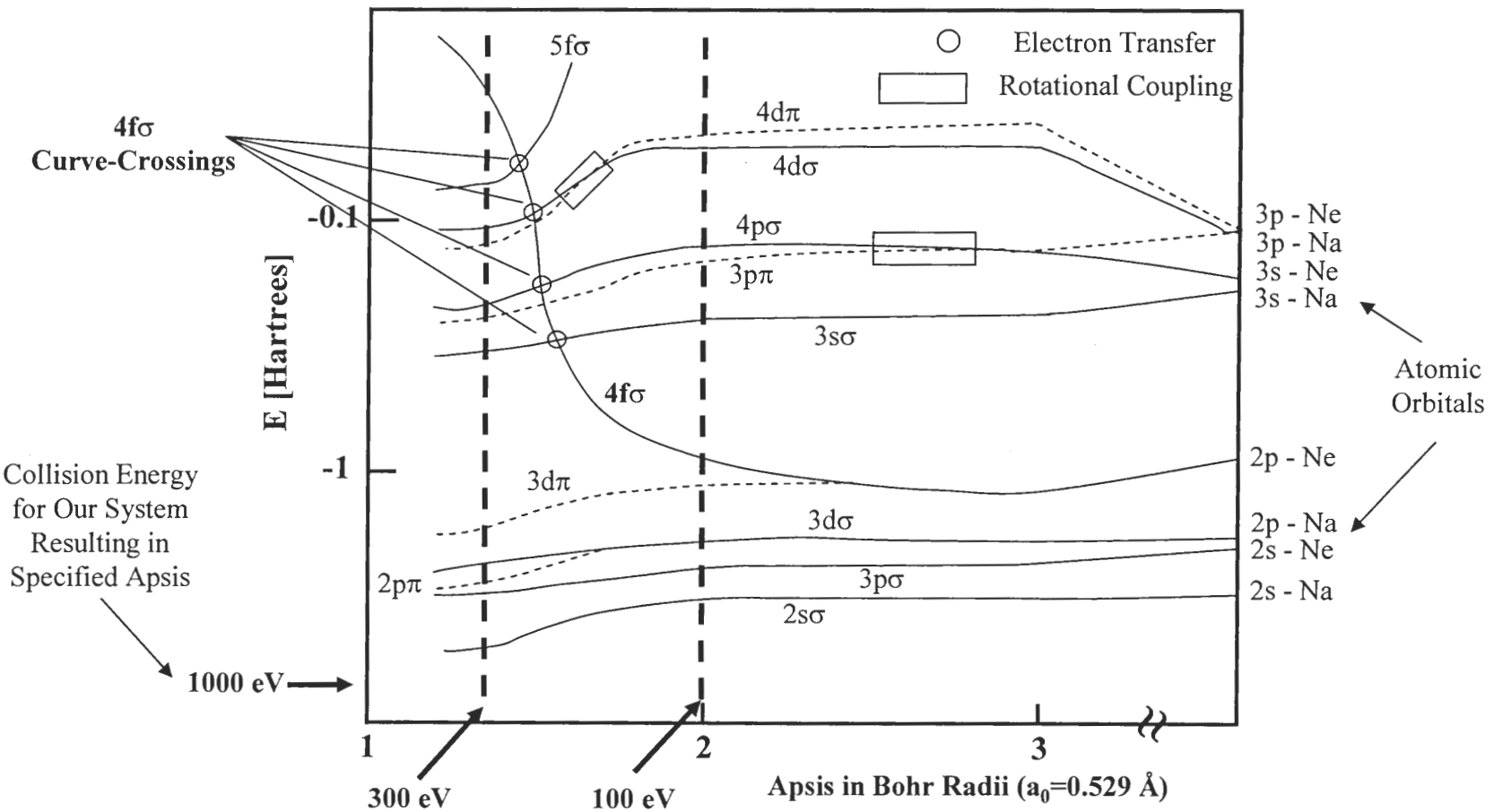

Figure 8.1: Molecular orbital correlation diagram for the $(NaNe)^+$ collision system. Data from Ostgaard *et al.* (1979). The energies listed correspond to collision apsides for 90° lab scattering angle that we can sample with our scattering system. When the 4fσ MO crosses other MO states (circles), one- and two-electron transfer processes can occur, resulting in excited Na and Ne states as the collision partners recede.

This electron promotion and swapping for the $(NaNe)^+$ system having one electron available for transfer between MO states can be described thematically as follows. The initial state of the collision is represented below (assume that Ne gives the Rydberg electron):

$$\left[Na^+\left(2p^6\right) + Ne^+\left(2p^5\right)\right] \text{ core + 1 Rydberg electron (from Ne)} \qquad (8.1)$$

As the collision partners recede, two outcomes from the $Na^+ \rightarrow Ne$ collision are possible, based on which nuclear core takes the Rydberg electron:

<u>Ne takes its own electron back</u>: (I) $Na^+\left(2p^6\right) + Ne^*\left(2p^5 - nl\right)$ (D) (8.2)

or

<u>Na takes the Ne electron</u>: (II) $Na^*\left(2p^6 - nl\right) + Ne^+\left(2p^5\right)$ (E) (8.3)

Likewise, a two-electron excitation can yield three outcomes:

$$\left[Na^+\left(2p^6\right) + Ne^{++}\left(2p^4\right)\right] \text{ core + 2 Rydberg electrons (both from Ne)} \qquad (8.4)$$

gives

<u>Ne takes both its electrons back</u>: (I) $Na^+\left(2p^6\right) + Ne^{**}\left(2p^4 - nln'l'\right)$ (D) (8.5)

<u>Na gets one, Ne gets one</u>: (II) $Na^*\left(2p^6 - nl\right) + Ne^{+*}\left(2p^4 - n'l'\right)$ (E) (8.6)

<u>Na takes both</u>: (III) $Na^{-*}\left(2p^6 - nln'l'\right) + Ne^{++}\left(2p^4\right)$ (E) (8.7)

The entire charge exchange process gets more complicated because the Na *or* the Ne can give the initial Rydberg electrons (one or two) as well as exchange them or take them back. Table 8.1 summarizes some of the outcomes which can occur for the $(NaNe)^+$ system for one and two-electron excitation processes depending on which atom gives the initial Rydberg electrons for the transition.

Table 8.1: Electronic excitations and exit channels which can occur for the gas-gas scattering system $(NaNe)^{+}$. Source column identifies # Rydberg electrons and their initial source for the transition. The direct or exchange transitions are listed with the initial core configuration. The exit channel column specifies the outcome that one would observe in the lab frame. Adapted from Ostgaard *et al*. (1979).

# - Source	Core States	Direct (D) or Exchange (E)	Exit Channels
1 - Ne	$Na^{+}\left(2p^{6}\right)+Ne^{+}\left(2p^{5}\right)$	D	$Na^{+}\left(2p^{6}\right)+Ne^{*}\left(2p^{5}-nl\right)$
1 - Ne	$Na^{+}\left(2p^{6}\right)+Ne^{+}\left(2p^{5}\right)$	E	$Na^{*}\left(2p^{6}-nl\right)+Ne^{+}\left(2p^{5}\right)$
1 - Na	$Na^{++}\left(2p^{5}\right)+Ne^{0}\left(2p^{6}\right)$	D	$Na^{+}\left(2p^{5}-nl\right)+Ne^{0}\left(2p^{6}\right)$
1 - Ne	$Na^{+}\left(2p^{6}\right)+Ne^{+}\left(2p^{5}\right)$	D (ionization)	$Na^{+}\left(2p^{6}\right)+Ne^{+}\left(2p^{5}\right)+e^{-}$
2 - Ne	$Na^{+}\left(2p^{6}\right)+Ne^{++}\left(2p^{4}\right)$	D	$Na^{+}\left(2p^{6}\right)+Ne^{**}\left(2p^{4}-nln'l'\right)$
2 - Ne	$Na^{+}\left(2p^{6}\right)+Ne^{++}\left(2p^{4}\right)$	E	$Na^{*}\left(2p^{6}-nl\right)+Ne^{+*}\left(2p^{4}-n'l'\right)$
2 - Na	$Na^{++}\left(2p^{5}\right)+Ne^{+}\left(2p^{5}\right)$	D	$Na^{+*}\left(2p^{6}-nl\right)+Ne^{*}\left(2p^{5}-n'l'\right)$
2 - Na	$Na^{++}\left(2p^{5}\right)+Ne^{+}\left(2p^{5}\right)$	E	$Na^{**}\left(2p^{5}-nln'l'\right)+Ne^{+}\left(2p^{5}\right)$
2 - Ne	$Na^{+}\left(2p^{6}\right)+Ne^{++}\left(2p^{4}\right)$	D (ionization)	$Na^{+}\left(2p^{6}\right)+Ne^{+*}\left(2p^{4}-nl\right)+e^{-}$ $Na^{+}\left(2p^{6}\right)+Ne^{++}\left(2p^{4}\right)+2e^{-}$

All of these potential charge exchange reactions have different energy deficits which are manifested as inelastic losses in the hard collision. One-electron processes are more favorable at larger apsis, while two-electron transitions occur for smaller apsides.

The energy deficit for the transition depends on the final states as well as which atoms provide the Rydberg electrons.

The reason for bringing up this entire discussion on the $Na^+ \rightarrow Ne$ system can be seen by the multiple curve-crossings on the MO correlation diagram (Fig. 8.1) and the rich structure in the charge exchange phenomena (Table 8.1). The collision apsides which we can sample in our experiment with 90° lab scattering angle are indicated with arrows on Fig. 8.1. As shown, tuning the Ne^+ projectile energy from 100 eV to 1000 eV allows for multiple curve-crossings where electron promotion or exchange can occur. These promotions/exchanges will manifest themselves as discrete inelastic losses in the projectile exit energy. From the charge exchange reactions listed, we can see that the projectile could exit the collision in a variety of excited neutral or excited ion states ─ depending on which process is dominant for a specific apsis range (which MO curve-crossings occur). Careful control of the projectile incident energy (which we have demonstrated for our system) would allow specific cross-over points to be sampled. One would expect that the exit energy of the neutral and ion should reflect which inelastic process occurs. Therefore, we would like to carefully examine the Ne^+ inelasticity and Ne^{++} formation (which there should be) with respect to projectile energy to see if the ISS or directly scattered neutral energy spectra contain the fine structure of the MO crossings.

Another obvious next step in Ne^+ scattering is to turn on the ionizer of the scattered product detector and measure energy losses for Ne^0 leaving the surface for Mg, Al, and Si targets (Na-especially, K, and Ca). It has been demonstrated in gas-gas scattering for the $Na^+ \rightarrow Ne$ system that the neutral spectrum shows inelastic losses that are clearly assignable to direct Na^* excitation as well as Ne^{+*} (Ostgaard). The energy losses for these excited neutral exit channels could clear up the picture of excitations in the hard collision for both Ne^0 and Ne^+ along with perhaps the Ne^{++} generation mechanism.

It would be quite interesting from a broader perspective to compare how the presence of the surface changes the charge transfer characteristics of the scattering process. The conduction band of the solid should have a strong influence on the charge state distribution of the scattered projectiles. We also believe that there is a lot of useful information hidden in the neutral exit energy spectrum. Very few measurements of the

neutral exit distributions from surface scattering have been reported in the literature. The high flux at lower impact energies and sensitive product detection capabilities of our system may enable some of these neutral studies. One has to only look back to Table 8.1 to see that several of the electron transfer processes in the $(NaNe)^+$ collision system can only be studied through the neutral exit energy distributions.

8.1.2 Ar^+ Projectiles

For an ion-solid system, $Ar^+ \rightarrow K$ and $Ar^+ \rightarrow Ca$ should be the first systems to study. It has been shown by many authors that in gas-gas scattering, the same excitation mechanisms are often operative for similar collisions, like $Ne^+ \rightarrow Ne$ and $Na^+ \rightarrow Ne$. Also, the $Ar^+ \rightarrow Ar$ collision in the gas phase shows a remarkable richness in the ion energy loss spectra just as $Ne^+ \rightarrow Ne$ (Barat *et al*., 1970). Multiple inelastic peaks associated with target atom and projectile excitations can be seen from the Ar^+ energy distribution:

$$Ar^0 \rightarrow Ar^*\left(3p^5 - nl\right) \quad \text{(direct)} \tag{8.8}$$

$$Ar^0 \rightarrow Ar^*\left(3s3p^6 - nl\right) \quad \text{(direct)} \tag{8.9}$$

$$Ar^+\left(3p^5\right) \rightarrow Ar^+\left(3p^4 3d\right) \quad \text{(direct ionization of projectile)} \tag{8.10}$$

It is highly likely that some of the same excitation phenomena in the $Ar^+ \rightarrow K$ system would occur as those in $Ar^+ \rightarrow Ar$ for the gas phase. In addition, the $K^+ \rightarrow Ar$ and $Na^+ \rightarrow Ne$ systems are ″superficially similar″ because electron transitions involving Ar─3p with K─4s/4p are in some ways analogous to transitions involving Ne─2p with Na─3s/3p. Does the Ar^+ inelasticity onset or Ar^{++} generation require an analogous orbital overlap in the $Ar^+ \rightarrow K$ collision as Ne^+ inelasticity and Ne^{++} formation in the $Ne^+ \rightarrow Na$ collision (Ar ─3s/3p with K ─3s/3p versus Ne ─2p with Na─ 2s/2p)? We surmise that $Ne^+ \rightarrow Na$ will show similar behavior to the systems we have tested: $Ne^+ \rightarrow$ Mg, Al, and Si?

Also, very recent Auger measurements for Ar^+ on K covered Al surfaces has demonstrated that K is sputtered from the surface as K^{**}, which autoionizes to K^+

(Sánchez *et al*., 2002). The K^{**} autoionization is believed to result from the $K^{**}\left(3s^2 3p^5 4s^2\right)$ state. Although they do not specify how the doubly excited state decays, we would imagine that it would be the following:

$$K^{**}\left(3s^2 3p^5 4s^2\right) \rightarrow K^{+}\left(3s^2 3p^6\right) + e^{-} \text{ at} \sim 14 \text{ eV} \tag{8.11}$$

The K^{**} excitation is surely a two-electron transition that would involve a charge exchange reaction something like the following (where both Rydberg electrons are provided by the K atom):

$$\left[Ar^{+}\left(3s^2 3p^5\right) + K^{++}\left(3s^2 3p^5\right)\right]_{CORE} + 2e^{-}_{fromK} \rightarrow$$
$$Ar^{+}\left(3s^2 3p^5\right) + K^{**}\left(3s^2 3p^5 - nln'l'\right) \tag{8.12}$$

Given this excitation scheme, the Ar^{+} exit energy should show a considerable inelastic loss associated with promotion of the two Rydberg electrons in K. The authors state that they do not know if the K^{**} state results from an $Ar^{+}\rightarrow K$ collision or a $K\rightarrow K$ collision (between two sputtered K atoms). Our system should be able to measure the Ar^{+} loss involved in reaction 8.12 and determine which collision causes the excitation.

8.1.3 Electron Spectroscopy

It is clear from the gas-gas scattering literature as well as ISS studies that electron emission during or shortly after the hard collision is invaluable in getting a clearer picture of electron transitions during the collision. Autoionization decay of Ne^{**} and Ne^{+**} (perhaps formed) is a tell-tale sign of inelastic collisions with strong excitations of the collision partners. In fact, it is doubtful if the ISS loss data alone for the inelastic Ne^{+} exit would have lead to the conclusion of a very favorable $Ne^{0}\rightarrow Ne^{**}$ transition at the higher collision energies (the Auger decay of Ne^{**} was the indicator ─ the ISS loss agreed with the $Ne^{0}\rightarrow Ne^{**}$ pump energy). We would like to see simultaneous Auger

measurements in our system along with the ISS information in the threshold impact energy region below 1 keV for Ne^+ on light targets. Because ISS measurements are not frequently combined with Auger *in the same system*, correlating the turn-on of ISS channels with Auger release from the projectile and target is very difficult. Undoubtedly, the only way to understand the rich charge exchange phenomena that occur when ions impact a surface is to combine detection of ions, neutrals, and electrons. We have the capability in our system to investigate the mass and energy space of ions and neutrals leaving the target surface, but electron information would be very advantageous.

8.2 Preliminary Studies of CF_3^+ Reactive Scattering

Scattering studies using CF_3^+ projectiles on Si(100) were conducted as preliminary work towards a larger, long-term goal of understanding the fundamental energetics and reaction mechanisms that occur during reactive ion bombardment of Si, as applied to dry plasma etching processes. These experiments with pure, mass-filtered beams of reactive projectiles in the low energy range from 50-500 eV are one of the main driving forces behind our whole low energy ion beamline system. This unique energy range is directly relevant to plasma processing because all dry etching processes are conducted with ion impact energies less than 500 eV. The 50-500 eV range is required in plasma etching to provide momentum assist to surface chemical reactions and stimulate etch product removal from the wafer surface *without* causing damage to the substrate from heavy sputtering at high impact energies. This unique energy regime and pure beams of CF_x^+ ions, when combined with mass and energy analysis of reaction products leaving the surface, represent the first time such an endeavor has ever been undertaken.

The experiments presented in this section just scratch the surface of processes occurring in CF_x etching of Si, but they truly demonstrate the *power* and *need* of such a complex scattering system as the one built for this dissertation project. One has only to look back to the introduction in Chapter 1 to appreciate the ramifications of conducting a fundamental study using one ion species at well defined energy along with broad based detection of the neutral and charged particle flux leaving the target surface. It is clear that a fundamental understanding of the complex mechanisms involved in reactive ion

etching requires all the pieces: (1) robust high density ion source, (2) mass-filtered ion beamline, (3) low tunable energy, (4) high current, and (5) detection of mass and energy of ions and neutrals leaving the substrate surface.

The first step in a study on CF_x etching of Si involves fundamental scattering experiments with one of the most common reactive ions found in the plasmas used for Si/SiO_2 etching: CF_3^+. We have shown earlier in Chapter 5 that pure ion beams of CF_3^+ projectiles can be generated in our ion beamline system using CF_4 / Ar / O_2 plasmas. We have used these beams for preliminary scattering experiments with CF_3^+ on Si(100) to ascertain what ion species leave the Si surface during bombardment at different impact energies in the 70-500 eV range. Even though this experiment seems rather simple and an ideal starting point for fundamental studies of CF_x etching mechanisms of Si, it has never really been done before. Our broad based detection capabilities allows for both mass and energy dispersion of the ion flux leaving the surface which can provide clues about surface processes. For instance, what is the fate of the CF_3^+ molecular ion as it hits the surface and which ion species are preferentially released from the reactive SiC_xF_y layer that forms on the Si surface during bombardment?

Figure 8.2 shows a summary of the ion species leaving a Si surface under CF_3^+ ion bombardment in the relevant ″etching″ energy range below 500 eV. Note the logarithmic scale for the total ion intensity. As shown, the main ion species leaving the surface are CF^+, C^+, Si^+, and surprisingly SiF^+. At the lowest impact energy (~70 eV), some CF_3^+ and CF_2^+ are seen, but they quickly disappear above 100 eV impact energy. The presence of CF_3^+ at low energy could signify molecular ion survival while the CF_2^+ may be caused by F-atom abstraction of the incoming projectile (dissociative scattering) or physical sputtering of CF_2-like species on the surface. It is interesting to compare these results with CF_3^+ scattering off fluorinated liquid surfaces by Koppers *et al.* (1996). For 100 eV impact of CF_3^+ on an inert liquid surface (perfluoropolyether (PFPE) or Fomblin oil), they see molecular ion survival along with dissociative scattering to yield CF_2^+ and CF^+ exit species between 40-80 eV. The PFPE liquid surface has been shown to be terminated entirely by $–CF_3$ and –F species with the ether oxygen atoms buried beneath the surface (King *et al.*, 1993, 1994).

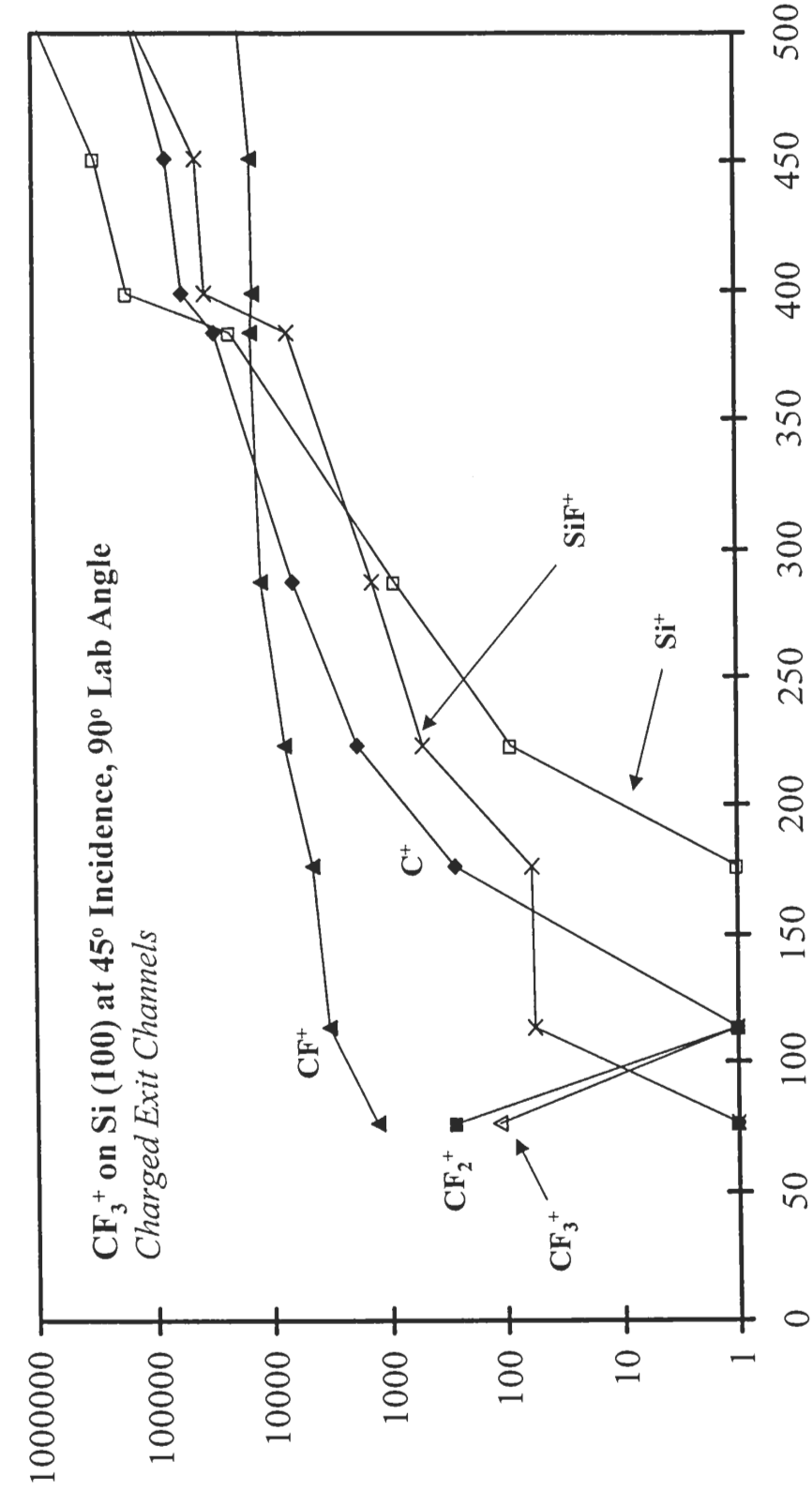

Figure 8.2: Charged exit channel intensity for CF_3^+ bombardment of Si(100) at 90° lab scattering angle.

In some sense, the collision phenomena that occur between the projectile ion and $–CF_x$ terminated surface for the PFPE case could also be important for Si because it is fairly well accepted that CF_x etching of Si proceeds through a reactive SiC_xF_y layer with dangling $–CF_x$ and $–SiF_y$ moieties (Lieberman and Lichtenberg, 1994). Koppers also found that the predominant ion exit for CF_3^+ scattering on PFPE at >250 eV impact energies was CF^+, with little or no CF_2^+ or CF_3^+. Our preliminary work echoes this behavior as well.

What is interesting at energies above 100 eV is the rise of the C^+ and SiF^+ exit channels. The large increase in SiF^+ from the surface suggests that as the impact energy gets higher, more projectile F atoms react to form dangling SiF_x species which are sputtered away as SiF^+ only (if they exit the surface in a charged state). We specifically looked for SiF_2^+ and SiF_3^+ leaving the surface and did not detect any signal for all the impact energies tested. It is most curious why SiF^+ is the only charged Si-containing species leaving the surface. Finally, the spectra shows the onset of Si^+ for impact energies above ~200 eV, which is a sure sign that the increased momentum of the CF_3^+ projectile is beginning to just sputter the target surface.

These studies give a flavor for the physical scattering behavior as well as some of the chemical reactions that are occurring on the surface during bombardment with just one incident ion species ─ CF_3^+. It is also clear from this one experiment that complex scattering behavior, especially for a reactive system, absolutely requires mass-filtering of the particle flux leaving the target surface to sort out all the exit channels. Turning on the ionizer to look at the neutrals along with energy analysis of the scattered flux will add a whole new dimension to fundamental scattering studies.

8.3 Future Studies for CF_x^+ Projectiles

The first set in a long line of CF_x^+ scattering studies off surfaces should begin with developing an understanding for how molecular ions of the CF_x^+ homologous series fragment on well defined surfaces. Inert metals like Au and Pt, where no reaction between the projectile and target atoms takes place, should be investigated to understand how the different CF_x ions break apart upon impact. The energetics of this dissociative

scattering process are very important from the perspective of exactly how the ion behaves in the collision. For example, in the CF_3^+-Au system, does the collision really occur ″atom to atom″ where the exit energy of the CF^+ daughter ion is given by BCA for CF (mass 31) on Au (mass 197) or does it occur as CF_3 (mass 69) on Au followed by inelastic loss from the CF_2-F bond breaking? This energy difference should be easy to see in the scattered ion energy spectrum of CF^+. In a sense, does the daughter ion form along the incoming path due to electron transfer with the surface *before* the hard collision or does it occur *during* the hard collision? Also, how is energy transferred to the surface and to the internal energy of the scattered ion? Such fundamental aspects of molecular ion scattering need to be answered.

Next, the CF_x^+ homologous series should be scattered off Si with analysis of both the ion and neutral fluxes leaving the surface. Specifically, gaseous products, such as SiF_2 and SiF_4, are thought to be the main removal mechanism for Si atoms off the surface (Coburn and Winters, 1978; Lieberman and Lichtenberg, 1994). We wonder where Si-containing ions leaving the surface fit into the current picture of etching of Si/SiO_2 with CF_x chemistries.

As mentioned in Chapter 1, Tachi *et al.* (1981) have studied the etch rate of Si as a function of impact energy for the CF_x^+ series. Their results show that CF_2^+ and C^+ are remarkable sticky at low impact energies and even deposit on the surface. How does this process, as the Si surface develops a CF_2 polymer-like layer, affect the scattering behavior? Do the projectile ions simply bounce off the ″inert″ surface layer as in the case of PFPE studied by Koppers *et al.* (1996)?

8.4 $XeF_2 + Ar^+$ and $XeF_2 + CF_x^+$ on Silicon

Scattering studies that are directly relevant to industrial processes are often impossible to realize in the lab. For instance, plasma etching of Si and SiO_2 occurs through continuous fluorination of the substrate surface by neutral F atoms from the gas phase of the plasma right along with energetic ion bombardment of the surface. Removal of Si occurs by momentum assisted chemical reactions, volatile product formation such as SiF_2 and SiF_4, and efficient ″sputtering″ of weakly bound SiF_x species on the surface.

SiO_2 etches because the carbon from the CF_x^+ projectile enables the formation of volatile, O-containing species such as CO, CO_2, COF and COF_2 (Lieberman and Lichtenberg, 1994).

However, a continuously fluorinated Si surface can be formed in the lab using XeF_2. XeF_2 has been shown to decompose on the Si surface to Xe and F_2 (Winter and Coburn, 1979). The F_2 spontaneously reacts and forms a nice, fluorinated Si reactive layer that closely approximates the substrate surface in an actual etching environment. The fluorinated Si surface is ideal for inert gas ion as well as reactive ion scattering experiments of direct relevance to plasma etching. A few studies with XeF_2 on Si have been done in the past, primarily to measure the etch rate for different projectile ion species as a function of the impact energy (Coburn *et al*., 1977). Almost every bit of this work was done at higher energies (>1 keV) and without mass-filtered projectile beams. One has to wonder the relevance of 1-5 keV impact energy for comparison with plasma etching where the ion energy is *always* less than 500 eV. No one has investigated the product distribution leaving the surface in detail for such a scenario, not to mention the energetics of scattering.

This one system of fluorinated Si with inert projectile experiments first (primarily Ar^+), followed by reactive ions like the CF_x homologous series, can improve understanding of the surface processes and reaction products involved in the real etching environment. These experiments have been talked about for 20 years in the plasma etching community and no one has ever stepped-up to do them. The combined capabilities of our detection system for mass and energy analysis of ions and neutrals leaving the fluorinated Si surface can finally look at a real etching system in a fundamental way.

Bibliography

Amano, J., Bryce, P., and Lawson, R. P. W., *J. Vac. Sci. Technol*. **13(2)**, 591 (1976).

Andersen, A. ed., *A Physicist's Desk Reference: Physics Vade Mecum*, 2nd ed., American Institute of Physics, New York (1989).

Ascione, F., Manico, G., Bonanno, A., Oliva, A., and Xu, F., *Surf. Sci*. **394**, L145 (1997).

Barat, M., Baudon, J., Abignoli, M., and Houver, J.C., *J. Phys., B* **3** (1970).

Barat, M. and Lichten, W., *Phys. Rev.* A **6**, 211 (1972).

Baragiola, R. A., Alonso, E. V., and Raiti, H.J.L., *Phys. Rev. A* **25(4)**, 1960 (1982).

Bello, I., Chang, E. H., and Lau, W .M., *J. Vac. Sci. Tech. A* **12(4)**, 1425 (1994).

Bertrand, P., Delannay, F., and Streyido, J. M., *J. Phys. E Sci. Inst.***10**, 403 (1977).

Blum, V., Brugger, A., Nixon, A. P., and Gallon, T. E., *J. Phys. Condens. Matter* **6**, 9677 (1994).

Bourne, H. C., Cloud, R. W., and Trump, J. G., *J. App. Phys*. **26(5)**, 596 (1955).

Briggs, D. and Seah, M. P., *Practical Surface Analysis: Ion and Neutral Spectroscopy*, 2nd ed., vol. 2, John Wiley and Sons, New York (1992).

Coburn, J. W., Winters, H. F., and Chuang, T. J., *J. App. Phys*. **48(8)**, 3522 (1977).

Coburn., J. W. and Winters, H. F., *J. App. Phys*. **50(5)**, 3189 (1978).

Coburn, J. W. and Winters, H. F., *J. Vac. Sci. Tech*. **16(2)**, 391 (1979).

Coggeshall, N., *J. App. Phys*. **18**, 855 (1947).

Considine, D. M. ed., *Van Nostrand's Scientific Encyclopedia*, 5th ed., Van Nostrand and Reinhold, New York (1976).

Craig, J. H. and Hock, J. L., *J. Vac. Sci. Tech*.**17(6)**, 1360 (1980).

Czanderna, A. W. and Hercules, D. M., *Ion Spectroscopies for Surface Analysis*, Plenum Press, New York (1991).

Dahl, D., *SIMION 3D v. 7.0*, Idaho National Engineering and Environmental Laboratory, Idaho Falls (2000).

Daly, N. R., *Rev. Sci. Inst*. **31(3)**, 264 (1959).

Dawson, P., *Quadrupole Mass Spectrometry and its Applications*, American Institute of Physics, New York (1995).

DiRubio, C. A., McEachern, R. L., McLean, J. G., and Cooper, B. H., *Phys. Rev. B* **54(12)**, 8862 (1996).

Dowek, D., *Thesis*, Université de Paris Sud, Orsay, France (1978).

Draxler, M., Gruber, R., Brongersma, H. H., and Bauer, P., *Phys. Rev. Lett*. **89(26)**, 263201-1 (2002).

Edelberg, E. A., Perry, A., Benjamin, N., and Aydill, E. S., *J. Vac. Sci. Tech. A* **17(2)**, 502 (1999).

Enge, H., *Rev. Sci. Inst*. **32**, 278 (1963).

Fano, U. and Lichten, W., *Phys. Rev. Lett* **14** (1965).

Fastrup, B., Hermann, G., and Smith, K. J., *Phys Rev. A* **3(5)**, 1591 (1971).

Fayeton, J., Andersen, N., and Barat, M., *J. Phys. B: At. Mol. Phys*. **9**, L149 (1976a).

Fayeton, J., *Thesis*, Université de Paris Sud, Orsay, France (1976b).

Firsov, O. B., *Sov. Phys – JETP* **5**, 1192 (1957).

Freeman, J. H., Temple, W., Beanland, D., and Gard, G. A., *Nuc. Inst. Meth.* **135**, 1 (1976).

Fuoco, E. R. and Hanley, L., *J. App. Phys*. **92(1)**, 37 (2002).

Gallon, T. E. and Nixon, A. P., *J. Phys. Condens. Matter* **4**, 9761 (1992).

Gordon, J. S., Bousetta, A., van den Berg, J. A., Armour, D. G., Kubiak, R., and Parker, E. H. C., *Nuc. Inst. Meth. Phys. Res. B* **55**, 314 (1991a).

Gordon, J. S., Armour, D. G., Donnelly, S. E., van den Berg, J. A., Marton, D., and Rabalais, J. W., *Nuc. Inst. Meth. Phys. Res. B* **59/60**, 312 (1991b).

Grizzi, O., Shi, M., Bu, H., Rabalais, J. W., and Baragiola, R. A., *Phys. Rev. B* **41**, 4789 (1990).

Guillemot, M., Maazouz, M. and Esaulov, V. A., *J. Phys. Condens. Matter* **8**, 1075 (1996a).

Guillemot, L., Lacombe, S., Tuan, V. N., Esaulov, V. A., Sanchez, E., Bandurin, Y. A., Dashchenko, A. I., and Drobnich, V. G., *Surf. Sci*. **365**, 353 (1996b).

Hagstrum, H., *Phys. Rev*. **96(2)**, 336 (1954).

Hart, R. G. and Cooper, C. B., *Surf. Sci*. **82**, L283 (1979).

Heiland, W., Shäffler, H. G., and Taglauer, E., *Surf. Sci*. **35**, 381 (1973).

Heiland, W., and Taglauer, E., *Nuc. Inst. Meth.* **132**, 535 (1976).

Holmes, A. J. T. and Thompson, E., *Rev. Sci. Inst*. **52(2)**, 172 (1981).

Hopwood, J., Guarnieri, C.R., Whitehair, S. J., and Cuomo, J. J., *J. Vac. Sci. Tech. A* **11**, 147 (1993).

Inghram, M. and Hayden, R., *A Handbook on Mass Spectroscopy*, Nuclear Science Series, Report No. 14, National Academy of Sciences, Pub. 311, Washington, D.C. (1954).

Ioup, G. E. and Thomas, B. S., *J. Chem. Phys.* **50(11)**, 5009 (1969).

Ishikawa, J., Takeiri, Y., and Takagi, T., *Rev. Sci. Inst.* **57(8)**, 1512 (1986).

Johnson, W. L. US Patent 5,234,529.

King, M. E., Nathanson, G. M., Hanning-Lee, M. A., and Minton, T. K., *Phys. Rev. Lett*. **70**, 1026 (1993).

King, M. E., Saecker, M. E., and Nathanson, G. M., *J. Chem. Phys*. **101**, 2539 (1994).

Lacombe, S., Esaulov, V., Guillemot, L., Grizzi, O., Maazouz, M., Mandarino, N., and Tuan, V. N., *J. Phys. Condens. Matter* **7**, L261 (1995).

Lau, W. M., Feng, X., Bello, I., Sant, S., Foo, K. K., and Lawson, R. P. W., *Nuc. Inst. Meth. Phys. Res. B* **59/60**, 316 (1991).

Lawson, J. D., *The Physics of Charged Particle Beams*, 2nd ed., Clarendon Press, Oxford (1988).

Lieberman, M. and Lichtenberg, A., *Principles of Plasma Discharges and Materials Processing*, John Wiley and Sons, New York (1994).

Lindhard, J. and Scharff, M., *Phys. Rev*. **124(1)**, 128 (1961).

Lindhard, J., Nielsen, V., and Scharff, M., *Fys. Medd. Dan. Vid. Selsk*. **36**, 1 (1968).

Lindhard, J., *Proc. Roy. Soc. A* **311**, 11 (1969).

Lipinsky, D., Jede, R., Ganschow, O., and Benninghoven, A., *J. Vac. Sci. Tech. A* **3**, 2007 (1985).

MacDonald, R. J. and O'Conner, D. J., *Surf. Sci*. **124**, 433 (1983).

Mahan, B., *The Classical Theory of Scattering*, Class Notes – Chemistry 370, Caltech (1986).

Massey, H. S. W. and Gilbody, H. B., *Electronic and Ionic Impact Phenomena*, v. 4 (1974).

Metz, W. A., Legg, K. O., and Thomas, E. W., *J. App. Phys*. **51(5)**, 2888 (1980).

McEachern, R. L., Goodstein, D. M., and Cooper, B. H., *Phys. Rev. B Condens. Matter* **39(15)**, 10503 (1989).

Mendelhall, M. and Weller, R., *Nuc. Inst. Meth. Phys. Res. B* **58**, 11 (1990).

Menzel, N. and Wittmaak, K., *Nuc. Inst. Meth. B* **7/8**, 366 (1985).

Miyake, K., Tachi, S., and Yagi, K., *J. App. Phys*. **53(4)**, 3214, 1982.

Möller, W., *Fundamentals of Ion-Surface Interactions*, Lecture, Technical University of Dresden (2001).

Morgensten, R., Niehaus, A., and Zimmermann, G., *J. Phys B* **13**, 4811 (1980).

Neihus, H., Heiland, W., and Taglauer, E., *Surf. Sci. Rep.* **17**, 213 (1993).

Neir, A., *Rev. Sci. Inst*. **11**, 212 (1940).

Neir, A., *Rev. Sci. Inst*. **18(6)**, 398 (1947).

Nixon, A. P., Gallon, T. E., Yousif, F., and Mathews, J. A. D., *J. Phys. Condens. Matter* **6**, 2681 (1994).

O'Conner, D. J. and Biersack, J. P., *Nuc. Inst. Meth. B* **15**, 14 (1986).

Oen, O. and Robinson, M., *Nuc. Inst. Meth*. **132**, 647 (1976).

Olsen, J. O., Andersen, T., Barat, M., Courbin-Gaussorgues, Ch., Sidis, V., Pommier, J., and Agusti, J., *Phys. Rev. A* **19**, 1457 (1979).

Ostgaard, O. J., Andersen, T., Barat, M., Courbin-Gaussorgues, Ch., Sidis, V., Pommier, J., Agusti, J., Andersen, N., and Russek, A., *Phys. Rev. A* **19**, 1457 (1979).

Pepper, S. V., *Surf. Sci*. **169**, 39 (1986).

Qin, F., Wang, X., Liu, Z., Yao, Z., Ren, Z., Su, S., Jiang, W., and Lau, W. M., *Rev. Sci. Inst*. **62(10)**, 2322 (1991).

Rabalais, J. W., Chen, J., Kumar, R., and Narayana, M., *J. Chem. Phys*. **12**, 6489 (1985a).

Rabalais, J. W., Chen, J., and Kumar, R., *Phys. Rev. Lett*. **55**, 1124 (1985b).

Rabalais, J. W., ed., *Low Energy Ion-Surface Interactions*, John Wiley & Sons, New York (1993).

Rabalais, J. W., *CRC Crit. Rev. Solid State Mater. Sci*. **14**, 319 (1998).

Rabalais, J. W., *Principles and Applications of Ion Scattering Spectrometry: Surface Chemical and Structural Analysis*, John Wiley and Sons, Inc., New Jersey (2003).

Sánchez, E. A., Grizzi, O., and Esaulov, V. A., *Surf. Sci*. **501**, 132 (2002).

Scoles, G. ed., *Atomic and Molecular Beam Methods*, vol. 1, Oxford Univ. Press, New York (1988).

Septier, A. ed., *Focusing of Charged Particles*, vol. 2, Academic Press, New York (1967).

Septier, A. ed., *Charged Particle Optics, Part C: Very High Density Beams*, Academic Press, New York (1983).

Shimizu, S., Tsukakoshi, O., Komiya, S., and Makita, Y, *Jap. J. App. Phys*. **24(9)**, 1130 (1985).

Slater, J., *Quantum Theory of Atomic Structure*, vol.1, McGraw-Hill, New York (1960).

Smith, D. P. and Goff, R. F., *Bull. Am. Phys. Soc*. **14**, 788 (1969).

Sobolewski, M., Olthoff, J., and Wang, Y., *J. App. Phys*. **85(8)**, 3966 (1999).

Souda, R., Yamamoto, K., Hayami, W., Aizawa, T., and Ishizawa, Y., *Phys. Rev. Lett*. **75**, 3552 (1995).

Souda, R., Yamamoto, K., Hayami, W., Aizawa, T., and Ishizawa, Y., *Surf. Sci.* **363**, 139 (1996).

Striganov, A. R. and Sventitskii, N. S., *Tables of Spectral Lines of Neutral and Ionized Atoms*, IFI/Plenum, New York (1968).

Tachi, S., Miyake, K., and Tokuyama, T., *Jap. J. App. Phys*. **20(6)**, L411 (1981).

Taglauer, E., and Heiland, W., *Surf. Sci*. **33**, 37 (1972).

Thomas, G. E., Beckers, L. J., Vrakking, J. J., and De Koning, B. R., *J. Cry. Growth* **56**, 557 (1982).

Tolstogouzov, A., Daolio, S., and Pagura, C., *Surf. Sci*. **441**, 213 (1999).

Tolstogouzov, A., Daolio, S., and Pagura, C., *Nuc. Inst. Meth. Phys. Res. B* **183**, 116 (2001).

Tolstogouzov, A., Daolio, S., Pagura, C., and Greenwood, C. L., *Surf. Sci.* **531**, 95 (2003).

Tongson, L. and Cooper, C., *Surf. Sci*. **52**, 263 (1975).

Tsukakoshi, O., Shimizu, S., Ogata, S., Sasaki, N., and Yamakawa, H., *Nuc. Inst. Meth. Phys. Res. B* **55**, 355, (1991).

UTI Instruments, *Notebook 73-4*, UTI Instruments, San Jose, California (1992).

Van Veen, G. N. A., Sanders, F. H. M., Dieleman, J., van Veen, A., Oostra, D. J., and de Vries, A. E., *Phys. Rev. Lett.* **57**, 739 (1986).

Weast, R, Astle, M., and Beyer, W., eds., *CRC Handbook of Chemistry and Physics*. 69th ed., CRC Press (1988).

Wehner, G. K., Stuart, R. V., and Rosenburg, D., *General Mills Report #2356*, General Mills Electronics Corp., Minneapolis (1962).

Williams, P. F., ed., *Plasma Processing of Semiconductors*, p. 529 (1997).

Winters, H. F. and Coburn, J. W., *App. Phys. Lett.* **34**, 70 (1979).

Winters, H. F., Coburn, J. W., and Chuang, T. J., *J. Vac. Sci. Tech. B* **1(2)**, 496 (1983).

Wittmaack, K., *Surf. Sci*. **345**, 110 (1996).

Wolf, B., ed., *Handbook of Ion Sources*, CRC Press, New York (1995).

Xu, F., Mandarino, N., Oliva, A., Zoccali, P., Camarca, M., Bonanno, A., and Baragiola, R. A., *Phys. Rev. A* **50**, 4040 (1994).

Xu, F., Manico, G., Ascione, F., Bonanno, A., and Oliva, A., *Phys. Rev. A* **57**, 1096 (1998).

Yamada, I., Inokawa, H., and Takagi, T., *Nuc. Inst. Meth. Phys. Res. B* **6**, 439 (1985).

Yang, M. C., Kim, C., Lee, H. W., and Kang, H., *Surf. Sci*. **358(1-3)**, 595 (1996).